Behaviour of Radium, Barium and the Rare Earth Elements in Mid-Atlantic Ridge Hydrothermal Plumes

Sean Selzer

St Edmund Hall

University of Oxford

A thesis submitted for the degree of Doctor of Philosophy

Hilary 2022

Hydrothermal activity influences the distributions of trace elements and isotopes (TEIs) in the ocean, which in turn impacts our understanding of oceanic TEI-cycling and the utility of TEIs as geochemical tools to study a variety of fundamental ocean processes. New data-sets have emerged in recent years that demonstrate importance of hydrothermal plumes for mediating seawater chemistry. Such influences are driven in part by vent fluid emissions, as well as the scavenging effects that mineral precipitates impose on deep waters circulating over ridge systems. Ridges themselves may also be important for driving changes to the physical mixing of deep ocean waters and the dispersion of hydrothermal TEI signatures. Herein, this thesis explores the behaviours of three potentially powerful but hitherto poorly understood marine tracers in hydrothermal plumes: short-lived radio-isotopes radium-223 and radium-224, the Eu anomaly (Eu*), and stable-isotopes barium-134 and barium-138. The data sets gathered for these studies derive from the sampling efforts along the Mid-Atlantic Ridge of GEOTRACES research cruise GA13 (JC156).

A validated Python program is presented to expedite the correction of raw data generated by Radium Delayed Coincidence Counting (RaDeCC) instruments and propagate related uncertainties.

The utility of radium-223 and -224 as tracers of hydrothermal neutrally buoyant plumes (NBPs) along the Mid-Atlantic Ridge (MAR) is investigated at Rainbow and TAG vent sites. Benthic inputs, likely to be hydrothermal sulphides, are common and constitute the dominant source of radium-223, and to a lesser extent radium-224, in the MAR axial valley. Elevated vertical diffusivities are calculated within the MAR axial valley from radium-223 and -224 water-column activity profiles.

The first analyses of dissolved Eu concentration ([Eu]) and Eu anomaly (Eu*) in NBPs at three vent sites show that hydrothermal Eu inputs are not expected to have an observable impact on seawater Eu*. Compiled Eu* values from global oceans show no significant variation in Eu* between ocean basins or with depth. Mean Eu* from compiled seawaters of 0.97 ($\pm$0.07, 2σ, PAAS-normalised) supports Post-Archaean Australian Shale (PAAS) and North American Shale Composite (NASC) as estimates of UCC Eu* inputs to the ocean.

The first coupled measurements of dissolved Ba concentration and $\delta^{138/134}$Ba in the hydrothermal NBP is presented. NBP waters at Rainbow and TAG display higher dissolved Ba concentrations and heavier $\delta^{138/134}$Ba values than surrounding ambient seawaters. Small hydrothermal Ba fractions calculated in NBP samples indicate that hydrothermal Ba inputs are unlikely to have an observable impact on the ocean Ba cycle. The extent of dilution occurring before an effective hydrothermal Ba-isotope composition is established is calculated to be 100 times smaller than previously assumed.

The results of this thesis evidence the utility of Ra- and Ba-isotopes as well as REEs for enhancing our increasingly complex understanding of hydrothermal plume processes at slow-spreading margins.

Behaviour of Ra, Ba and the Rare Earth Elements in Mid-Atlantic Ridge Hydrothermal Plumes

Sean Selzer

St Edmund Hall

University of Oxford

A thesis submitted for the degree of

Doctor of Philosophy

Hilary 2022

For Bengert, Ivy, Raymond and Susan.

Acknowledgments

First and foremost, I would like to thank my supervisors: Will Homoky, Amber Annett, Alan Hsieh and Gideon Henderson. Your support, mentorship and intellectual guidance have been invaluable, I left every meeting feeling more optimistic about my projects than when I came in.

I am also grateful that I have made some great friends during my time in Oxford, each inspirational in their own way.

Finally, I would like to acknowledge the unconditional support of my family who have always celebrated my education.

Abstract

Hydrothermal activity influences the distributions of trace elements and isotopes (TEIs) in the ocean, which in turn impacts our understanding of oceanic TEI-cycling and the utility of TEIs as geochemical tools to study a variety of fundamental ocean processes. New datasets have emerged in recent years that demonstrate importance of hydrothermal plumes for mediating seawater chemistry. Such influences are driven in part by vent fluid emissions, as well as the scavenging effects that mineral precipitates impose on deep waters circulating over ridge systems. Ridges themselves may also be important for driving changes to the physical mixing of deep ocean waters and the dispersion of hydrothermal TEI signatures. Herein, this thesis explores the behaviours of three potentially powerful but hitherto poorly understood marine tracers in hydrothermal plumes: short-lived radio-isotopes radium-223 and radium-224, the Eu anomaly (Eu*), and stable-isotopes barium-134 and barium-138. The data sets gathered for these studies derive from the sampling efforts along the Mid-Atlantic Ridge of GEOTRACES research cruise GA13 (JC156).

A validated Python program is presented to expedite the correction of raw data generated by Radium Delayed Coincidence Counting (RaDeCC) instruments and propagate related uncertainties.

The utility of radium-223 and -224 as tracers of hydrothermal neutrally buoyant plumes (NBPs) along the Mid-Atlantic Ridge (MAR) is investigated at Rainbow and TAG vent sites. Benthic inputs, likely to be hydrothermal sulphides, are common and constitute the dominant source of radium-223, and to a lesser extent radium-224, in the MAR axial valley. Elevated vertical diffusivities are calculated within the MAR axial valley from radium-223 and -224 water-column activity profiles.

The first analyses of dissolved Eu concentration ([Eu]) and Eu anomaly (Eu*) in NBPs at three vent sites show that hydrothermal Eu inputs are not expected to have an observable impact on seawater Eu*. Compiled Eu* values from global oceans show no significant variation in Eu* between ocean basins or with depth. Mean Eu* from compiled seawaters of 0.97 ($\pm$0.07, 2σ, PAAS-normalised) supports Post-Archaean Australian Shale (PAAS) and North American Shale Composite (NASC) as estimates of UCC Eu* inputs to the ocean.

The first coupled measurements of dissolved Ba concentration and $\delta^{138/134}$Ba in the hydrothermal NBP is presented. NBP waters at Rainbow and TAG display higher dissolved Ba concentrations and heavier $\delta^{138/134}$Ba values than surrounding ambient seawaters. Small hydrothermal Ba fractions calculated in NBP samples indicate that hydrothermal Ba inputs are unlikely to have an observable impact on the ocean Ba cycle. The extent of dilution occurring before an effective hydrothermal Ba-isotope composition is established is calculated to be 100 times smaller than previously assumed.

The results of this thesis evidence the utility of Ra- and Ba-isotopes as well as REEs for enhancing our increasingly complex understanding of hydrothermal plume processes at slow-spreading margins.

Contents

List of Figures

List of Tables

Chapter 1

Introduction

1.1 Context

Mid-ocean ridge (MOR) hydrothermal activity is an important component of the Earth-Ocean-Atmosphere system, impacting heat, water mass and chemical budgets (Elderfield and Schultz, 1996). Hydrothermal plume processes have long been thought to influence global trace element and isotope (TEI) ocean biogeochemistry due to the similarity of the mixing time of the thermohaline conveyor and residence time of the oceans with respect to hydrothermal plume mixing (Coale et al., 1991; Mackey et al., 2002; Toner et al., 2009; Tagliabue et al., 2010). The residence time of the oceans with respect to hydrothermal plume entrainment is approximately 10^3–10^4 years, while for the complete hydrothermal pathway this increases to 10^6 years.

First discovered by Corliss et al. (1979) at the Galápagos Rift, submarine hydrothermal circulation occurs frequently along the 55 000 km global mid-ocean ridge (MOR) network and at hot-spots, where heat is convected up from the lower mantle (figure 1.1). High temperature venting occurs along all mid-ocean ridges at all spreading rates and therefore in all ocean basins (Baker and German, 2004). To date, only one third of the strike length of global spreading margins has been systematically surveyed, indicating that the majority of hydrothermal vent sites along these margins are yet to be discovered (figure 1.1)(Beaulieu et al., 2015). As well as assessing the ubiquity of seafloor hydrothermal venting, it is important to understand how hydrothermal circulation alters the chemistry of seawater that is subducted, transported and emitted back into the ocean.

The basic architecture of a mature black smoker hydrothermal system (figure 1.2) - the

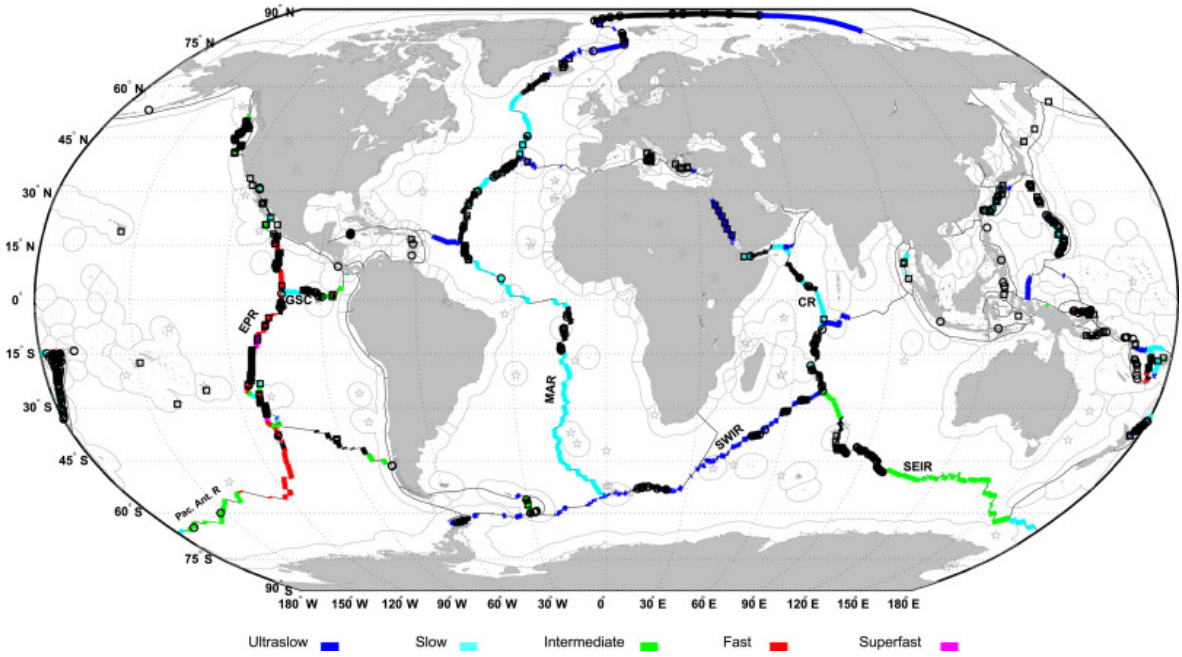

Figure 1.1: Map depicting the global ridge crest (reproduced from Beaulieu et al. (2015). The rate of spreading at different points along the global ridge crest is depicted with colour: ultraslow (blue), slow (light blue), intermediate (green), fast (red) and superfast (pink). Those areas marked in black have undergone systematic survey.

most iconic manifestation of hydrothermal activity - has been characterised by combining evidence from modern MORs and ancient sulfide deposits (Alt, 1995; Galley and Koski, 1999; Hannington et al., 1995). Below the seafloor, seawater undergoes heating and chemical alteration as it percolates through crustal rock, transforming into a heated solution, enriched in some TEIs while depleted in others. The composition of hydrothermal vent fluids is therefore modified by the following processes: magmatic degassing, phase-separation, water-rock interaction and, for low-temperature circulation (<120 °C), biological processes (Holland, 2003; Kashefi and Lovley, 2003; German and Seyfried, 2014). This newly formed hydrothermal fluid, buoyant due to its increased temperature and reduced salinity, rises toward the seafloor and emanates into the water-column (Rona and Speer, 1989; German et al., 1996a; McDonough, 2014).

As fluids rise from the seafloor, known as the "buoyant plume" (BP), they entrain surrounding seawater causing an increase in plume volume until neutral buoyancy is achieved, after which the plume continues to experience mixing and advection in ambient ocean waters; forming the "neutrally-buoyant plume"(NBP). Where hydrothermal fluids are emitted into oxic overlying waters at high temperatures, many reduced species in solution rapidly oxidize and precipitate, for example the precipitation and removal of Fe via Fe-(oxy)hydroxides (Eld-

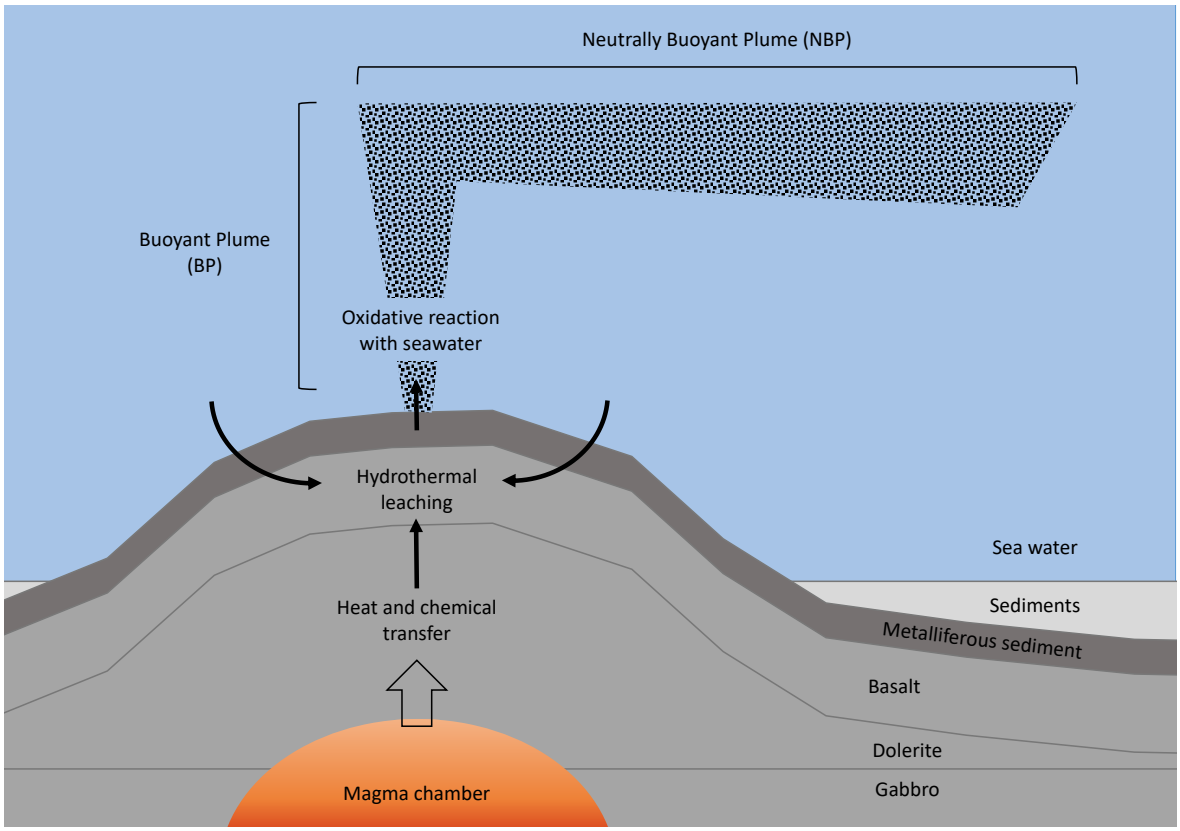

Figure 1.2: Mid-ocean ridge high-temperature hydrothermal circulation and hydrothermal plume production (adapted from figure 5.1b, German and Seyfried (2014)). Seawater percolates downward into the crust, where it is subject to heating and chemical transfer from the mantle such as mantle degassing. Fluids are modified by water-rock interaction and phase-separation throughout their circulation in the sub-seafloor hydrothermal system. Buoyant heated fluids then rise toward the seafloor and are emitted into overlying, oxidizing seawaters, forming the buoyant plume (BP). After sufficient entrainment of surrounding seawaters, the plume spreads laterally along a surface of equal density. This is the neutrally-buoyant plume (NBP).

erfield and Schultz, 1996; Lam et al., 2015). At these "black smoker" and "white smoker" vent sites, precipitates mainly consist of metal-oxides and -sulfides but can include other minerals such as barite.

In combination with high plume particulate density, the strong propensity of some elements to adsorb to particles results in these elements being removed not only from hydrothermal solutions but from ambient seawater too. In this way, hydrothermal activity can act as a net sink for some elements, such as rare earth elements (REEs), rather than a net source, as with Mn, Fe. Hydrothermal activity therefore exerts an influence on the distributions of TEIs in the ocean which in turn impacts our understanding of how these TEIs are cycled and how they might be used as geochemical tools to study ocean processes.

1.2 Trace elements and isotopes in hydrothermal plumes

1.2.1 Radium isotopes

Radium is a radioactive element, with four naturally occurring isotopes found in the ocean: Radium-223, -224, -226, and -228, with half lives of 11.4 days, 3.6 days, 1602 years and 5.7 years respectively (figure 1.3). While radium-223 is part of the uranium-235 decay chain, and radium-226 is part of the uranium-238 decay chain, radium-224 and -228 are both generated in the thorium-232 decay chain. Radium is assumed to behave conservatively within the ocean and each radium isotope radioactively decays with a different but known half-life. These attributes make radium isotopes powerful, time-sensitive tracers of processes such as mixing and dilution. They have been used to trace and quantify important ocean processes in coastal (Tamborski et al., 2020; Moore, 2000b), shelf-sea (Hendry et al., 2019), open ocean surface (Charette et al., 2007) and deep water settings (Kipp et al., 2018).

Elevated activities of short-lived radium isotopes, radium-223 and radium-224, have been measured in hydrothermal fluid end-members at the Puna Ridge, Juan de Fuca Ridge (JdFR) and the Reykjanes Ridge (Moore et al., 2008; Kadko and Butterfield, 1998; Kadko et al., 2007). Radium isotopes are therefore potential time-sensitive tracers of mixing and transport during hydrothermal circulation and in hydrothermal plumes on time-scales of days to weeks.

Kipp et al. (2018) used radium-224/radium-228 isotope ratios at the Trans-Atlantic Geotraverse (TAG) vent site NBP to estimate plume age while Neuholz et al. (2020) modelled plume mixing and advection using short-lived radium isotopes at Brothers volcano, in the Kermadec Arc. Implicit in both the estimation performed by Kipp et al. (2018) and the models employed by Neuholz et al. (2020) are a number of assumptions.

One key assumption that must be made when short-lived radium isotopes are used to quantify plume dispersion rates or age plume samples is that any radium detected in a water sample must originate from the site of focussed venting under investigation. Any contribution of radium isotopes to the water sample from other sources would modify the isotope activities observed and render any age or rate calculated from these observed activities inaccurate. Indeed, Neuholz et al. (2020) states that the 'apparent ages' calculated are qualitative rather than quantitative while Kipp et al. (2018) was unable to age plume samples using radium-223 due to a significant bottom water source of radium-223 at TAG vent site. Further measurements of short-lived radium isotope activities with greater resolution at hydrothermal

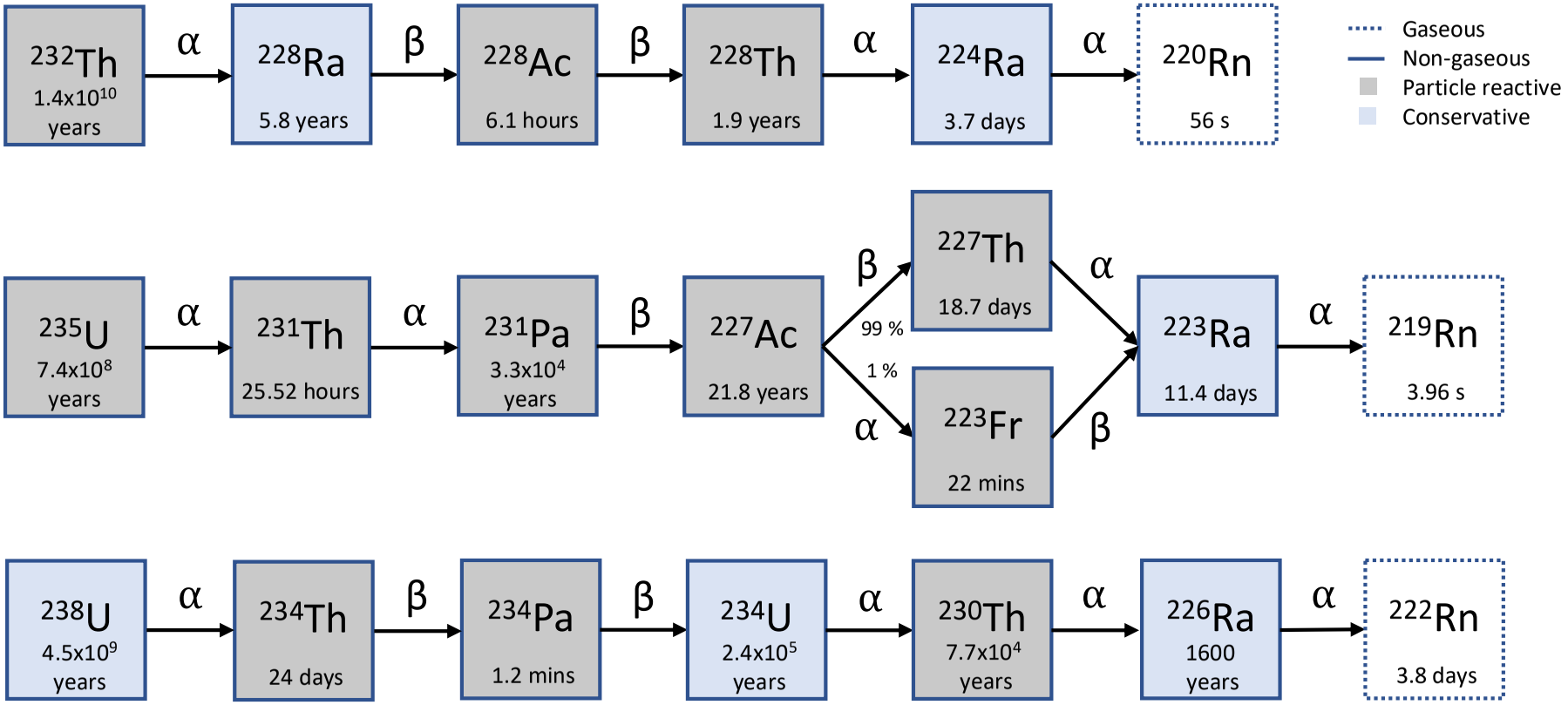

Figure 1.3: The generation of the radium quartet via radioactive decay from thorium-232, uranium-235 and uranium-238. Partial decay chains of thorium-232, uranium-235 and uranium-238 are displayed, showing the type of decay occurring between each isotope. The state and chemical behaviour of each element is indicated by colour and border type: particle reactive (grey), conservative or quasi-conservative (blue), gaseous (dashed border) and non-gaseous (solid border).

vent sites could help determine the ubiquity and strength of bottom water sources relative to hydrothermal venting.

In chapter 3, short-lived radium isotope activity measurements of unprecedented resolution are presented from two hydrothermal vent sites along the MAR. These activities are used to explore the dominance of bottom water sources within the axial valley, and test the validity of the point-source assumption used previously by other work. Strong vertical gradients in both radium-223 and -224 are then used to estimate vertical diffusivity within the MAR axial valley, to evaluate its significance for the vertical flux of nutrients and TEIs from the axial valley into surrounding ocean waters.

1.2.2 Rare Earth Elements (REEs)

The rare earth elements are a series of fifteen lanthanide elements (atomic number, $Z = 57 - 71$) with the addition of yttrium ($Z = 39$) and scandium ($Z = 21$) (Nozaki, 2001). The chemical coherence of the REE series and sensitivity of the REE pattern to geochemical and physical processing provides opportunities to investigate processes controlling the composition of natural waters. The major input of REEs to ocean is from weathering of Upper Continental Crust (UCC) while the dominant sink is removal of REEs to sediments via adsorption to sinking particles. Hydrothermal fluids are $10^2 - 10^4$ times enriched in REEs compared to seawater (German et al., 1990; Klinkhammer et al., 1995; Douville et al., 2002).

Due to the extremely acidic, high-temperature and highly reducing conditions present in sub-seafloor hydrothermal systems, high-temperature vent fluids obtain a unique REE pattern. The most prominent feature of the hydrothermal REE pattern is the enrichment of Eu with respect to Gd and Sm, known as a positive Eu anomaly (Eu*). Elderfield et al. (1988) hypothesised that the elevated Eu/Sm ratio in hydrothermal vent fluids might trace the input of REEs to the ocean from hydrothermal systems globally.

In order to impart a measurable change to the pattern of seawater, the positive Eu anomaly in hydrothermal fluids must survive plume particle scavenging and be transmitted by a large enough flux. If hydrothermal inputs of REEs to the ocean do not have a measurable impact on the REE pattern of seawater then seawater REE patterns may record the variety of REE patterns of UCC surrounding each basin.

Mitra et al. (1994) measured REE patterns in hydrothermal fluids and in the buoyant

plume at TAG hydrothermal vent site, observing that even the most dilute samples (seawater/hydrothermal fluid ratio ≈ 700) displayed Eu* significantly higher than ambient seawater. The NBP, later in the evolution of the plume, can reach seawater/fluid ratios in excess of 10^4 (Feely et al., 1994). Although buoyant plume measurements from Mitra et al. (1994) support the hypothesis of Elderfield et al. (1988), in order to fully assess the utility of Eu* in quantifying the hydrothermal REE flux to the ocean, measurements of REE concentrations from the NBP are needed.

In chapter 4, measurements of REE concentrations in NBPs at Lucky Strike, Rainbow and TAG vent sites along the MAR are presented. These measurements are used to estimate a global hydrothermal flux and assess the change in mean seawater Eu* expected from hydrothermal REE inputs. In addition, further REE concentration measurements from the GEOTRACES GA13 section are used with previous REE concentration data from the GEOTRACES international data product 2017 (Schlitzer et al., 2018) to investigate variability in Eu* in the global ocean and assess the accuracy of shale composite UCC Eu* values.

1.2.3 Barium isotopes

Barium is a group 2 element with five stable isotopes: Barium-134, -135, -136, -137 and -138. Barite has been used as a tracer of past ocean productivity (Paytan et al., 1996; Paytan and Griffith, 2007), seawater alkalinity (Jeandel et al., 1996; Rubin et al., 2003) and ocean circulation (Lea and Boyle, 1989), while Ba_{xs} has been applied as a tracer of past ocean productivity and seawater alkalinity (Dymond et al., 1992; McManus et al., 1999). Important gaps in our understanding of the ocean Ba cycle however remain, including the precise mechanisms and depths for barite formation and Ba removal.

Ba is actively cycled in the oceans, with a nutrient-like distribution exhibiting surface depletion, deep-water enrichment and a north-south increase in deep-water concentration (Horner et al., 2015; Bates et al., 2017). The main process controlling seawater $\delta^{138/134}$Ba is the formation and dissolution of barite which preferentially incorporates light Ba isotopes from solution (Von Allmen et al., 2010; Böttcher et al., 2018). The main input to the ocean is from rivers and is isotopically light (Cao et al., 2020; Hsieh and Henderson, 2017; Gou et al., 2020). The main sink of Ba from seawater is into marine sediments as precipitated barite which is also isotopically light (Horner et al., 2017; Bridgestock et al., 2018; Crockford

et al., 2019). Barium isotopes therefore display potential utility as tracers of oceanic barium cycling.

Large-scale circulation acts to distribute and mix barium isotope signals, meaning that the dissolved Ba distribution in the ocean represents a combination of removal and regeneration processes with mixing and advection (Horner et al., 2015; Bates et al., 2017; Hsieh and Henderson, 2017). Ba-isotopic variations in the deep ocean are clearly influenced by large-scale ocean circulation; deep ocean variation is well explained by conservative mixing of major South Atlantic water masses, each possessing a distinct Ba concentration ([Ba]) and Ba-isotopic ratio $\delta^{138/134}Ba_{NIST}$ (Bates et al., 2017). Hsieh and Henderson (2017) noted measurements made by Bates et al. (2017) that appear to deviate from a conservative mixing line connecting North Atlantic deep water (NADW) and Antarctic bottom water (AABW). These authors proposed isotopically heavy inputs from hydrothermal venting or sediments as potential causes of non-conservative behaviour of barium in deep Atlantic waters, but lacked sufficient data to test these hypotheses.

The first coupled measurements of barium concentration and barium isotopes in hydrothermal vent fluids led Hsieh et al. (2021) to calculate an effective hydrothermal end-member, after precipitation of barite, that is isotopically heavy with respect to barium. Using this effective hydrothermal barium end-member, it was calculated that some deep Atlantic waters contain a hydrothermal barium fraction of ≈ 9 %. Given these large hydrothermal fractions in deep waters sampled far from any mid-ocean ridge, samples from a hydrothermal NBP would be expected to contain even higher hydrothermal Ba fractions.

In chapter 5 the first coupled barium concentration and $\delta^{138/134}$Ba data from the Rainbow and TAG NBPs on the MAR are presented. These data are used to assess the likelihood of a hydrothermal cause for observed non-conservative barium behaviour in the deep Atlantic. In addition, two end-member mixing models are employed with He- and Ba-isotopes to quantify the amount of seawater dilution hydrothermal fluids undergo before the effective hydrothermal barium end-member from Hsieh et al. (2021) is established.

1.3 Thesis aims and structure

The overarching aim of this thesis is to investigate the behaviour of radium, barium and the rare earth elements (REEs) at Mid-Atlantic Ridge hydrothermal vent sites. The thesis is

divided into four key chapters that will each address a specific set of objectives:

- Chapter 2 will present and validate a Python program that automates and expedites the correction of raw data and propagation of related uncertainties from RaDeCC instruments.

- Chapter 3 will assess the use of radium-223 and -224 as tracers of hydrothermal NBPs at two MAR hydrothermal vent sites while investigating previously observed bottom water sources of radium-223 and -224. Using water-column activity profiles of radium-223 and -224, vertical diffusivities in the MAR axial valley will be estimated.

- Chapter 4 will use dissolved concentrations of REEs at three hydrothermal vent sites to estimate the hydrothermal flux of Eu to the ocean and therefore the influence of hydrothermal inputs on the Eu* of seawater. Further REE concentration measurements from the GEOTRACES GA13 transect will also be used in conjunction with GEOTRACES IDP 2017 data to assess the variability of seawater Eu* globally with implications for the accuracy of UCC inputs estimated from shale composites.

- Chapter 5 will investigate a previous estimate of effective hydrothermal Ba end-member as an explanation for observations of non-conservative behaviour of Ba in Atlantic deep-waters. Barium isotope and helium isotope data will also be employed in two end-member mixing models to quantify dilution that occurs before the effective Ba endmember is established.

Finally, chapter 6 will summarise and discuss wider implications of the results and conclusions from previous chapters as well as suggesting opportunities for future investigation.

Chapter 2

RaDeCC Reader: Fast, accurate and automated data processing for Radium Delayed Coincidence Counting systems

This chapter has been reproduced verbatim from Selzer et al. (2021) (see Appendix, Section A.2)

2.1 Abstract

A Python program is presented to expedite the process of correcting raw data and propagating the related uncertainties from Radium Delayed Coincidence Counting (RaDeCC) instruments. The performance of the program was validated against an established method with real data. Excellent agreement between determinations of excess radium-223, actinium-227, excess radium-224, thorium-228 and radium-226 was achieved, with minor discrepancies in the results attributed to logical improvements in our implementation. The RaDeCC Reader program is able to process one thousand data files in only a few minutes, and thereby offer distinct advantages in processing speed combined with reliable accuracy of data processing implementations.

2.2 Introduction

Radium is a valuable tracer for environmental geochemistry due to the conservative nature of radium in seawater and the predictable rates of decay of its isotopes. Disequilibria between these isotopes can allow the quantification of rates of exchange between natural reservoirs (Cochran, 1982). The development of Radium Delayed Coincidence Counting (RaDeCC) systems has made radium-based studies in aqueous environments more feasible (Moore and Arnold, 1996). For example, radium isotopes are increasingly used to trace, quantify and advance understanding of many fundamental ocean processes in coastal (Tamborski et al., 2020; Moore, 2000b), shelf sea (Hendry et al., 2019), open ocean surface (Charette et al., 2007) and deep water settings (Kipp et al., 2018).

To measure the activities of radium-223 and radium-224 in aqueous environments, sample water is commonly pumped through manganese oxide impregnated acrylic or polyethylene fibres (Moore, 1976). These fibres extract radium, its parent isotopes thorium and actinium, and other species with high affinity for MnO_2, from the water via binding to the MnO_2 functional groups present on the fibres. The precise activities of radium isotopes on these fibres can be determined by counting their daughter isotopes radon and polonium using a scintillation counting technique that is optimally performed by the RaDeCC apparatus (https://www.radecc.com) (Moore and Arnold, 1996).

The RaDeCC system of delayed coincidence counting was originally devised by Giffin et al. (1963) and forms the basis of the RaDeCC apparatus devised by Moore and Arnold (1996). The RaDeCC apparatus measures the activities of radon isotopes – the nuclides produced from radium decay - emanating from sample fibres over the course of a counting period, herein termed "read". The flow of helium through a closed loop carries this radon between the sample fibre container and the scintillation cell. Radon decay in the scintillation cell produces an alpha particle which is detected, generating a signal which is routed to three channels: total counts, radon-219 and radon-220. The total counts channel records a count when any signal is received. In the radon-219 and radon-220 channels the system looks for a second count, corresponding to the subsequent decay of daughters polonium-215 and polonium-216 (respectively) after a short delay for the signal to stabilise: 0.01 ms for the radon-219 channel and 5.61 ms for the radon-220 channel (Moore and Cai, 2013). After these delays a gate is opened in each channel (5.6 ms and 600 ms for radon-219 and radon-

220, respectively; Moore and Arnold (1996)) in which an additional signal of alpha decay is required in order to register a count. During a read the RaDeCC software logs the counts and accumulated counts per minute for each channel at regular user-defined intervals to a text file.

Factors that need to be corrected for in the raw output include: interference between the detector channels for radon-219 and -220 and chance coincidence events; the counting efficiency and background (blank) of each detector; decay that occurred between sampling and measurement; rescaling sample activities to their original sample volumes (Giffin et al., 1963; Moore and Arnold, 1996). The expressions used to propagate uncertainties associated with these corrections were derived by Garcia-Solsona et al. (2008).

The amount of radium parent isotope on the MnO_2 coated fibres determines the rate of production of the radon isotope daughter, and therefore the activity sustained in the flow of helium through a closed loop between the sample and the RaDeCC system. The decay of actinium and thorium on the fibres supplements the amount of 'excess' radium-223 and radium-224 that is initially present (creating supported activity) leading to the activities of radon-219 and radon-220 initially measured by the RaDeCC system. These supported activities must be accounted for to accurately determine the excess, or unsupported, activities of radium-223 and radium-224. Finally, there is the ingrowth of radon-222 from its long-lived parent isotope, radium-226, recorded by the total channel. The rate of radon-222 ingrowth can be used to estimate the activity of radium-226 (Geibert et al., 2013). To perform the necessary raw data correction and uncertainty propagation calculations, many workers construct large Excel spreadsheets and individually import their saved read file outputs from RaDeCC apparatus. Although this process allows a very granular view of the raw data and can serve its purpose well, it remains time intensive and large sets of data are susceptible to user-error. A faster, user-defined automation that preserves details of the calculation processes could therefore offer significant improvements to data processing speed and the reliability of outputs. Herein, we present our approach to expedite the process of correcting raw data and propagating the related uncertainties from Radium Delayed Coincidence Counting (RaDeCC) instruments using a newly designed program, RaDeCC Reader. We prove the validity of our new method by comparing results obtained with RaDeCC Reader to those we obtained by a previously established method using real data collected from karstic spring-,

coastal- and open-ocean water samples.

2.3 Theory

2.3.1 Calculation of excess radium-223 and radium-224 activities

To convert raw decay counting statistics into the activity of radium-223 or radium-224 of a sample, a number of factors must be considered and corrected for. A table of variables and their units is included for reference (Table 2.1).

Uncertainties in the raw counts must also be propagated through each of these corrections to determine uncertainties in final calculated activities. An erroneously registered count due to chance coincidence events (Y CC, in cpm) is the first correction to be made. An erroneous count can be made when a decay event that is unrelated to the isotope of interest occurs while the detector-gate for that isotope's channel is open. These can originate from the background activity in the detectors or the decay of radon-222 while the 219 or 220 channels are open. The counts per minute (cpm) attributed to chance coincidence events are subtracted from the count rate in the relevant channel. Expressions to calculate the contribution of chance coincidence events in each channel (Equations 2.1, 2.2) were derived by Giffin et al. (1963) and were included by Garcia-Solsona et al. (2008), where cpm total, cpm219 and cpm220 are the counts per minute in the total, 220 and 219 counting channels respectively. The constant values 0.01 and 0.000093 are the duration of time, in seconds, that the 220- and 219-gates are open.

$$\text{Y 220 CC} = \frac{(\text{cpm total} - \text{cpm220} - \text{cpm219})^2 \times 0.01)}{1 - ((\text{cpm total} - \text{cpm220} - \text{cpm219}) \times 0.01)} \tag{2.1}$$

$$\text{Y 219 CC} = \frac{(\text{cpm total} - \text{corr220} - \text{cpm219})^2 \times 0.000093}{1 - ((\text{cpm total} - \text{corr220} - \text{cpm219}) \times 0.000093)} \tag{2.2}$$

These chance coincidence events are then subtracted from the counts per minute in the relevant channel to determine the coincidence corrected counts (corr220, corr219).

$$\text{corr220} = \text{cpm220} - \text{Y 220 CC} \tag{2.3}$$

$$\text{corr219} = \text{cpm219} - \text{Y 219 CC} \tag{2.4}$$

Variable	Unit	Description
Y 219 CC	cpm	Erroneously registered 219 channel chance coincidence counts
Y 220 CC	cpm	Erroneously registered 220 channel chance coincidence counts
cpm219	cpm	counts per minute (219 channel)
cpm220	cpm	counts per minute (220 channel)
cpm total	cpm	counts per minute (total channel)
corr219	cpm	cpm219 corrected for Y 219 CC
corr220	cpm	cpm220 corrected for Y 220 CC
final219	cpm	corr219 corrected for cross-channel interference
final220	cpm	corr220 corrected for cross-channel interference
E219	-	Detection efficiency of the 219 channel
E220	-	Detection efficiency of the 220 channel
$\text{Ratio}_{219/220}$	-	Detection efficiency ratio of the 219 and 220 channels
P_{219}	-	Probability of radon-219 decaying in the cell
P_{220}	-	Probability of radon-220 decaying in the cell
L_{219}	-	Loss resulting from the 219 channel delay and window settings
L_{220}	-	Loss resulting from the 220 channel delay and window settings
bkgcorr223	cpm	final219 corrected for background
bkgcorr224	cpm	final220 corrected for background
dpm223	cpm	bkgcorr223 corrected for detection efficiency
dpm224	cpm	bkgcorr224 corrected for detection efficiency
vdpm223	dpm/m^3	dpm223 corrected for sample volume
vdpm224	dpm/m^3	dpm224 corrected for sample volume
$^{223}_{\text{i}}\text{Ra}$	dpm/m^3	vdpm223 for the initial read (including supported fraction)
$^{223}_{\text{s}}\text{Ra}$	dpm/m^3	vdpm223 for the initial read (supported fraction only)
$^{224}_{\text{i}}\text{Ra}$	dpm/m^3	vdpm224 for the initial read (including supported fraction)
$^{224}_{\text{s}}\text{Ra}$	dpm/m^3	vdpm224 for the initial read (supported fraction only)
λ_{223}	days^{-1}	Decay constant for radium-223
λ_{224}	days^{-1}	Decay constant for radium-224
$^{223}_{\text{xs}}\text{Ra}$	dpm/m^3	Excess radium-223 activity
$^{224}_{\text{xs}}\text{Ra}$	dpm/m^3	Excess radium-224 activity
vdpm226	dpm/m^3	Radium-226 activity
$\text{vdpm226}_{\text{initial}}$	dpm/m^3	Radium-226 activity initially measured in sample
slope of cpm total	cpm/min	Gradient of counts over time in the total channel
m	-	Radium-226 conversion factor
E226	-	Detection efficiency for radium-226
Volume	L, kg	Volume or mass of sample water

Table 2.1: Glossary of variable terms used, their descriptions and units.

In certain circumstances the decays associated with radon-219 can be erroneously registered in the 220-channel. This can happen if two atoms of radon-219 decay within the time that

the 220 channel is open. Radon-220 can also cause interference in the radon-219 channel since the gate for this channel is open for enough time that 2.55% of radon-220 decay events occur while the gate is open. Expressions to account for these cross-channel interferences were devised by Giffin et al. (1963) and adapted by Moore and Arnold (1996).

$$\text{final 220} = \text{corr220} - \frac{(1.6 \times \text{corr219})^2 \times 0.01}{1 + (1.6 \times \text{corr219}) \times 0.01} \tag{2.5}$$

$$\text{final 219} = \text{corr219} - (\text{corr220} \times 0.0255) \tag{2.6}$$

In addition, background measurements may be run with MnO_2-coated fibres that were not used for sampling, assessing any counts due to contamination on the fibre or within the RaDeCC apparatus itself, although the need for a background correction varies with sample type and application. Where required, the background count rate (in cpm) in each channel is averaged over multiple reads for each detector. The averaged background count rate from the applicable detector and channel is then subtracted from final220 and final219 before detector efficiencies are accounted for (bkgcorr224, bkgcorr223 respectively; Equations 2.7, 2.8).

$$\text{bkgcorr224} = \text{final220} - \text{bkg220}_{\text{Average}} \tag{2.7}$$

$$\text{bkgcorr223} = \text{final219} - \text{bkg219}_{\text{Average}} \tag{2.8}$$

The detection efficiencies, E219 and E220, are evaluated by measuring the activities of standards with a known amount of radium-223 or radium-224 adsorbed to their fibres and comparing these measured activities (in cpm) to their known activities (in dpm) after corrections for decay since manufacture (Equations 2.9, 2.10). These standards are made by adsorbing known activities of thorium-232 or actinium-227 in secular equilibrium with their daughter isotopes, radium-224 and radium-223 respectively.

$$\text{E220} = \frac{\text{final220 (standard))}}{\text{thorium-232}} \tag{2.9}$$

$$\text{E219} = \frac{\text{final219 (standard))}}{\text{actinium-227}} \tag{2.10}$$

Alternatively E219 can be determined from E220 using equations 2.11 and 2.12 (Moore and

Cai, 2013).

$$\text{Ratio}_{\text{E219/E220}} = \frac{P_{219} \times (1 - L_{219})}{P_{220} \times (1 - L_{220})} \tag{2.11}$$

$$\text{E219} = \text{E220} \times \text{Ratio}_{\text{E219/E220}} \tag{2.12}$$

In which E220 is the 220-channel system efficiency, P is the probability of the radon isotope decaying in the counting cell and L is the fractional loss due to delay and window settings. Fraction loss (L) will depend on the default RaDeCC apparatus time constants or those set by the operator as described by Moore and Cai (2013). The ratio E219/E220 for the RaDeCC with default settings and normal configuration is 0.91 (Moore and Cai, 2013).

The counts per minute due to radon-219 and radon-220 are converted to disintegrations per minute (dpm) by dividing final220 or final219 by the detection efficiency of the channel, (E219 or E220, respectively; Equations 2.13, 2.14) (Giffin et al., 1963; Moore and Arnold, 1996).

$$\text{dpm224} = \frac{\text{bkgcorr224}}{\text{E220}} \tag{2.13}$$

$$\text{dpm223} = \frac{\text{bkgcorr223}}{\text{E219}} \tag{2.14}$$

Finally, the dpm values are divided by the sample volume (or mass) to produce the volume-corrected radium-223 (vdpm223) and radium-224 (vdpm224) sample activities (both in dpm m-3) for each read (Equations 2.15, 2.16).

$$\text{vdpm224} = \frac{\text{dpm224}}{\text{volume}} \times 1000 \tag{2.15}$$

$$\text{vdpm223} = \frac{\text{dpm223}}{\text{volume}} \times 1000 \tag{2.16}$$

To obtain the excess radium-224 and radium-223 activities of the samples at the time of sampling, two further factors must be accounted for: decay of the isotope between sampling and measurement and any activity supported by the parent isotope. The respective parent or supporting isotopes of radium-223 and radium-224 are actinium-227 and thorium-228.

In order to distinguish the activities of parent and daughter isotopes, each sample must be analysed multiple times at different intervals relative to the time of collection. The 1st interval read, performed as soon after sampling as possible, is a measurement of radium-223

and radium-224 activity, this will be a combination of excess and supported activities. A 2nd interval, 7-10 days after sampling, can provide a more accurate radium-223 activity due to reduced interference from radium-224 and radon-220 decay (Moore, 2008), and is essential in instances where the 220/219 count rate is greater than 10, or greater than 4 and the 220 channel exceeds 5 cpm (Diego-Feliu et al., 2020). Eventually, >99% of measured radium-224 and radium-223 activities will be supported by their parent isotopes. This occurs after 25 days for radium-224 and after 80 days for radium-223, and dictates the timing of 3rd and 4th intervals. In effect, 3rd and 4th interval reads provide an indirect measurement of these parent isotope activities, thorium-228 and actinium-227 respectively.

$$^{224}_{xs}\mathrm{Ra} = \frac{^{224}_{i}\mathrm{Ra} - ^{224}_{s}\mathrm{Ra}}{e^{-\lambda_{224}\times t}} \tag{2.17}$$

$$^{223}_{xs}\mathrm{Ra} = \frac{^{223}_{i}\mathrm{Ra} - ^{223}_{s}\mathrm{Ra}}{e^{-\lambda_{223}\times t}} \tag{2.18}$$

Excess radium-224 ($^{224}_{xs}$Ra) and excess radium-223 ($^{223}_{xs}$Ra) at the time of sampling is then calculated via equations 2.17 and 2.18, where $^{223}_{i}$Ra and $^{224}_{i}$Ra are the radium-223 activity of the 1st or 2nd interval read and the radium-224 activity of the 1st interval read, $^{223}_{s}$Ra the activity supported by actinium-227 decay (4th interval) and $^{224}_{s}$Ra the radium-224 activity supported by thorium-228 decay (3rd interval). The time between sampling (in days) and the first measurement of each isotope is denoted by t and the respective decay constants of radium-223 and radium-224 by λ_{223} and λ_{224}. For all calculations, including detector efficiencies, error propagation follows the equations presented in Garcia-Solsona et al. (2008).

2.3.2 Calculation of radium-226 activity

The activity of long-lived radium-226 is measured indirectly via the rate of ingrowth of its decay product, radon-222. The half-life of radon-222 is 3.8 days, so as radium-226 in the sample decays over the course of a read, radon-222 accumulates in the system. This accumulation is seen in the total channel, with counts in the total channel increasing throughout the read in proportion to the radium-226 activity of the sample (Geibert et al., 2013). The slope of cpm total versus time during a run thus provides a measure of the radium-226 activity of the sample, based on the conversion factor 'm', which has a theoretical value of 1.80 $\pm$ 0.7×10^{-4} min^{-1}. The uncertainty in m originates from the range of radium-226 count rate

(40 cpm to 475 cpm) used in simulations by Diego-Feliu et al. (2020).

Each RaDeCC detector must also be calibrated by measuring a standard with known radium-226 activity, calculated as for E220 in equation 2.19. Volume-corrected radium-226 activity of the sample (vdpm226, in dpm/m^3) is then calculated using equation 20, where 'vdpm226initial' is the initial volume corrected radium-226 activity (in cpm/m^3; equation 2.20) and 'E226' is the efficiency of system in determining radium-226 activity. This method was devised by Geibert et al. (2013) and modified by (Diego-Feliu et al., 2020).

$$\text{vdpm226}_{\text{initial}} = \frac{\text{slope of cpm total}}{m \times \text{Volume}} \times 1000 \tag{2.19}$$

$$\text{vdpm226} = \frac{\text{vdpm226}_{\text{initial}}}{\text{E226}} \tag{2.20}$$

2.4 Implementation: The RaDeCC Reader program

The RaDeCC Reader program is a collection of python scripts that quickly processes RaDeCC output files. The program works from a single folder containing all read files including those of standards and backgrounds (or blanks), sample log sheets and a small amount of user input via a graphical user interface (GUI; figure 2.1). From this folder, it creates an organised directory of read files, a table of calculated detector efficiencies with propagated uncertainties and a table of corrected excess radium-223, excess radium-224, thorium-228, actinium-227 and radium-226 activities (in dpm/m3) (figure 2.2). The tabulated outputs also detail each correction and its propagated uncertainty for each read of each sample. Additional transparency is provided by plots of counts-per-minute vs. time for the 219, 220 and total channels, produced for each read (figure 2.3) as well as plots depicting any anomalous spikes that have been automatically removed. Data quality warnings and errors are also flagged alongside calculated results in output tables as outlined in Section 2.4.1.

2.4.1 Essential information for the program

The RaDeCC Reader program receives information in three ways: text files output by the RaDeCC apparatus, the sampling log-sheet and the graphical user interface (GUI). Information entered into the GUI entry fields are used to aid the program in file-handling and provide standard and instrument specific parameters required for the data corrections and

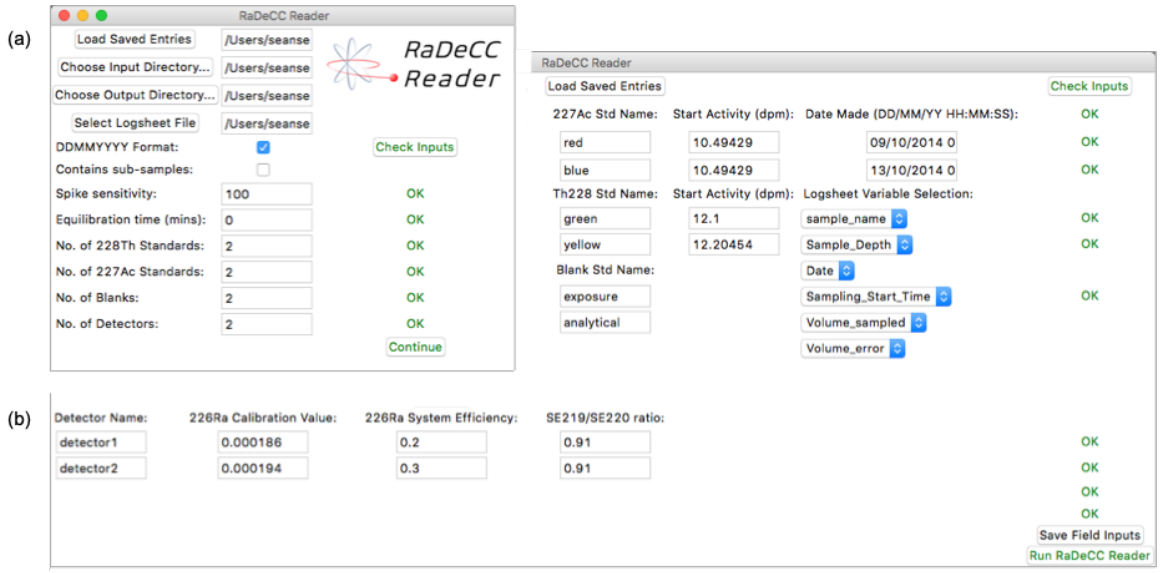

Figure 2.1: Details of the Graphical User Interface (GUI) used to operate RaDeCC Reader. This provides a verifiable summary of editable and necessarily user defined input parameters. Including (a) input and output file directories, date and data formats, calculation preferences, and the inventory of standards, backgrounds and detectors, and (b) details of individual detector names and efficiencies, standard names and activities, background names, and logsheet variables. In all fields of the GUI users may save and load previous inputs and check inputs before running the RaDeCC Reader program.

uncertainty propagations. Once completed these GUI entries can be saved by the user and reloaded for subsequent runs of the program.

Directories The first entry fields in the GUI are the input and output directories (figure 2.1a) and the log-sheet. The input directory is where the program will find all the input read files and the log-sheet. The output directory is where the program will place the organised read files, the log-sheet file and output files.

Log-sheets: Linear and Branched sample sets Log-sheets form the basis of the eventual output files, in which all the metadata contained within a log-sheet will be included. A log-sheet must contain information that is essential to data correction calculations: sample names, sample volumes and mid-point sampling times; as well as any sub-sample names (for herein so-called 'branched' datasets) if applicable. There should be a column displaying each of these variables in a log-sheet. Any additional information contained in a log-sheet (e.g. the latitude, longitude and depth of individual samples) is preserved in the output files and will not interfere with the calculations but may prove useful for later analysis. An example log-sheet file is included in the Supplementary Information. The date format convention for

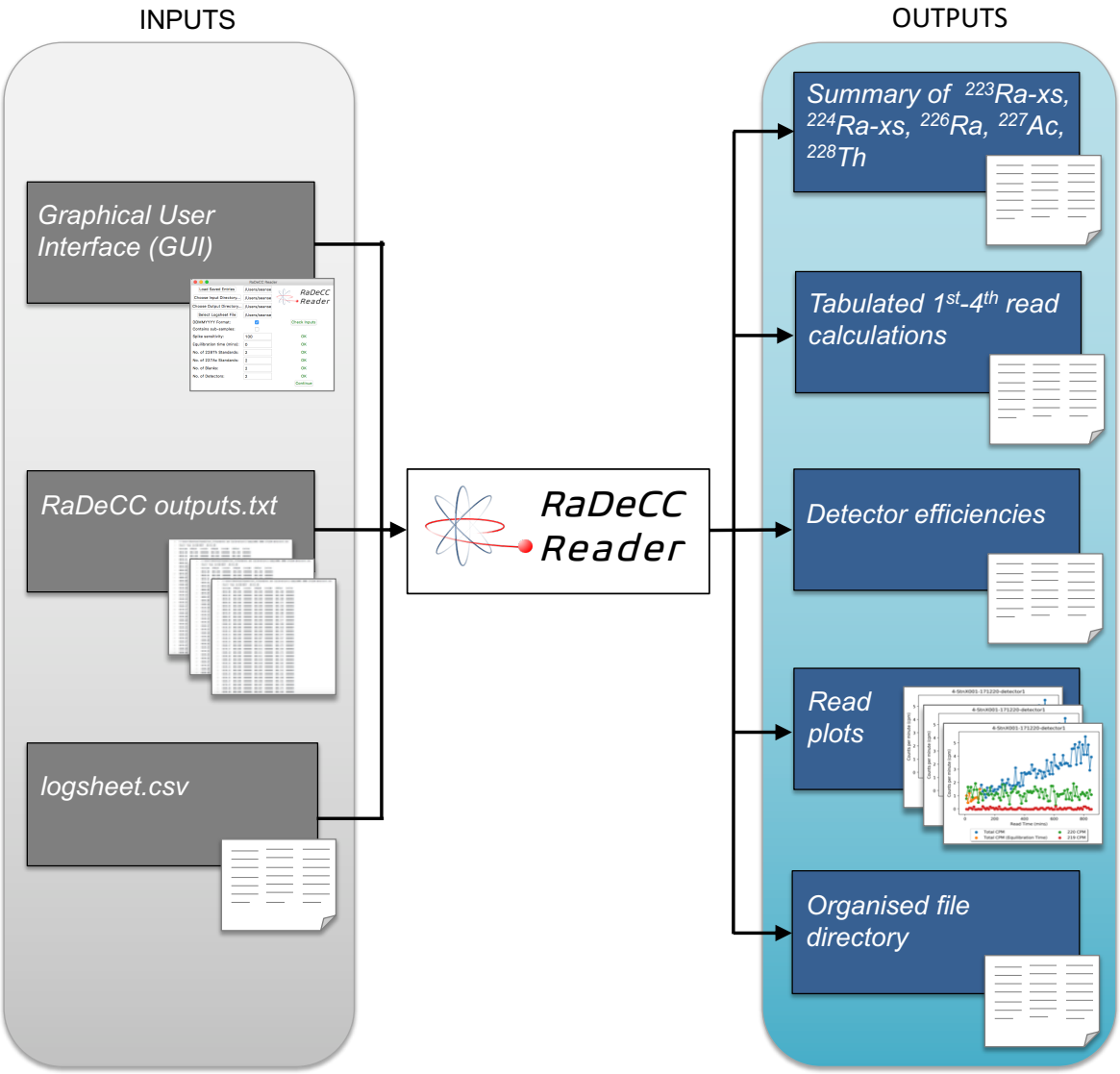

Figure 2.2: Summarised inputs and outputs of the RaDeCC Reader program.

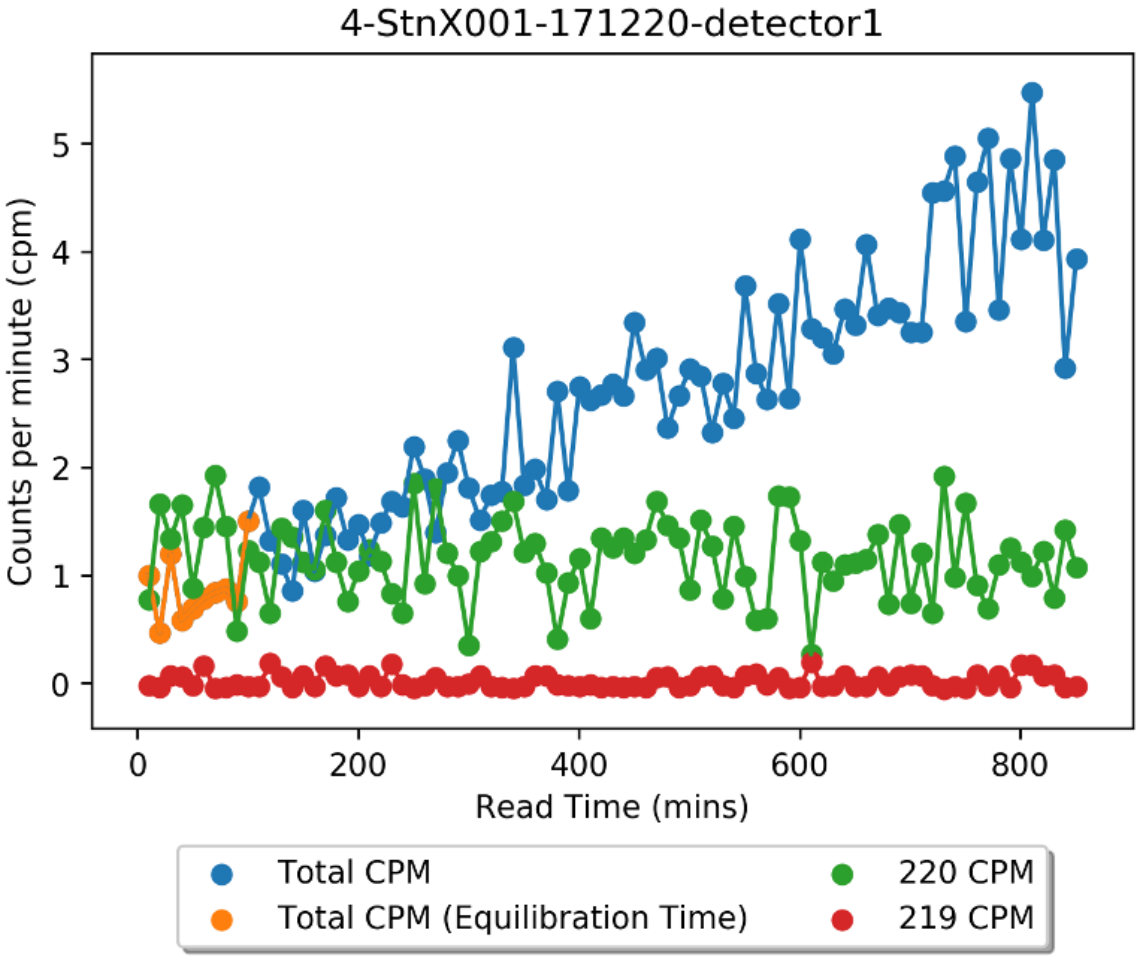

Figure 2.3: An example of a read plot produced by RaDeCC Reader of counts per minute for the total, radon-219 and radon-220 channels over the course of a sample read. Spikes in counts per minute (any counts that exceeded the default '*Spike sensitivity*' constant) have been removed. Counts in the total channel that are used in the estimation of radium-226 activity are shown in blue. Counts in the total channel that are ignored in the estimation of radium-226 activity during a user-defined period of detector equilibration are shown in orange.

read files and the log-sheet must be consistent and can be indicated via a tick-box in the GUI.

Data outputs can be organised differently to assist the user. How data outputs will be organised depends on whether or not the user indicates a sample set includes sub-samples. Herein sample sets that do not contain sub-samples (e.g. multiple locations sampled once, or time series at a single location) are termed 'linear'. Sample sets with sub-samples (e.g. multiple locations each sampled at multiple times, or a series of depth profiles) are termed 'branched'. In the case of a sample set where some samples have sub-samples, this could be processed using the branched setting. In this case, samples without subsamples would be seen as samples with one subsample each. The distinction between linear and branched can be indicated via a tick-box in the GUI.

File naming and identifiers In order to acquire raw data, the program requires the text files generated by the RaDeCC systems for sample, standard and (if required) background reads. The formatting of these filenames needs to be consistent and must include information on the sample (and sub-sample) name and the detector used. For example, '1-StnX001-A001-010220-det1.txt', contains the sample name 'StnX001', subsample name 'A001' and the detector name 'det1'. The number '1' at the start of the file name designates the read interval (e.g. 1 for radium-224 quantification), although this is recorded by the program it is not used in excess calculations. Instead, the program assigns a read interval automatically by calculating the elapsed time between sampling and RaDeCC analysis. It is important to note that sample and sub-sample names must be distinct from each other, no sample name should contain another sample name within it (StnX1 and StnX10, for example). Once the first panel of entries is completed in the GUI (figure 2.1a), these entries are checked by the program, and if verified, the user can proceed to the second panel in the GUI to assign details of the standards and backgrounds.

Information on detectors, standards and backgrounds Upon verified completion of the first panel of entries in the GUI (figure 2.1a), a second panel will appear requesting inputs for individual detectors (names, *E219/E220* ratios, radium-226 slope calibration values and radium-226 system efficiency values) and details specific to individual standards (names, dates of manufacture and initial activity) (figure 2.1b). Only an identifying name is requested for

background runs. If background measurements are not required then the 'No. of Background Standards' field can be set to '0' in panel 1 of the GUI (figure 2.1a). These inputs are all required for the calculation of detector efficiencies and the resulting corrections to the raw data.

Assigning variables The final GUI entries are the titles of log-sheet columns containing sample name, sub-sample name, sample volume, sample volume error, sampling date and sampling time. These column titles should not contain spaces and must be selected via the drop-down lists that appear in the second panel of the GUI after a log-sheet file is selected in the first (figure 2.1b). Once these details are completed and verified, the user can then proceed to run the RaDeCC Reader. A step-by-step explanation of information input and program setup is also provided in the *Instructions.md* or *Instructions.txt* files in the GitHub repository along with example data to check that the program is functioning properly.

2.4.2 How it works

Data, directories and detector efficiencies Upon clicking the 'Run RaDeCC Reader' button, the directory building function will create an organised directory of read and logsheet files using input from the GUI as well as sample and sub-sample names in the logsheet.

The directory_filler function will then use each folder/sub-folder name as a search criteria and search through the main folder of reads for files that match each folder name and then subsample. When a match occurs, the file is copied to the folder it was matched with. Any files not matching sample/sub-sample folder names or standard or background folder names will be copied to the miscellaneous (*misc.*) folder.

Once the directory is built and populated with reads, a dataframe of detector efficiencies is produced. The efficiencies calculation function searches through the appropriate standard and background subfolders for each detector specified by the user in the GUI. The program creates a dataframe of corrected reads for each standard with the appropriate channel efficiency for each read calculated as well as a dataframe of background reads. These offer the user a more granular view of read results when validating the average efficiencies displayed in the summary efficiencies dataframe. These four dataframes are automatically exported as .csv files. The detector efficiency of the 219-channel for each detector is calculated using the actinium-227 standard as well as the method devised by (Moore and Cai, 2013), based on system volume

and 220-channel efficiency using the thorium-232 standard. In parallel, the two separate 219-channel efficiencies are used to calculate two separate final corrected radium-223 values. Use of radium-223 values based on the Moore and Cai (2013) method requires verification of an E219/E220 ratio (2.4.1): the Reader includes the value determined by Moore and Cai for the standard RaDeCC configuration as a default.

The program uses the sample name (and sub-sample name) in each row of the logsheet as search criteria, finding the corresponding read files to scan. Using the data scanned from the read files the program performs the appropriate corrections and related propagation of uncertainties. For each read, these new corrected values along with their uncertainties are combined with the sample's corresponding metadata from the logsheet and entered as a new row in the read results dataframe.

First level corrections Every read file for each sample/sub-sample is scanned, the interval logged data is extracted from the text file, and the first level of corrections are performed (Garcia-Solsona et al., 2008). These include:

- Chance coincidence counts per minute in the 219 and 220 channels (Y 219 CC, Y 220 CC)
- Corrections for 220 interference in the 219 channel (to give final219)
- Corrections for 219 interference in the 220 channel (to give final220)
- Total counts corrected for counts due to 219 or 220 (to give corr total)

As the program scans through a read, each interval is evaluated using the guidelines outlined by Diego-Feliu et al. (2020) for the measurement and quantification of radium-223 and radium-224 (figure 2.4). For each read, the program records the percentage of intervals for which quantification of radium-223 or radium-224 is not recommended and logs these percentages in an error column of the read results dataframe. This allows the user to quickly establish whether an anomalous result might be due to cross-talk or other interferences. The scanning of read files is not obstructed by files with lines enclosed by quotation marks or extra lines added by a pause function.

Spike removal If the number of counts in either the total, 219- or 220-channel during one time interval is higher than the next interval by more than the '*Spike sensitivity*' constant

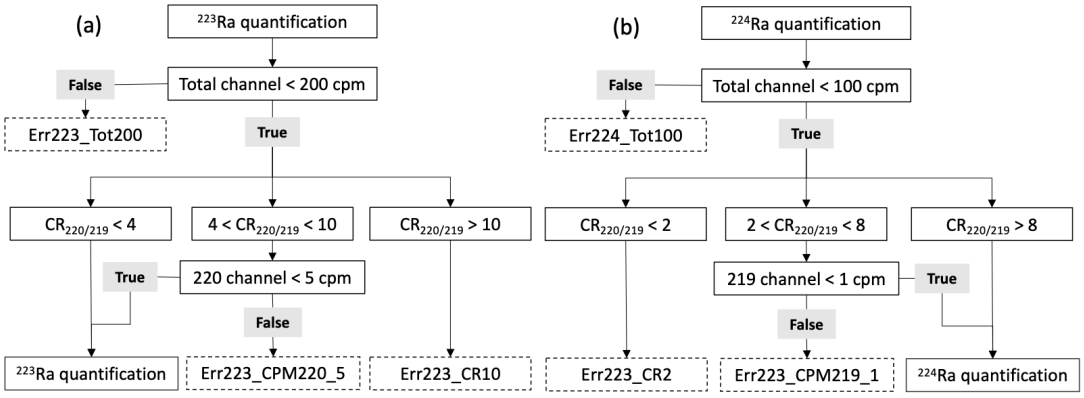

Figure 2.4: Flow charts of the guidelines for quantifying radium-223 (a) and radium-224 (b) using RaDeCC apparatus (modified after Diego-Feliu et al. (2020). $CR_{220/219}$ is the count rate ratio of the 220-channel to the 219-channel.

the program removes this time interval as it is considered to contain a counting anomaly - likely due to a spike in the electrical supply to the RaDeCC apparatus. If an anomaly is removed, the value of the anomaly is recorded in the *Spike_Value* column of the results dataframe. The calculated counts per minute values of each interval are then averaged over the whole read. The '*Spike sensitivity*' constant is set at 1×10^6 counts by default, meaning that spike removal is inactive, but may be activated via a change in the '*Spike sensitivity*' constant value by the user to allow for higher or lower sample activities.

Radium-226 estimates from radon-222 ingrowth and Raw Data Plots The rate of radon-222 ingrowth seen in the Total channel (cpm total) is calculated in order to estimate the activity of radium-226 in the sample. The equilibration time variable (0 minutes as default) allows the user to set the time required for the radon-222 activity throughout the RaDeCC circuit to accumulate sufficiently to be detectable in the total channel. The time interval is set by the user in the GUI prior to initiating a read and is the number of minutes between the software logging each line of the output file (figure 2.1a). The time interval is used by the RaDeCC Reader program here to decide how many lines to miss at the start of the read file before calculating radon-222 ingrowth and therefore the radium-226 activity estimate. A plot of read-time vs. total counts per minute (cpm total), 219 channel counts per minute (cpm219) and 220 channel counts per minute (cpm220) for each read is saved in the '*Read Plots*' folder (figure 2.3). These plots provide a graphical view for raw data quality

assessment by the user, for instance to evaluate system stability as well as the build-up of radon-222 during each read. Estimated radium-226 activity will only be calculated from reads with durations >600 minutes, shorter reads may be less reliable due to the short period for ingrowth of radon-222 to occur. In the event of a short read, the 'Err226_short_read' error is logged in the read results dataframe.

Second level corrections and output After the first level of corrections is complete, generating values for final219, final220 and cpm total for radium-226 estimation, the read results dataframe containing these new values is passed on to the second level of calculations. Second level corrections expand the read results dataframe with the calculated values and propagated uncertainties as described by Garcia-Solsona et al. (2008). Second level corrections include:

- Detector background corrections in all channels
- Corrections for detector channel efficiencies
- Corrections for sample volume, producing volume corrected activity (vdpm)

These final calculations complete the series of corrections and uncertainty propagations providing disintegrations per minute per 1000 L (dpm/m^3) for radium-223 and radium-224 as well as an estimate of radium-226 activity (dpm/m^3) for each read. These individual read results are saved as a table in comma-separated-value (.csv) format before being combined to calculate sample activities.

Sample activity calculations and outputs The final stage of calculations is the combination of read-specific values calculated in the results dataframe to calculate excess radium-223, excess radium-224, radium-226, actinium-227 and thorium-228 activities for each sample.

The 2^{nd} and 4^{th} interval reads of each sample/sub-sample are combined using equation 2.14 to calculate excess radium-223. For the calculation of excess radium-224, 1^{st} and 3^{rd} interval reads are combined using equation 2.13. In many circumstances 1^{st} interval reads are sufficient to accurately quantify radium-223 activity, so if 2^{nd} interval reads are unavailable, excess radium-223 is calculated using 1^{st} reads. Similarly, if 3^{rd} reads are unavailable, excess radium-224 is calculated using 4^{th} interval reads. Actinium-227 activity is essentially the supported radium-223 activity calculated for the 4^{th} (or 3^{rd}) interval read of a sample/sub-sample while thorium-228 is the supported radium-224 activity calculated for the 3^{rd} (or

4^{th}) interval read of a sample/sub-sample. If the results dataframe contains more than one read of a particular sample/sub-sample for a given interval (1^{st}-4^{th}), the average activity of the relevant reads will be used in the calculation. The radium-226 activity of a sample is determined by averaging the radium-226 activity of reads >600 minutes in duration. Any radium-226 activities that are more than one standard deviation from the mean are then removed, and a new average is calculated. The results of these final calculations are tabulated in a summary dataframe and exported as a comma-separated value (.csv) file. Any read-interval substitutions in the calculation of excess activities are logged in the error column of this summary dataframe alongside any errors raised using the logic outlined by Diego-Feliu et al. (2020) for all read results used.

2.5 Validation

2.5.1 Experimental design

To evaluate the performance and accuracy of the RaDeCC Reader program, the processing time and corrected data outputs from real sample, standard and background determinations by RaDeCC instruments were compared to those derived from a Microsoft Excel implementation of the calculations outlined by Garcia-Solsona et al. (2008) and Geibert et al. (2013).

A total of 208 raw data files from 44 samples were used for the purpose of this evaluation. Open ocean samples (106 raw data files, 19 seawater samples) were collected from 60-100 litres of seawater using MnO_2 impregnated fibres, during the along southwest Greenland during the ICY-LAB expedition aboard RRS *Discovery* in 2017 (Hendry et al., 2019). Coastal surface seawater samples (approximately 0.5 m depth) (40 raw data files, 9 surface samples) and karstic spring-water samples (62 raw data files, 16 samples) were collected offshore of the Calanques of Marseille-Cassis on 27–28 March 2018 aboard the R/V *Antédon* II, by trace-metal clean submersible pump and scuba-divers respectively (Tamborski et al., 2020).

The range of 219, 220 and total count rates (219: 0 - 6.3 cpm, 220: 0 – 16.8 cpm, total: 0 – 35 cpm) and counting times (60-4002 minutes) tested here, are realistic ranges encountered in submarine aquifer and open ocean fieldwork and 35% of the maximum quantification limit of the RaDeCC apparatus (Diego-Feliu et al., 2020). These samples, previously published in Hendry et al. (2019) and Tamborski et al. (2020), were calibrated using standards prepared at LEGOS, OMP (Toulouse, France) with solutions of ^{228}Th (in equilibrium with ^{232}Th) and

^{227}Ac obtained from the International Atomic Energy Agency (Monte Carlo, Monaco). Here we repeat their raw data processing using our standardised Excel-based methodology and compare the outputs to those obtained using the RaDeCC Reader. This approach allows any disparity in results to be attributed to differences in implementation. Nine variables were compared: the corrected activities of excess radium-223, actinium-227, excess radium-224, thorium-228 and radium-226, and the propagated uncertainties for excess radium-223, actinium-227, excess radium-224 and thorium-228.

2.5.2 Results and discussion

Implementation time of either method is certain to vary between users. For new users of the RaDeCC Reader time will be needed to name and organise files and prepare logsheets. In this exercise, however, the implementation of the Excel-based methodology took an experienced user over 2 hours to process the outputs from standards, backgrounds and 30 samples; amounting to a total of 233 raw data files. This compared to a processing time of 2 minutes to perform the equivalent functions using the RaDeCC Reader, a time saving that would be magnified with larger datasets or familiarity with the required file naming conventions.

Excellent agreement (R2 >0.99, Standard Error <0.02) was seen for the corrected activities and propagated uncertainties of excess radium-223 and excess radium-224 (figure 2.5) as well as actinium-227, thorium-228 (figure 2.6). The small amount of variance seen, possibly due to a difference in the treatment of background measurements, is an order of magnitude smaller than any propagated uncertainties associated with the activities determined in this study. Radium-226 activity determined by our Excel method and the RaDeCC Reader also displayed very strong agreement, with greater variance than was seen for the short-lived radium isotopes or their supporting isotopes ($R^2 = 0.99$, Standard Error = 0.02, figure 2.6). We attribute this greater variance between methods to the fact that radium-226 activities determined by RaDeCC apparatus are inherently less precise than those determined for excess radium-223, actinium-227, excess radium-224 and thorium-228. The activity of radium-226 is measured via the ingrowth of its daughter-isotope radon-222 and therefore the slope of the activity in the total channel with time. Many workers may choose not to include a portion of measurements at the start of a read to allow for the partial pressure of radon-222 in the system to accumulate above background. This equilibrium time may not be applied uni-

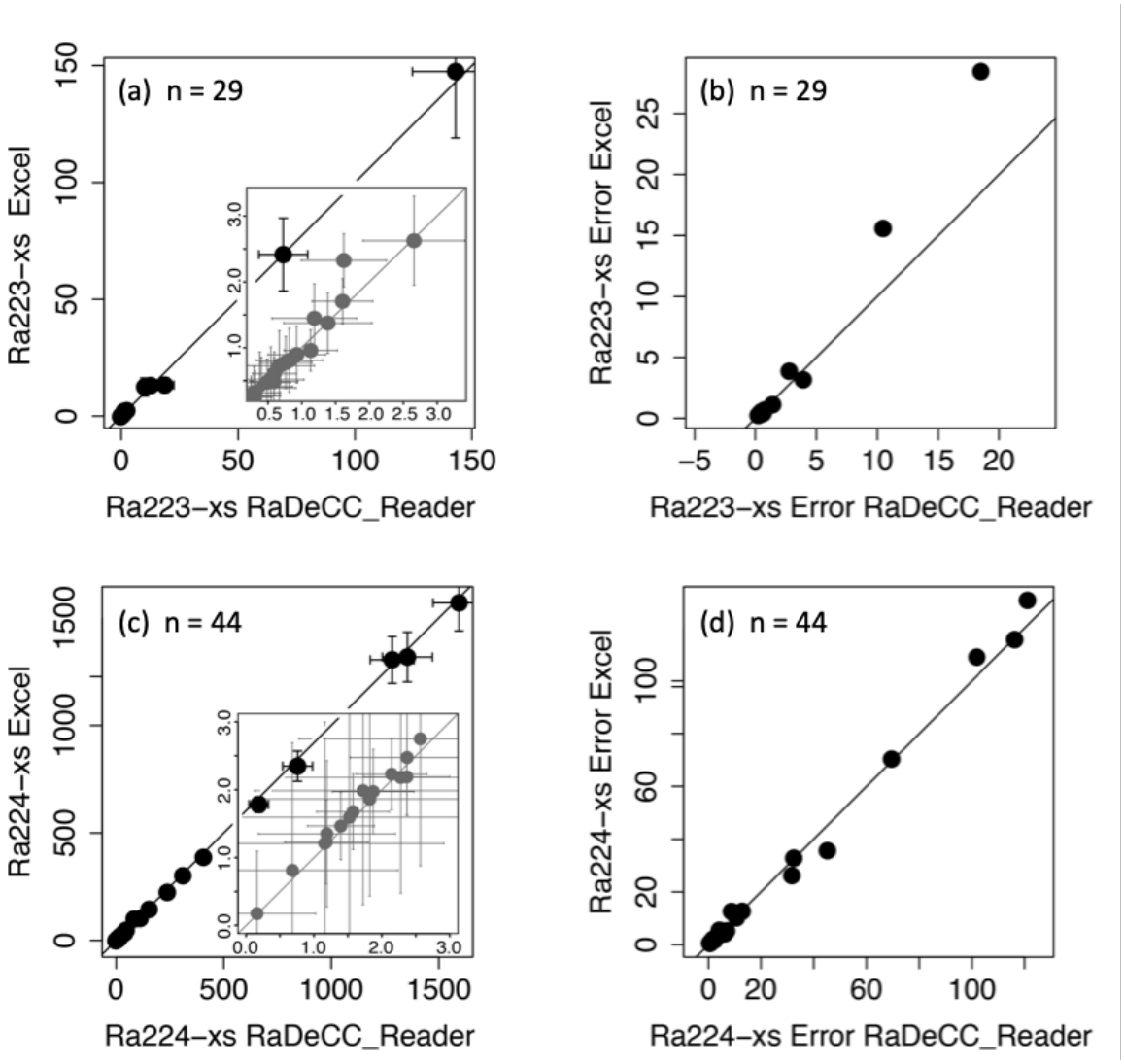

Figure 2.5: Validation of RaDeCC Reader outputs. Volume corrected activities and propagated uncertainties of excess radium-223 (a, b) and excess radium-223 (c, d) determined by the RaDeCC Reader program vs. an Excel implementation. Individual reads are plotted as black circles in units of dpm/m^3, relative to a 1:1 line. Inset plots (a, c) show the agreement between RaDeCC Reader program and the Excel implementation for samples in the low activity range.

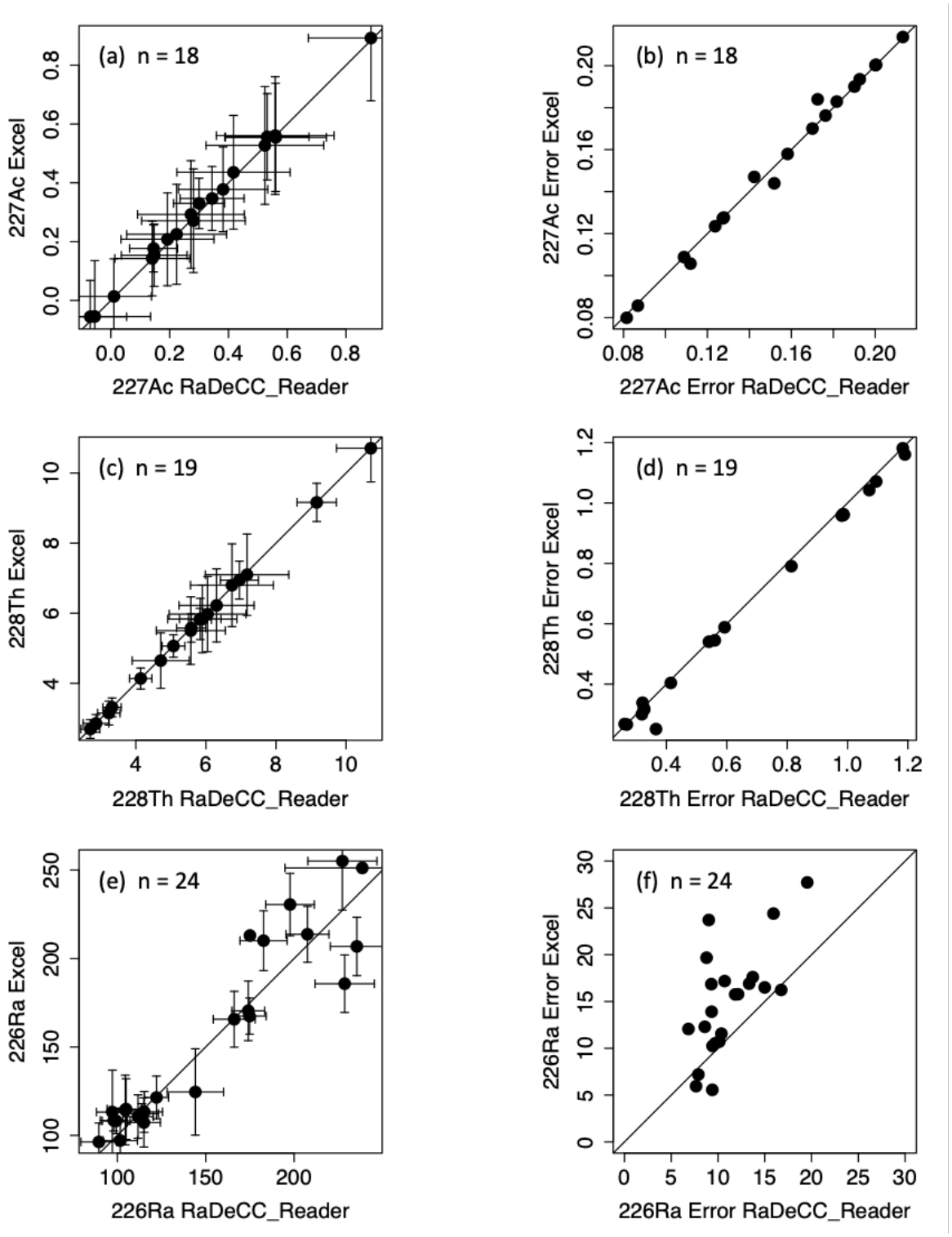

Figure 2.6: Volume corrected activities (dpm/m^3) of actinium-227 (a), thorium-228 (c) and radium-226 (e). Propagated uncertainties associated with the calculation of actinium-227 (b), thorium-228 (d) and radium-226 are also included. Individual samples are plotted as black circles in units of dpm/m^3, relative to a 1:1 line.

formly, whereas the RaDeCC Reader's user defined equilibration time is applied to all reads consistently. The slope in total activity with time is also sensitive to system leaks as well as the length of time a sample is measured for, particularly for samples with low activity, and therefore should be evaluated separately for samples with markedly different total activities.

2.6 Conclusion

We have developed a program that simplifies and expedites the process of correcting raw RaDeCC data, propagating related uncertainties and calculating the activities of excess radium-223, actinium-227, excess radium-224, thorium-228 and radium-226. With a logsheet and read file names in the required format, the RaDeCC Reader program is capable of processing a substantial real data set in a matter of minutes, and is therefore able to save users considerable time and effort in data processing when compared to previous and widely used Excel-based methodologies. By letting users evaluate their sampling methods and analytical performance more efficiently, the RaDeCC Reader has potential to enhance experimental design, for example, during maritime research expeditions. RaDeCC Reader maintained the accuracy of results attributed to previous methods, and preserved transparency of data processing by displaying the values of each stage of calculation, providing a view of the original raw data via saved plots and flagging results with data quality warnings. We attribute minor discrepancies in calculated excess radium-223, actinium-227, excess radium-224 and thorium-228 activities between methods to a difference in background treatment by the RaDeCC Reader's implementation. This provided no significant changes to the results from samples used in our test, however the implementation used by RaDeCC Reader mitigated the risk of greater inaccuracies that might have arisen from raw data files containing larger or more frequent counting anomalies.

Chapter 3

Short-lived radium isotopes at the Mid-Atlantic Ridge (MAR)

3.1 Abstract

Radium has proven to be a powerful tracer of physical transport processes in the ocean do to the near-conservative behaviour and predictable decay rates of its isotopes. Recently short-lived radium isotopes have been used to quantify hydrothermal plume dispersion rates; the application of radium-223 and -224 in these settings, however, rests on a number of assumptions about local radium inputs and cycling. In this study, the utility of short-lived radium isotopes as tracers of hydrothermal neutrally buoyant plumes is investigated. Twelve radium-223 and -224 water column activity profiles, sampled at or near Rainbow and TAG, expand on a previous observation of benthic radium-223 and -224 inputs at the base of the TAG mound. In these profiles, it is clear that benthic inputs of short-lived radium isotopes are not exclusive to the immediate vicinity of high temperature venting but appear to occur frequently within the axial valley, constituting the dominant source of radium-223, and to a lesser extent radium-224. Modelling of radium-isotope decay and synthesis of published concentrations of uranium-235, protactinium-231 and thorium-232 in open ocean and hydrothermal sediments suggest that hydrothermal sulfide deposits are the most probable major benthic source of radium-223 at Rainbow and TAG. Mean K_v values derived from axial radium-223 and -224 water-column activity profiles are $790\,cm^2\,s^{-1}$ ($\pm 650\,cm^2\,s^{-1}$, 2 S.D.) and $1870\,cm^2\,s^{-1}$ ($\pm 1640\,cm^2\,s^{-1}$, 2 S.D.) respectively; significantly higher than previously

calculated for MAR spur topography and Atlantic abyssal plains.

3.2 Introduction

Radium is assumed to behave conservatively in seawater. This means that, while subject to physical transport processes, it is assumed to be chemically unreactive and only removed from the dissolved phase by radioactive decay; the predictable decay of these isotopes affords an opportunity to measure the rates of physical transport processes. Use of short-lived radium isotopes as tracers in coastal settings is well established (Moore, 2000b,a).

Radium isotopes are expected to be enriched in hydrothermal fluids due to input from uranium and thorium bearing host rock under high-temperature acidic conditions (Ditchburn et al., 2012). Elevated activities of radium-223 and radium-224 have been measured in hydrothermal fluid end-members at the Puna Ridge, Juan de Fuca Ridge (JdFR) and the Reykjanes Ridge (Moore et al., 2008; Kadko and Butterfield, 1998; Kadko et al., 2007). Radionuclides may enter hydrothermal fluids via the following processes: fluid alteration of basalt, in-situ decay of parent isotopes and recoil effects from the decay of parent isotopes in basalt. The activity of these radionuclides in vent fluids is therefore determined by sub-seafloor fluid residence time, circulation depth in the crust and host-rock composition.

Where vent fluids are emitted from the sub-seafloor to seawater, radium isotopes are mixed and diluted extensively with seawater, while continuing to undergo their predictable rates of radioactive decay. The predictable rate of decay for each isotope provides opportunities to measure the rates of processes, like mixing and dilution, occurring in the plume (Neuholz et al., 2020). Before the study undertaken by Charette et al. (2015) there was no data on radium systematics within large-scale hydrothermal plumes, despite evidence of enrichment in hydrothermal fluids (Krishnaswami and Turekian, 1982; Kadko, 1996). At Trans-Atlantic Geotraverse (TAG) vent site, elevated activities of excess radium-224, radium-226, radium-228 and actinium-227 were observed at depths coincident with the hydrothermal neutrally-buoyant plume (Charette et al., 2015; Kipp et al., 2015a, 2018).

Longer lived radium-isotopes allow the quantification of processes operating on timescales of months to years and have traditionally been easier to measure than short-lived isotopes as samples could be measured on land rather than at sea. Radon-222 has long been used to investigate the dispersion of hydrothermal plumes (Rudnicki and Elderfield, 1992). Radium-

223 and -224 have half-lives similar to that of radon-222 and so are also potential tracers of hydrothermal plume dispersion as they provide the ability to date plume material on shorter timescales. Radium-223 (half-life = 11.4 days) and -224 (half-life = 3.7 days) allow for the investigation of mixing processes on timescales of approximately 2 months and 3 weeks respectively. When sampling remote mid-ocean ridge (MOR) vent sites, analyses of their activities must begin at sea due to the short half-lives of these two isotopes.

Advances in sampling methods (Henderson et al., 2013) and ship-board analyses (Moore and Arnold, 1996; Moore, 2000b,a) made the investigation of short-lived radium isotopes in remote ocean waters possible. Kadko et al. (2007) used radium-224/radium-223 ratios to establish that mixing and secondary precipitation reactions during upwelling of hydrothermal fluids were minimal, allowing further constraint of the water-rock ratio in the Reykjanes system. An inventory of excess radium-223 activity was used to quantify fluid flux through the Puna ridge (Moore et al., 2008). At TAG, Kipp et al. (2018) determined a plume age at TAG of 2.7-7.5 days using radium-224/radium-228 ratios in the vent fluid and in the plume. These radium-ages can then be applied to estimate the transport and residence time of trace metals in the plume. Neuholz et al. (2020) expanded on the work of Kipp et al. (2018) in the use of short-lived radium isotopes to quantify process timescales in hydrothermal plumes, focussing on a volcanic arc system rather than an MOR. The estimation of plume ages and the timescales of plume processes using short-lived radium isotopes requires important assumptions to be made.

In order to validate the assumptions necessary for interpreting and deriving ages from radium activities, the sources, movement and sinks of radium in these settings must be constrained. Neuholz et al. (2020) stated that the 'apparent ages' they derived from radium-isotopes, while useful, were only semi-quantitative due to large analytical uncertainties and the possibility of other sources of radium biasing the calculations. Kipp et al. (2018) observed a large benthic source of radium-223 at TAG that obscured a potential plume signal while on the EPR a potential plume radium-224 signal was obscured by a large benthic source. These studies suggest that hydrothermal vent fields may have multiple sources leading to sampled waters containing radium from a mixture of end-members. Such a scenario could generate plume-ages that are unreliable.

This study uses an unprecedented sampling and analytical resolution of short-lived radium

isotopes in two hydrothermal settings of the Mid-Atlantic Ridge to address two goals: (1) to identify the sources responsible for radium-223 and -224 activities in the water column; (2) to estimate the rates of physical mixing responsible for plume dispersion at sites on the Mid-Atlantic Ridge.

3.3 GEOTRACES GA13 Cruise and sample collection

3.3.1 Site selection and context

All samples described were collected on the GEOTRACES FeRidge expedition (GA13) to the Mid-Atlantic Ridge (MAR) on board RRS *James Cook*. The expedition was completed in a single leg, departing from Southampton (UK) on 20 December 2017 and arriving in Guadeloupe on 1 February 2018. Sampling was conducted at two well studied, tectonically hosted vent sites: Rainbow and Trans-Atlantic Geotraverse (TAG) (German et al., 2010a; Szitkar and Dyment, 2015).

The Rainbow vent field, located at 36°14' N on the MAR, was first identified by German et al. (1996b) and includes 10 discrete high temperature (ca. 365°C) concentrated flow vent sites (Fouquet et al., 1998). The vent field is located in a northward boundary current with a root mean square velocity of 5.5 cm/s at a depth of 2300m, stronger deep currents of approximately 10 cm/s have been observed in the non-buoyant plume (German et al., 2010a). High temperature venting at Rainbow also displays an exceedingly high Fe:S ratio of 24:1, this is likely due to its ultramafic setting (Douville et al., 2002). Upon emission into north Atlantic deep waters (NADW), CH_4 and total dissolvable Mn (TDMn) have exhibited conservative behaviour in the near field plume at Rainbow (German et al., 2010a). The neutrally buoyant hydrothermal plume can be found at approximately 2000 m to 2200 m depth at Rainbow as evidenced by light scattering spectroscopy (LSS) depth profiles (figure 3.4).

Found at 26°N on the MAR, TAG vent field was the first high-temperature hydrothermal vent field to be discovered on a slow spreading ridge (Rona et al., 1986). The TAG active mound, situated within the TAG vent field (26°08'N, 44°49'W), primarily consists of massive sulfide deposits and measures approximately 250 m wide and 50 m tall (Rona and Speer, 1989). Although significant high-temperature black smoker venting has been observed at the TAG mound, other modes of venting have also been documented, including intermediate-temperature blue-white and white smokers as well as clear solutions emanating via fractures

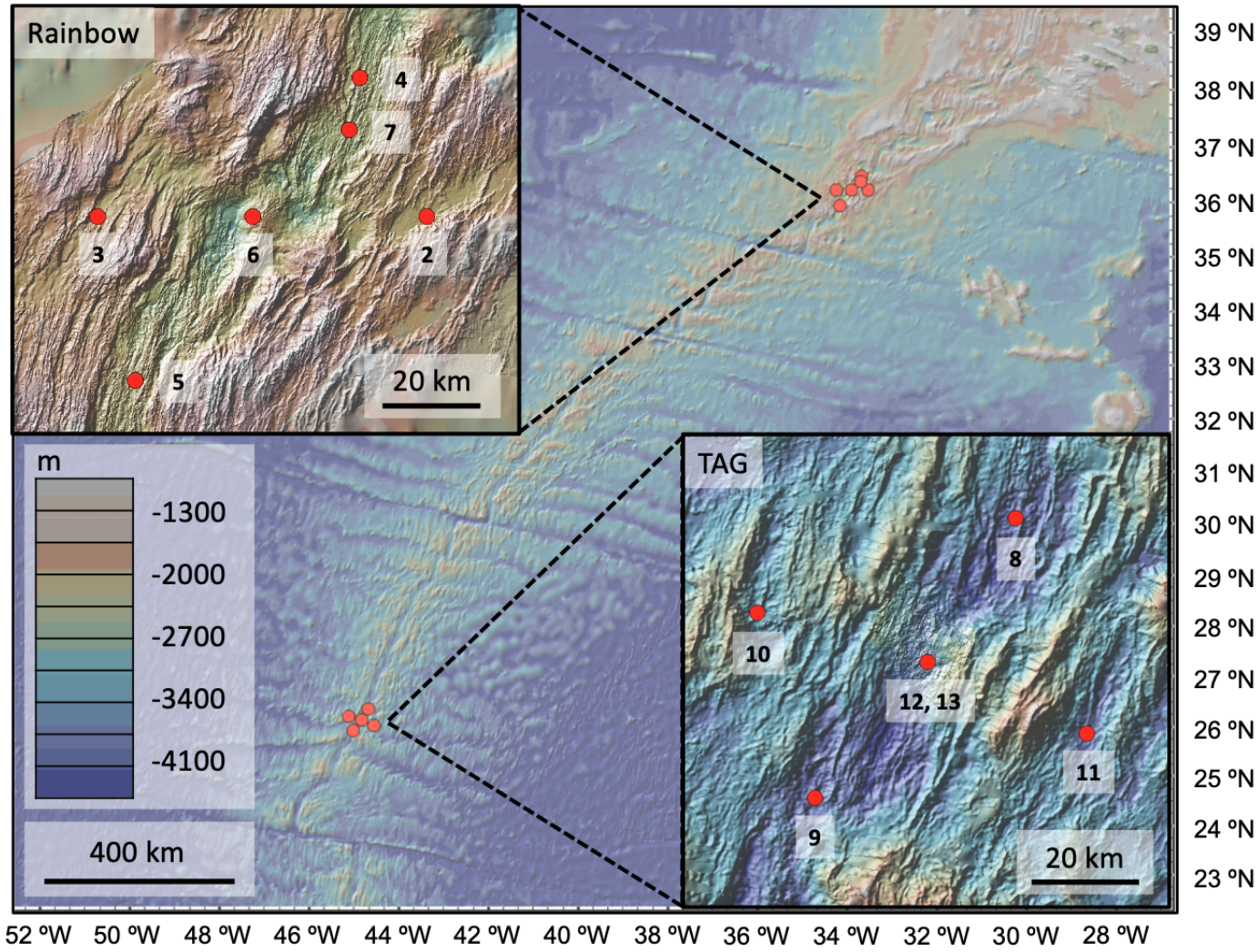

Figure 3.1: A map of cast locations at two hydrothermal vent sites on the Mid-Atlantic Ridge, Rainbow and TAG (red dots). Each cast consisted of 4-6 depths, sampled using Stand-Alone Pumping Systems to collect radium, thorium and actinium isotopes on MnO_2-impregnated fibre cartridges. Bottom bathymetry is depicted using a colour-scale.

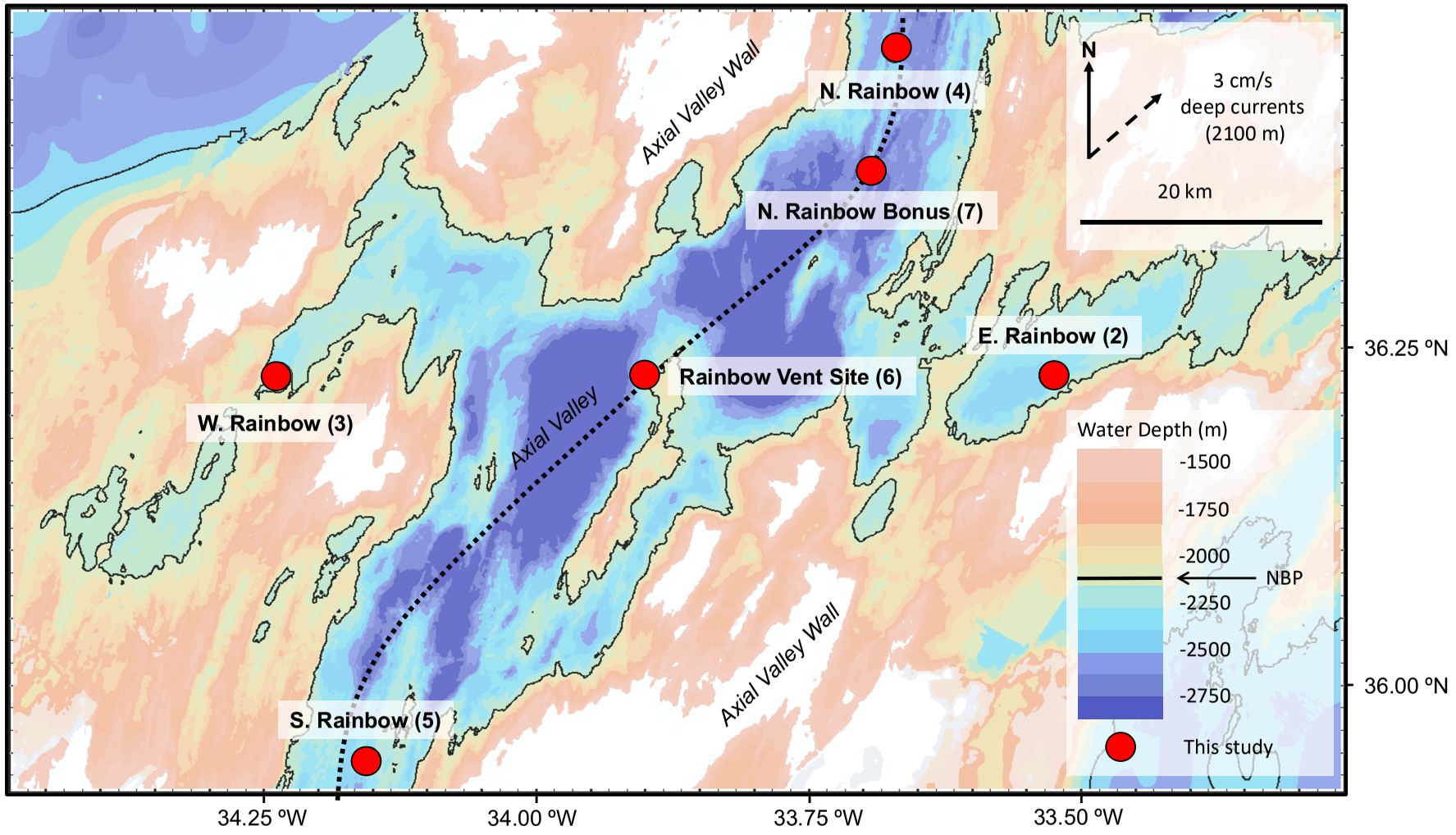

Figure 3.2: A map of radium sampling stations close to Rainbow vent site. Bathymetry is indicated by a colour scale while the depth of the neutrally-buoyant plume is marked by the solid black contour line. The main axial valley is labelled with a black dashed line with prevailing current direction and velocity indicated in the top right key.

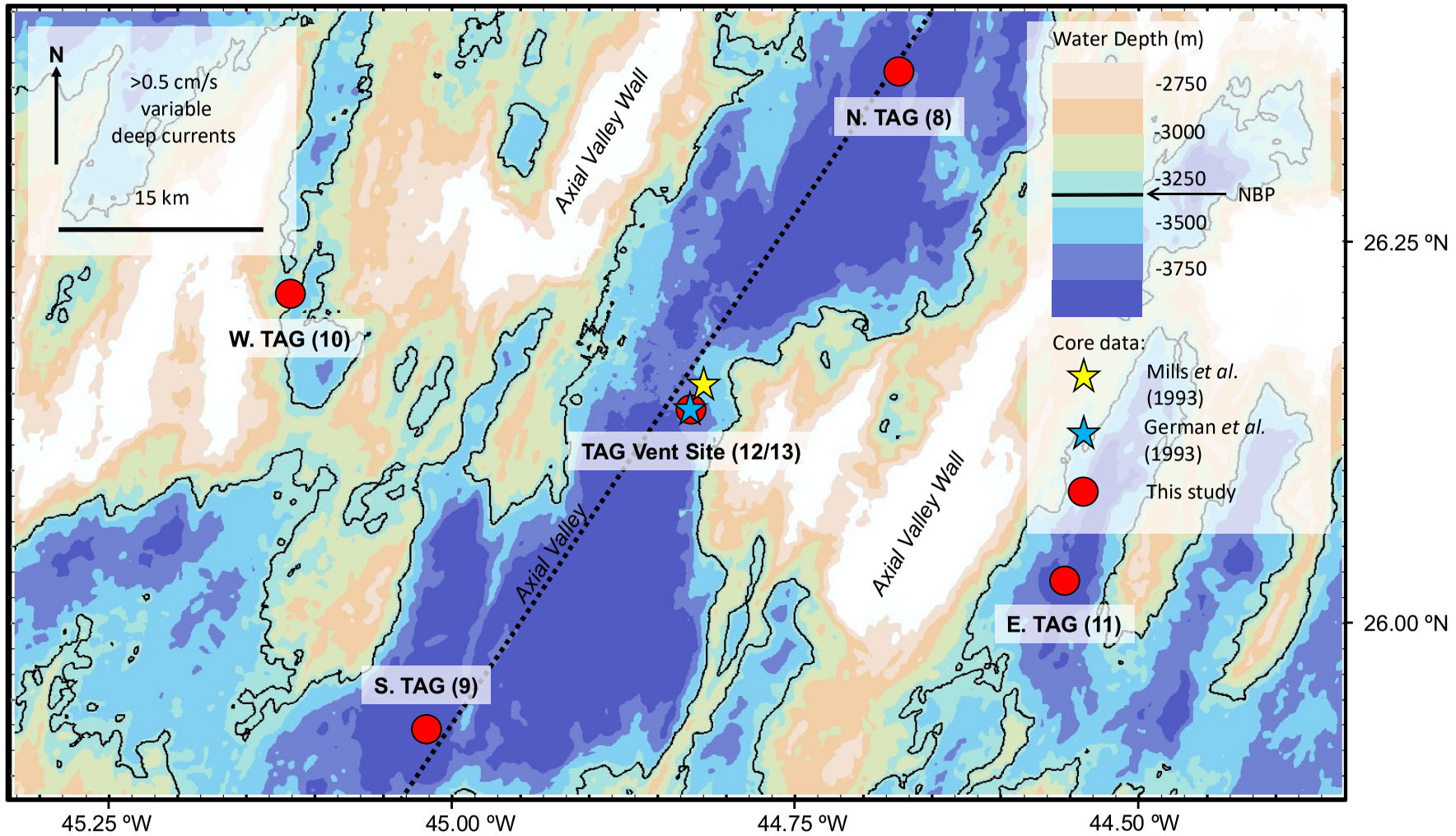

Figure 3.3: A map of radium sampling stations close to TAG vent site. Bathymetry is indicated by a colour scale while the depth of the neutrally-buoyant plume is marked by the solid black contour line. The main axial valley is labelled with a black dashed line, prevailing currents at this sight are slower than at Rainbow and more variable in direction. Star symbols mark the sites of sediment cores taken previously (Mills et al., 1993; German, 1993)

and diffuse venting (Rona and Speer, 1989). The hydrothermal plume and mound were inferred by Rona and Speer (1989) to have grown in size and complexity as the hydrothermal flow and discharge regimes developed over the past 1×10^4 years. At TAG, the neutrally buoyant plume depth, as indicated by LSS, is at approximately 3225 m to 3425 m water depth.

3.3.2 Sample collection

Samples for dissolved radium-223, -224 and parent actinium-227 and thorium-228 isotopes were collected using six Challenger Oceanic Stand-Alone Pumping Systems (SAPS) fixed to a steel coring wire at intervals before being lowered to sampling depth. Each SAPS was fitted with a pre-filter mesh (51 micron) and poly-ether sulfone (PES) (0.8 micron) or glass microfibre (GF/F) (0.7 micron) filter followed by two MnO_2-impregnated acrylic fibre cartridges fitted in series (Bourquin et al., 2008; Le Roy et al., 2019). Two MnO_2 fibre cartridges were fitted in series in order to quantify the scavenging efficiency of the cartridges for each isotope. Each SAPS system was filled with Milli-Q water immediately prior to deployment in order to minimize backward flow during placement at sampling depth before pumping began. During deployment each SAPS pumped 300-1000 L of seawater through the filters and cartridges over a period of approximately 1.5 hours. Once the SAPS were retrieved, filter housings were disconnected and drained using a vacuum pump. PES filters were processed under trace metal clean conditions while GF/F filters were air dried. MnO_2-impregnated acrylic fibre cartridges were immediately drained under gravity, washed with approximately 1 L of Milli-Q water and dried for one hour using a compressed air system, prior to ship-board analysis by radium delayed coincidence counting (RaDeCC).

3.4 Analytical Techniques

Originally devised by Giffin et al. (1963), delayed coincidence counting forms the basis of the Radium delayed coincidence counting (RaDeCC) apparatus created by Moore and Arnold (1996). The RaDeCC measures the activities of radon isotopes emanating from a radium laden sample cartridge over the course of a counting period, known as a 'read'. Activities of radium-223 and radium-224 can be calculated from the measured activities of radon-219 and radon-220 respectively.

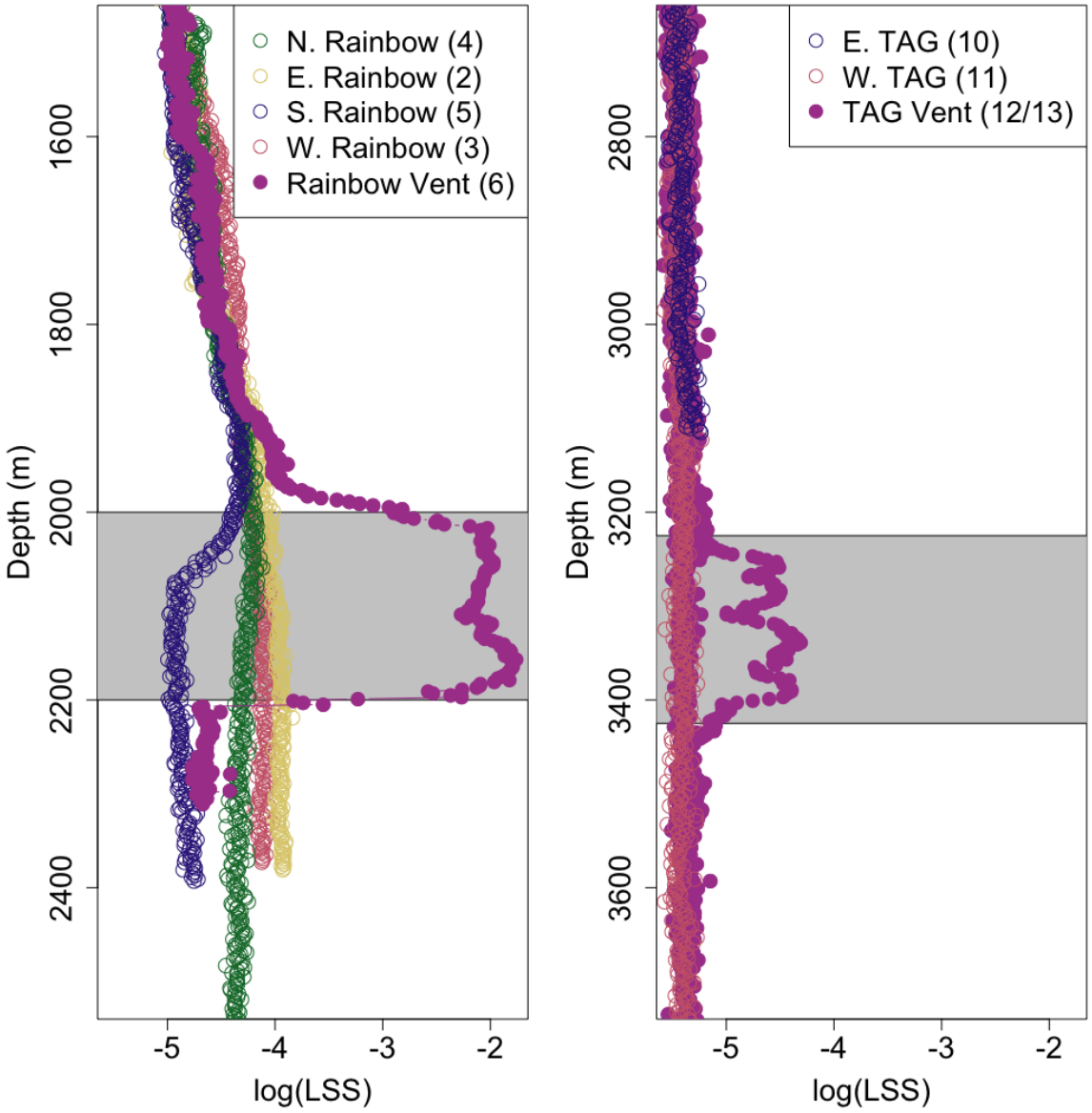

Figure 3.4: Bottom water depth profiles of LSS (Light Scattering Spectroscopy) at sampling sites at Rainbow (left) and TAG (right) vent sites as well as surrounding stations to the N, S, E and W. The area shaded in grey indicates the depths that are designated "NBP depths" due to the presence of LSS excursions.

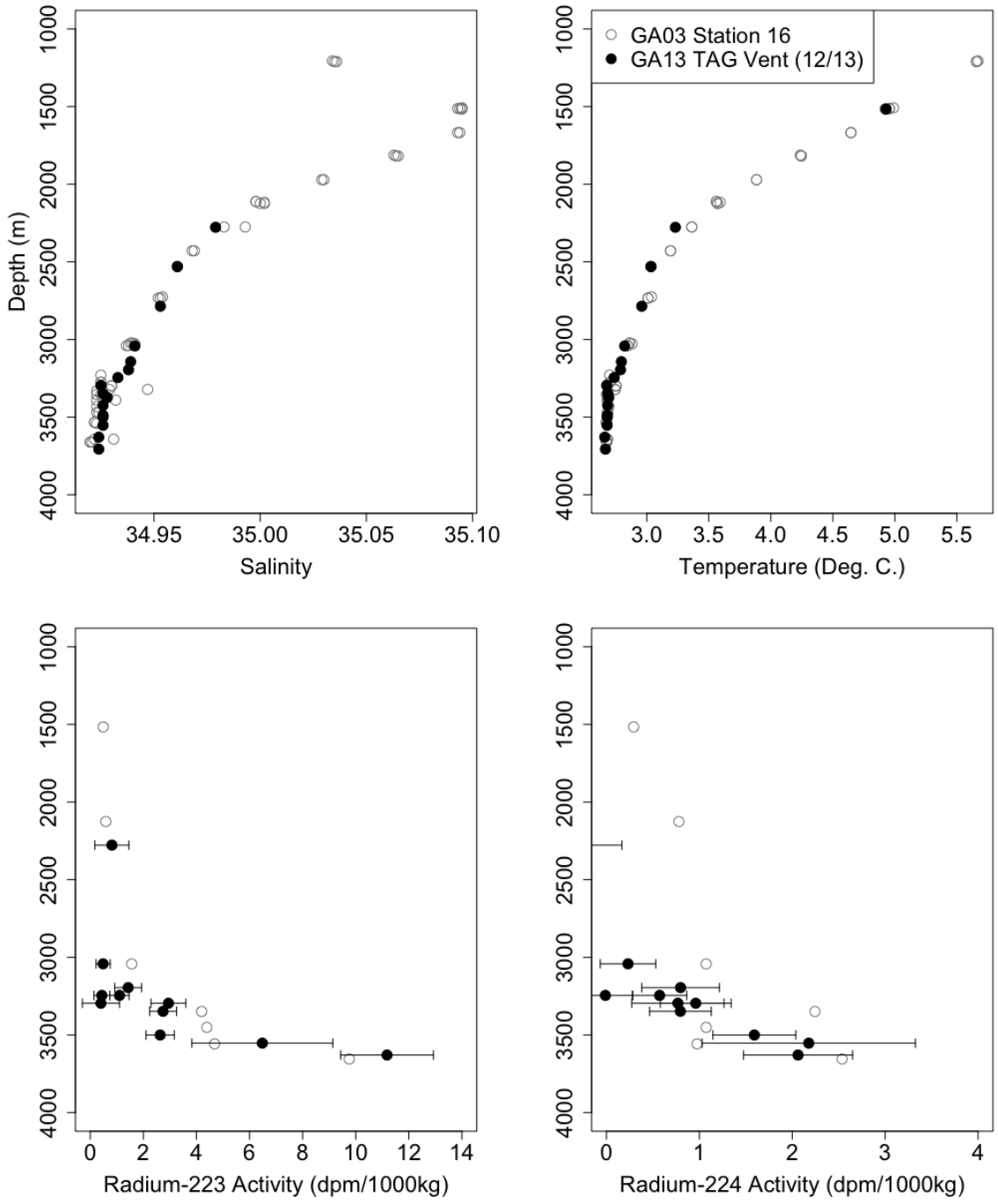

Figure 3.5: A data comparison from the GEOTRACES intercalibration site showing salinity, temperature, radium-223 activity and radium- 224 activity profiles measured above the TAG vent site by the current study (GA13 in 2017, 2018), and a previous study (GA03 in 2010, 2011) reported by Charette et al. (2015).

Once dry, sample cartridges were loaded into Radium Delayed Coincidence Counters (RaDeCCs) and measured for radium-223 and -224 activities (Moore and Arnold, 1996). Each RaDeCC system was purged with helium gas for two minutes before the system was closed and allowed to equilibrate for two minutes before decay counting began. Sample cartridges were each counted for approximately 10 hours. Samples were counted within 36 hours of sampling in order to measure the activity of radium-224. Samples were counted again 2 weeks after sampling to measure the activity of radium-223 without any interference from the decay of radium-224 and radon-220. Third and fourth counts of samples were completed at 1 and 3 months post collection respectively. The third count measured the supported radium-224 (via thorium-228) while the fourth measured supported radium-223 (via actinium-227). All counts had a duration of 6-10 hours.

RaDeCC detectors were calibrated by frequent analysis of fibre and cartridge standards. Our fibre standard was prepared with an activity of 12.494 dpm on 27/09/2009 at the International Atomic Energy Agency (IAEA) and has since been used for detector calibration of published results (Annett et al., 2013; Hsieh et al., 2013; Scholten et al., 2010). Cartridge standards were prepared at the Alfred Wegener Institute in Bremerhaven, Germany, by adding actinium-227 (13.59 dpm) and thorium-228 (14.39 dpm) to two separate cartridges on 05/12/2017. During the preparation of both fibre and cartridge standards, the spikes were added to $\approx$ 200 mL of Milli-Q water and brought to a pH $\approx$ 7.5 using Na_2CO_3 to achieve the correct binding pH. Fibre standards were analysed 8-18 times and cartridge standards were analysed 3-6 times (cartridge), for each individual detector throughout the duration of the study. Repeat analyses were performed in the standard configuration as well as the cartridge configuration to assess long-term detector performance as well as detector performance in a configuration matching sample analyses. The standard deviation in detector efficiency determined by repeat standard analyses was $5-13\%$ for the 220 channel. The 220 channel efficiency was determined by standard analyses while the 219 channel efficiency was calculated using the adjustment coefficient recommended by Moore and Cai (2013).

Background activities were evaluated by measuring a MnO2-impregnated cartridge that had not been used for sampling, thus incorporating any contamination that the samples may have acquired between sampling and measurement in addition to contamination within the instrument. Background values, 0.007 dpm for the 219 channel and 0.06 dpm for the

220 channel, are two orders of magnitude smaller than uncertainties associated with sample measurements.

The RaDeCC Reader program written by Selzer et al. (2021) (Chapter 2) was used when implementing the raw count corrections and error propagations devised by Garcia-Solsona et al. (2008) and updated by Diego-Feliu et al. (2020).

Analytical results were further validated via comparison with a GEOTRACES intercalibration station (GA03, Station 16); The results of this comparison are displayed in figure 3.5. Radium-223 activities measured by the two cruises agree very well while agreement between radium-224 profiles, with low activities, is less ideal. Consequently, the radium-223, radium-224, actinium-227 and thorium-228 values displayed in figures 3.6 and 3.7 as well as in the appendix (table A.1) have met the required standards set by the GEOTRACES Data Management Committee to have been archived for public use in the 2021 GEOTRACES IDP.

3.5 Results

Water-column depth profiles of radium-223 and radium-224 from 12 stations at Rainbow and TAG vent sites show significant variability and distinct patterns (figures 3.6, 3.7). The maximum radium-223 sample activity of 21.5 ± 2.4 dpm/m^3 was measured at 2534 m depth at the N. Rainbow (4) cast, north of Rainbow vent site. The maximum radium-224 sample activity of 9.5 ± 1.2 dpm/m^3 was measured at 2428 m depth at the N. Rainbow (4) cast, north of Rainbow vent site. Samples with activities below detection limits were primarily seen at shallower depths and away from vent sites, hence away from potential benthic or hydrothermal sources.

Neutrally buoyant plumes were identified by anomalies observed via light scattering spectroscopy (LSS) (figure 3.4). The depth ranges of these anomalies were then used to designate which samples were coincident with the neutrally buoyant plume. At Rainbow and TAG vent sites, the neutrally buoyant plume depth ranges identified were 2100 ± 100 m and 3325 ± 100 m respectively.

Except for one site, the majority of waters sampled at Rainbow vent site carried very low radium-223 and radium-224 activities. Apart from deepest two samples at N. Rainbow (4), radium-224 activities measured in all samples proximal to Rainbow were found to be 2 ± 2 dpm/m^3, showing no discernable patterns or trends with depth. At N. Rainbow (4), north of

Rainbow vent site, a decrease is apparent in radium-223 activity with height from the seafloor (2611 m), from 21.5 ± 2.4 dpm/m^3 to 3.1 ± 1.9 dpm/m^3 between 2534 m and 2233 m depth. Elevated radium-223 activities at N. Rainbow (4) are coincident with elevated radium-224 activities; 9.5 ± 1.2 dpm/m^3 at 2428 m, 7.2 ± 1.2 dpm/m^3 at 2534 m.

At the TAG study site, the maximum radium-223 sample activity was 19.1 ± 2.5 dpm/m^3 from TAG vent (12) at 3652 m depth above TAG mound, the deepest sample of the TAG vent (12) cast. From this maximum value at the bottom of the cast, radium-223 activity decreased rapidly to 3.7 ± 1.0 dpm/m^3 at 3508 m depth. A similar pattern was apparent at S. TAG (9) to the south of TAG vent site; Four samples between depths of 3636 m and 4154 m were measured with activities ranging from 13.0 ± 1.7 dpm/m^3 to 15.4 ± 1.7 dpm/m^3. North of TAG mound, the N. TAG (8) cast also indicated a strong benthic source with a similar depth profile pattern to S. TAG (9) and TAG vent (12); here a radium-223 activity of 10.3 ± 1.0 dpm/m^3 was measured at a depth of 3586 m decreasing to <1.2 dpm/m^3 above 3419 m. These three casts (N. TAG (8), S. TAG (9) and TAG vent (12)) show a consistent pattern within the axial valley of strong activity gradients away from high activities at the seafloor.

At depths coincident with the TAG neutrally buoyant plume, two separate casts above the TAG hydrothermal mound provided significantly different radium-223 activities. At a depth of 3307 m, a radium-223 activity of 4.8 ± 1.3 dpm/m^3 was measured on the TAG vent (12) cast while at 3312 m depth on the TAG vent (13) cast a value of 0.4 ± 1.3 dpm/m^3; at this site Charette et al. (2015) observed an excess radium-223 activity of 3.6 dpm/m^3 at a depth of 3301.4m, falling in between the activities observed in this study.

The highest radium-224 activity measured near the TAG study site, 4.1 ± 0.7 dpm/m^3, was situated to the north at 3800 m depth at N. TAG (8). The lowest radium-224 activities were seen at W. TAG (10) and E. TAG (11), to the west and east respectively. Elevated radium-224 activities were seen at the bottom of all axial casts (N. TAG (8), S. TAG (9), TAG vent (12)), falling in the range of 2.7-4.8dpm/m^3 between depths of 3657 m and 3940 m. This depth range falls just below the bottom bound of the TAG neutrally buoyant plume.

At depths corresponding to the TAG neutrally buoyant plume, radium-224 activities of 0.8 ± 1.1 dpm/m^3 and 1.2 ± 0.6 dpm/m^3 were observed at depths of 3307 m and 3332 m respectively. These values are lower but within analytical error of that observed by Charette

et al. (2015) of 1.6 dpm/m^3 at a depth of 3301.4 m.

Excess activities of radium-223 and -224 observed at TAG and Rainbow are similar in magnitude to those observed by Moore et al. (2008). In comparison to measurements at the Kermadec Arc by Neuholz et al. (2020), radium-223 activities observed in the current study display higher maximum values and a greater range while radium-224 activities are an order of magnitude smaller. These short-lived radium isotopes activities in open ocean hydrothermal settings are approximately 100- to 1000-fold smaller than those observed in coastal and estuarine settings (Boehm et al., 2004; Hwang et al., 2005; Luek and Beck, 2014; Tamborski et al., 2018)

3.6 Discussion

3.6.1 Hydrothermal controls on radium at the MAR

The major sink of short-lived radium isotopes in deep-sea hydrothermal settings is decay; the sources of short-lived radium isotopes are more numerous and diverse (figure 3.8).

High temperature venting and the resultant hydrothermal plumes were initially, and intuitively, envisaged as the major source of radium-223 and -224 at Rainbow and TAG. Hydrothermal fluids can however reach bottom waters via diffuse or low-temperature venting, a second potential source (Elderfield and Schultz, 1996). In addition, Moore et al. (2008) illustrated that seawater circulating at low-temperatures through basalts can become enriched in radium-223 due to recoil from actinium-227 generated by protactinium-231 adsorbed onto the basalt surfaces. Previous investigations at TAG found large radium-223 activities in bottom waters and attributed these signals to either diffuse venting or diffusion from metalliferous sediments rich in actinium-227 or protactinium-231 or perhaps both (Charette et al., 2015; Kipp et al., 2015b, 2018). Sediment cores taken by German (1993) and Mills et al. (1993) support the possibility of a sediment source and provide an additional possibility: uranium-rich sulfides incorporated into sediments via mass wasting of hydrothermal mound sulfide deposits.

Mills et al. (1993) suggested a mechanism that might allow the accumulation of U in sulfide rich hydrothermal sediments: diffusion of seawater uranium into particles containing sulfides that are undergoing oxidation, with subsequent reductive fixation of uranium at the oxide-sulfide boundary. This accumulation of uranium in sulfide rich particles could conceivably

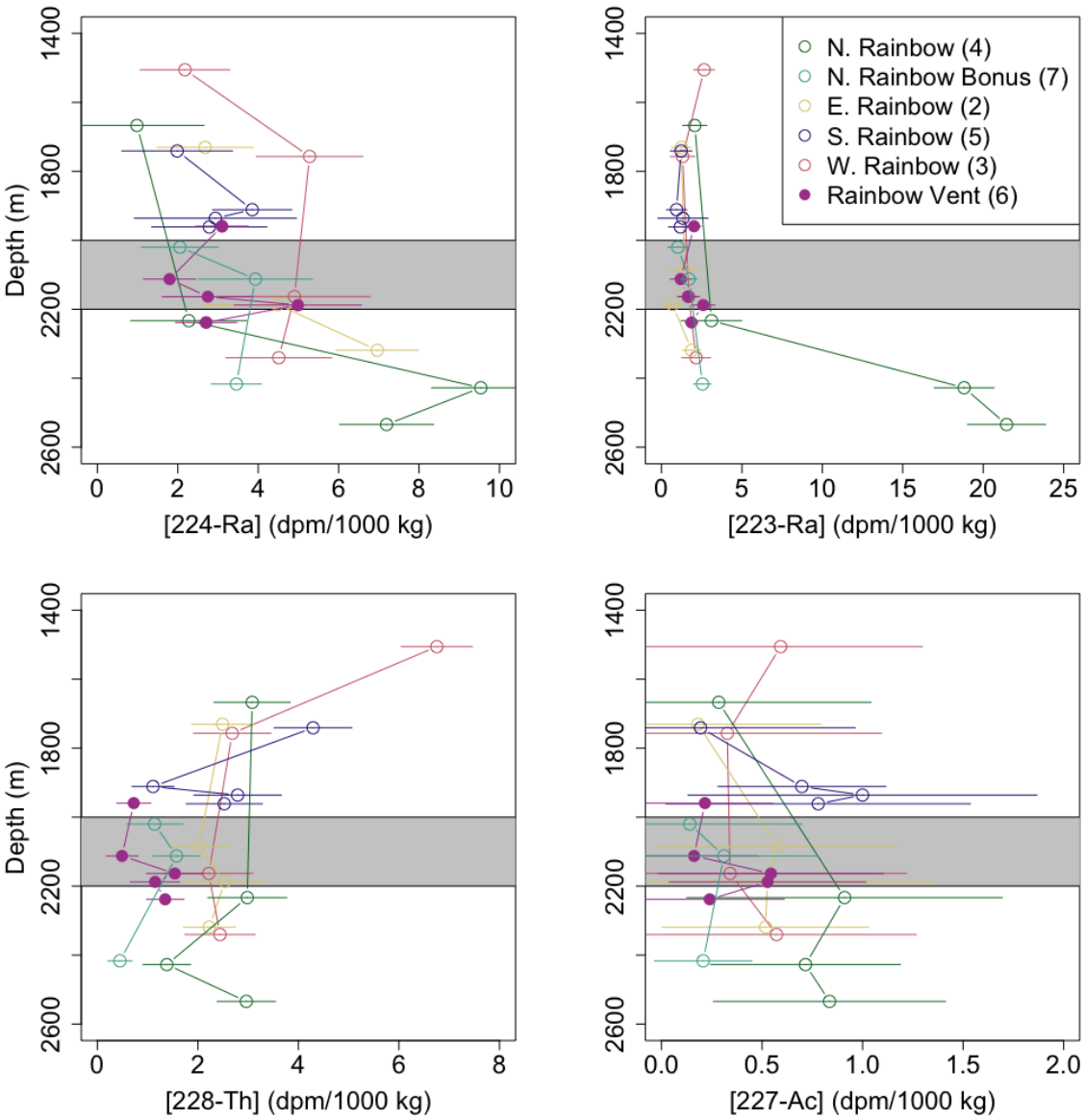

Figure 3.6: Plots of excess radium-224, excess radium-223, actinium-227 and thorium-228 against depth at Rainbow vent site. NBP depths, determined by elevations in transmissivity, are indicated by grey shading. Radium-223 and -224 distributions are most elevated near the bottom of axial profiles while thorium-228 activities are suppressed at NBP depth.

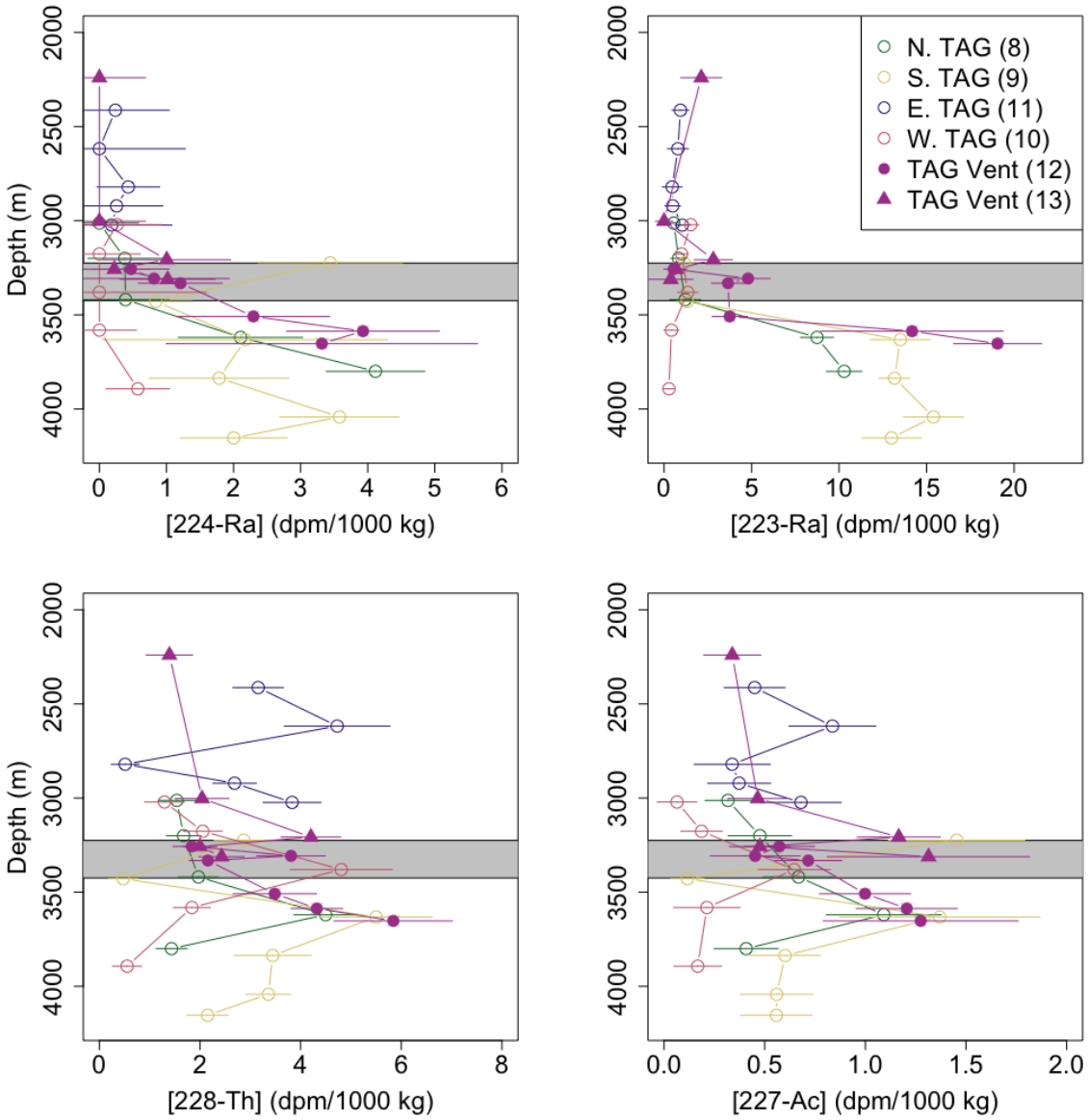

Figure 3.7: Plots of excess radium-224, excess radium-223, actinium-227 and thorium-228 against depth at TAG vent site. NBP depths, determined by elevations in transmissivity, are indicated by grey shading. Radium-223 and -224 distributions are most elevated near the bottom of axial profiles while thorium-228 and actinium-227 display similar patterns with depth.

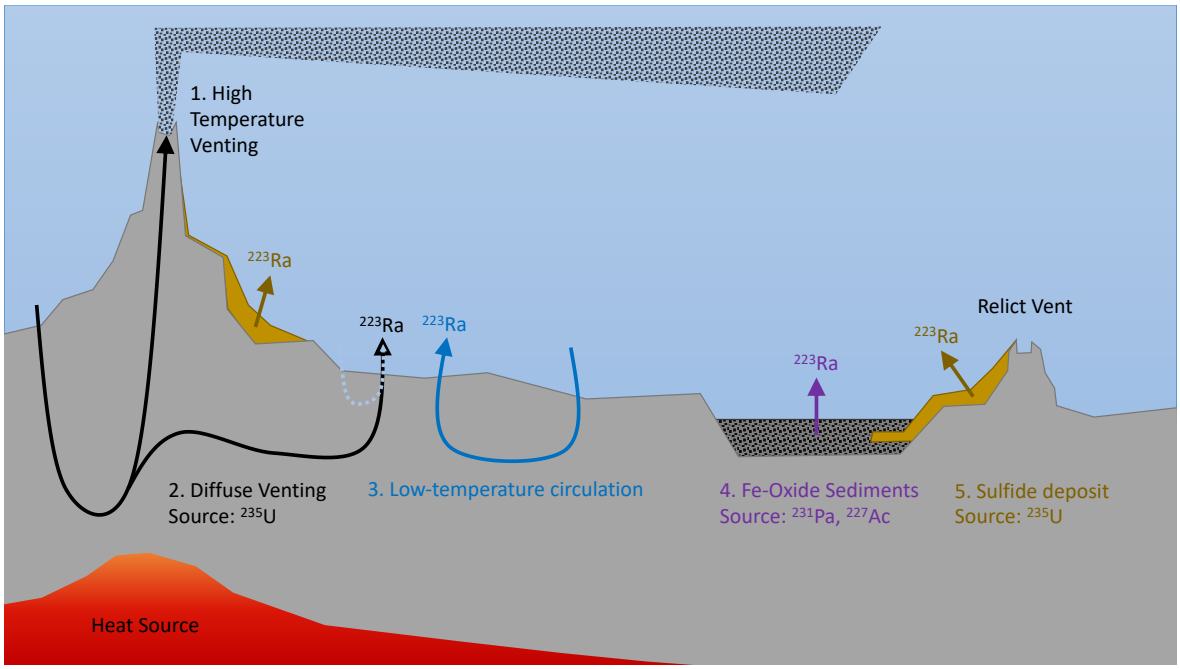

Figure 3.8: An illustration of the potential sources of radium-223 to waters overlying hydrothermal vent sites, as inferred from previous studies (Mills et al., 1993; German, 1993; Elderfield and Schultz, 1996; Moore et al., 2008; Charette et al., 2015; Kipp et al., 2015a, 2018).

occur on a large scale within the axial valley and over long periods of time. Uranium-235 fixed in sulfide rich sediments would support the activities of daughter-isotopes: protactinium-231, actinium-227 and radium-223. Radium-223 originating from sulfide-fixed uranium-235 could then be transported to overlying waters either by diffusion or by thermally-driven circulation of overlying waters through the sediments.

Some TEIs, for example the Rare Earth Elements (REEs, chapter 4), originating from bottom sources can be entrained into the hydrothermal plume; due to the short half-lives of radium-223 and -224, entrainment from sources more than a few metres from the vent orifice is considered to be negligible (German et al., 2010b).

The magnitude of these sources relative to each other is important in determining which processes can be accurately investigated using short-lived radium isotopes in these settings.

3.6.2 Potential benthic sources of radium-223

There are potentially two benthic sources of radium-223 to seawater in the axial valley of the MAR: low temperature diffuse venting and diffusion from various types of underlying sediments. Sediments have been proposed as the source of benthic radium-223 signals previously

(Charette et al., 2014; Kipp et al., 2015a, 2018), while low-temperature fluid circulation has been proposed as a source of radium-223 at the Puna Ridge by Moore et al. (2008) and might explain observations of high excess radium-223 activities near the seafloor at TAG vent site (Charette et al., 2015; Kipp et al., 2018). We can evaluate the potential contribution of these different sources of radium-223 to the ocean by examining the activity ratios of radium-223 and radium-224 found in the water-column.

If we assume TAG axial bottom elevations in radium-223 activity represent a diffuse vent source originating from the same end-member as the high-temperature fluids and therefore starting with the same radium-224/radium-223 activity ratio, then we can apply equation 3.1 from Neuholz et al. (2020) to model the evolution of this ratio over time, a rearrangement of equation 3.4.

$$T = -\frac{\ln(AR_x) - \ln(AR_{vent})}{\lambda_s - \lambda_l} \tag{3.1}$$

AR_{vent} is the activity ratio of radium-224 to radium-223 in source vent fluids, while AR_x is the same activity ratio in the sample and the decay constants of the shorter- and longer-lived isotopes are denoted by λ_s and λ_l respectively.

The radium-224/radium-223 activity ratios and radium-223 activities observed at neutrally-buoyant plume depth (NBP, figure 3.9) and at the bottom of axial profiles (BW, figure 3.9) can then be compared in their relations to the model. This approach assumes that sub-surface fractionation, original end-member ratio and any additional input is equivalent for diffuse vent fluids and high-temperature vent fluids before they emerge into overlying waters.

Figure 3.10a shows the modelled evolution of radium-223:radium-224 activity ratios during plume dispersion. The starting end-member radium-224/radium-223 activity ratio and radium-223 activity were estimated to be $21.2 \pm 6.7 (2\sigma, n = 12)$ and 302 ± 138 dpm/m^3 (2σ, $n = 12$) respectively based on the mean of Juan de Fuca Ridge, Puna Ridge and Reykjanes Ridge values reported by Kipp et al. (2018). From this starting value the ratio decays according to equation 3.1. In figure 3.10A the age ranges of bottom samples ($30 - 40$ days) and plume depth samples ($27 - 44$ days) can be calculated from the radium-224/radium-223 activity ratio ranges observed at these sites. The age and activity ratio ranges for bottom and NBP depth samples are represented by hashed and clear boxes respectively. The calculated age ranges for the two sites are indistinguishable due to the similarity in observed radium-224/radium-223 ratios.

The most significant difference observed between bottom water and NBP samples is the radium-223 activity. At TAG, samples at the bottom of all axial valley casts are approximately 5 times larger than those coincident with NBP depths. Figure 3.10B displays the decay of radium-223 from a starting activity of 302 ± 138 dpm/m^3 (2σ, $n = 12$) over time; here, the age ranges (box widths) are inherited from 3.10A while the radium-223 activity ranges are represented by box heights. The departure of samples from model behaviour can be explained by dilution, scavenging, a different end-member character or a combination of all three.

Similarly to helium, radium isotopes are assumed to behave conservatively in seawater (Porcelli and Swarzenski, 2003). Helium isotopes (δ^3He) are a well established tracer of hydrothermal plumes in the ocean (Rudnicki and Elderfield, 1992; Lupton, 1998; Jean-Baptiste et al., 2004). First recognised by Clarke et al. (1969), excess ^{3}He is defined in equation 3.2 where R/R_a is calculated via equation 3.3.

$$\delta^3 He = (\frac{R}{R_a} - 1) * 100 \tag{3.2}$$

$$\frac{R}{R_a} = \frac{\frac{^3He}{^4He\,sample}}{\frac{^3He}{^4He\,atmos.}} \tag{3.3}$$

R_a is equal to $1.39 \pm 0.01 \times 10^{-6}$ and represents primordial He extracted from the upper mantle via hydrothermal activity. The conservative behaviour of He-isotopes in seawater provides a useful comparison with radium.

If dilution is invoked to explain radium-223 deficiency, it would imply that vent-derived radium-223 was more dilute in NBP samples than it is bottom water samples. Less dilute bottom samples would be expected to exhibit stronger hydrothermal plume tracer signals than NBP samples such as elevated δ^3He; δ^3He was 4-fold lower than NBP samples in all axial bottom samples at TAG, making dilution alone an unlikely explanation. Further investigation of this hydrothermal end-member is currently impossible without short-lived radium isotope data from TAG high-temperature vent fluids.

Given the lack of δ^3He anomalies in axial bottom samples as well as the apparent ubiquity of radium-223 maxima at those depths, a sediment source remains a possible explanation. Sediments generating the observed radium-223 signals would require sufficient parent isotopes

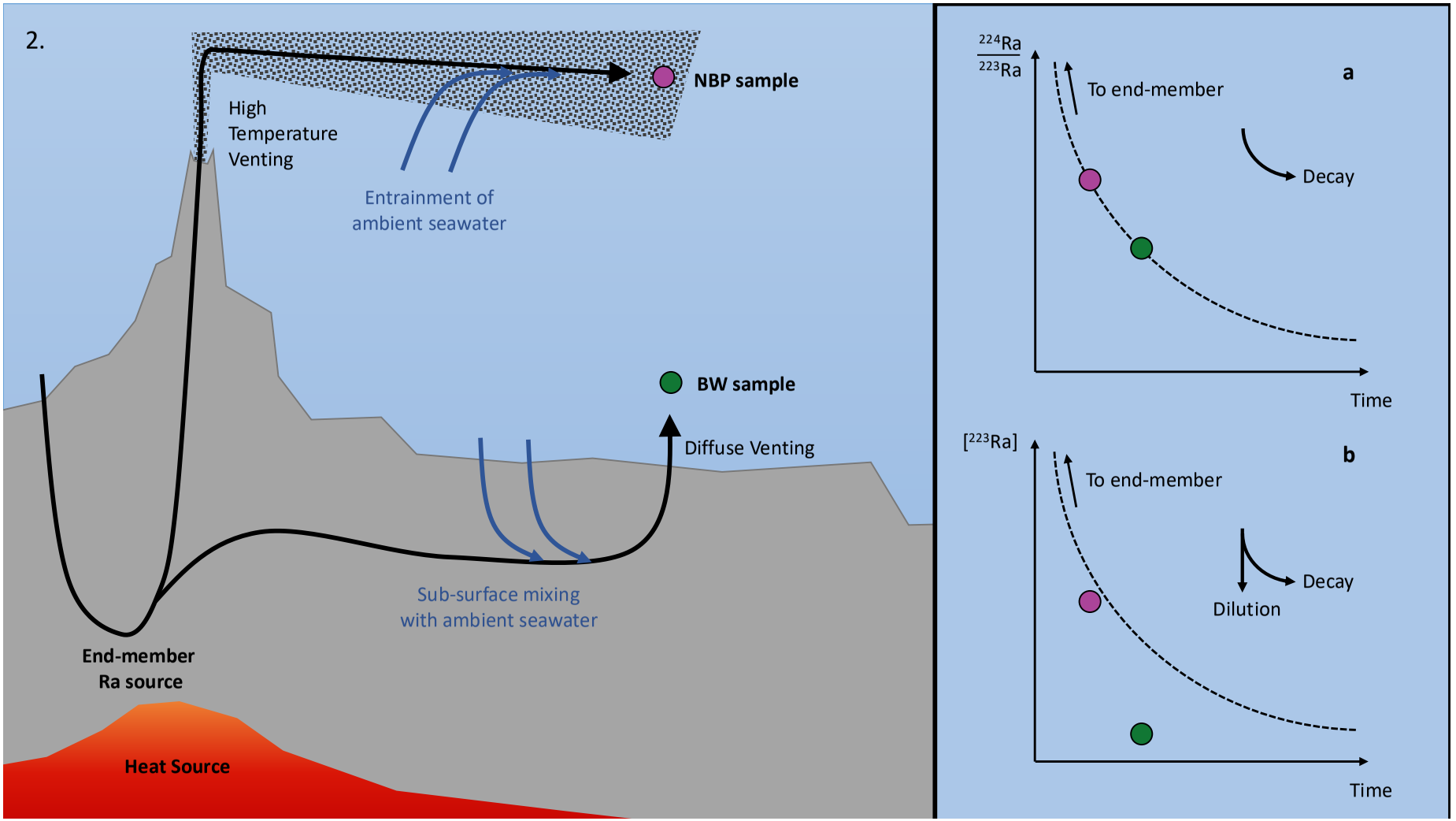

Figure 3.9: This diagram depicts an idealised model of diffuse venting (source 2. in figure 3.8). In this model both the neutrally-buoyant plume sample (NBP, purple) and the bottom water sample (BW, green) contain radium from the same end-member. On the right are two graphs showing the change in (a) radium-224/radium-223 ratio and (b) radium-223 activity over time. The radium-224/radium-223 ratio (a) is unaffected by dilution while the radium-223 activity (b) of the BW is further from the model (dashed line) than NBP implying that BW is more dilute.

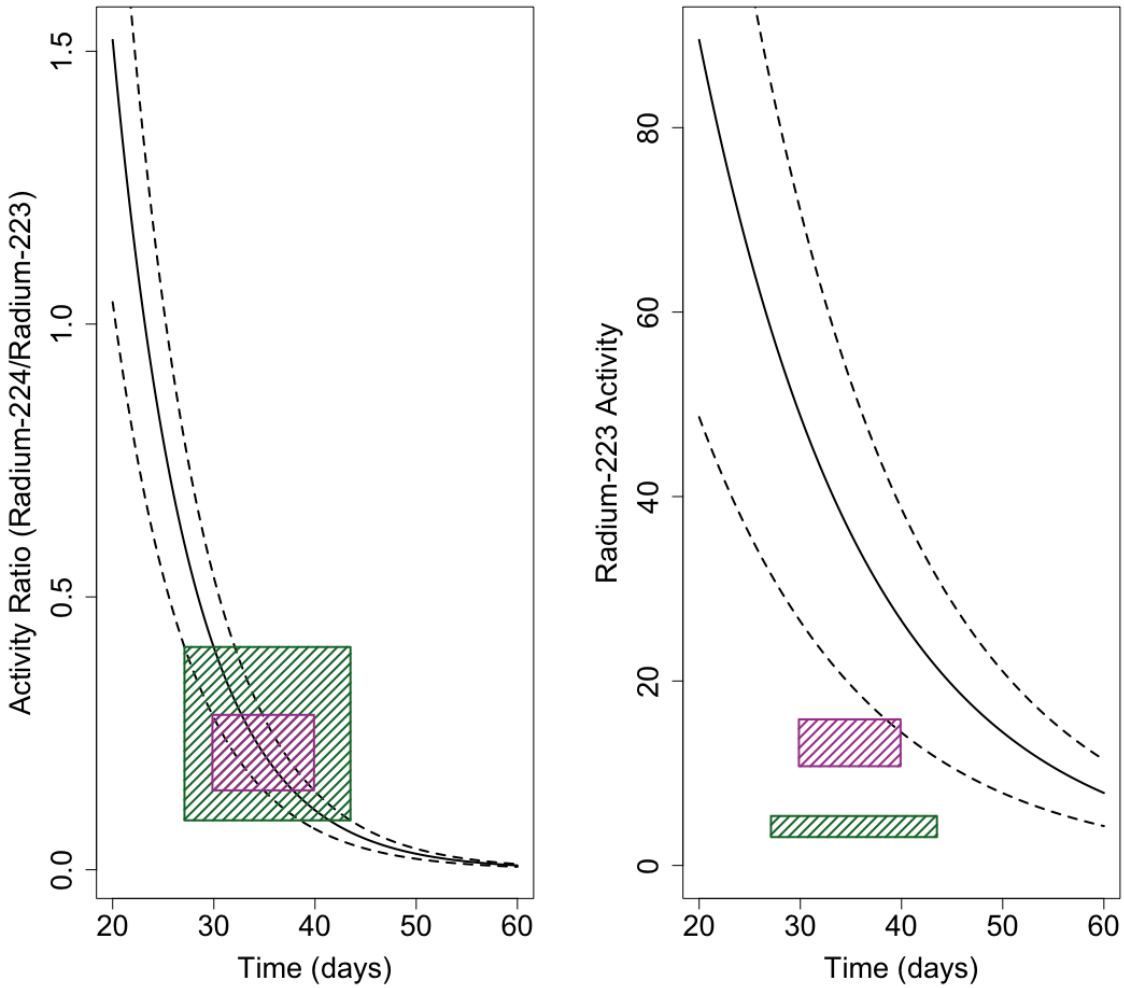

Figure 3.10: A: A model of the evolution of hydrothermal fluid end-member 224-radium/223-radium activity ratio over time (black solid line) with 2σ error plotted as dashed lines. Observed radium-224/radium223 activity ranges ($\bar{x} \pm 2\sigma$) determine the height of the plotted boxes while the widths are determined be the age range calculated from the activity ratio ranges. B: A model of hydrothermal fluid radium-223 activity over time (black solid line) with 2σ error plotted as dashed lines. The vertical dimensions of the boxes are determined by the radium-223 activity range ($\bar{x} \pm 2\sigma$) while the horizontal dimensions are inherited from the age range calculated in A. The hashed purple boxes represent TAG axial valley bottom samples (n=12) (BW, figure 3.9) while the hashed green boxes represent TAG neutrally-buoyant plume depth samples (n=2) (NBP, figure 3.9). Model starting radium-224/radium-223 activity ratio and radium-223 activity were estimated to be $21.2 \pm 6.7 (2\sigma,\ n = 12)$ and 302 ± 138 dpm/m^3 (2σ, $n = 12$) respectively based on the mean of values reported by Kipp et al. (2018).

to supply the flux of radium-223 to the overlying waters. These parent isotopes include actinium-227, protactinium-231 and uranium-235. The large radium-223 signals observed in the axial valley of the MAR, accompanied by high radium-223/radium-224 activity ratios, are absent above open ocean sediments along the GEOTRACES GA03 cruise (Charette et al., 2014). If sediments were responsible for the large radium-223 signals seen in the MAR axial valley then these sediments should either have a larger activity ratio ([231Pa]/[232Th]) or higher activities of these isotopes than the North Atlantic open ocean sediments of equivalent water depth. Alternatively, more effective transport of radium-isotopes out of the sediments might explain the difference in bottom water radium-223 activity in the axial valley compared to the abyssal plains.

Sediments surrounding TAG, enriched in particle scavenged actinium-227 of hydrothermal origin, have previously been proposed as the source of radium-223 to the overyling bottom waters (Kipp et al., 2015a). Scavenging of protactinium-231 by plume particulate with subsequent deposition and release of radium-223 via actinium-227 has also been proposed (Charette et al., 2014; German et al., 1991). Alternatively both actinium-227 and protactinium-231 could be supported in sediments rich in uranium-235. Intermittent activity at the TAG vent field over the last 120,000 years provides enough time for seawater uranium to accumulate in sediments via reductive fixation in sulfide rich sediments or scavenging by Fe-(oxy)hydroxide or Mn-oxide rich metalliferous sediments. Such a long period of accumulation of uranium-235 in sediments would also allow secular equilibrium to be achieved between uranium-235 and its daughter isotopes (Lalou et al., 1990).

Measured uranium-235 activities of hydrothermal plume fallout material are equivalent to open ocean sediments while hydrothermal sulfide deposit material display uranium-235 activities 6 times higher (Mills et al., 1993). Mills et al. (1993) hypothesised that as pore waters diffuse through sulfide deposit material, sulfide grains are oxidised with pore water U fixation occurring at the oxide/sulfide boundary of the sulfide grain. Since radium-223 is part of the uranium-235 decay chain, it is possible that high activities of uranium-235 in hydrothermal sulfide deposits could result in high radium-223 activity within these deposits; this radium-223 could then be transported, via diffusion or low temperature hydrothermal circulation, into overlying waters. This mechanism, requires the uranium-235 rich sediments to be $> 3 \times 10^4$ years old in order to allow secular equilibrium to be achieved with protactinium-

231. A measurement made by German (1993) in a hydrothermal sulphide deposit at TAG, however, displays a [protactinium-231]/[uranium-235] activity ratio of 0.37. This sulphide deposit was located on TAG hydrothermal mound and so was likely to be considerably younger than deposits that may exist at relict vent sites within the MAR axial valley.

Since radium-223 and radium-224 have known but different half-lives, the radium-223 / radium-224 ratio should behave predictably and can be used to further investigate potential sediment sources (equation 3.4).

$$\frac{[^{223}Ra]_t}{[^{224}Ra]_t} = \frac{[^{223}Ra]_0 * e^{-\lambda_{223}t}}{[^{224}Ra]_0 * e^{-\lambda_{224}t}} \tag{3.4}$$

Using equation 3.5 it is possible to estimate an approximate radium-223/radium-224 activity ratio that would be present in waters diffusing from a sediment in which the radio-isotopes were equilibrated with their respective parent isotopes.

$$\frac{[^{223}Ra]_{Pred.}}{[^{224}Ra]_{Pred.}} = \frac{[^{231}Pa]}{[^{232}Th]} \tag{3.5}$$

A high radium-223/radium-224 ratio can be produced either by a source with a large activity ratio of protactinium-231 to thorium-232 ([231Pa]/[232Th]) or by a source with a low ratio but high activities of both isotopes. The latter would allow time for the radium-223/radium-224 ratio to rise, since radium-224 has a shorter half-life than radium-223, before the activities of both isotopes fall below detection limits (equation 3.4).

Atlantic open ocean sediment uranium-235, protactinium-231 and thorium-232 activities along with predicted radium-223/radium-224 activity ratio (equation 3.4) were plotted against water depth (figure 3.11). Although high uranium-235 activity was measured in hydrothermal sulfide deposits, protactinium-231 activities in those deposits were lower than open-ocean sediments at equivalent water depth. Although thorium-232 activities in south Atlantic open ocean sediments were low, thorium-232 activites measured in sulfide deposits were lower, resulting in similar maximum predicted radium-223/radium-224 activity ratios for open ocean sediments and hydrothermal sulfide deposits.

The radium-223/radium-224 activity ratios presented here from five water-column activity depth profiles in the vicinity of TAG averaged 5.4, comfortably below the maximums displayed in both open ocean sediments and hydrothermal sulfide deposits. Assuming a

conservative sediment density of 1 g/cm^3 and the maximum radium-223 activity seen axial bottom waters, 21.5 dpm/m^3, then one cubic metre of bottom water would only need to reach secular equilibrium with underlying sediment to a depth of approximately $4 \times 10^{-}4$ cm. Although the interaction of bottom waters with sediments and pore-waters far more complex than this simple calculation assumes, the result implies open ocean sediments could support high radium-223 activities with high radium-223/radium-224 ratios in bottom waters given sufficient equilibration time or bottom-water-sediment interaction to sufficient depth (Hamilton, 1976). Hydrothermal sulfide deposits and plume fallout material would need to achieve equilibrium with a greater depth of sediment/deposit then open ocean sediments due to lower inherent protactinium-231 activities.

To summarize, modelling of radium-223 and -224 decay shows that diffuse venting of a high-temperature hydrothermal end-member cannot explain observations of elevated radium-223 at the bottom of axial valley profiles. Examination of possible sediment sources of radium-223 favours a sulfide deposit source and open ocean sediments, although it is difficult to rule out other sediment sources without further knowledge of the mechanisms governing sediment-seawater interaction in these settings. In axial valleys where the lateral movement of bottom waters may be restricted and/or thermally-driven circulation of bottom waters through sediments may occur, the flux of radium-isotopes into overlying waters could be elevated. These findings indicate that caution is needed when using short-lived radium isotopes to quantify rates of physical processes in MAR hydrothermal settings, since these isotopes are likely to originate from multiple sources.

3.6.3 Using short-lived radium isotopes to determine hydrothermal plume age

Although a newer study by Neuholz et al. (2020) at Brothers Volcano (Kermadec Arc) applies short-lived radium isotopes in a submarine hydrothermal setting, the previous investigation of short-lived radium isotopes in TAG hydrothermal plume by Kipp et al. (2018) remains the dataset most comparable to this study. Taking slightly different approaches, both Kipp et al. (2018) and Neuholz et al. (2020) applied radium isotopes to assess plume ages.

Kipp et al. (2018) assumed the TAG end-member fluid radium-224/radium-228 ratio ($\frac{[^{224}Ra]}{[^{228}Ra]}_{vent fluids}$) to be the mean of activity ratios observed at the Juan de Fuca and Reykjanes

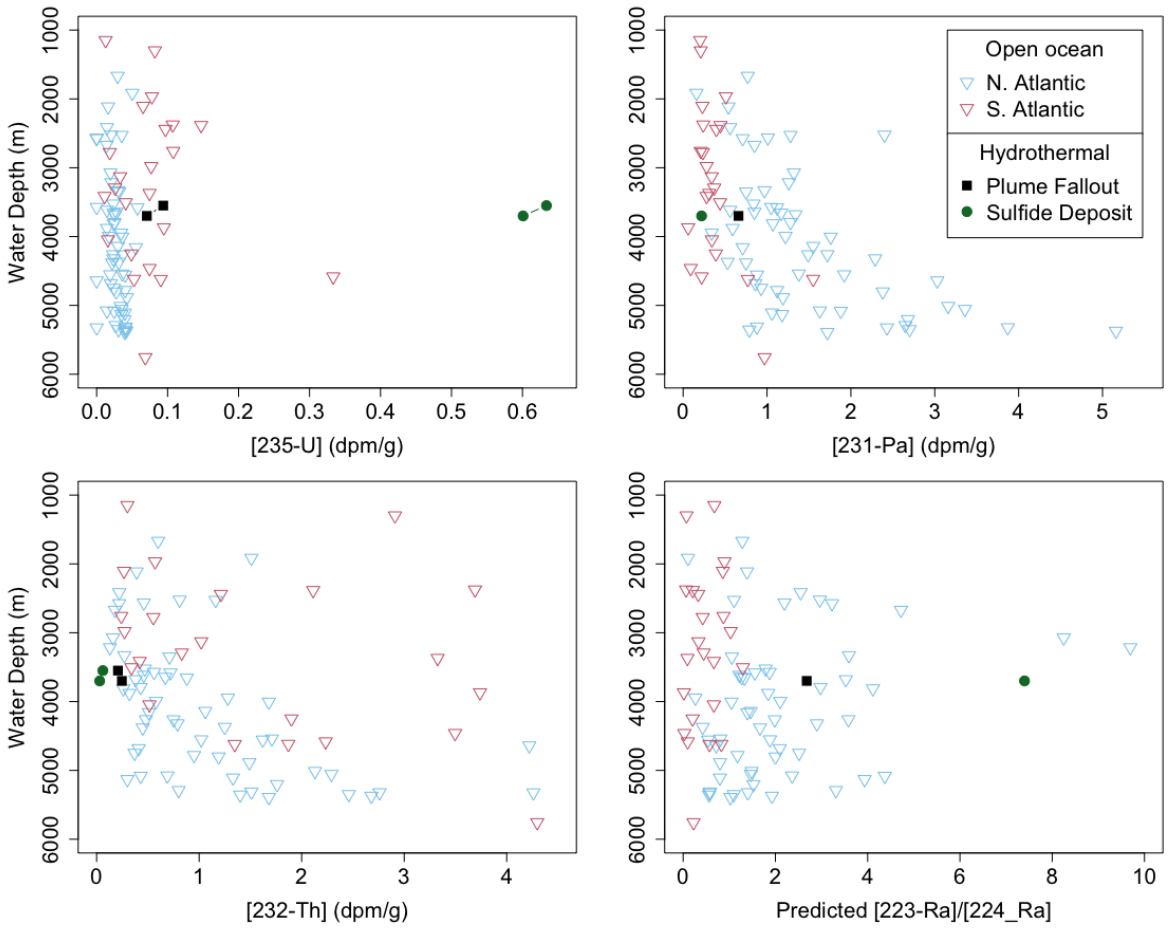

Figure 3.11: Plots of radionuclide activity in sediments with water depth (top left: 235-Uranium, top right: 231-Protactinium and bottom left : 232-Thorium). The bottom left plot shows the radium-223/radium-224 ratio predicted by the activities of 231Pa, 235U and 232Th in these sediments. Data from two hydrothermal sediment cores near TAG vent site were divided into two sediment types 'plume fallout material' and 'sulfide deposit material'. North Atlantic data:(Bacon and Rosholt, 1982; Ku et al., 1972; Lippold et al., 2012, 2016; Negre et al., 2010; Roberts et al., 2014), South atlantic data :(Walter et al., 1997), TAG sediment core data:(Mills et al., 1993; German, 1993).

Ridges. The activity ratio that was observed in the TAG plume ($\frac{[^{224}Ra_{xs}]}{[^{228}Ra_{ht}]}_{plume}$) was then used to calculate the time since venting or 'plume age' (t, equation 3.6).

$$\frac{[^{224}Ra_{xs}]}{[^{228}Ra_{ht}]}_{plume} = \frac{[^{224}Ra]}{[^{228}Ra]}_{ventfluids} * e^{-\lambda_{224}t} \tag{3.6}$$

This approach makes a number of necessary assumptions: any excess activity of radium-224 and -228 is introduced solely at the source, there is no fractionation of the two radium isotopes and that the mean end-member activity ratio used is representative of TAG vent fluids. It is important to assess how robust each these assumptions are at TAG vent site, particularly in light of our observations of widespread benthic enrichments of radium-224.

The first assumption is that the excess activities of radium-224 and radium-228 are introduced exclusively at TAG vent site. This assumption is safer for radium-224 due to its short radioactive half-life, any alternate source would need to be close to the sampling location or the source location. A significant benthic input is apparent in the depth profile of radium-224 activity presented by Kipp et al. (2018) over TAG (GA03, Station 16), although this signal appears to have decayed below the plume. The current study has greatly expanded the spatial resolution of short-lived radium isotope data at TAG with satellite casts as can be seen in figure 3.1. Variable but elevated excess radium-224 activities at the bottom of all axial casts at TAG suggest that benthic inputs of radium-224 are common and possibly dominant within the axial valley near TAG. These observations challenge the assumption of a sole source of excess radium-224 activity to mid-depth samples. It was due to large benthic inputs of radium-223 that Kipp et al. (2018) did not use radium-223 activities to estimate plume age at TAG; our high-resolution data suggests that radium-224 activities may be similarly compromised.

For the longer-lived radium-228, assumption of a sole hydrothermal source is more problematic. Kipp et al. (2018) calculated hydrothermal excess radium-228 activities by subtracting an assumed constant 'background activity' measured at off-axis sites from the activities observed in the plume. This allows the isolation of proximal sources of excess radium-228 activity from those further afield but introduces further uncertainty. The background radium-228 activity calculated was 0.12±0.14 dpm/100L (1σ, n = 45); the standard deviation was not propagated through the subtraction calculation and so not included in final hydrothermal excess radium-228 activities (Kipp et al., 2018). Given that the peak plume radium-228 activity

reported at this station is 0.4 dpm/100L, inclusion of uncertainty associated with the mean background radium-228 activity would have significant effect on uncertainty associated with radium-224/radium-228 activity ratio, and estimated plume age.

The second assumption, that there is no fractionation of the two radium isotopes, is supported by the conservative behaviour of radium in seawater. The most likely source of potential fractionation would be due to particulate scavenging; radium has a well known affinity for Mn-oxyhydroxides (Moore and Reid, 1973). Kipp et al. (2018) concluded that scavenging causes negligible loss of radium-226 activity from the dissolved phase after they found that radium-226 activities on particles represented <0.1 % of dissolved radium-226.

Finally, it is assumed that the radium-224/radium-228 ratio in TAG fluids is similar to those of other vent fluids because radium-224 and radium-228, from the same U-series decay chain, are likely to be in secular equilibrium (Kipp et al., 2018). Although a source of uncertainty, this assumption is necessary since short-lived radium isotope activities in TAG vent fluids have not been measured.

Expanding on the work of Kipp et al. (2018), Neuholz et al. (2020) calculated neutrally buoyant plume age using short-lived radium isotope ratios at Brothers Volcano (Kermadec Arc). Once introduced into deep-waters the activities of radium isotopes are controlled by radioactive decay, dilution and mixing. Dilution and mixing simultaneously act on all elements in hydrothermal plumes and are governed by advection, the physical transport of the fluid parcel containing radium isotopes, and eddy diffusion, the omnidirectional dispersion of radium isotopes into surrounding waters. Neuholz et al. (2020) used two radium dispersion models: one purely driven by horizontal advection, the other purely driven by eddy diffusion. In each instance the alternate process was assumed to be negligible.

When modelling radium dispersion by horizontal advection, Neuholz et al. (2020) made plume age calculations using equation 3.1, previously presented by Moore (2000a). This approach assumes that the system is at steady state with a sole source of excess radium-223 and -224 activity in a constant ratio. This ratio then evolves due to the different decay rates of the two isotopes. In addition, advective transport is assumed to be dominant, and the neutrally buoyant plume is assumed to be transported without entrainment of bottom waters.

When modelling radium dispersion by eddy diffusion Neuholz et al. (2020) used an analytical reactive transport model to evaluate the influence of eddy diffusion in 2-D space. A

similar approach was taken by Moore (2000b) but in one dimension rather than two. This reactive transport model assumes the following: constant horizontal diffusion and advection, conservative behaviour of radium isotopes (except for decay) and a single site of radium-isotope introduction at the source vent site.

These two additional approaches used by Neuholz et al. (2020) rest on very similar assumptions as the approach of Kipp et al. (2018) at TAG; critically, a single source of the radium isotopes used in the estimation of plume age. Our observations of large benthic inputs of radium-223 and -224 within the TAG axial valley as well as north of Rainbow vent site combined with a lack of significant plume-associated elevations in the activities of these isotopes challenges the utility of models assuming a single source in these locations. The improved spatial resolution of our measurements demonstrates the proximity of axial valley benthic inputs to sites of active venting, indicating that such inputs are not negligible, even in the near-field. Since no anomalies in radium-223 and -224 activities were observed in the NBP but large anomalies were observed near the seafloor at all profiles within the MAR axial valley, it is perhaps possible to assume the inverse: high-temperature hydrothermal inputs are negligible in comparison to benthic inputs. This would allow the calculation of vertical diffusivity within the axial valley.

3.6.4 Vertical diffusivities from radium-223 and radium-224 activity gradients

The calculation of vertical diffusivity (K_v) requires a discernable concentration gradient over a defined spatial scale. Only vertical profiles that met these criteria were included in calculations of K_v. Given the lack of observable plume-associated radium-223 and radium-224 anomalies (figures 3.6, 3.7) and lack of correlation between radium-223 and -224 activities and concentrations of dissolved Mn, Fe or xsHe, horizontal advection of an additional hydrothermal end-member has been assumed to be negligible.

A previous study at the Endeavour segment of the Juan de Fuca Ridge showed that radon-222 measured in the non-buoyant plume was entrained from a bottom source rich in the isotope (Kadko et al., 1990). At Rainbow vent field German et al. (2010a) argued that entrainment of bottom sources more than a few metres from the vent would be unlikely based on a hydrothermal plume model by Speer and Rona (1989) with additional evidence from

Fe:Mn ratios. If it is assume that plume sources of radium-223 and -224 are negligible and that any bottom source is unlikely to be entrained and advected horizontally, then we can use radium-223 and -224 to calculate vertical diffusivity at these sites.

Vertical diffusivities were calculated by fitting equation 3.7, from (Chung and Kim, 1980), to a plot of height above bottom sample versus the natural log of the radium-223 activity and, separately, radium-224 activity.

$$\ln C_z = -\sqrt{\frac{\lambda}{K_v}} \times z + \ln C_0 \tag{3.7}$$

Where C_0 is the radium isotope activity at the bottom of the water-column profile, C_z is the radium isotope activity at distance z from the bottom, λ is the radium isotope decay constant and K_v is the vertical diffusivity.

The assumptions made by the 1-dimensional diffusion equation 3.7 are the same as those made by Moore (2000b) when calculating the horizontal eddy-diffusion coefficient K_h. Firstly, diffusion is assumed to be the dominant transport process with a constant K_v; transport and input perpendicular to the 1-dimensional model are assumed to be negligible. In reality, radium-isotopes may be released from sediments or deposits on the seafloor, entrained into the hydrothermal plume and advected horizontally along isopycnals, increasing the K_v values calculated from vertical activity profiles. If present, vertical advection upward from the seafloor would also increase the calculated K_v while advection downward or horizontally would decrease the calculated K_v.

Secondly, the tracer, radium-223 or -224, is assumed to only be input at the bottom of the vertical profile used to calculate each K_v. Additional input of radium-223 or -224 to a vertical profile from another source would increase the K_v calculated from that profile unless addition occurs at the bottom. K_v values calculated in figure 3.12 are therefore likely to incorporate the effects of unknown and/or unconstrained tracer-sources and transport processes. This means that such 'effective' K_v values represent the sum of transport and input processes affecting the tracer and so should be interpreted qualitatively; in this context, a high K_v indicates elevated vertical transport but does not accurately quantify or distinguish transport processes.

As can be seen in figure 3.12, there is some agreement in slope between the two radium-223 profiles at rainbow vent site providing K_v values within 2σ uncertainty of each other and a mean K_v of $1290\,\mathrm{cm^2\,s^{-1}}$ ($\pm 700\,\mathrm{cm^2\,s^{-1}}$ 2 S.D.). The N. TAG (8) and S. TAG (9) radium-

223 profiles also display similar K_v values with an average of $600\,cm^2\,s^{-1}$ ($\pm 370\,cm^2\,s^{-1}$ 2 S.D.). Vertical diffusivity from the radium-223 profile sampled above TAG vent site is $171\,cm^2\,s^{-1}$ ($\pm 110\,cm^2\,s^{-1}$ 2 S.D.). These five axial profiles provide a mean K_v of $790\,cm^2\,s^{-1}$ ($\pm 650\,cm^2\,s^{-1}$, 2 S.D.).

In contrast to radium-223 derived K_v values, those derived from depth profiles of radium-224 are approximately $3-5$ times higher. The difference in K_v values derived from each isotope may be explained by differential diffusion due to the difference in the decay constants of the isotopes leading to differences in the isotope distribution length scale relative to the length scale of mixing in these settings (Stachelhaus and Moran, 2012). Alternatively, differences in K_v could be caused by large uncertainties due to a small number of data points, variability in radium sources or spatial and temporal variability in mixing (Moore, 2000b; Charette et al., 2007; Colbert and Hammond, 2007). Both isotopes indicate higher K_v at Rainbow than TAG. The mean radium-224 derived K_v from three axial profiles was $1870\,cm^2\,s^{-1}$ ($\pm 1640\,cm^2\,s^{-1}$, 2 S.D.); a relatively similar value to that provided by radium-223.

The values calculated in the present study are interpreted qualitatively as they do not isolate processes relating to diffusion but incorporate advection and potential short-lived radium isotope signals from unknown sources. Although qualitative, our values indicate that vertical diffusivity within the axial valley of the MAR is up to 1000-fold higher than that calculated for rough MAR spur topography (0.3-0.6 $cm^2\,s^{-1}$; 95% confidence bounds) or the smooth abyssal plains of the Brasil basin ($0.1\,cm^2\,s^{-1}$) (Polzin et al., 1997). Our values are also significantly larger than those found using SF_6 tracer experiments along the axial trough of the East Pacific Rise at 9°30'N ($2\,cm^2\,s^{-1}$) (Watson and Ledwell, 2000; Jackson et al., 2010). The deeper, wider MAR axial valley may display larger vertical diffusivity due to the presence of thicker benthic boundary layers caused by turbulent mixing within the axial valley. Elevated vertical water mass tranport could increase the flux of TEIs from hydrothermal plumes, metal rich sediments and sulfide deposits out of the axial valley, impacting the distribution of elements and isotopes that trace and facilitate biogeochemical and physical processes throughout the ocean. Improved understanding of the ubiquity and magnitude of local sources of radium-223 and -224 as well as measurement of direction, variability and magnitude of advection within the MAR axial valley and overlying waters would allow further

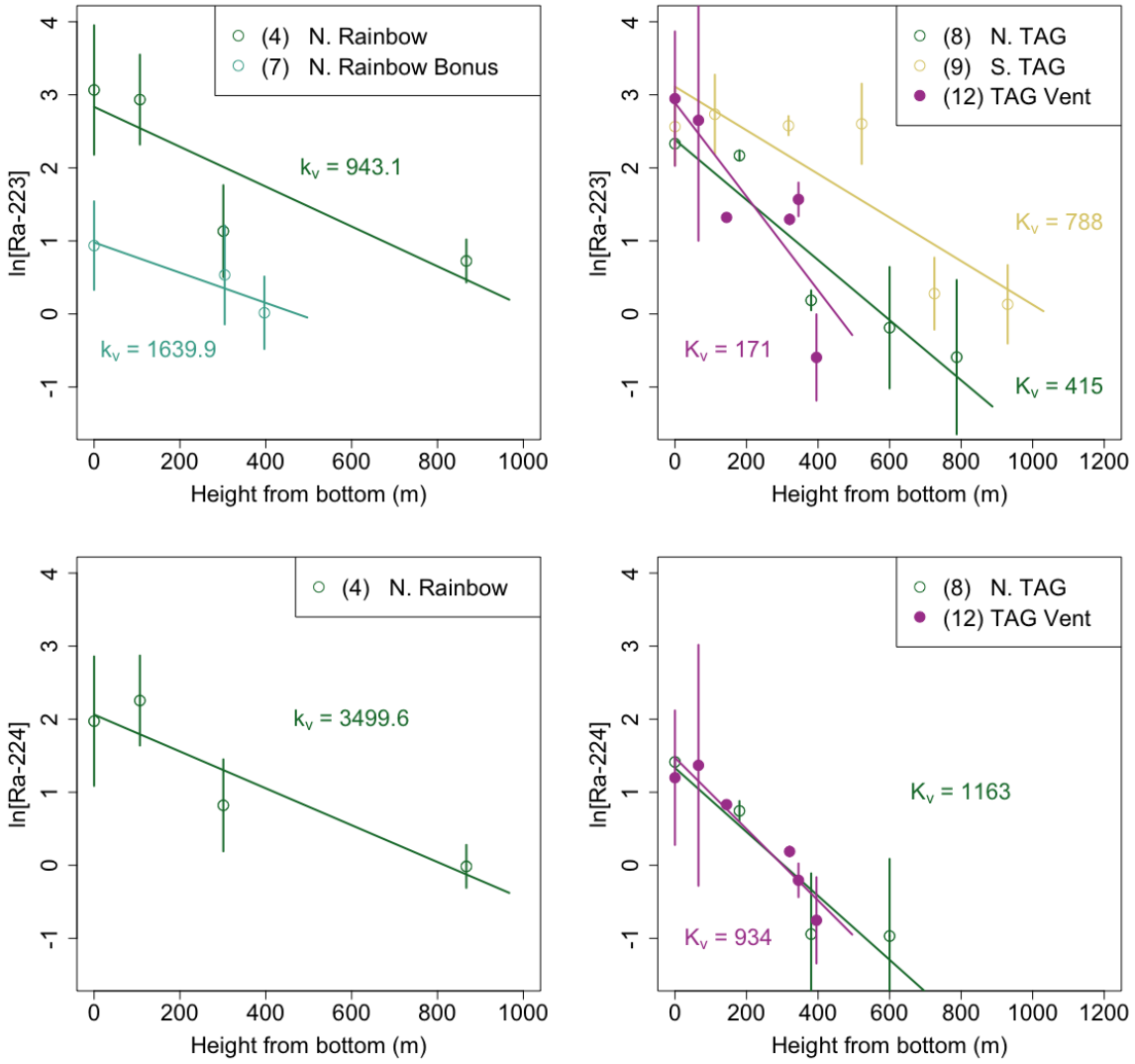

Figure 3.12: Natural log plots of excess radium-223 and excess radium-224 (dpm/1000L) versus height from bottom sample. The vertical diffusivity (K_v, cm^2s^{-1}) is inversely proportional to the square of the gradient of the fit via equation 3.7.

constraint of local vertical diffusivity and more appropriate use of short-lived radium isotopes as tracers in these settings.

3.7 Conclusions

Twelve radium-223 and radium-224 depth profiles indicate sediment as the dominant source of short-lived radium isotopes at two vent fields on the MAR. Modelling of radium-isotope decay and synthesis of published uranium-235, protactinium-231 and thorium-232 activities in open ocean and hydrothermal sediments suggests hydrothermal sulfides are most likely the major source of radium-223 in these settings. Evidence of benthic sources of short-lived radium isotopes suggests that ageing the hydrothermal plume using radium-223 or -224 is not possible in these locations and that caution should be exercised in the use of these isotopes elsewhere.

Vertical diffusivity (K_v) values calculated from axial MAR profiles of radium-223 and -224 activities provide a mean K_v of $790\,cm^2\,s^{-1}$ ($\pm 650\,cm^2\,s^{-1}$, 2 S.D.) and $1870\,cm^2\,s^{-1}$ ($\pm 1640\,cm^2\,s^{-1}$, 2 S.D.) respectively, significantly higher than previously calculated for MAR ridge flanks and Atlantic abyssal plains. Increased vertical diffusivities at mid-ocean ridge hydrothermal vent sites could lead to significant fluxes from TEI-rich sediments and hydrothermal plumes, impacting local and global TEI budgets and potentially enhancing ocean primary productivity with resulting impacts on carbon cycling and climate.

Chapter 4

Constraints on seawater and crustal REE patterns from measurement of dissolved Eu anomalies in seawater

4.1 Abstract

The positive Eu anomaly (Eu*), characteristic of hydrothermal vent fluids, shows potential as a tracer of hydrothermal inputs in the ocean. Hydrothermal plumes, however, act as a net sink of rare earth elements (REEs) from seawater. If hydrothermal inputs do not impact seawater Eu* values then any variation in seawater Eu* may record differences in upper continental crustal (UCC) inputs to the ocean. This study investigates the impact of hydrothermal inputs on seawater Eu* using concentration measurements of dissolved rare earth elements (REEs) from a transect of water column profiles along the Mid-Atlantic Ridge (MAR). Significant dissolved Eu anomalies are apparent in three separate neutrally buoyant plumes on the MAR. These Eu anomalies are only transmitted to surrounding ocean waters by the 0.02% of hydrothermal end-member Eu that survives removal from solution by particle scavenging. Mid-ocean ridge hydrothermal inputs are not expected to have a measurable impact on whole-ocean Eu*. A comparison of four ocean basins showed no significant variation in Eu* between basins or with depth, indicating that Eu* is well mixed in the ocean with respect to its inputs. Seawater Eu* therefore provides an assessment of the average upper-continental crustal Eu* input to the ocean. The global mean seawater Eu* calculated in this

study suggests an upper continental crustal Eu* of 0.97 ($\pm$0.07, 2σ, PAAS-normalised), supporting the use of values from Post-Archaean Australian Shale (PAAS) and North American Shale Composite (NASC) for upper continental crustal Eu*.

4.2 Introduction

The chemical coherence of the rare earth elements (REEs) and the sensitivity of the REE pattern to geochemical and physical processing provides opportunities to investigate mechanisms that control the composition of natural waters and partitioning of elements between natural reservoirs (Elderfield et al., 1990). REEs enter the ocean from multiple sources with the total REE flux into the ocean $\approx 2.6(\pm 1.2) \times 10^6$mol/year (Elderfield and Schultz, 1996; Alibo and Nozaki, 1999; Nozaki, 2001). The majority of REEs are removed to sediments via adsorption to sinking particles (Nozaki, 2001). The dominant input of REEs to the ocean is from weathering of the upper continental crust (UCC) and is approximately equal to the total REE flux. Hydrothermal fluids are rich in REEs with concentrations $10^2 - 10^4$ times higher than ambient seawater (German et al., 1990; Klinkhammer et al., 1995; Douville et al., 2002). Rapid and extensive scavenging in particle-rich hydrothermal plumes removes more REEs from solution than are input by hydrothermal fluids, leading mid-ocean ridge (MOR) hydrothermal sites to be viewed as net sinks for REEs in the ocean (Zheng et al., 2016). Using Nd-isotopes, Stichel et al. (2018) calculated that hydrothermal scavenging provided a global Nd sink of 3.4×10^6 mol/year, while Rudnicki and Elderfield (1993) estimated a total hydrothermal plume removal rate for Nd of 8.8×10^6 mol/year.

Although MOR hydrothermal sites are likely to be net sinks, this does not preclude the survival and mixing of a hydrothermal REE signal with surrounding seawater. The most characteristic hydrothermal REE signal is a positive Eu anomaly (Eu*) (figure 4.1). A Eu anomaly is when the concentration of Eu is enriched or depleted relative to Sm and Gd when all concentrations are normalised to a standard such as shale or chondrite (equation 4.1); many workers have used Post-Archaean Australian Shale (PAAS) (Taylor and McLennan, 1985).

$$\mathrm{Eu}^* = \frac{[\mathrm{Eu}]_{\text{Shale-Normalised}}}{\frac{1}{2}[\mathrm{Sm}]_{\text{Shale-Normalised}} + \frac{1}{2}[\mathrm{Gd}]_{\text{Shale-Normalised}}} \tag{4.1}$$

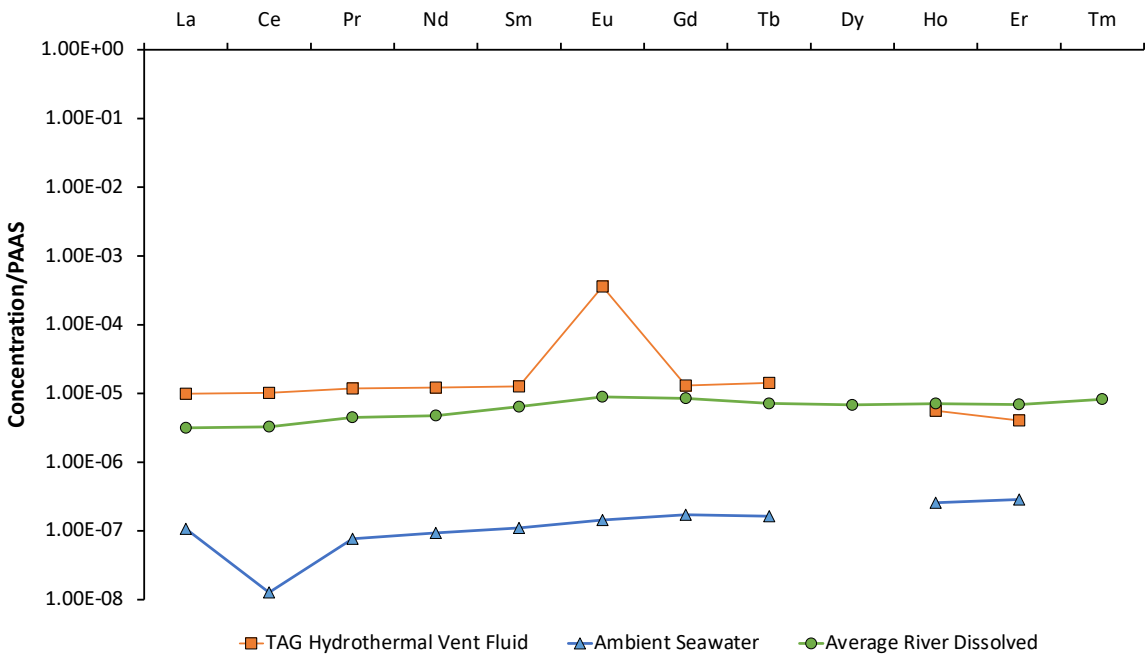

Figure 4.1: Dissolved REE patterns of average river water, seawater and hydrothermal vent fluids. The concentration of each REE divided by its concentration in PAAS is plotted for the dissolved fraction of average river water (Gaillardet et al., 2004), seawater and hydrothermal fluid (German et al., 1990).

Where $[Eu]_{Shale\text{-}Normalised}$, $[Sm]_{Shale\text{-}Normalised}$ and $[Gd]_{Shale\text{-}Normalised}$ are the shale-normalised concentrations of Eu, Sm and Gd respectively.

The dominant process setting hydrothermal REE patterns is ion-exchange during the alteration of hydrothermal plagioclases (Klinkhammer et al., 1994). Among the rare earth elements Eu is unique in favouring a divalent rather than trivalent cation at high temperatures ($> 250°C$) and in plagioclase (Douville et al., 1999). When normalised to shale, hydrothermal end-members display a 10- to 100-fold enrichment of Eu, relative to neighbours Gd and Sm (figure 4.1); within the ocean, this distinctive REE pattern has only been observed in hydrothermal fluids. Elderfield et al. (1988) speculated that the hydrothermal Eu* signal may be useful in quantifying hydrothermal inputs to the oceans in a review of the ocean chemistry of rare earth elements. If the hydrothermal Eu* signal does not impact the REE pattern of seawater then any variation in seawater REE pattern may record differences in the REE patterns of upper continental crustal (UCC) inputs. Eu* may therefore trace the origin of terrigeneous matter entering the ocean; similarly to Nd-isotopes which display varied compositions in crustal rocks and, since their residence times are shorter than the timescale of ocean circulation, ocean basins (Mearns, 1988; Grousset et al., 1992; Lacan et al., 2012).

Mitra et al. (1994) measured REE concentrations in hydrothermal end-member fluids and in the buoyant plume at TAG hydrothermal vent site, concluding that the overall effect of scavenging reactions eliminates the impact of hydrothermal REE inputs on ocean chemistry. German et al. (1990) found that REEs in hydrothermal fluids are not fractionated when removed from solution by plume particle scavenging while Mitra et al. (1994) noted that even the most dilute samples ($\approx$ 700 times dilution) displayed Eu* significantly higher than ambient seawater. These findings imply that, despite extensive scavenging, the distinctive hydrothermal Eu anomaly may survive to be mixed with surrounding deep ocean waters. Measurements of dissolved Eu concentration and Eu* in the neutrally buoyant plume (NBP), where hydrothermal fluid is diluted to $\approx 10^4$ times and the majority of particle scavenging has taken place, could further constrain the impact of hydrothermal fluxes on seawater Eu*.

In this study, depth profiles of [Eu], Eu* and δ^3He values at three MAR vent sites are used to determine post plume-scavenging inputs to the ocean, while further Eu* data from the GEOTRACES GA13 transect are combined with GEOTRACES International Data Product (IDP2017) values from four ocean basins to assess global Eu* variability and the applicability of various shale composites as proxies for continental crustal inputs.

4.3 Sites and sampling

Seawater samples analysed in this study were collected during the JC156 expedition (20/12/2017 - 01/02/2018) as part of the GEOTRACES GA13 section, on board the RRS *James Cook* (figure 4.2).

In this study a total of 208 samples were measured for dissolved REE concentrations, taken from 23 water-column profiles. This included three sites of high-temperature hydrothermal venting: Lucky Strike (37.29°N, 32.28°W), Rainbow (36.23°N, 33.90°W) and TAG (26.14°N, 44.83°W), where the neutrally-buoyant hydrothermal plume was distinguished from surrounding ambient seawaters by dissolved concentrations of mangenese ([Mn]) and δ^3He values.

Seawater was collected for REE analyses in 20 L niskin bottles fitted to a stainless steel CTD frame before being filtered through an Acropak (0.45 µm) filter into precleaned 250 mL low density polyethylene Nalgene bottles. The bottled samples were acidified to pH 2 on the ship using ultra pure HCl under a class 100 laminar-flow hood within a class 100 clean air

container.

4.4 Analytical techniques

Sample analyses were carried out at the University of Oxford following Hathorne et al. (2012). Approximately 15 mL of seawater was spiked with indium to attain an In concentration of 5 ppb. Blanks consisted of 15 mL of MilliQ water, acidified to pH 2 with 25 µL of 6 M HCl and spiked with indium, attaining an In concentration of 5 ppb.

Samples were analysed using a PerkinElmer NexION350D ICP-MS with an online Elemental Scientific seaFAST chromatography system and an Elemental Scientific Apex Omega desolvator. Precision, determined by repeated measurement of an in-house seawater standard, was 2% (2σ, n=20). We verified the accuracy of measurements by comparison with GEOTRACES inter-calibration values. Our concentration values for Sm, Eu and Gd, used in the calculation of Eu*, fell within the bounds of inter-lab reproducibility (10%) reported by Van De Flierdt et al. (2012) (appendix, table A.4).

4.5 Results

In figure 4.3 we have plotted the dissolved concentration of Eu ([Eu]) and Eu* against depth for a composite of all 23-water column profiles. Profiles above high-temperature vent sites are highlighted in colour while water column profiles taken off-axis are distinguished by grey triangles. When viewed as a composite, general trends in the behaviour of [Eu] and Eu* are apparent.

[Eu] displays a nutrient-like profile with surface depletion due to particle scavenging and regeneration with depth due to particle dissolution (figure 4.3). The highest dissolved concentrations of Eu are found in the deepest samples while the samples containing the lowest concentrations of Eu are found in particle-rich environments: surface waters and at depths corresponding to hydrothermal NBPs.

Eu* values - calculated from PAAS-normalised dissolved concentrations of Gd, Eu and Sm - show strikingly little variation with depth, providing an average Eu* of 0.98 ($\pm 0.004, 2\sigma$); samples from the Rainbow NBP are a visible exception. Upon closer inspection, NBP Eu* anomalies are evident at two more MAR vent sites: Lucky Strike and TAG (figure 4.4).

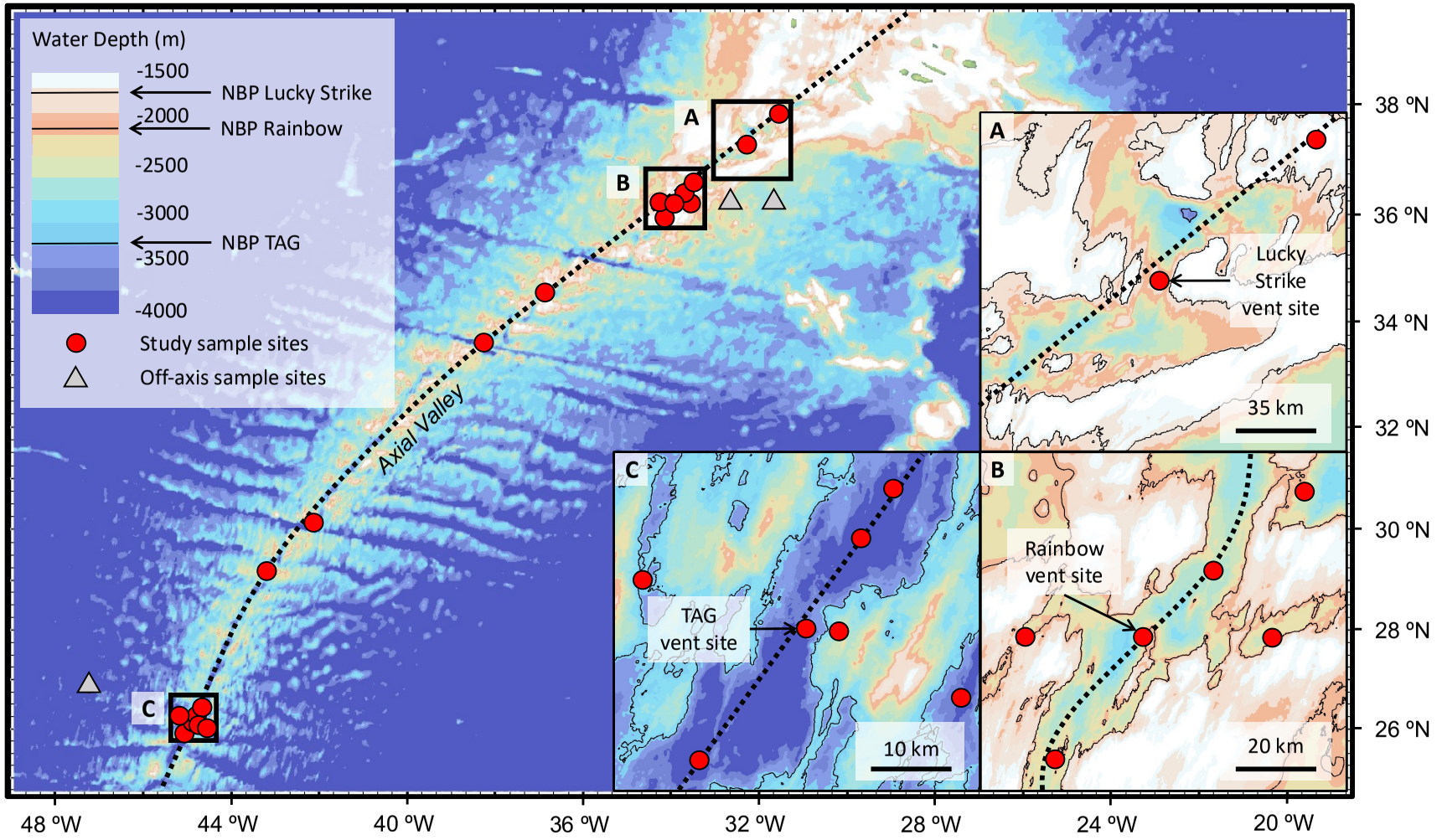

Figure 4.2: Map of REE sample sites along the GEOTRACES GA13 transect. Panel A (inset) details the sampling location above Lucky Strike hydrothermal vent site and the topography of the surrounding axial valley. Panels B (inset) and C (inset) similarly show the Rainbow and TAG hydrothermal sites, respectively. Grey triangles indicate those sample profiles used as "background" seawater values in figure 4.4. In all panels the dotted black line marks the approximate line of the MAR axial valley. Colour-scale representation of bathymetry includes contour lines indicating where bottom topography rises above that of local hydrothermal NBP depth at each vent site.

When water column profiles are viewed at individual vent sites, local NBP features are apparent. Figure 4.4 shows [Mn], δ^3He, [Sm], [Eu] and Eu* with depth for water column profiles at Rainbow (top), TAG (middle) and Lucky Strike (bottom). The data plotted with grey triangles are depth profiles that were taken off axis but at similar latitudes to vent sites and serve as an ambient background seawater signal. Coincident excursions in [Mn] and δ^3He provide a reliable estimate of NBP water-depth at Rainbow (2000 m to 2200 m), TAG (3200 m to 3400 m) and Lucky Strike (1650 m to 1850 m) vent sites. [Mn] and δ^3He data were provided by J. Resing (personal communication, 21/06/2021) and A. Tagliabue (personal communication, 21/06/2021).

Rainbow displayed the highest NBP [Mn] maximum (296.8 ± 0.6pmol/kg); approximately 30 times that of the Lucky Strike NBP maximum and 10 times that of the TAG NBP maximum. TAG displayed the highest NBP δ^3He maximum ($42.57 \pm 0.6\%$), although δ^3He maxima at Rainbow and Lucky Strike were within 15% of TAG. Dissolved concentrations of Eu and Sm were depleted significantly below background values at depths coincident with the NBP. The largest NBP depletions of [Eu] and [Sm] are seen at TAG followed by Lucky Strike and then Rainbow. Eu* values show significant positive excursions at depths coincident with the NBP at all three vents sites studied; the largest excursion is apparent in the Rainbow NBP with a mean PAAS-normalised Eu* of 1.26 ($\pm 0.07, 2\sigma$), followed by TAG and Lucky Strike with Eu* values of 1.14 ($\pm 0.06, 2\sigma$) and 1.11 ($\pm 0.06, 2\sigma$) respectively; these values fall within error of those previously measured in the TAG plume by Stichel et al. (2018).

4.6 Discussion

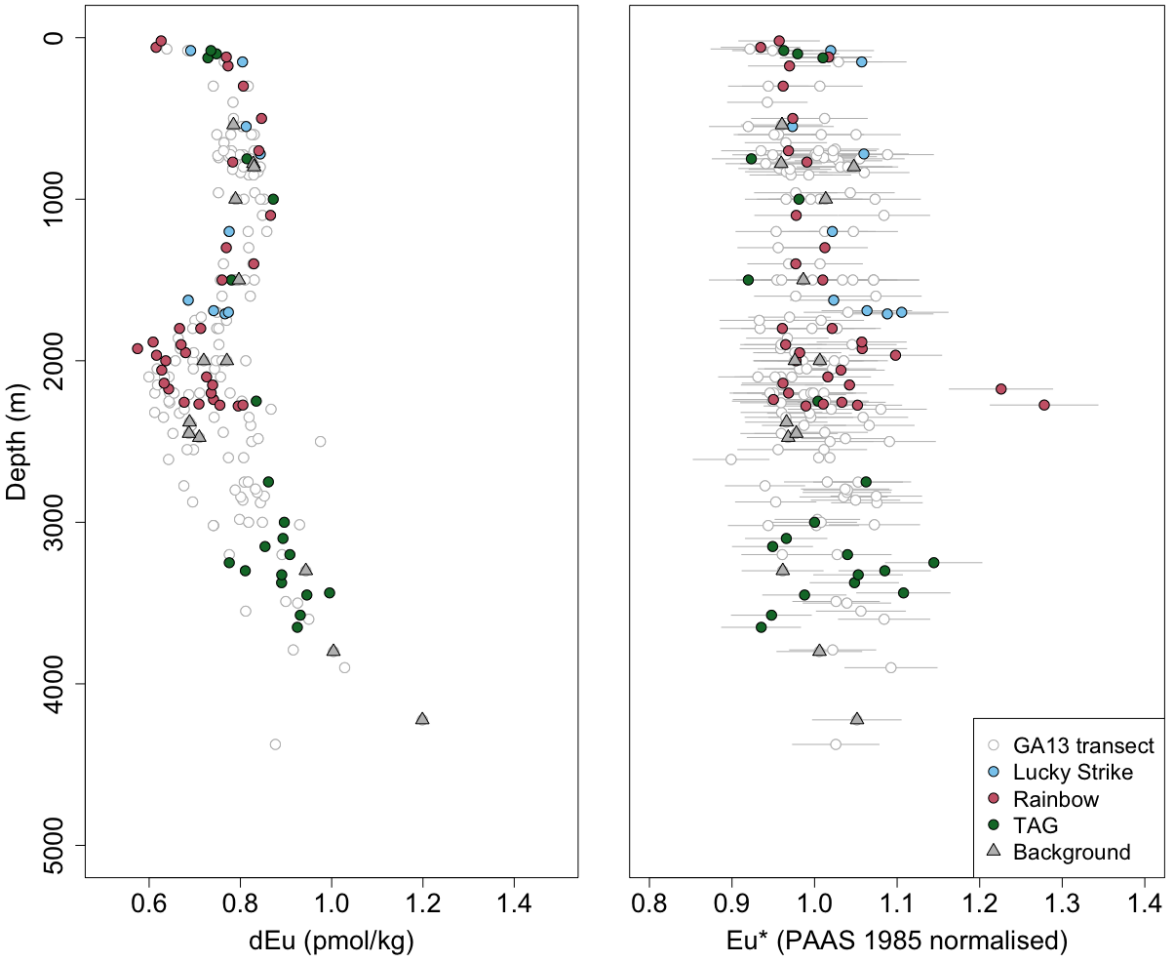

Figure 4.3: A compilation of 23 depth profiles of [Eu] (left) and Eu* (right) for all GA13 samples. The GA13 transect followed the MAR from approximately 38°N to 26°N, sampling between the surface and within 100 m of the seafloor. Four depth profiles taken above vent sites are plotted with colour: Lucky Strike (blue), Rainbow (pink), TAG (green). Samples plotted as grey triangles are from two off-axis "background" stations. All error bars indicate 2σ error; those that are not visible are within the size of the data marker. Eu follows a nutrient-like behaviour with surface depletion and increasing concentration with depth. Although there are two anomalously high values in the Rainbow NBP, Eu* shows no significant trends with depth.

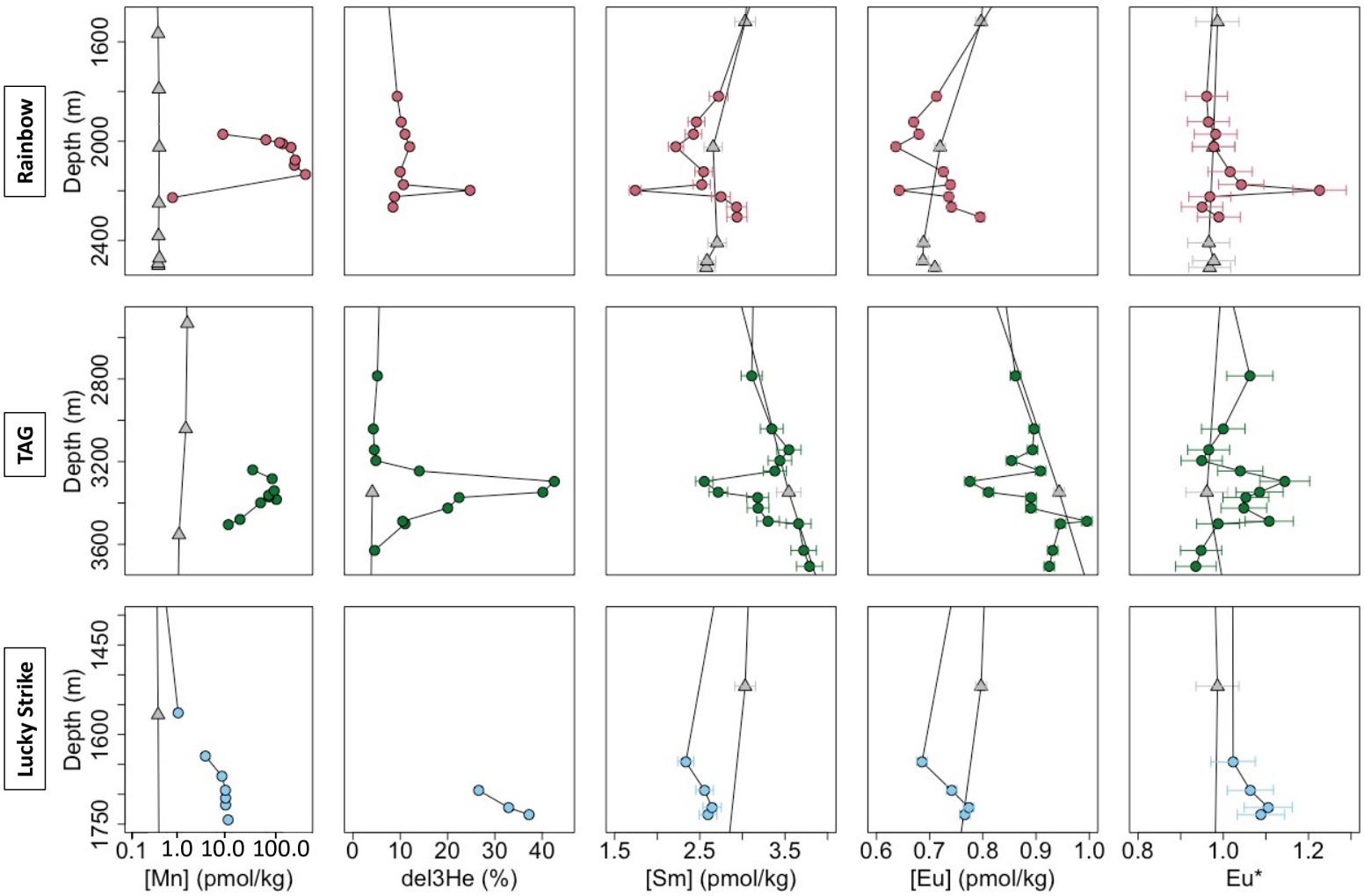

Figure 4.4: Depth profiles showing the impact of the NBP on dissolved Eu* at Rainbow, Lucky Strike and TAG. From left to right [Mn], δ^3He, [Sm], [Eu] and Eu* are plotted for three hydrothermal vent sites: Rainbow (top), TAG (middle) and Lucky Strike (bottom). In each pane, coloured points correspond to waters sampled above the vent site while grey triangles indicate background values, sampled off-axis. All error bars indicate 2σ error; those that are not visible are within the size of data marker.

Constant	Value	Units	Source
δ^3He_{HT} (Rainbow)	651($\pm$65)	%	Jean-Baptiste et al. (2004)
δ^3He_{HT} (TAG)	685($\pm$69)	%	Rudnicki and Elderfield (1992)
δ^3He_{HT} (Lucky Strike)	713($\pm$71)	%	Jean-Baptiste et al. (1998)
δ^3He_{SW} (Atlantic)	7.5($\pm$2.5)	%	A. Tagliabue (pers. comm., 21/06/2021)
$[He]_{HT}$ (Rainbow)	2.67($\pm$0.13)	µM	Jean-Baptiste et al. (2004)
$[He]_{HT}$ (TAG)	2.00($\pm$0.10)	µM	Rudnicki and Elderfield (1992)
$[He]_{HT}$ (Lucky Strike)	0.70($\pm$0.04)	µM	Jean-Baptiste et al. (1998)
$[He]_{SW}$ (Atlantic)	1.85($\pm$0.09)	pM	A. Tagliabue (pers. comm., 21/06/2021)
$[Eu]_{HT}$ (Rainbow)	$3(\pm0.3) \times 10^4$	pM	Douville et al. (2002)
$[Eu]_{HT}$ (TAG)	$2.6(\pm0.26) \times 10^3$	pM	German et al. (1990)
$[Eu]_{HT}$ (Lucky Strike)	$5.6(\pm0.56) \times 10^2$	pM	Klinkhammer et al. (1995)
$[Eu]_{SW}$	1.0($\pm$0.05)	pM	Nozaki (2001)
Eu^{*xs}_{HT} (Rainbow)	$5.5(\pm1.1) \times 10^3$	%	Douville et al. (2002)
Eu^{*xs}_{HT} (TAG)	$2.8(\pm0.6) \times 10^3$	%	German et al. (1990)
Eu^{*xs}_{HT} (Lucky Strike)	$2.6(\pm0.5) \times 10^3$	%	Klinkhammer et al. (1995)
Eu^{*xs}_{SW}	0	%	= PAAS (Taylor and McLennan, 1985)
T_{res}(Eu)	570($\pm$250)	years	Alibo and Nozaki (1999)
$\Delta(mass)_{HT}$	$3(\pm1.5) \times 10^{13}$	kg/year	Elderfield and Schultz (1996)
$mass_{Ocean}$	$1.33(\pm0.03) \times 10^{21}$	kg	Charette and Smith (2010)

Table 4.1: A table displaying the constants used in equations 4.2 to 4.4

4.6.1 Fraction of vent REEs surviving MOR scavenging

The fraction of vent fluid REEs that survive removal from solution by particle scavenging in the plume is calculated in three stages. The first stage assumes that He is an inert plume tracer and uses the unique [He] and δ^3He values of hydrothermal vent fluids to calculate the fraction of water in the NBP that is vent fluid. The second stage combines literature values of Eu* in vent fluids with measured values of [Eu] and Eu* in seawater and the NBP to calculate [Eu] in the vent fluid. The final stage compares the calculated [Eu] in vent fluid with direct measurements of vent fluid [Eu] from the literature to calculate the percentage of vent fluid Eu that is removed from solution before being measured in the NBP. This approach was followed at three hydrothermal vent sites along the MAR: Lucky Strike, Rainbow and TAG. All literature values used in equations 4.2 to 4.4 can be found in table 4.1.

Stage one: We can calculate the mass fraction of hydrothermal fluid (f) in our NBP seawater samples using a two end-member mixing model from Hsieh and Henderson (2017) in which the plume is designated as the mixture while hydrothermal fluids and seawater are the end-members (equation 4.2).

$$f = \frac{[\mathrm{He}]_{\mathrm{plume}}\delta^3\mathrm{He}_{\mathrm{plume}} - [\mathrm{He}]_{\mathrm{SW}}\delta^3\mathrm{He}_{\mathrm{SW}}}{[\mathrm{He}]_{\mathrm{HT}}\delta^3\mathrm{He}_{\mathrm{HT}} - [\mathrm{He}]_{\mathrm{SW}}\delta^3\mathrm{He}_{\mathrm{SW}}} \tag{4.2}$$

The f values that were calculated used vent fluid He concentrations ($[\mathrm{He}]_{\mathrm{HT}}$) and He-isotope values ($\delta^3\mathrm{He}_{\mathrm{HT}}$, equation 3.2) specific to each site (table 4.1). $[\mathrm{He}]_{\mathrm{plume}}$ and $\delta^3\mathrm{He}_{\mathrm{plume}}$ were determined by measurement of samples from each NBP while ambient seawater $[\mathrm{He}]_{\mathrm{SW}}$ and $\delta^3\mathrm{He}_{\mathrm{SW}}$ values used are displayed in table 4.1. Across Rainbow, Lucky Strike and TAG, small mass fractions of hydrothermal fluid (f) indicate extensive entrainment of ambient seawater, resulting in NBP seawater/fluid ratios of up to 5×10^4 (table 4.2).

Stage two: Eu* (equation 4.1) is first converted into a percentage in excess of PAAS (Eu*= 1), Eu*^{xs}, via equation 4.3.

$$\mathrm{Eu}^{*xs} = (\mathrm{Eu}^* - 1) \times 100 \tag{4.3}$$

The mass fraction value (f, equation 4.2), along with [Eu] and Eu^{*xs} is then used in a second two end-member mixing model to calculate hydrothermal [Eu] (equation 4.4).

$$[Eu]_{HT} = \frac{[Eu]_{Plume}Eu^{*xs}_{Plume} - (1-f)[Eu]_{SW}Eu^{*xs}_{SW}}{fEu^{*xs}_{HT}} \tag{4.4}$$

In equation 4.4, $[Eu]_{Plume}$ and Eu^{*xs}_{Plume} represent values observed in the NBP at each of the three vent sites while $[Eu]_{SW}$, Eu^{*xs}_{SW} and Eu^{*xs}_{HT} can be found in table 4.1. The [Eu] calculated in vent fluids at this stage is small ($\approx 1-2$ pmol/kg).

Stage three: Since δ^3He acts conservatively, using a mass fraction value calculated from δ^3He will assume the same conservative behaviour for Eu. Equation 4.4 will therefore underestimate the concentration of Eu dissolved in hydrothermal end-member fluids in proportion to the dissolved Eu removed from solution by particle scavenging. Mitra et al. (1994) showed that, although Eu was extensively scavenged in the TAG buoyant plume, positive Eu* values were apparent even in the most dilute samples (seawater/fluid ratio ≈ 700); our data extends that of Mitra et al. (1994) to seawater/fluid ratios of $< 5 \times 10^4$. The ratios of calculated [Eu] to measured [Eu] in vent fluids indicate that between 0.01 and 0.17% of Eu in MOR vent fluids survives the mixing and scavenging of the plume to enter the global ocean (table 4.2), while >99.8% is removed to sediments (figure 4.5). Stichel et al. (2018) found that only 0.1% of hydrothermal Nd escapes plume to mix with seawater, a value that agrees well with those found for Eu in this study. Hydrothermal sediments are therefore a local reservoir of REEs with REE pattern similar to that of hydrothermal fluids.

If REEs in hydrothermal sediments were reduced, they could be released into the dissolved phase of overlying waters, presenting an additional dissolved source of REEs with a positive Eu*. This flux would essentially represent a more circuitous route for REEs that originate from the same hydrothermal fluid source as dissolved REEs in the NBP and, if included, would add to the ultimate fraction of hydrothermal REEs that impact the seawater REE pattern. Although not included in equations 4.2 to 4.4, the impact of REE release from hydrothermal sediments on the fraction of hydrothermal REEs ultimately entering the open ocean is assumed to be negligible.

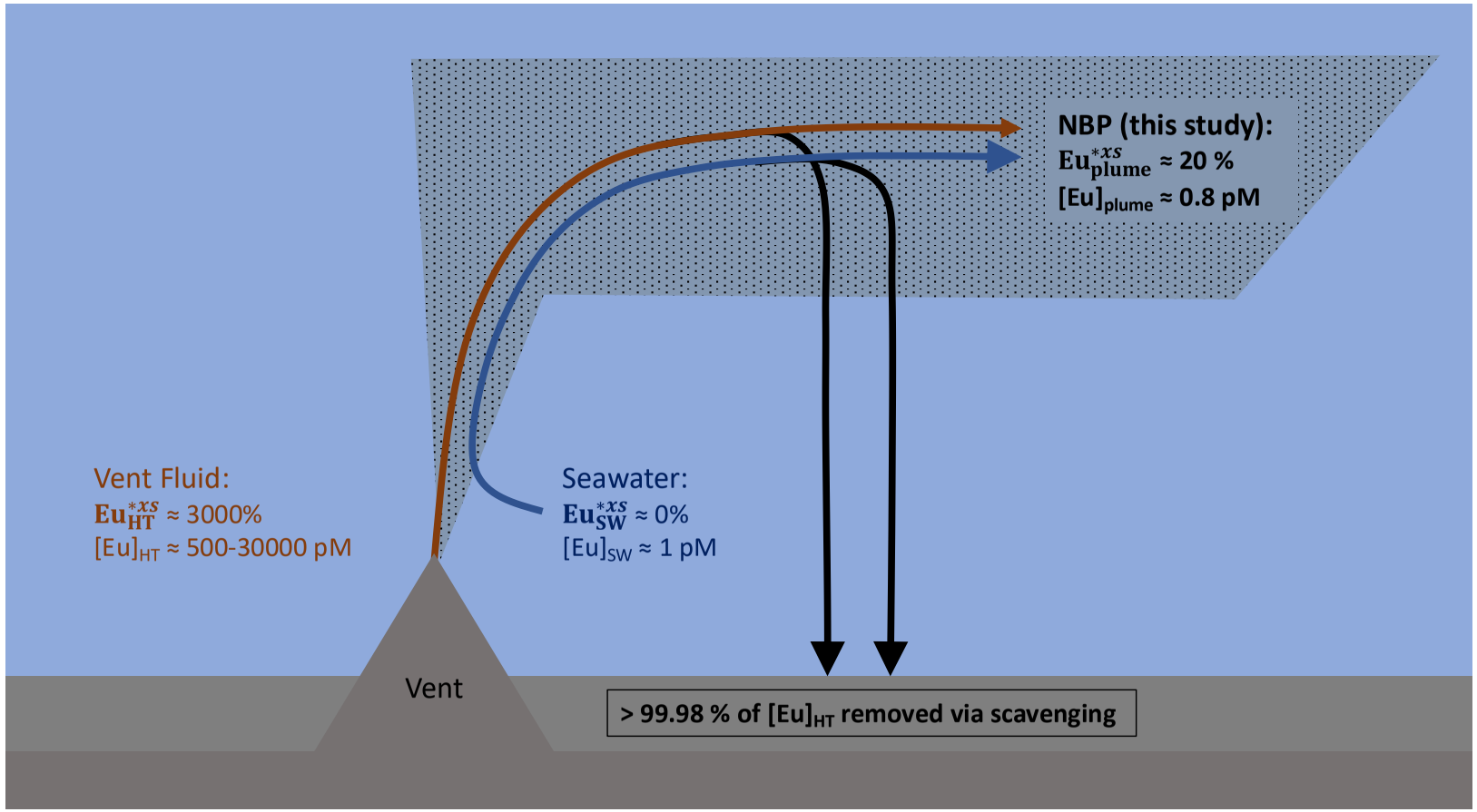

Figure 4.5: An illustration of the evolution of [Eu] and Eu* in a hydrothermal plume. Hydrothermal vent fluids, rich in Eu ($[Eu]_{HT}$) with a large Eu* (Eu^{*xs}_{HT}), enter overlying ambient seawater containing low concentrations of Eu ($[Eu]_{SW}$) and Eu^{*xs} of 0 (Eu^{*xs}_{SW}). A mixture of these two end-members then undergoes extensive particle scavenging in the buoyant and neutrally-buoyant plume, removing the vast majority of Eu from solution. Measurements of Eu concentration ($[Eu]_{plume}$) and Eu^{*xs} in the plume (Eu^{*xs}_{plume}) allow the extent of Eu removal to be estimated. The discrepancy between calculated and literature values of [Eu] in hydrothermal vent fluids indicates that $> 99.98\%$ of Eu dissolved in hydrothermal fluids is removed via plume particle scavenging (German et al., 1990; Klinkhammer et al., 1995; Douville et al., 2002).

Vent Site	f (%)	$[Eu]_{HT}$ calc. (pM)	$[Eu]_{HT}$ meas. (pM)	$[Eu]_{HT}$ calc./$[Eu]_{HT}$ meas. %
Rainbow	2×10^{-3}	$1.8(\pm 0.4)$	3.0×10^{4}	0.01
TAG	4×10^{-3}	$1.0(\pm 0.2)$	2.7×10^{3}	0.04
Lucky Strike	3×10^{-3}	$0.9(\pm 0.2)$	5.6×10^{2}	0.17

Table 4.2: A table displaying the results of mixing-model calculations for Rainbow, TAG and Lucky Strike. 'f' is calculated using equation 4.2 while '$[Eu]_{HT}$ calc.' is found using equations 4.3 and 4.4. '$[Eu]_{HT}$ meas.' refers to literature end-member values for each vent site which can be found in table 4.1. The ratio of calculated $[Eu]_{HT}$ to measured $[Eu]_{HT}$ provides an estimate of the fraction of Eu dissolved in hydrothermal end-members that is not removed from solution in the NBP by particle scavenging.

4.6.2 Impact of hydrothermal inputs on Eu* of the global ocean

Observations of the hydrothermal Eu* anomaly in NBPs and estimations of surviving hydrothermal [Eu] concentration can be coupled with literature assessment of global high-temperature fluid flow through MORs and a global flux of Eu into the ocean, enabling an assessment of the whole-ocean Eu* expected from hydrothermal activity.

$$\Delta(Eu)_{HT} = [Eu]_{HT} \times \Delta(mass)_{HT} \tag{4.5}$$

$[Eu]_{HT}$ (equation 4.4) can be multiplied by an estimated global high-temperature water flux ($\Delta(mass)_{HT}$, table 4.1) to find a global hydrothermal Eu flux to the ocean, $\Delta(Eu)_{HT}$ (equation 4.5).

A simple Eu budget of the ocean illustrates the relative magnitude of hydrothermal flux in comparison to total flux (figure 4.6). Such a small global hydrothermal flux of Eu to the oceans agrees with previous indications of quantitative scavenging of dissolved REEs in hydrothermal plumes (German et al., 1990; Mitra et al., 1994; Bau and Dulski, 1999)

Upper continental crustal flux ($\Delta(Eu)_{UCC}$) can then be calculated by subtracting $\Delta(Eu)_{HT}$ from $\Delta(Eu)_{Total}$. In addition, the $\Delta(Eu)_{HT}$ / $\Delta(Eu)_{Total}$ ratio can be calculated using data from each vent site (table 4.3). The change in whole-ocean Eu* expected from high-temperature hydrothermal activity is $+0.001 \pm 0.0005$, almost two orders of magnitude smaller than measurement precision (0.08).

Although removal of Eu via particle scavenging as well as transport of UCC material to the oceans causes fractionation across the REE series, it does not appear to impact Eu* which maintains a constant value with depth (figure 4.3 (right)). Based on these calculations,

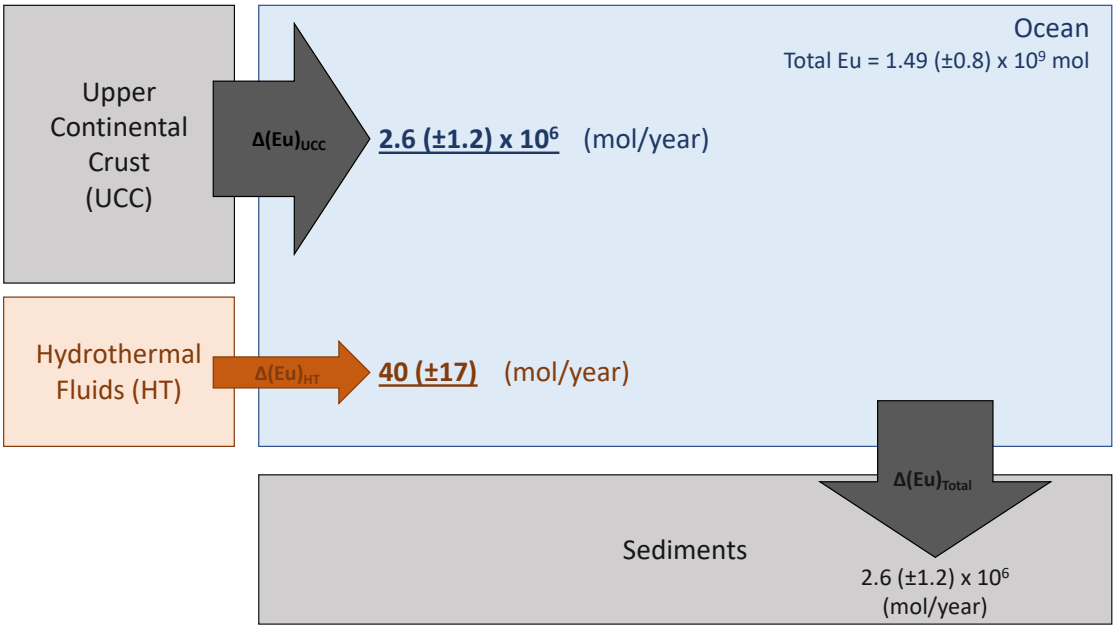

Figure 4.6: A simple steady state box model of Eu in the ocean. Total removal flux from, and therefore total input flux to, the ocean is estimated using Eu residence time and mean seawater Eu concentration (Alibo and Nozaki, 1999; Nozaki, 2001). Hydrothermal flux is estimated using measured NBP Eu* and [Eu] values and existing hydrothermal end-member and seawater Eu* and [Eu] values (German et al., 1990; Klinkhammer et al., 1995; Douville et al., 2002).

hydrothermal input from MORs will not have any observable impact on the Eu* of the global ocean.

Vent Site	f (%)	$[Eu]_{HT}$ calc. (pM)	$[Eu]_{HT}$ meas. (pM)	$\frac{\Delta Eu_{HT}}{\Delta Eu_{Total}}$ %
Rainbow	2×10^{-3}	3.9	3.0×10^{4}	0.002
TAG	4×10^{-3}	1.5	2.7×10^{3}	0.001
Lucky Strike	3×10^{-3}	1.5	5.6×10^{2}	0.001

Table 4.3: A table displaying estimates of global high-temperature hydrothermal Eu flux to the oceans using observations at Rainbow, TAG and Lucky Strike

4.6.3 Eu* comparison of major oceans

If hydrothermal inputs from MORs do not influence the Eu* of seawater, then inter-basin differences in seawater Eu* would be caused by differences in the compositions of UCC surrounding each basin. To assess inter-basin variability, dissolved Eu concentrations and Eu* values from nine GEOTRACES expeditions in four ocean basins (Arctic, Atlantic, Southern, Pacific) were compared (figure 4.7). Depth profiles of dissolved Eu concentration indicate a

variety of concentrations and areas of removal, such as Pacific and Southern ocean surface waters, as well as input, evident in Arctic Ocean surface waters. Despite the apparent variety of conditions, no significant variation in Eu* was measured between basins or with depth.

Mean PAAS-normalised Eu* values of each basin display a range of 7%, from 0.94 in the Southern Ocean to 1.01 in the Arctic Ocean. Although our mean Eu* values display standard errors of $< 6\%$ (2σ) within each basin due to a large number of data points, systemic error related to inter-lab differences increases the uncertainty of individual Eu* values to 20%; based on values from GEOTRACES intercalibration (Van De Flierdt et al., 2012). The lack of observable difference in Eu* between basins indicates that variation in UCC REE compositions is not large enough to support inter-basin difference. The ocean is therefore well mixed relative to variation in the Eu* of inputs.

4.6.4 Assessing shale composites as indicators of average upper-continental crust values

Since ocean Eu* has no observable input from MORs and is well mixed, it can provide a better assessment of the global average Eu* than a composition of a limited number of shales. Mean seawater Eu* can therefore be used to assess which shale composite is most representative of average UCC inputs to the ocean. The global mean seawater Eu* suggests an upper continental crustal Eu* of 0.97 (± 0.07, 2σ). Based on figure 4.9, we recommend the values established by Taylor and McLennan (1985) for PAAS (1.00) and Gromet et al. (1984) for NASC (0.99) as the most representative of continental crustal inputs of Eu* to the ocean.

In this study global GEOTRACES data has proven a powerful investigative tool in comparing the Eu* of different ocean basins. In the future, high precision measurements of REE patterns in seawater may provide an assessment of differences in Eu* between major continental areas. Precision of dREE values may be improved from 20% to $< 10\%$ by analysing samples from all ocean basins via one method in the same laboratory. Improvement in analytical method may also be needed in order to approach a precision of approximately 1% required to assess differences in Eu* between major ocean basins and continental areas.

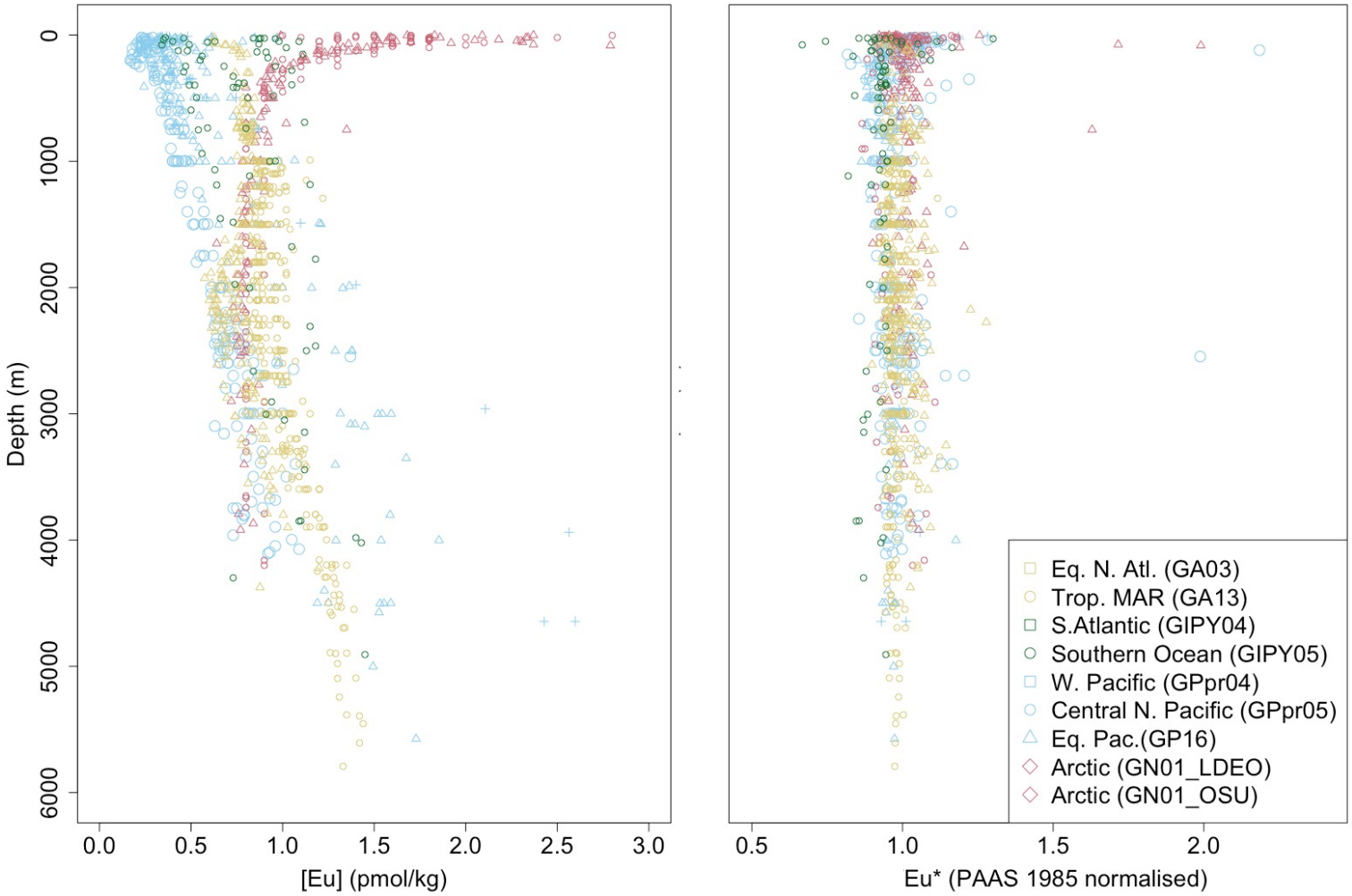

Figure 4.7: Depth plots of [Eu] and Eu* from nine GEOTRACES cruises in the North Atlantic, Southern, Pacific and Arctic oceans, including data from this study (GA13). While [Eu] varies with depth and ocean basin, Eu* remains relatively constant, indicating that Eu* is insensitive to REE fractionation and likely well mixed throughout the global ocean.

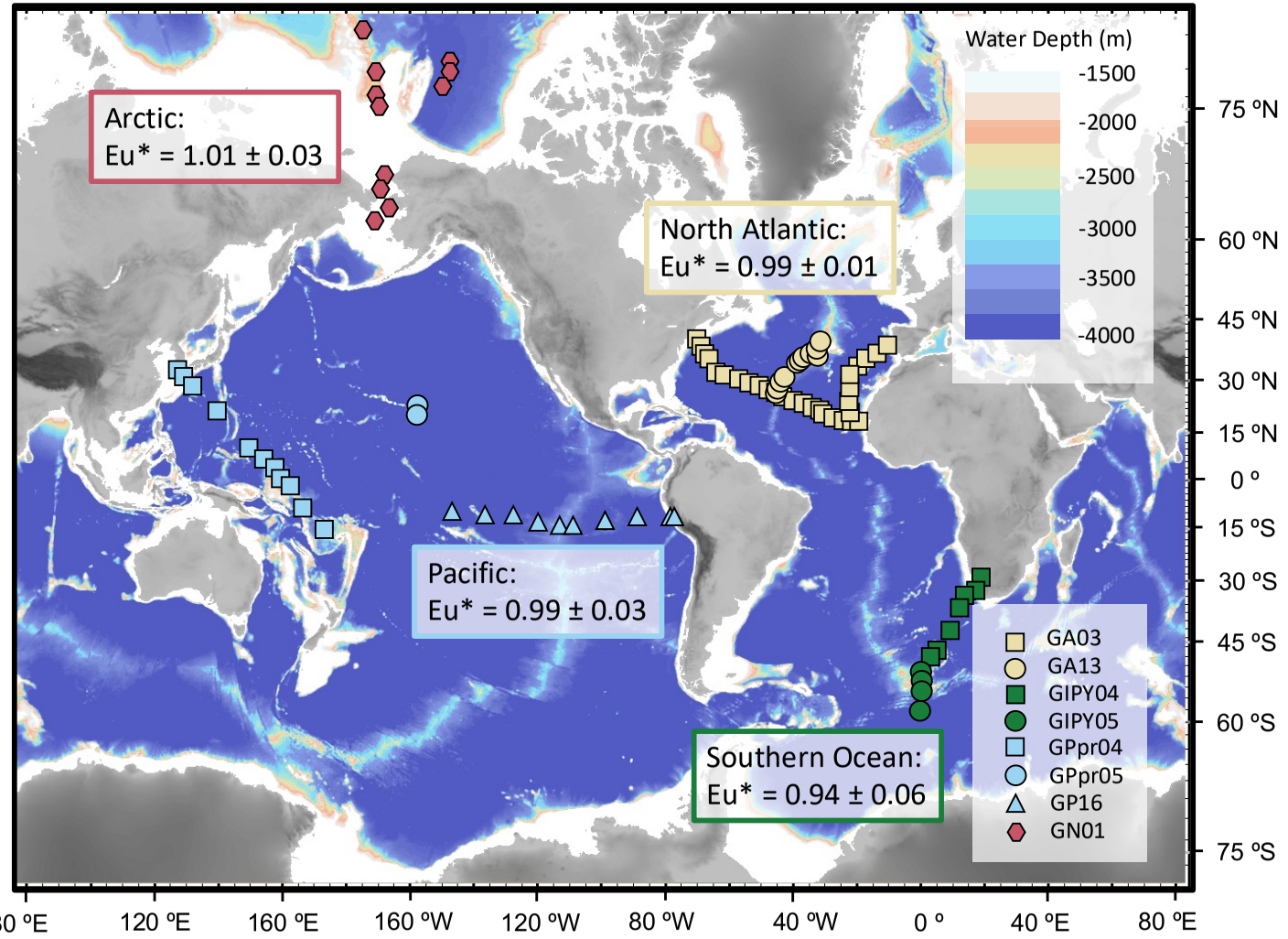

Figure 4.8: A map of mean dissolved Eu* values in major oceans. A compilation of 106 water column profiles from 9 GEOTRACES expeditions. Eu* values were calculated in each ocean basin using the dissolved REE concentration data available from GEOTRACES IDP2017 data (Schlitzer et al., 2018); Eu* values in the North Atlantic include GEOTRACES GA13 data analysed in this study. All uncertainties are two times the standard error (2σ). In each ocean basin the mean dissolved Eu* value was found to be within error of 1 when normalised to PAAS (Taylor and McLennan, 1985).

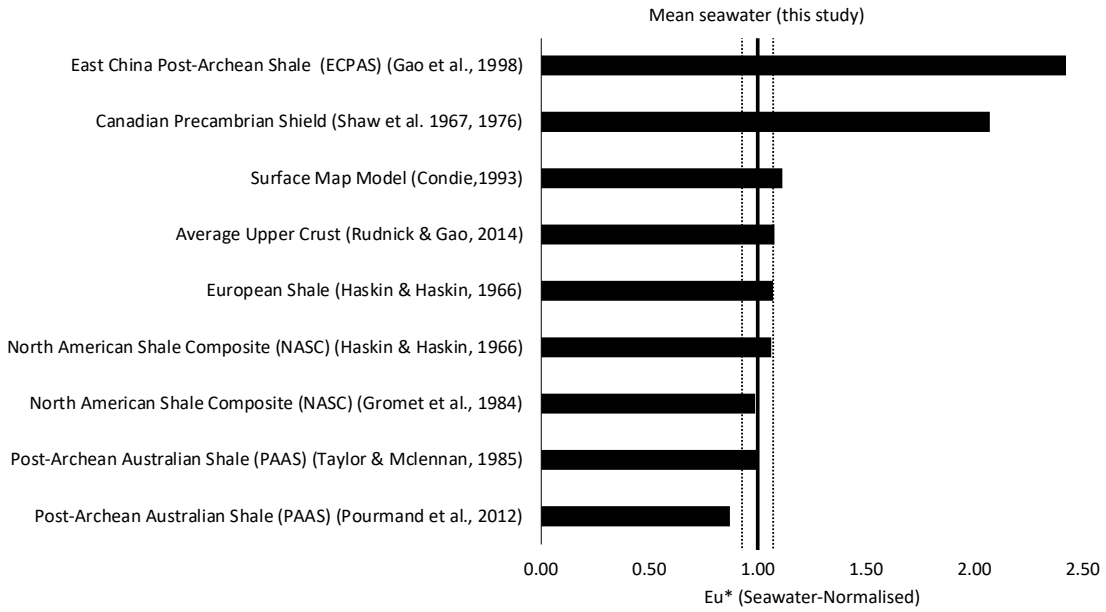

Figure 4.9: A comparison of Eu* values in various Upper Continental Crust proxies, including shale composites and geological models. All Eu* values are normalised to mean seawater (this study). The solid black line indicates mean seawater Eu* (= 1) while dashed lines indicate an uncertainty of 0.07 (2SD). When assessed by mean seawater Eu*, PAAS (Taylor and McLennan, 1985) and NASC (Gromet et al., 1984) appear to be most representative of UCC Eu* inputs to the ocean.

4.7 Conclusions

Significant dissolved Eu anomalies were observed in three different neutrally buoyant plumes on the MAR, indicating that some relict hydrothermal Eu* signal does escape plume particle scavenging. The relict hydrothermal Eu* in the plume, however, is transmitted only by the 0.02% of hydrothermal end-member Eu that survives removal from solution by particle scavenging. The change in whole-ocean Eu* expected from high-temperature hydrothermal activity is $+0.001 \pm 0.0005$, almost two orders of magnitude smaller than measurement precision of 0.08.

A lack of a measurable Eu anomaly in the global ocean due to hydrothermal input, coupled to the lack of any differential fractionation of Eu relative to other REEs during estuarine transport to the ocean, means that seawater Eu* provides an assessment of the average upper-continental crust value. The global mean seawater Eu* suggests an upper continental crustal Eu* of 0.97 (± 0.07, 2σ); this supports the use of values established by Taylor and McLennan (1985) for PAAS (1.00) and Gromet et al. (1984) for NASC (0.99) for upper continental crustal REE pattern.

Determining the composition of the Upper Continental Crust (UCC) is important because the UCC contains a significant proportion of the bulk silicate Earth's incompatible elements, including U, Th and Ba (35 % to 55 %) and is therefore a key component of whole-Earth mass balance calculations (Rudnick and Fountain, 1995). The bulk composition of the UCC also aids understanding of the processes that generate the Earth's crust and how it might be modified over time (Rudnick and Gao, 2014). The global mean seawater Eu* value found in this study validates previous estimates for the UCC, future studies with high precision measurements of REE patterns in seawater could provide an assessment of differences of Eu* between major ocean basins and continental areas.

Chapter 5

Barium isotopes in Mid-Atlantic Ridge hydrothermal plumes: Investigating the effective barium end-member

5.1 Abstract

Observations of the non-conservative behaviour of Ba in Atlantic deep waters contradict a general pattern dominated by large-scale conservative mixing of Ba end-members in the deep oceans. An isotopically-heavy effective hydrothermal end-member, calculated using Ba-isotope measurements of hydrothermal fluids, provides one possible explanation for the apparent non-conservative behaviour in deep waters. In this study, we provide the first coupled measurements of dissolved Ba and $\delta^{138/134}$Ba in hydrothermal neutrally-buoyant plumes. Plume waters, at Rainbow and TAG vent sites, display heavier $\delta^{138/134}$Ba values and higher dissolved Ba concentrations than surrounding ambient seawaters. Hydrothermal Ba fractions of $2.9 \pm 1.5\%$ and $2.7 \pm 1.3\%$ were calculated in Rainbow and TAG neutrally-buoyant plumes, respectively. Since NBP hydrothermal Ba fractions are lower than those of some Atlantic deep waters, an assumption that observed deviation from conservative mixing in deep waters can be attributed to hydrothermal inputs would indicate unknown hydrothermal sources to those deep waters. The magnitude of dilution of hydrothermal fluids that occurs before plume

barite precipitation ceases, and an effective hydrothermal Ba isotope ratio is established, is calculated to be more than 100-fold smaller than previously thought. This small dilution factor indicates that barite precipitation is rapid with dissolved Ba concentrations likely falling below saturation within the early buoyant plume. This study therefore shows that, while the rapid precipitation of barite from hydrothermal fluid - seawater mixing generates an isotopically heavy effective hydrothermal Ba end-member in the dissolved phase, hydrothermal inputs are unlikely to have a measurable impact on seawater $\delta^{138/134}$Ba values.

5.2 Introduction

Barium isotopes are powerful potential tracers of oceanic Ba-cycling as well as large-scale mixing because they are sensitive to biogeochemical and physical processes (Bates et al., 2017). The precipitation of barite in ocean waters is a non-conservative biogeochemical process that preferentially incorporates lighter Ba-isotopes into the precipitate (Von Allmen et al., 2010). Although seawater is generally undersaturated with respect to $BaSO_4$, surface ocean biologically mediated precipitation in micro-environments that are super-saturated with respect to $BaSO_4$, is supported by previous studies (Dehairs et al., 1980; Collier and Edmond, 1984; Ganeshram et al., 2003; González-Munoz et al., 2003; Griffith and Paytan, 2012). Dissolved Ba concentrations in below 2000 m, however, are believed to be predominantly controlled by, and therefore may trace, large-scale ocean mixing (Bates et al., 2017). There are however observations within some deep Atlantic waters that display non-conservative behaviour; Hsieh and Henderson (2017) argued that multiple samples in the North and South Atlantic displayed non-conservative behaviour that might be explained by an isotopically-heavy deep water source of Ba such as hydrothermal venting or sedimentary inputs.

Hydrothermal fluids are rich in many trace elements including Ba, with concentrations of $1 - 119$ µmol/kg (Von Damm et al., 1985; Butterfield et al., 1994; Charlou et al., 1996; Seyfried Jr et al., 2011); approximately 1000-fold higher than deep Atlantic waters ($\approx 50-100$ nmol/kg) (Horner et al., 2015; Hsieh and Henderson, 2017). The first coupled measurements of dissolved Ba concentration and Ba-isotopes in vent fluids were made by Hsieh et al. (2021) at six different hydrothermal sites in the Atlantic and Pacific oceans. Hydrothermal fluids are extensively modified by rapid precipitation of barite upon mixing with seawater, making it difficult to constrain the hydrothermal Ba-isotope signal that is transmitted to deep waters.

The precipitation of barite occurs while the fluid/seawater saturation index with respect to barite is >1. The barite saturation index can be calculated for various temperatures and pressures using a model developed by Monnin (1999) (equations 5.1 - 5.7). The barite saturation index is given by equation 5.1:

$$\Omega_{\text{barite}} = \frac{IAP}{K_{sp}} \tag{5.1}$$

where IAP is the ionic activity product while K_{sp} is the solubility product. The ionic activity product can be found using equation 5.2:

$$IAP = [\text{Ba}^{2+}] \times [\text{SO}_4^{2-}] \times \gamma^2_{\text{BaSO}_4} \tag{5.2}$$

where $[\text{Ba}^{2+}]$ and $[\text{SO}_4^{2-}]$ are the mole concentrations of Ba and SO_4 respectively and γ_{BaSO_4} is the activity coefficient. Hsieh et al. (2021) used a value calculated by Monnin (1999) of $\gamma_{\text{BaSO}_4} = 0.1442$ (1°C, 500 bar, [Ba] = 360 nM).

The solubility product for barite at a given temperature and pressure, $\ln K_{sp}(T, P)$, can be calculated by accounting for the change in the solubility product with pressure, starting with the solubility product at a reference pressure ($\ln K_{sp}(T, P_0)$). This is given by equation 5.3:

$$\ln K_{sp}(T, P) = \ln K_{sp}(T, P_0) - \frac{\Delta_r \overline{V}^0}{RT} \times (P - P_0) \tag{5.3}$$

where $\Delta_r \overline{V}^0$ represents the standard molal volume of the dissolution reaction, R is the gas constant, T and P are the temperature and pressure and P_0 can be found from the heat capacity of the dissolution reaction. If the heat capacity can be assumed to be constant over the temperature range of interest, then $\ln K_{sp}(T, P_0)$ can be found using equation 5.4:

$$\ln K_{sp}(T, P_0) = A + B \ln T + \frac{C}{T} \tag{5.4}$$

where A, B and C are given by equations 5.5, 5.6 and 5.7 respectively:

$$A = \frac{\Delta_r S^0}{R} - \frac{\Delta_r C_p^0}{R} \times [1 + \ln T_0] \tag{5.5}$$

$$B = \frac{\Delta_r C_p^0}{R} \tag{5.6}$$

$$C = -\frac{\Delta_r H^0}{R} + \frac{T_0 \Delta_r C_p^0}{R} \tag{5.7}$$

where $\Delta_r S^0$, $\Delta_r C_p^0$ and $\Delta_r H^0$ are the standard entropy, heat capacity and enthalpy of the dissolution reaction. Using this model, Monnin (1999) calculated a $\ln K_{sp} = -9.957$ (1°C, 500 bar). The 'effective' hydrothermal end-member that mixes conservatively with ambient seawaters, after barite precipitation has ceased, was then calculated to be isotopically heavy using this K_{sp}, $\delta^{138/134}$Ba $\approx 1.7 \pm 0.7$‰ (Hsieh et al., 2021).

Using this hydrothermal end-member, it was estimated that some Atlantic deep waters contain a hydrothermal Ba fraction of $3 - 9\%$ despite being distant from any mid-ocean ridge system (Hsieh et al., 2021). Such large hydrothermal Ba fractions at these sites indicates hydrothermal venting as a potential source of Ba and explanation for non-conservative behaviour in deep waters. Observations of significant excursions in Ba concentrations and Ba-isotope values in a hydrothermal plume would confirm isotopically heavy hydrothermal inputs and allow further investigation of the evolution of the effective hydrothermal end-member suggested by Hsieh et al. (2021).

In this study, the first coupled Ba concentration and Ba-isotope values ($\delta^{138/134}$Ba) from two neutrally buoyant plumes (NBPs) on the Mid-Atlantic Ridge (MAR), are used to validate the proposed hydrothermal end-member and to constrain at which stage of hydrothermal plume development the conservative hydrothermal Ba end-member is established.

5.3 Site selection and sample collection

Seawater samples analysed in this study were collected during the JC156 expedition (20/12/2017 - 01/02/2018) on board the RRS *James Cook* as part of the GEOTRACES GA13 section (González-Santana et al., 2021).

A total of 308 discrete seawater samples were taken while 12 samples from three water column profiles were selected for dissolved Ba concentration and $\delta^{138/134}\text{Ba}_{\text{NIST}}$ analyses. Of these samples, five were at Rainbow vent site (S6, 36.23°N, 33.90°W), five were collected at a station near Rainbow vent site (S2, 36.23°N, 33.53°W) while a further two were collected in the TAG NBP (26.14°N, 44.83°W). These two vent sites were selected for investigation because hydrothermal fluid dissolved Ba concentration and $\delta^{138/134}\text{Ba}_{\text{NIST}}$ values have been measured previously at these sites by Hsieh et al. (2021). At these two vent sites, the hydrothermal

NBP was distinguished from surrounding ambient seawaters using dissolved concentrations of Mn and δ^3He values. Samples from NBP depths were selected for analyses as well as depth above and below the plume at Rainbow vent site.

Seawater was collected for Ba concentration and $\delta^{138/134}$Ba analyses in 20 L Niskin bottles fitted to a stainless steel CTD frame. These seawater samples were then filtered through an Acropak (0.45 µm) filter into precleaned 250 mL low density polyethylene Nalgene bottles. Bottled samples were then acidified to pH 2 using ultra pure HCl under a class 100 laminar-flow hood in a class 100 clean air container.

5.4 Analytical methods

5.4.1 Seawater Ba-isotope method

Following the method described in Hsieh and Henderson (2017) which was adapted from Foster et al. (2004): Seawater (50 mL)(approximately 250 ng of Ba) was weighed and spiked with a ^{137}Ba - ^{135}Ba double-spike, allowing for the correction of any mass fractionation that may occur during chemical purification or instrument analysis. A total Ba ratio of approximately 0.4 was targeted for the spike/sample mixture, based on estimated Ba concentration at the sampling site; these estimations were based on Ba concentrations measured in the North Atlantic (Schlitzer et al., 2018). The double spike was calibrated by measuring the spike, the unspiked standard (NIST3104a) and varying mixtures of the two. In addition, The double spike was also calibrated against the certified Ba concentration of NIST3104a (10.014 ± 0.036 mg/g, Lot No. 070222) to get the sample Ba concentration. 3 mL of 0.9 M Na_2CO_3 solution was added to each spiked sample to co-precipitate Ba with $CaCO_3$; Ba was removed from the Na_2CO_3 solution via co-precipitation of Ba with $CaCO_3$ induced by the addition of Ca^{2+}. Precipitates were centrifuged and the seawater decanted. The precipitates were then rinsed with H_2O before being dissolved in 2 mL 3 M HCl for column separation. Column separation was performed using AG50-X8 (200-400 mesh, 2 mL volume) to separate Ba from Ca, Mg, Sr and REEs.

Ba-isotope analyses were performed on a TIMS Triton instrument at the University of Oxford, with a sample loading method modified after Carlson et al. (2007). Purified samples and standards were dissolved in 2 µL distilled HCl before they were loaded onto a single rhenium filament. 0.68 A was continuously applied to the rhenium filament as samples and

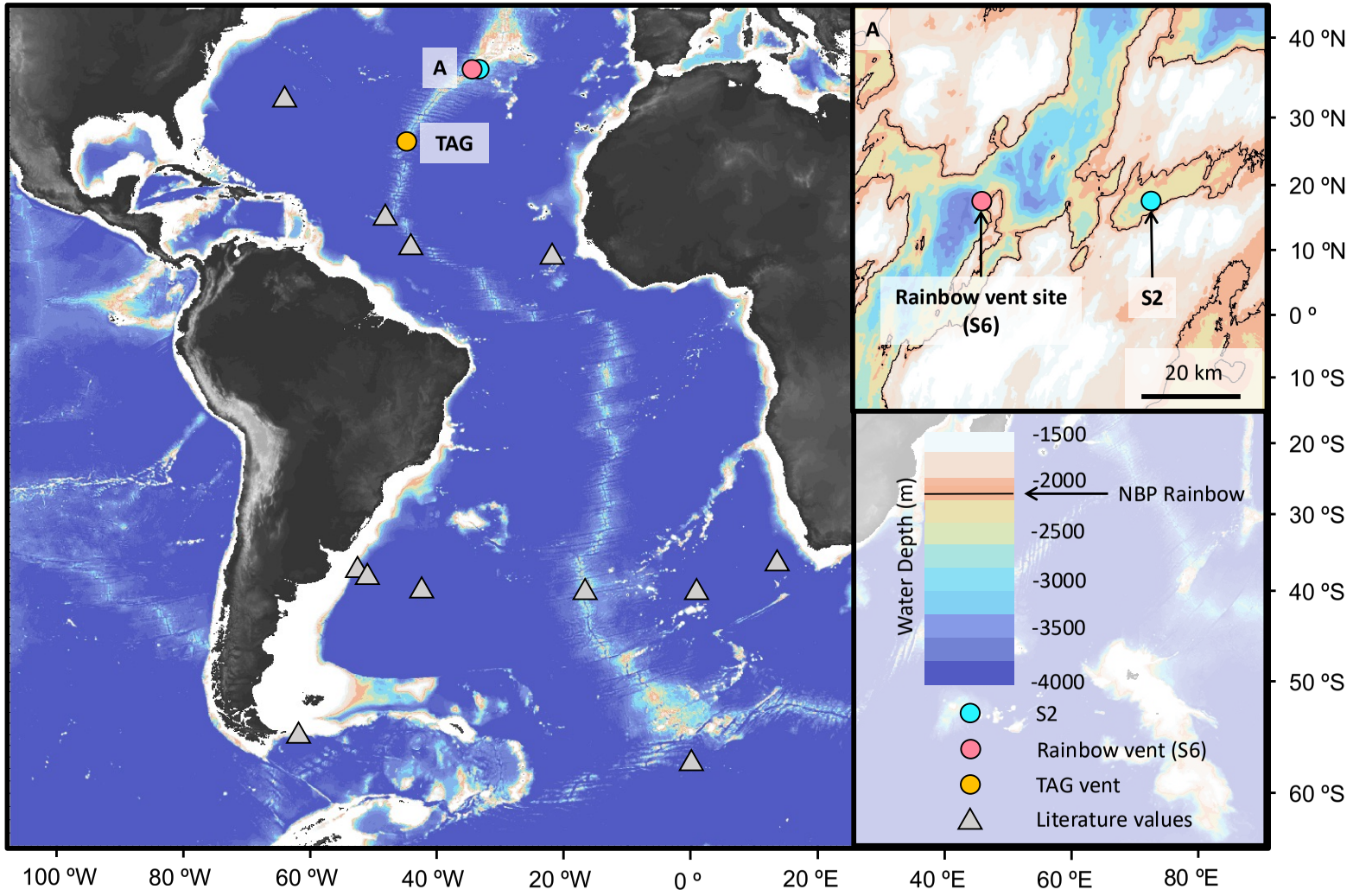

Figure 5.1: A map of locations sampled for Ba concentration and $\delta^{138/134}Ba_{NIST}$ by this study (GEOTRACES GA13) and previous studies (Horner et al., 2015; Bates et al., 2017; Hsieh and Henderson, 2017; Bridgestock et al., 2018; Hemsing et al., 2018).

standards were loaded. 2 µL (50 mg Ta_2O_5 with 3 mL 5 % H_3PO_4) was then loaded on top of the dried samples and standards.

During analysis, Ba-138, 137, 136, 135, 134, Ce-140 and La-139 ion beams were monitored in 7 faraday cups simultaneously. Ba-isotope data was reported in δ-notation (‰)($\delta^{138/134}$Ba) relative to Ba standard NIST3104a (equation 5.8).

$$\delta^{138/134}\text{Ba}(‰) = \left[\frac{(\frac{^{138}Ba}{^{134}Ba})_{sample}}{(\frac{^{138}Ba}{^{134}Ba})_{\text{NIST3104a}}} - 1 \right] \times 1000 \tag{5.8}$$

Reproducibility of Ba-isotope analysis in this study is generally better than 0.015 ‰ (2 standard deviations, n = 2) based on reported NIST3104a. External reproducibility was also tested by measuring a second standard, NBS-127, obtaining a $\delta^{138/134}\text{Ba} = 0.30 \pm 0.01$($\pm$2SE, n=1), which was in agreement with previous measurements (Hsieh and Henderson, 2017; Crockford et al., 2019; Tian et al., 2019; Tieman et al., 2020; Bridgestock et al., 2021). The procedural blank was 1.3 ng Ba or <0.52 % of total sample mass ($\approx$ 250 ng Ba).

5.5 Results

The depths of the hydrothermal NBP at Rainbow and TAG vent sites were established using two traditional plume tracers (figures 5.2, 5.3): dissolved Mn concentrations, provided by J. Resing (personal communication, 21/06/2021), and δ^3He values, provided by A. Tagliabue (personal communication, 21/06/2021). The depth ranges of elevations in these two tracers were then used to designate which samples were coincident with the NBP at each vent site. At Rainbow and TAG vent sites, the NBP depth ranges were estimated to be 2100 ± 100 m and 3350 ± 125 m respectively.

At Rainbow, two water column profiles of dissolved Ba and $\delta^{138/134}$Ba were measured, one above Rainbow vent site (S6) and one $\approx$ 20km to the east (S2), to serve as a background comparison (figure 5.2). Note that the water column profile for barium values to the east of Rainbow (S2) is located $\approx$ 20 km from the vent site (S6) in an area that is likely to be topographically isolated, while the 'off-axis' water-column profiles that provide background dissolved seawater Mn concentrations and δ^3He values are further from the vent site, off the main axis of the MAR. For Rainbow and TAG vent sites these corresponding off-axis depth profiles are GEOTRACES GA13 Station 10 (36.23 °N, −32.65°E) and GEOTRACES GA13

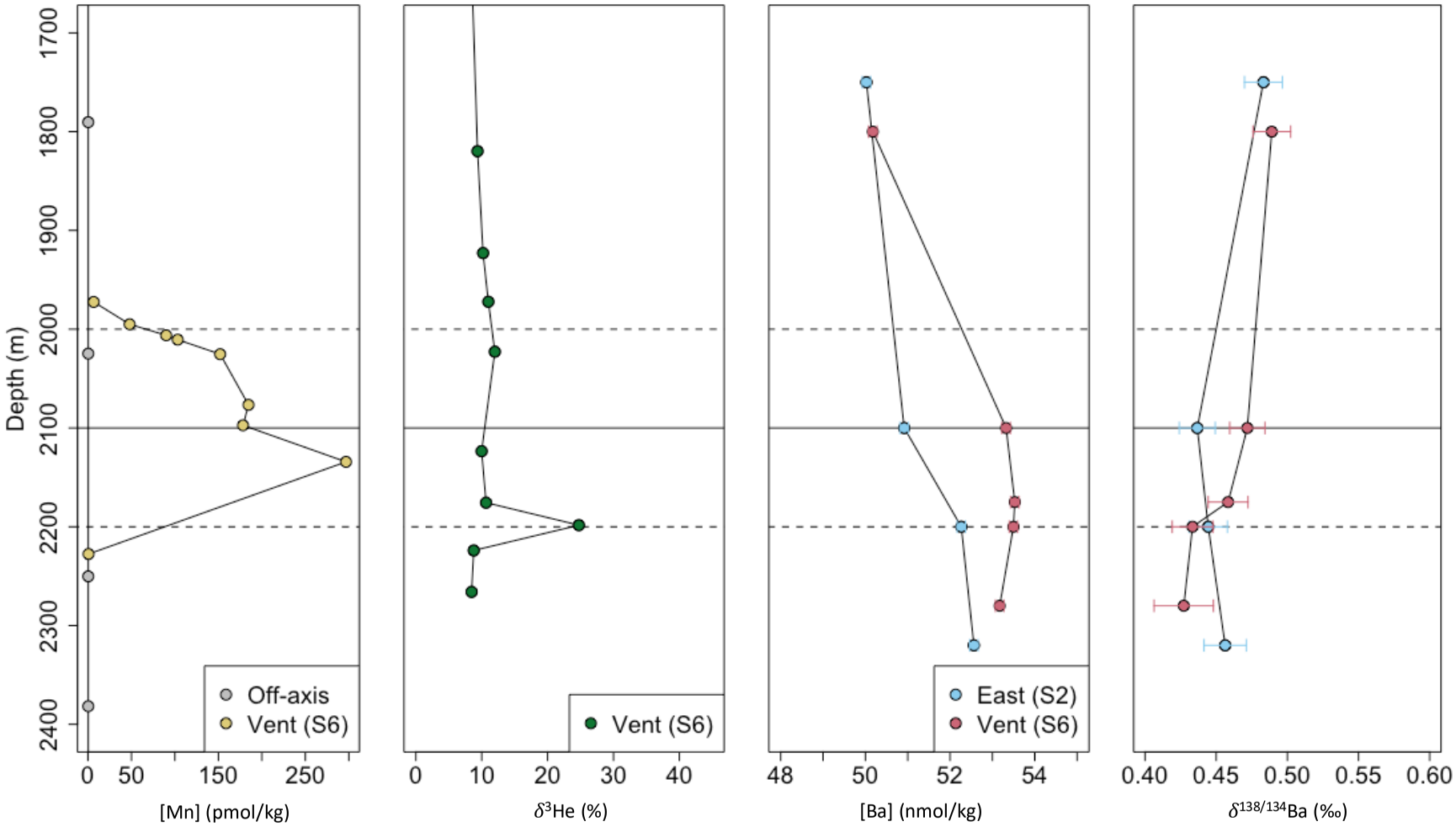

Figure 5.2: Water column profiles of traditional plume tracers, Ba concentration and Ba-isotopes at Rainbow vent site. Four seawater depth profiles displaying dissolved Mn concentration ([Mn]), helium anomaly (δ^3He), dissolved Ba concentration ([Ba]) and Ba-isotopes ($\delta^{138/134}$Ba). In the depth profile of dissolved [Mn], measurements at Rainbow vent site are contrasted with an off-axis site which serves as a background. A clear plume signal is visible between 2000 m and 2200 m in the [Mn] profile and at 2200 m in the δ^3He profile at Rainbow vent site, supporting an estimated plume depth of 2100 ± 100 m (horizontal black lines, dashed lines indicate estimated uncertainty in NBP depth). At the vent site (S6, pink circles) dissolved Ba and $\delta^{138/134}$Ba values are most elevated above background (S2, blue circles) at NBP depth.

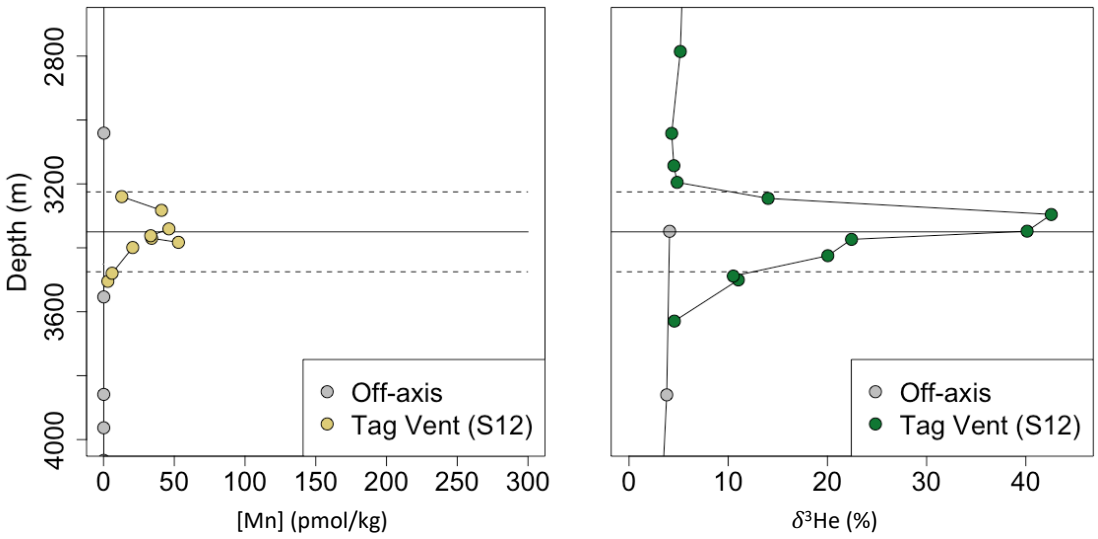

Figure 5.3: Water column profiles of traditional plume tracers at TAG vent site and an off-axis site. Two seawater depth profiles displaying dissolved Mn concentration ([Mn]) and helium anomaly (δ^3He). In the depth profiles of dissolved [Mn] and δ^3He, measurements at TAG vent site are contrasted with an off-axis site which serves as a background. A clear plume signal is visible in the [Mn] profile and the δ^3He profile at TAG vent site, supporting an estimated plume depth of 3350 ± 125 m (horizontal black lines, dashed lines indicate estimated uncertainty in NBP depth).

Station 28 (28.86 °N, −47.23°E) respectively. All barium concentration and barium-isotope data collected in this study can be found in table A.5.

Above the NBP at approximately 1800m depth, a dissolved Ba concentration of 50.0 ± 0.1 nM measured above the vent site is similar to the concentration measured to the east of the vent site (50.2 ± 0.1 nM). Values of $\delta^{138/134}$Ba above the Rainbow NBP (1800 m: 0.489 ± 0.013 ‰) are not significantly different to those observed at a similar depth at S2 to the east (1750 m: 0.483 ± 0.013 ‰).

At NBP depth (2100m), a dissolved Ba concentration of 53.3 ± 0.1 nM observed above the main vent site (S6) is significantly elevated in comparison to 50.9 ± 0.1 nM at 2100 m at S2. NBP $\delta^{138/134}$Ba values at Rainbow (2100 m: 0.472 ± 0.012 ‰) are significantly heavier than those observed at S2 (2100 m: 0.437 ± 0.013 ‰).

At the deeper limit of the NBP depth at Rainbow, dissolved Ba concentrations at the vent site (2175 m: 53.5 ± 0.1 nM, 2200m: 53.5 ± 0.1 nM) are still elevated in comparison to S2 (2200 m: 52.3 ± 0.1 nM) but by a smaller margin, while $\delta^{138/134}$Ba values (2175 m: 0.458 ± 0.014 ‰,2200 m: 0.433 ± 0.014 ‰) are within error of $\delta^{138/134}$Ba observed at S2 again (2200 m: 0.444 ± 0.013 ‰). Since these two Rainbow vent site samples cannot be placed in the NBP with a great degree of certainty, they are not considered 'NBP samples' in analyses and calculations conducted in section 5.6.

Below the plume, in the deepest samples, dissolved Ba concentrations at Rainbow vent site (2280 m: 53.2 ± 0.1 nM) remain higher than at S2 (2320 m: 52.6 ± 0.1 nM) but the margin reduces further. Here, the observed $\delta^{138/134}$Ba value at S6 (2280 m: 0.427 ± 0.021 ‰) is significantly lighter than at S2 (2320 m: 0.456 ± 0.015 ‰), despite being at a slightly shallower depth.

Two further samples from the TAG NBP were also analysed for dissolved Ba and $\delta^{138/134}$Ba (S12). These samples, however, do not have equivalent data at a nearby station to a provide a 'background' ambient seawater comparison. Predictably, dissolved Ba concentrations in the TAG NBP are higher and $\delta^{138/134}$Ba values lighter than those measured in the Rainbow NBP since TAG vent site is situated approximately 1000 m deeper in the ocean than Rainbow vent site; dissolution of sinking particles delivers isotopically-light Ba to deeper waters.

5.6 Discussion

5.6.1 Dissolved Ba isotopes in the NBP

Two water column profiles of dissolved Ba concentration and $\delta^{138/134}$Ba at Rainbow vent site allow the comparison of NBP waters above the vent site with nearby 'background' seawater. Above NBP depth (2100 ± 100m) and at its deeper limit $\delta^{138/134}$Ba at Rainbow vent site are not significantly different to those measured $\approx$ 20km to the east at our 'background' profile (S2). At NBP depth (S6, 2100 m) $\delta^{138/134}$Ba measured above the vent are significantly heavier than those measured in 'background' waters (S2, 2100 m); this is also the depth at which dissolved Ba concentration at the vent site (S6, 2100 m) was most elevated in comparison to 'background' seawater (S2, 2100 m). This novel observation of elevations in $\delta^{138/134}$Ba and dissolved Ba concentration at NBP depth is consistent with input of isotopically heavy Ba to seawaters at sites of hydrothermal venting as suggested by Hsieh et al. (2021).

5.6.2 Implications for hydrothermal Ba-isotopes and non-conservative deep water mixing

Hsieh et al. (2021) estimated a hydrothermal Ba fraction of $3 - 9\%$ in some Atlantic deep waters by conservatively mixing three end-members: AABW ([Ba]$\approx$ 103nM, $\delta^{138/134}$Ba $\approx$ +0.25‰), NADW ([Ba]$\approx$ 51nM, $\delta^{138/134}$Ba $\approx$ +0.45‰) and an effective hydrothermal end-point Ba composition ([Ba]$\approx$ 200nM, $\delta^{138/134}$Ba $\approx$ +1.7‰) (Horner et al., 2015; Hsieh and Henderson, 2017; Hsieh et al., 2021). If such a significant fraction of deep Atlantic Ba is of hydrothermal origin, then hydrothermal NBP Ba would likely contain an even larger hydrothermal fraction. Here, the same mixing model and end-members are used to calculate the hydrothermal Ba fraction present in NBP samples from Rainbow and TAG hydrothermal vent sites.

$$P = [\mathrm{Ba}] \times \delta^{138/134}\mathrm{Ba} \tag{5.9}$$

Following the approach of Hsieh et al. (2021), equation 5.9 calculates the product (P) of the dissolved Ba concentration ([Ba]) and the isotopic ratio ($\delta^{138/134}$Ba).

$$f_{\mathrm{HT}} + f_{\mathrm{AABW}} + f_{\mathrm{NADW}} = 1 \tag{5.10}$$

Equation 5.10 shows that the sum of the mass fractions of hydrothermal fluid (f_{HT}), AABW (f_{AABW}) and NADW (f_{NADW}) is equal to 1, meaning that there are no other inputs to the mixture.

$$P_{\mathrm{mix}} = f_{\mathrm{HT}}P_{\mathrm{HT}} + f_{\mathrm{AABW}}P_{\mathrm{AABW}} + f_{\mathrm{NADW}}P_{\mathrm{NADW}} \tag{5.11}$$

The product P_{mix} of a modelled seawater sample is then a weighted average of the products of AABW (P_{AABW}), NADW (P_{NADW}) and an effective hydrothermal end-member (P_{HT}) where the weighting is determined by the mass fraction values (f_{AABW}, f_{NADW}, f_{HT}) (equation 5.11).

In figure 5.4 (modified from Hsieh et al. (2021), figure 7), a three end-member mixing model was used to calculate a conservative mixing line between AABW and NADW, where the hydrothermal Ba fraction (f_{HT}) equals 0%; further dashed lines then indicate incremental increase of $\mathrm{F_{Ba\text{-}HT}}$ (equation 5.12).

$$\mathrm{F_{Ba\text{-}HT}} = f_{\mathrm{HT}} \times \frac{[\mathrm{Ba}]_{\mathrm{HT}}}{[\mathrm{Ba}]_{\mathrm{SW}}} \tag{5.12}$$

The fraction of modelled seawater barium that is sourced from the effective hydrothermal Ba end-member ($\mathrm{F_{Ba\text{-}HT}}$) is found by multiplying the ratio of hydrothermal fluid Ba concentration ($[\mathrm{Ba}]_{\mathrm{HT}}$) to seawater sample Ba concentration ($[\mathrm{Ba}]_{\mathrm{SW}}$) by the fraction of sample water mass that is hydrothermal fluid (f_{HT})(equation 5.12). The end-member values used are the same as those used by Hsieh et al. (2021) but the depth range of data points from previous Atlantic studies is restricted to $>$ 2000m in order to aid comparison to plotted data from this study at Rainbow and TAG vent sites in Atlantic ocean waters.

Figure 5.4 clearly shows that the Ba concentration and $\delta^{138/134}\mathrm{Ba_{NIST}}$ values of our samples are predominantly influenced by the mixing of deep water masses, AABW and NADW. Barium in seawater samples from the casts near (S2) and above (S6) Rainbow vent site are comprised of mostly NADW. Samples from TAG NBP appear to contain a much larger component of Ba from AABW than waters near Rainbow because TAG is situated in deeper more southern waters.

Of the seawaters sampled in this study, TAG NBP samples (S12) contain the largest fraction of hydrothermal Ba (approximately $3.5 \pm 1.5\%$). The Rainbow NBP sample (ap-

proximately $2.9 \pm 1.5\%$) is within error of the TAG NBP samples and contains a greater fraction of hydrothermal Ba than any other sample collected at or near Rainbow (S2, S6). Importantly, the hydrothermal Ba fractions in both NBPs are notably lower than calculated for some deep Atlantic waters, despite the distance of those waters from any mid-ocean ridge. One sample measured by Bates et al. (2017) shows an apparent $F_{Ba\text{-}HT} = 9 \pm 4\%$ implying the existence of nearby hydrothermal activity, or another cause for deep water non-conservative behaviour; the nearby Sierra Leone Rise has previously been suggested as an independent centre of volcanism (Sheridan et al., 1969).

Given the observed hydrothermal Ba fractions of $2 - 5\%$ in Rainbow and TAG hydrothermal NBPs, isotopically-heavy hydrothermal Ba inputs can explain non-conservative Ba behaviour in deep waters only if there are hydrothermal inputs very close to those sites, otherwise alternate sources such as Ba addition from sediments, as suggested by Hsieh and Henderson (2017), may need to be invoked.

5.6.3 Early dilution of the effective Ba hydrothermal end-member

When estimating the mass fraction of hydrothermal plume water in deep Atlantic waters, a two stage water dilution factor of $1.4 - 3.6$ ($\times 10^4$) was calculated by Hsieh et al. (2021); the first stage of water dilution, from vent fluids to effective Ba end-member was assumed to have a factor of ≈ 500. When combined with dissolved He concentration and δ^3He values, coupled measurements of dissolved Ba concentration and $\delta^{138/134}$Ba in this study provide a means of estimating the first stage dilution factor.

Helium is a well established conservative tracer in hydrothermal plumes (Rudnicki and Elderfield, 1992; Jean-Baptiste et al., 1998, 2004). The effective hydrothermal Ba end-member should mix conservatively with surrounding ambient waters since it is formed after Ba concentration falls below saturation ($\Omega_{barite}<1$) and scavenging removal of Ba from the dissolved phase is assumed to be relatively small (Feely et al., 1996; Hsieh et al., 2021);

The difference between the two tracers is in the magnitude of hydrothermal fluid dilution that occurs before the formation of the hydrothermal end-member. For helium, this is assumed to be equal to 0 since primordial ^{3}He is added to hydrothermal fluids from the mantle, deep below the seafloor (Clarke et al., 1969). Away from surface waters where barite precipitates in biological microenvironments (Bishop, 1988; Monnin et al., 1999; Ganeshram

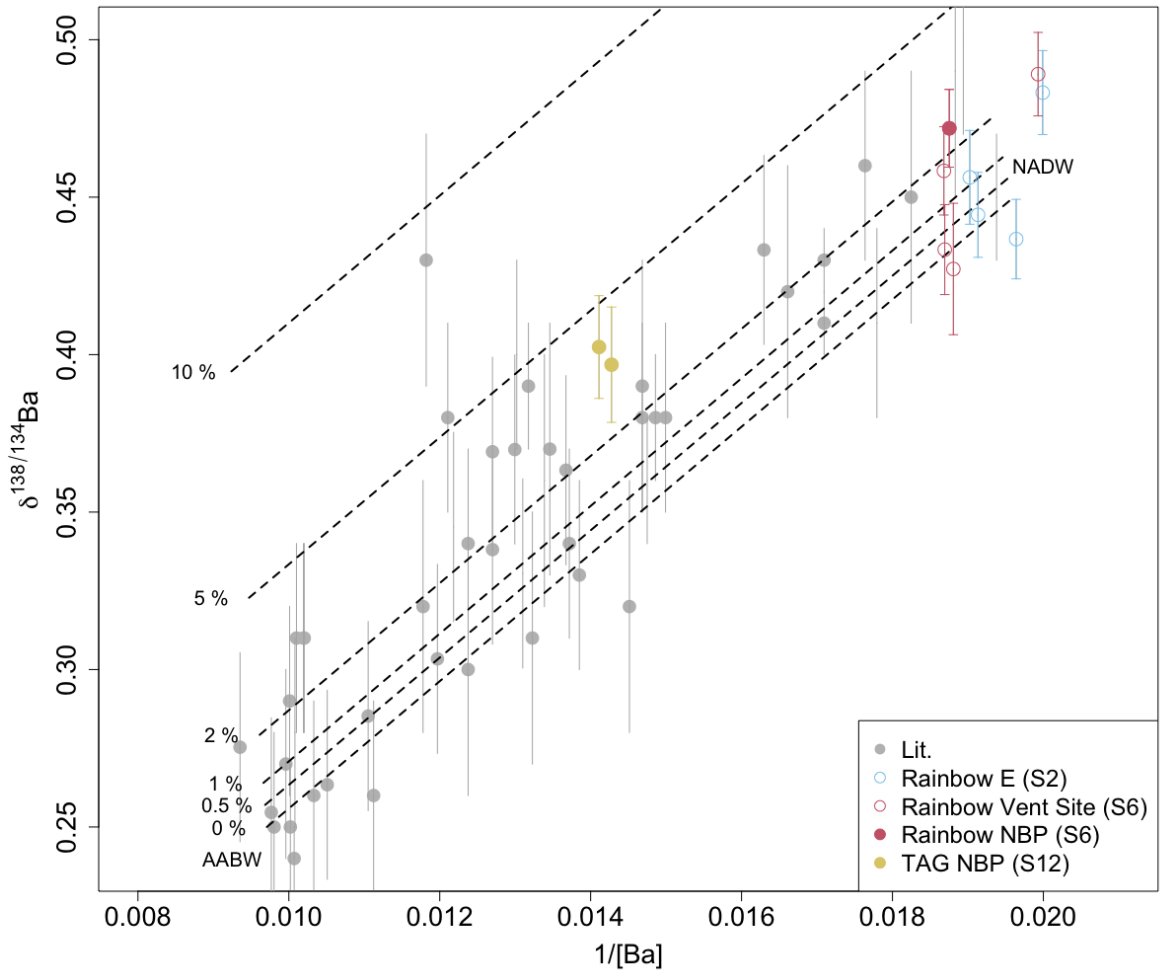

Figure 5.4: A plot of dissolved 1/[Ba] vs $\delta^{138/134}\mathrm{Ba}_{\mathrm{NIST}}$ for seawater samples from the Atlantic Ocean. Plotted data include measurements made in this study (coloured markers) and previously measured Atlantic waters from depths >2000m (Horner et al., 2015; Bates et al., 2017; Hsieh and Henderson, 2017; Bridgestock et al., 2018; Hemsing et al., 2018). Modified after Hsieh et al. (2021), dashed lines indicate the fraction of hydrothermal barium input; the 0% line is the conservative mixing line between AABW ([Ba]≈ 103nM, $\delta^{138/134}$Ba ≈ +0.25‰) and NADW ([Ba]≈ 51nM, $\delta^{138/134}$Ba ≈ +0.45‰) (Horner et al., 2015; Hsieh and Henderson, 2017). Although NBP samples show the largest fractions of hydrothermal input within our dataset, deep Atlantic waters measured by Bates et al. (2017) (9.286°N, 21.633°W) exceed these values despite being far from any MOR.

et al., 2003; Gonzalez-Muñoz et al., 2012), the effective Ba end-member calculated by Hsieh et al. (2021) is formed after extensive barite precipitation, when the Ba concentration declines below saturation with respect to barite formation ($\Omega_{\text{barite}}<1$); Since there is not enough SO_4 to form barite in hydrothermal end-member fluids, some entrainment of SO_4-rich seawater is required before the effective hydrothermal Ba end-member can be formed. The magnitude of dilution of hydrothermal fluids between the formation of the two tracers is directly-proportional to the ratio of water mass fractions derived from each tracer.

A two end-member conservative mixing model from Hsieh and Henderson (2017) can be used with He and then with Ba to find two estimations of the water mass fraction (f) of hydrothermal fluids in NBP samples (equations 5.13, 5.14).

$$f_{\text{HT-He}} = \frac{[\text{He}]_{\text{NBP}} \times \delta^3\text{He}_{\text{NBP}} - [\text{He}]_{\text{SW}} \times \delta^3\text{He}_{\text{SW}}}{[\text{He}]_{\text{HT}} \times \delta^3\text{He}_{\text{HT}} - [\text{He}]_{\text{SW}} \times \delta^3\text{He}_{\text{SW}}} \tag{5.13}$$

In equation 5.13, $f_{\text{HT-He}}$ is found from the dissolved He concentration ($[\text{He}]_{\text{HT}}$) and isotopic value ($\delta^3\text{He}_{\text{HT}}$) of hydrothermal fluids and those of seawater ($[\text{He}]_{\text{SW}}$, $\delta^3\text{He}_{\text{HT}}$) and NBP water ($[\text{He}]_{\text{NBP}}$, $\delta^3\text{He}_{\text{NBP}}$).

$$f_{\text{HT-Ba}} = \frac{[\text{Ba}]_{\text{NBP}} \times \delta^{138/134}\text{Ba}_{\text{NBP}} - [\text{Ba}]_{\text{SW}} \times \delta^{138/134}\text{Ba}_{\text{SW}}}{[\text{Ba}]_{\text{HT}} \times \delta^{138/134}\text{Ba}_{\text{HT}} - [\text{Ba}]_{\text{SW}} \times \delta^{138/134}\text{Ba}_{\text{SW}}} \tag{5.14}$$

The same approach is taken in equation 5.14 using Ba concentration ([Ba]) and Ba-isotope values ($\delta^{138/134}$Ba). At Rainbow, measurements from samples at S2 ($\approx$ 20km east of Rainbow vent site) were used as seawater (SW) values for Ba- isotopes, while at TAG Ba concentration and $\delta^{138/134}$Ba values from Bermuda Atlantic Time-series Study (BATS) Hydrostation S (2998m), were taken to represent ambient seawater (Hsieh and Henderson, 2017).

In the Rainbow NBP, $f_{\text{HT-He}}$ was estimated to be $0.21 \pm 0.1\%(\pm 2\text{SE})$ while two samples in the TAG NBP provide a mean $f_{\text{HT-He}}$ of $0.41 \pm 0.04\%(\pm 2\text{SE})$. These compare with $f_{\text{HT-Ba}}$ values of $0.7 \pm 0.3\%(\pm 2\text{SE})$ for a Rainbow NBP sample and $0.9 \pm 0.5\%(\pm 2\text{SE})$ for an average of two TAG NBP samples. The magnitude of dilution between the formation of He and Ba end-members is $\approx f_{\text{HT-Ba}}/f_{\text{HT-He}}$, resulting in values of $3.7 \pm 1.8(\pm 2\text{SE})$ and $2.3 \pm 1.2(\pm 2\text{SE})$ at Rainbow and TAG vent sites respectively (figure 5.5)

The similarity of f values derived from He and Ba indicates that a very small amount of

seawater entrainment is required to start the precipitation of barite, which is then completed with little further dilution of fluids. Barite precipitation and the resultant decline of dissolved Ba concentration below saturation is therefore exceedingly rapid; this makes sense considering that the stoichiometric ratio of seawater dissolved $SO_4{}^c$oncentration to vent fluid dissolved Ba concentration is more than 250-fold. Hsieh et al. (2021) used a ratio of hydrothermal fluid / effective hydrothermal end-member Ba concentration ratio of 100/0.2 (µmol/kg) to estimate a maximum hydrothermal fluid dilution of ≈ 500 before the effective end-member is established. Hydrothermal fluid mass fraction values found in these two plumes provide fluid dilution factors more >100-fold smaller than this previously estimated maximum.

NBP particulate values of Ba concentration and $\delta^{138/134}$Ba could improve our understanding of the evolution of the hydrothermal Ba end-member in the plume. Such values may further confirm barite as the dominant sink of dissolved Ba in the early hydrothermal plume and evaluate if NBP barite contains a different isotope ratio to biogenetic or pelagic barite.

5.7 Conclusions

The first coupled measurements of dissolved Ba and $\delta^{138/134}$Ba in hydrothermal NBPs were made at Rainbow and TAG vent sites, along the MAR. NBP waters display heavier $\delta^{138/134}$Ba values and higher dissolved Ba concentrations than surrounding ambient seawaters. Using a three end-member mixing model, hydrothermal Ba fractions in NBP waters were calculated to be 2.9±1.5% at Rainbow and 3.5±1.5% at TAG; lower than those of some Atlantic deep waters sampled far from the MAR, implying unknown hydrothermal sources or alternate causes for non-conservative Ba behaviour in deep waters. He- and Ba- derived water mass fractions were used to show that the magnitude of dilution of hydrothermal fluids that occurs before an effective hydrothermal Ba end-member is established is more than 100-fold smaller than maximum previously assumed. This small dilution factor indicates that barite precipitation in hydrothermal fluids requires very little dilution with entrained seawater.

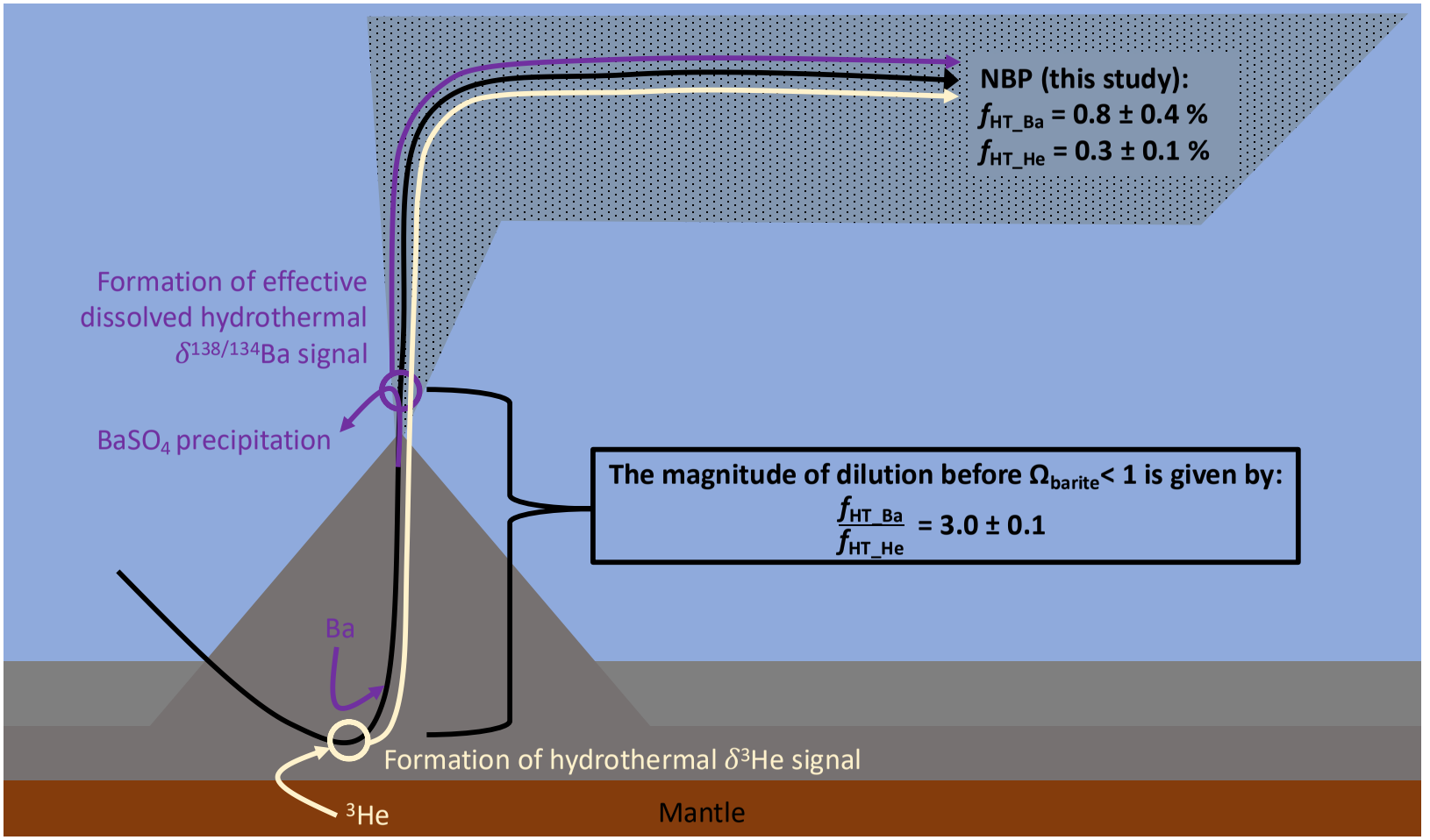

Figure 5.5: A simplified diagram depicting the formation of hydrothermal He and Ba end-members and the comparison of hydrothermal end-member mass fractions derived from He and Ba in the NBP. Primordial ^{3}He is added to fluids from the mantle and mixed conservatively until measured in the NBP. Ba is added to fluids below the seafloor before barite precipitation upon interaction with SO_4-rich seawater, forming an effective hydrothermal end-member with a heavy $\delta^{138/134}$Ba value. The magnitude of dilution of hydrothermal fluids occurring between the formation of He and Ba end-members can be estimated via the ratio of hydrothermal mass fraction values derived from each element via a two end-member conservative mixing model.

Chapter 6

Summary and conclusions

This thesis investigated behaviour of radium, barium and the rare earth elements (REEs) at Mid-Atlantic Ridge hydrothermal vent sites. The findings of these investigations show that chemical fluxes from mid-ocean ridge (MOR) hydrothermal sites are regulated by complex interactions between direct chemical inputs from hydrothermal fluids, relict hydrothermal deposits and sediments, dynamic chemical and physical processing in the hydrothermal plumes and physical transport processes influenced by local ridge topography. A summary of the key aims of this thesis can be found in section 1.3. Below, the key findings from each chapter are summarised and their resulting impacts discussed.

6.1 RaDeCC Reader

In chapter 2, RaDeCC Reader, a Python program that expedites the process of correction and the propagation of uncertainties applied to raw data generated by Radium Delayed Coincidence Counting (RaDeCC) instruments is presented and validated. The reduced processing time offered by RaDeCC Reader, means that results derived from ship-based sample analyses could more readily be used as feedback for the adaption of survey designs or sampling strategies during fieldwork campaigns. In addition, a more uniform approach to implement the latest data correction and uncertainty propagation techniques, ought to result in more robust and reliable data outputs.

A graphical user interface (GUI) is incorporated so that the RaDeCC Reader might be used by more RaDeCC users. The more widely the program, or any standard method of data correction, is used, the more comparable results will be between RaDeCC users since both

the analytical method and the raw data correction are significant to final data values and their inter-comparability.

The RaDeCC Reader could still be improved by addition of functionality for specific radium-isotope applications. Correction of radium-228 activities has been incorporated but is yet to be validated. The calculation of system efficiency change due to the change in the total volume of the RaDeCC system is not yet automated, although the coefficient can be input. The addition of missing functionality would expand the utility of the program and encourage adoption by more RaDeCC users. Since RaDeCC Reader is open source, it can be further refined and expanded by anyone in the future.

6.2 Short-lived radium isotopes

The utility of short-lived radium isotopes as tracers of NBP dispersion has been evaluated at sites along the MAR (Chapter 3). Contrary to expectation, benthic inputs appear to be the dominant source of short-lived radium isotopes at Rainbow and TAG vent sites. Sulfide-rich sediments are the most likely major contributor to benthic inputs; possibly due to diffusion of seawater uranium-235 into particles containing sulfides that are undergoing oxidation, with subsequent reductive fixation of uranium-235 at the oxide-sulfide boundary. The exact composition of sources to bottom waters in the MAR axial valley, however, remains unconstrained. This discovery hints at the possible utility of short-lived radium isotopes in detecting the presence of seafloor sulfide deposits without disturbing fragile deep seafloor ecosystems.

The dominance of benthic inputs means that it is not possible to use radium-223 and -224 to trace plume dispersion in these settings, as has previously been postulated. However, short-lived radium isotopes may still trace plume dispersion at hydrothermal sites where fluids contain high radium isotope activities and no additional sources of radium isotopes nearby. At fast spreading ridges, such as the East Pacific Rise, there is no major axial valley in which sediments and deposits might accumulate to provide additional sources of radium isotopes, meaning that plume dispersion tracing with radium-223 and radium-224 is more likely to be possible. Within axial valleys at slow spreading ridges where benthic inputs of these isotopes dominate, radium-223 and -224 may be employed to trace vertical transport processes.

Mean vertical diffusivity (Kv) profiles calculated for sites on the MAR (see Section 3.6.4) are significantly higher than previously calculated for MAR spur topography (Polzin et al., 1997). The individual source contributions of radium-223 and -224 in these settings are not sufficiently disentangled and quantified to allow the K_v values derived from these isotopes to offer more than a qualitative upper bound on diffusivity rates in this region. Seawater radium isotope distributions reflect all the processes acting on the atoms, including those that are unknown, and provide a mean outcome from the journeys of many atoms; similar to a Lagrangian model. Therefore, while it is possible to measure seawater radium isotope activities precisely, it remains difficult to disentangle the effects of diffusion and convection processes acting on those isotopes to derive an accurate quantitative rate value for either process. An alternative way to determine the rates of physical processes is by in-situ physical measurements, comparison of these direct measurements with values derived from radium-isotopes might validate the use of these isotopes to trace physical processes in axial valley settings.

In order for short-lived radium isotopes to be used as plume tracers at any hydrothermal vent sites in the future, a clear understanding of the radium sources specific to each ridge setting is required. This knowledge would be essential for future sites not yet evaluated for radium fluxes or distribution, where alternative venting styles and mineral deposits may alter the relative significance of plume and sediment sources of radium to the water column. After all, the water-column radium-223/radium-224 activity ratios of sulfide deposit and plume-fallout sediment materials have not yet been measured, values presented in figure 3.11 (Section 3.6.2) are only theoretical values extrapolated from uranium-series analyses of sediment cores collected by Mills et al. (1993) and German (1993).

6.3 The Eu anomaly

Dissolved concentration measurements of rare earth elements (REEs) in seawater along the MAR have shown, for the first time, that significant dissolved positive Eu* anomalies survive in the NBP despite extensive scavenging by plume particles (Chapter 4). Only 0.02% of Eu in hydrothermal fluids, however, survives plume scavenging and mixes with surrounding deep ocean waters. This means that hydrothermal inputs of Eu are not expected to have an observable impact on seawater Eu* values. These findings from three study sites on the MAR,

however, may not to completely represent the diverse modes and settings of hydrothermal venting globally.

The flux of hydrothermal Eu into the ocean is regulated by the concentration of Eu in hydrothermal fluids and the efficiency with which Eu is removed from solution by particle scavenging in the hydrothermal plume. The dominant control is likely to be the efficiency of plume scavenging, which in the modern ocean is dependent on the composition and density of particulate in the plume. Hydrothermal fluids emanating from more mafic host-rock will likely contain more Fe and Mn, generating more particulate rich in Fe-(oxy)hydroxides and Mn-oxides, which in turn increases the rate of removal of Eu from solution in the plume. Like Fe and Mn, fluid Eu concentration will also vary depending on host-rock composition but since hydrothermal plumes are considered to be net sinks of REEs, it appears that there is an excess of scavenging capacity in observed plumes. In past, oxygen-poor oceans, hydrothermal inputs may have exerted a stronger influence over seawater Eu*, if plumes were less rich in Fe-(oxy)hydroxide and Mn-oxide rich particles and scavenging removal would have been less efficient.

In the modern ocean, our well constrained minor contribution of MOR hydrothermal inputs to seawater Eu* values, means that Eu* may be most well suited as a tracer of UCC inputs. Hydrothermal inputs at MORs appear to have no observable impact on seawater Eu*, which is well mixed with respect to inputs from the Upper Continental Crust (UCC) and therefore provides an assessment of the average UCC Eu* value. A mean seawater value of 0.97 ($\pm$0.07, 2σ) supports PAAS (1.00) and NASC (0.99) values determined by Taylor and McLennan (1985) and Gromet et al. (1984) respectively. Isolated seas with inputs from a limited number of distinct UCC inputs such as the Baltic, Mediterranean, Red, Black and Caspian seas may yield seawater Eu* significantly different to the open-ocean mean found in chapter 4 and allow the assessment of average Eu* values of distinct sections of UCC.

Deriving an average composition for the upper continental crust (UCC) is valuable because it provides insights into the relative contribution of the crust to the global biogeochemical budget and the origin of the continents (Rudnick and Gao, 2014). Estimating the average composition of UCC has traditionally been approached by averaging many samples from the exposed surface of the crust or by averaging compositions of the insoluble components of fine-grained clastic sedimentary rocks (Clarke, 1889; Taylor and McLennan, 1985) or glacial

deposits (Goldschmidt, 1933). Mean seawater Eu* provides an independent validation of the UCC Eu* values derived from these traditional methods and a more direct measurement of dissolved input to the ocean.

6.4 Barium isotopes

The first coupled measurements of dissolved Ba concentration and barium isotopes ($\delta^{138/134}$Ba) in hydrothermal NBPs display higher Ba concentrations and heavier $\delta^{138/134}$Ba values than surrounding ambient seawater (Chapter 5). Low hydrothermal Ba fractions in the hydrothermal NBP ($1.4 - 4.4\%$) suggest that hydrothermal Ba inputs to the ocean are unlikely to exert a major influence on seawater Ba-isotope values; providing a new and valuable development in our understanding of the oceanic Ba-cycle.

Hsieh et al. (2021) found that barium isotope composition in vent fluids is primarily driven by barite precipitation with a similar fractionation factor across the hydrothermal vent sites studied. Findings from Section 5.6.1 are therefore likely to apply to a wide range of hydrothermal settings since, in most cases, the host-rock composition is not likely to have a large impact on the effective hydrothermal Ba-isotope ratio. Similarly, the maximum Ba concentration supporting the effective hydrothermal end-member, and therefore the magnitude of the hydrothermal Ba flux to the ocean, is determined by the SO_4 concentration of surrounding ambient seawaters rather than attributes of hydrothermal circulation.

Investigation of NBP particulate samples could assess $\delta^{138/134}$Ba of NBP barite for comparison with values measured in natural minerals, experimental precipitates and hydrothermal dregs (Von Allmen et al., 2010; Hsieh et al., 2021). This comparison could validate the hydrothermal barite fractionation factor determined by Hsieh et al. (2021) and be used to calculate an effective hydrothermal Ba-isotope ratio.

The amount of seawater entrained into vent fluids before an effective hydrothermal Ba-isotope ratio is formed was found to be $>$ 100-fold smaller than previously thought. The seawater/vent-fluid water mass ratio calculated ($1.1 - 5.5$), indicates that barite precipitation is exceedingly rapid, requiring very little seawater entrainment and occurring close to the vent orifice or even in the subsurface, prior to venting, as previously postulated (Hsieh et al., 2021).

Appendix A

Appendix

A.1 Data tables

Table A.1: Dissolved activities of radium-223, radium-224, actinium-227 and thorium-228 from the JC156 expedition onboard RRS *James Cook*, GEOTRACES GA13.

Station	Lat. °N	Lon. °E	Depth m	Ra-223 dpm/m^3	2σ dpm/m^3	Ac-227 dpm/m^3	2σ dpm/m^3	Ra-224 dpm/m^3	2σ dpm/m^3	Th-228 dpm/m^3	2σ dpm/m^3
1	41.383	-13.888	43.5	0.0	0.3	0.1	0.1	0.0	1.1	8.7	0.7
1	41.383	-13.888	134.1	0.4	0.3	0.0	0.1	0.0	0.9	13.1	0.6
1	41.383	-13.888	295.9	0.2	0.3	0.0	0.1	0.0	1.1	9.3	0.7
1	41.383	-13.888	837.9	0.3	0.2	0.0	0.1	0.0	1.5	5.8	1.1
1	41.383	-13.888	852.9	0.2	0.3	0.0	0.1	0.0	1.1	9.4	0.8
2	36.230	-33.527	1505.6	2.6	0.6	0.6	0.1	2.2	1.1	6.8	0.7
2	36.230	-33.527	1756.9	1.3	0.8	0.3	0.2	5.3	1.3	2.7	0.8
2	36.230	-33.527	2163.2	1.7	0.7	0.3	0.2	4.9	1.9	2.2	0.9
2	36.230	-33.527	2340.5	2.2	0.9	0.6	0.2	4.5	1.3	2.4	0.7
3	36.230	-34.236	1730.5	1.2	0.6	0.2	0.2	2.7	1.2	2.5	0.6
3	36.230	-34.236	2186.5	0.7	0.6	0.5	0.2	4.5	1.8	2.5	0.8
3	36.230	-34.236	2318.9	1.9	0.5	0.5	0.1	7.0	1.0	2.2	0.5
4	36.471	-33.671	1667.0	2.1	0.7	0.3	0.2	1.0	1.7	3.1	0.8
4	36.471	-33.671	2233.3	3.1	1.9	0.9	0.5	2.3	1.4	3.0	0.8
4	36.471	-33.671	2427.6	18.8	1.9	0.7	0.2	9.5	1.2	1.4	0.5
4	36.471	-33.671	2534.3	21.5	2.4	0.8	0.2	7.2	1.2	3.0	0.6
5	35.945	-34.155	1741.0	1.2	0.7	0.2	0.2	2.0	1.4	4.3	0.8
5	35.945	-34.155	1911.2	0.9	0.6	0.7	0.2	3.9	1.0	1.1	0.4
5	35.945	-34.155	1936.0	1.3	1.6	1.0	0.5	2.9	2.0	2.8	0.9
5	35.945	-34.155	1961.3	1.2	0.7	0.8	0.2	2.8	1.4	2.5	0.8
6	36.230	-33.902	1959.3	2.0	0.5	0.2	0.1	3.1	0.7	0.7	0.3
6	36.230	-33.902	2112.5	1.2	0.7	0.2	0.1	1.8	0.6	0.5	0.3
6	36.230	-33.902	2163.5	1.6	0.6	0.5	0.2	2.7	1.1	1.5	0.6
6	36.230	-33.902	2187.8	2.6	0.7	0.5	0.1	5.0	1.6	1.1	0.5
6	36.230	-33.902	2238.3	1.9	0.4	0.2	0.1	2.7	0.8	1.3	0.4
7	36.381	-33.694	2020.0	1.0	0.6	0.1	0.1	2.1	1.0	1.1	0.6
7	36.381	-33.694	2112.5	1.7	0.5	0.3	0.1	3.9	1.4	1.6	0.5
7	36.381	-33.694	2416.7	2.5	0.5	0.2	0.1	3.5	0.6	0.5	0.2
8	26.360	-44.675	3012.5	0.6	0.3	0.3	0.1	0.0	0.6	1.5	0.4
8	26.360	-44.675	3200.0	0.8	0.4	0.5	0.2	0.4	0.5	1.7	0.3
8	26.360	-44.675	3419.3	1.2	0.9	0.7	0.2	0.4	0.6	2.0	0.4

8	26.360	-44.675	3619.9	8.7	0.9	1.1	0.3	2.1	0.9	4.5	0.6
8	26.360	-44.675	3800.0	10.3	1.0	0.4	0.2	4.1	0.7	1.4	0.3
9	25.930	-45.019	3223.7	1.1	0.6	1.5	0.3	3.4	1.1	2.9	0.6
9	25.930	-45.019	3428.6	1.3	0.6	0.1	0.1	0.8	0.5	0.5	0.3
9	25.930	-45.019	3631.9	13.5	1.7	1.4	0.5	2.2	2.1	5.5	1.1
9	25.930	-45.019	3836.4	13.2	0.9	0.6	0.2	1.8	1.0	3.4	0.8
9	25.930	-45.019	4042.3	15.4	1.7	0.6	0.2	3.6	0.9	3.4	0.4
9	25.930	-45.019	4153.9	13.0	1.7	0.6	0.2	2.0	0.8	2.2	0.4
10	26.215	-45.118	2413.1	0.9	0.5	0.4	0.2	0.2	0.8	3.2	0.5
10	26.215	-45.118	2617.9	0.8	0.6	0.8	0.2	0.0	1.3	4.7	1.0
10	26.215	-45.118	2820.5	0.5	0.6	0.3	0.2	0.4	0.5	0.5	0.3
10	26.215	-45.118	2921.2	0.5	0.4	0.4	0.2	0.3	0.7	2.7	0.4
10	26.215	-45.118	3023.3	1.0	0.4	0.7	0.2	0.2	0.9	3.8	0.6
11	26.029	-44.553	3021.1	1.5	0.5	0.1	0.1	0.3	0.7	1.3	0.4
11	26.029	-44.553	3176.5	1.0	0.4	0.2	0.1	0.0	0.6	2.1	0.4
11	26.029	-44.553	3380.0	1.3	0.6	0.6	0.2	0.0	1.6	4.8	1.0
11	26.029	-44.553	3581.5	0.4	0.4	0.2	0.2	0.0	0.6	1.8	0.4
11	26.029	-44.553	3892.9	0.3	0.3	0.2	0.1	0.6	0.5	0.6	0.3
12	26.139	-44.826	3256.9	0.6	0.6	0.6	0.2	0.5	0.6	1.8	0.4
12	26.139	-44.826	3307.2	4.8	1.3	0.5	0.2	0.8	1.1	3.8	0.7
12	26.139	-44.826	3331.9	3.7	0.9	0.7	0.2	1.2	0.6	2.2	0.4
12	26.139	-44.826	3508.3	3.7	1.0	1.0	0.2	2.3	1.1	3.5	0.8
12	26.139	-44.826	3586.8	14.2	5.2	1.2	0.3	3.9	1.1	4.3	0.5
12	26.139	-44.826	3652.5	19.1	2.5	1.3	0.5	3.3	2.3	5.8	1.2
13	26.139	-44.826	2240.4	2.1	1.2	0.3	0.1	0.0	0.7	1.4	0.5
13	26.139	-44.826	3002.6	0.0	0.5	0.5	0.1	0.0	0.7	2.0	0.5
13	26.139	-44.826	3207.0	2.8	1.1	1.2	0.2	1.0	1.0	4.2	0.6
13	26.139	-44.826	3257.6	0.7	0.6	0.5	0.2	0.2	0.5	2.0	0.3
13	26.139	-44.826	3311.6	0.4	1.3	1.3	0.5	1.0	0.7	2.4	0.4

Table A.2: Dissolved REE concentrations from the JC156 expedition onboard RRS *James Cook*, GEOTRACES GA13.

Station	Depth	La	Ce	Pr	Nd	Sm	Eu	Gd	Tb	Dy	Ho	Er	Tm	Yb	Lu
	m	pg/g	pg/g	pg/g	pg/g	pg/g	pg/g	pg/g	pg/g	pg/g	pg/g	pg/g	pg/g	pg/g	pg/g
6	810	2.993	0.443	0.526	2.317	0.459	0.119	0.678	0.107	0.802	0.210	0.700	0.102	0.691	0.125
6	780	3.038	0.457	0.531	2.296	0.477	0.120	0.689	0.109	0.815	0.215	0.725	0.102	0.704	0.130
6	725	3.046	0.434	0.535	2.345	0.480	0.123	0.699	0.110	0.799	0.213	0.713	0.105	0.712	0.128
8	1710	2.774	0.456	0.453	1.918	0.390	0.116	0.587	0.094	0.719	0.183	0.633	0.095	0.641	0.116
8	1700	2.793	0.409	0.465	1.953	0.398	0.118	0.575	0.093	0.690	0.193	0.653	0.099	0.656	0.115
8	1690	2.825	0.538	0.471	1.953	0.384	0.113	0.583	0.092	0.680	0.190	0.637	0.094	0.629	0.116
8	1625	2.767	0.685	0.456	1.869	0.351	0.104	0.575	0.092	0.696	0.188	0.641	0.097	0.625	0.116
8	1200	2.963	0.461	0.506	2.147	0.433	0.118	0.622	0.098	0.754	0.202	0.685	0.101	0.685	0.122
8	720	2.960	0.393	0.521	2.180	0.438	0.128	0.666	0.105	0.791	0.199	0.672	0.097	0.649	0.116
8	550	2.992	0.482	0.530	2.254	0.468	0.123	0.691	0.106	0.813	0.204	0.688	0.096	0.634	0.114
8	150	2.288	0.971	0.453	1.902	0.408	0.122	0.646	0.101	0.780	0.200	0.685	0.095	0.595	0.108
8	80	2.073	1.042	0.405	1.704	0.375	0.105	0.565	0.096	0.722	0.187	0.631	0.091	0.586	0.097
9	2210	2.674	0.387	0.433	1.882	0.376	0.104	0.588	0.094	0.704	0.170	0.663	0.097	0.681	0.124
9	2200	2.637	0.386	0.434	1.908	0.374	0.108	0.599	0.087	0.703	0.211	0.650	0.098	0.656	0.118
9	1800	2.733	0.405	0.472	1.919	0.405	0.114	0.605	0.093	0.710	0.188	0.658	0.097	0.646	0.120
9	1500	2.985	0.423	0.520	2.204	0.423	0.120	0.633	0.107	0.776	0.203	0.692	0.100	0.682	0.124
9	1200	2.943	0.411	0.522	2.210	0.469	0.130	0.670	0.113	0.831	0.210	0.699	0.102	0.719	0.127
10	2475	2.954	0.558	0.473	2.037	0.387	0.108	0.627	0.096	0.749	0.205	0.693	0.104	0.715	0.132
10	2450	2.888	0.561	0.461	1.951	0.389	0.104	0.586	0.096	0.726	0.202	0.685	0.102	0.711	0.131
10	2380	2.798	0.519	0.469	2.010	0.406	0.105	0.584	0.097	0.713	0.194	0.672	0.102	0.691	0.128
10	2000	2.912	0.485	0.469	2.093	0.399	0.109	0.622	0.099	0.752	0.209	0.708	0.100	0.718	0.130
10	1500	3.175	0.898	0.554	2.426	0.456	0.121	0.666	0.112	0.799	0.224	0.731	0.108	0.722	0.133
10	780	3.002	0.403	0.531	2.271	0.485	0.126	0.714	0.107	0.845	0.227	0.726	0.106	0.722	0.128
10	540	2.844	0.460	0.505	2.214	0.452	0.119	0.681	0.105	0.787	0.209	0.695	0.099	0.660	0.118
11	2874	3.017	0.571	0.484	2.100	0.409	0.106	0.604	0.093	0.708	0.170	0.669	0.100	0.707	0.130
11	2774	2.921	0.532	0.467	1.981	0.382	0.103	0.613	0.087	0.700	0.172	0.668	0.098	0.676	0.128
11	2050	2.918	0.486	0.504	2.105	0.407	0.113	0.641	0.102	0.762	0.187	0.696	0.103	0.701	0.130
11	1800	2.977	0.485	0.494	2.177	0.443	0.114	0.674	0.102	0.760	0.195	0.701	0.103	0.712	0.126
11	1400	3.173	0.471	0.538	2.308	0.467	0.126	0.717	0.107	0.824	0.194	0.743	0.109	0.732	0.135
11	830	2.995	0.395	0.542	2.351	0.487	0.127	0.719	0.112	0.833	0.192	0.733	0.106	0.707	0.127
11	600	2.833	0.437	0.513	2.161	0.465	0.118	0.667	0.105	0.780	0.185	0.684	0.099	0.675	0.119
12	2350	2.606	0.484	0.412	1.772	0.343	0.096	0.535	0.085	0.660	0.183	0.631	0.093	0.648	0.111

12	2320	2.632	0.408	0.396	1.763	0.338	0.093	0.544	0.086	0.701	0.191	0.644	0.095	0.664	0.113
12	2200	2.643	0.377	0.403	1.729	0.354	0.093	0.539	0.083	0.677	0.188	0.656	0.098	0.661	0.113
12	2150	2.669	0.381	0.404	1.760	0.352	0.094	0.540	0.083	0.693	0.190	0.645	0.098	0.664	0.113
12	2100	2.587	0.350	0.393	1.706	0.324	0.091	0.539	0.083	0.671	0.187	0.637	0.096	0.653	0.113
12	2000	2.731	0.345	0.445	1.929	0.392	0.106	0.588	0.090	0.732	0.196	0.670	0.098	0.673	0.116
12	1500	2.977	0.771	0.506	2.143	0.437	0.115	0.662	0.101	0.799	0.210	0.706	0.106	0.712	0.118
12	1000	2.994	0.412	0.528	2.236	0.467	0.123	0.694	0.111	0.804	0.211	0.712	0.106	0.723	0.116
12	720	2.896	0.435	0.528	2.276	0.454	0.126	0.692	0.105	0.814	0.207	0.699	0.103	0.682	0.127
12	550	2.873	0.454	0.522	2.258	0.470	0.122	0.740	0.107	0.835	0.216	0.721	0.104	0.677	0.111
12	70	1.915	1.092	0.372	1.631	0.352	0.097	0.604	0.095	0.726	0.193	0.643	0.095	0.583	0.094
13	2325	2.728	0.378	0.416	1.867	0.365	0.101	0.564	0.090	0.696	0.191	0.655	0.101	0.676	0.113
13	2200	2.692	0.354	0.420	1.845	0.365	0.098	0.579	0.090	0.711	0.190	0.649	0.100	0.670	0.114
13	2100	2.815	0.386	0.430	1.859	0.355	0.098	0.599	0.091	0.729	0.207	0.682	0.101	0.686	0.118
13	2000	2.773	0.353	0.436	1.744	0.358	0.100	0.573	0.088	0.723	0.194	0.666	0.102	0.677	0.115
13	1750	2.869	0.367	0.473	1.965	0.404	0.106	0.636	0.097	0.768	0.205	0.700	0.108	0.715	0.120
13	1500	3.057	0.457	0.514	2.140	0.462	0.119	0.676	0.104	0.797	0.211	0.715	0.105	0.721	0.120
13	1000	2.989	0.415	0.558	2.370	0.476	0.129	0.699	0.114	0.838	0.222	0.720	0.105	0.711	0.113
13	850	2.767	0.371	0.515	2.302	0.462	0.124	0.682	0.108	0.776	0.204	0.679	0.104	0.697	0.121
13	700	2.875	0.380	0.542	2.304	0.459	0.119	0.698	0.108	0.797	0.203	0.693	0.099	0.663	0.107
13	300	2.479	0.738	0.479	2.064	0.415	0.113	0.670	0.105	0.810	0.205	0.679	0.095	0.633	0.100
14	2611	2.706	0.375	0.446	1.973	0.385	0.098	0.605	0.093	0.721	0.194	0.667	0.099	0.683	0.110
14	2550	2.745	0.610	0.452	1.882	0.383	0.106	0.574	0.087	0.671	0.184	0.636	0.096	0.635	0.116
14	2450	2.702	0.399	0.436	1.940	0.375	0.099	0.567	0.090	0.707	0.184	0.643	0.095	0.659	0.107
14	2260	2.627	0.401	0.420	1.872	0.351	0.098	0.578	0.084	0.697	0.187	0.641	0.096	0.660	0.109
14	2250	2.598	0.404	0.436	1.859	0.360	0.098	0.578	0.086	0.687	0.185	0.638	0.095	0.647	0.111
14	2100	2.660	0.336	0.403	1.838	0.345	0.096	0.574	0.086	0.690	0.190	0.649	0.099	0.644	0.110
14	1700	2.767	0.407	0.460	2.003	0.390	0.114	0.606	0.094	0.732	0.192	0.684	0.097	0.660	0.118
14	1500	2.928	0.370	0.523	2.330	0.455	0.126	0.698	0.109	0.820	0.208	0.720	0.105	0.712	0.115
14	1300	3.042	0.431	0.549	2.371	0.470	0.124	0.717	0.112	0.818	0.194	0.744	0.105	0.731	0.133
14	960	2.879	0.384	0.520	2.227	0.436	0.126	0.669	0.105	0.769	0.194	0.698	0.100	0.693	0.128
14	725	2.882	0.366	0.537	2.335	0.455	0.121	0.692	0.106	0.819	0.226	0.702	0.102	0.676	0.109
14	400	2.720	0.561	0.510	2.200	0.459	0.119	0.693	0.105	0.802	0.213	0.682	0.097	0.643	0.102
14	80	1.941	0.957	0.373	1.736	0.382	0.104	0.615	0.096	0.729	0.203	0.628	0.092	0.581	0.092
15	2350	2.982	0.529	0.492	2.131	0.417	0.113	0.648	0.100	0.774	0.212	0.698	0.103	0.720	0.120
15	2100	2.996	0.484	0.502	2.186	0.413	0.115	0.663	0.103	0.806	0.219	0.707	0.106	0.729	0.119
15	1950	2.804	0.418	0.442	1.957	0.361	0.106	0.625	0.091	0.735	0.200	0.670	0.100	0.672	0.112

15	1925	2.750	0.413	0.439	1.896	0.370	0.102	0.594	0.091	0.721	0.199	0.658	0.098	0.675	0.112
15	1900	2.728	0.359	0.433	1.941	0.376	0.101	0.588	0.092	0.728	0.207	0.662	0.098	0.684	0.113
15	1860	2.750	0.343	0.425	1.912	0.370	0.101	0.580	0.091	0.723	0.206	0.659	0.097	0.662	0.113
15	1730	2.851	0.382	0.486	2.022	0.395	0.108	0.625	0.094	0.745	0.209	0.687	0.102	0.695	0.115
15	1400	2.783	0.414	0.494	2.195	0.407	0.116	0.642	0.101	0.779	0.199	0.690	0.101	0.695	0.127
15	850	3.027	0.403	0.545	2.375	0.476	0.126	0.708	0.110	0.844	0.236	0.717	0.106	0.690	0.114
16	2280	3.011	0.526	0.498	2.277	0.442	0.121	0.673	0.103	0.805	0.218	0.734	0.109	0.727	0.122
16	2240	2.913	0.462	0.498	2.194	0.441	0.113	0.643	0.105	0.783	0.211	0.706	0.104	0.706	0.118
16	2200	2.883	0.454	0.474	2.134	0.413	0.112	0.640	0.103	0.761	0.205	0.705	0.105	0.701	0.114
16	2175	2.433	0.430	0.326	1.444	0.262	0.098	0.461	0.069	0.602	0.173	0.592	0.091	0.618	0.107
16	2150	2.776	0.434	0.454	2.013	0.379	0.112	0.602	0.093	0.747	0.195	0.687	0.100	0.669	0.114
16	2100	2.844	0.438	0.460	1.984	0.383	0.110	0.606	0.093	0.771	0.203	0.706	0.104	0.693	0.115
16	2000	2.577	0.372	0.406	1.780	0.334	0.097	0.565	0.085	0.702	0.189	0.653	0.095	0.654	0.109
16	1950	2.724	0.367	0.412	1.860	0.365	0.103	0.593	0.088	0.713	0.198	0.710	0.103	0.696	0.117
16	1900	2.756	0.396	0.421	1.892	0.370	0.102	0.591	0.091	0.729	0.204	0.684	0.102	0.687	0.113
16	1800	2.866	0.364	0.466	2.035	0.409	0.108	0.620	0.096	0.765	0.205	0.695	0.106	0.705	0.119
16	1400	3.116	0.403	0.533	2.299	0.471	0.126	0.707	0.108	0.845	0.236	0.754	0.110	0.724	0.120
16	1100	3.161	0.579	0.568	2.527	0.493	0.132	0.736	0.116	0.878	0.231	0.756	0.111	0.739	0.122
16	700	3.009	0.395	0.544	2.327	0.476	0.128	0.727	0.112	0.845	0.216	0.727	0.104	0.675	0.112
16	500	2.939	0.452	0.544	2.392	0.469	0.129	0.735	0.110	0.868	0.227	0.742	0.105	0.683	0.108
16	300	2.672	0.743	0.492	2.154	0.448	0.123	0.712	0.111	0.825	0.216	0.711	0.103	0.659	0.106
16	175	2.352	0.843	0.449	1.987	0.440	0.117	0.666	0.106	0.818	0.213	0.687	0.101	0.651	0.104
16	120	2.153	0.880	0.429	1.936	0.414	0.117	0.635	0.101	0.792	0.202	0.668	0.097	0.621	0.097
16	60	1.824	1.007	0.359	1.534	0.339	0.093	0.570	0.089	0.720	0.198	0.610	0.088	0.556	0.088
16	20	1.821	1.032	0.367	1.593	0.340	0.095	0.564	0.087	0.711	0.183	0.621	0.088	0.559	0.087
18	2550	2.778	0.482	0.445	1.974	0.385	0.104	0.605	0.095	0.719	0.195	0.672	0.101	0.694	0.130
18	2400	2.760	0.459	0.455	1.939	0.377	0.105	0.595	0.091	0.703	0.190	0.662	0.095	0.681	0.124
18	2300	2.645	0.449	0.429	1.846	0.370	0.103	0.550	0.088	0.677	0.187	0.643	0.096	0.683	0.123
18	2200	2.605	0.390	0.423	1.824	0.348	0.099	0.562	0.088	0.672	0.203	0.660	0.096	0.681	0.120
18	2050	2.508	0.359	0.398	1.751	0.332	0.094	0.531	0.088	0.645	0.176	0.626	0.092	0.638	0.119
18	1800	2.672	0.405	0.443	1.883	0.365	0.106	0.600	0.094	0.706	0.197	0.678	0.097	0.673	0.124
18	1200	2.939	0.446	0.497	2.212	0.441	0.118	0.685	0.109	0.799	0.217	0.730	0.103	0.721	0.129
18	690	2.748	0.389	0.473	2.130	0.424	0.116	0.613	0.102	0.760	0.196	0.654	0.096	0.638	0.117
18	500	2.732	0.480	0.495	2.176	0.422	0.119	0.652	0.100	0.764	0.204	0.679	0.097	0.644	0.115
38	2275	2.788	0.583	0.450	1.904	0.398	0.115	0.598	0.095	0.706	0.195	0.649	0.097	0.661	0.124
38	2274	2.629	0.517	0.404	1.859	0.336	0.122	0.536	0.085	0.671	0.186	0.633	0.097	0.657	0.122

38	2268	2.658	0.485	0.438	1.929	0.367	0.108	0.603	0.089	0.705	0.194	0.662	0.097	0.675	0.125
38	2257	2.607	0.452	0.429	1.926	0.354	0.103	0.554	0.088	0.700	0.185	0.641	0.095	0.670	0.123
38	2139	2.570	0.450	0.409	1.811	0.348	0.096	0.562	0.087	0.671	0.181	0.629	0.095	0.673	0.120
38	2058	2.406	0.400	0.385	1.754	0.318	0.095	0.523	0.079	0.643	0.174	0.615	0.092	0.638	0.121
38	1966	2.340	0.385	0.342	1.550	0.293	0.094	0.483	0.075	0.612	0.171	0.591	0.087	0.620	0.118
38	1925	2.328	0.373	0.352	1.539	0.283	0.087	0.468	0.073	0.603	0.160	0.587	0.089	0.619	0.116
38	1884	2.335	0.355	0.351	1.632	0.299	0.092	0.497	0.076	0.617	0.157	0.590	0.088	0.609	0.117
38	1800	2.536	0.377	0.421	1.847	0.338	0.101	0.564	0.087	0.689	0.174	0.628	0.095	0.652	0.121
38	1500	2.715	0.447	0.464	2.181	0.410	0.115	0.633	0.093	0.753	0.190	0.655	0.097	0.684	0.126
38	1300	2.762	0.431	0.497	2.253	0.414	0.117	0.638	0.098	0.757	0.187	0.649	0.098	0.672	0.124
38	770	2.812	0.403	0.518	2.259	0.430	0.119	0.665	0.102	0.781	0.188	0.662	0.099	0.673	0.122
20	2250	3.029	0.635	0.494	2.236	0.415	0.122	0.681	0.099	0.744	0.190	0.675	0.101	0.703	0.131
20	2050	2.684	0.470	0.451	1.971	0.359	0.106	0.584	0.091	0.719	0.180	0.670	0.096	0.681	0.122
20	960	2.779	0.432	0.479	2.208	0.429	0.114	0.638	0.099	0.784	0.189	0.683	0.102	0.702	0.129
20	650	2.835	0.500	0.513	2.270	0.452	0.116	0.648	0.097	0.745	0.184	0.665	0.093	0.633	0.116
21	4375	3.613	0.686	0.585	2.541	0.488	0.133	0.700	0.107	0.794	0.210	0.720	0.107	0.738	0.134
21	3550	3.240	0.512	0.518	2.213	0.440	0.123	0.628	0.098	0.731	0.190	0.698	0.103	0.690	0.130
21	3020	3.148	0.504	0.507	2.146	0.415	0.113	0.612	0.096	0.739	0.193	0.679	0.101	0.682	0.127
21	3020	3.158	0.511	0.502	2.218	0.444	0.113	0.646	0.098	0.737	0.195	0.687	0.100	0.702	0.129
21	1900	2.862	0.510	0.470	2.080	0.397	0.114	0.602	0.095	0.733	0.194	0.682	0.101	0.667	0.123
21	835	2.775	0.392	0.490	2.122	0.432	0.122	0.618	0.104	0.772	0.203	0.681	0.101	0.652	0.118
23	762	2.888	0.586	0.516	2.223	0.450	0.125	0.663	0.104	0.745	0.195	0.674	0.095	0.637	0.116
23	743	2.648	0.488	0.476	2.084	0.427	0.114	0.607	0.098	0.745	0.191	0.639	0.094	0.594	0.111
23	737	2.714	0.471	0.490	2.060	0.415	0.118	0.635	0.097	0.735	0.190	0.650	0.095	0.609	0.112
23	730	2.680	0.460	0.464	2.006	0.411	0.114	0.627	0.099	0.733	0.191	0.643	0.098	0.602	0.111
23	724	2.631	0.454	0.462	1.970	0.414	0.118	0.581	0.099	0.728	0.179	0.636	0.094	0.608	0.112
23	700	2.690	0.430	0.488	2.129	0.442	0.116	0.615	0.100	0.744	0.191	0.651	0.097	0.608	0.111
23	600	2.617	0.499	0.473	2.036	0.436	0.114	0.655	0.102	0.763	0.186	0.669	0.095	0.624	0.114
24	3015	3.548	0.844	0.608	2.429	0.507	0.141	0.699	0.108	0.800	0.209	0.705	0.108	0.721	0.131
24	2982	3.172	0.588	0.525	2.202	0.430	0.121	0.671	0.101	0.739	0.198	0.683	0.099	0.680	0.126
24	2879	3.177	0.570	0.538	2.224	0.435	0.128	0.653	0.098	0.755	0.199	0.691	0.104	0.685	0.127
24	2863	3.158	0.563	0.538	2.251	0.434	0.122	0.631	0.102	0.747	0.199	0.692	0.099	0.682	0.128
24	2843	3.073	0.522	0.513	2.215	0.446	0.122	0.630	0.097	0.752	0.193	0.680	0.101	0.687	0.132
24	2838	3.115	0.505	0.508	2.213	0.440	0.130	0.660	0.099	0.753	0.191	0.687	0.101	0.699	0.133
24	2815	3.187	0.526	0.521	2.273	0.444	0.127	0.672	0.099	0.767	0.198	0.711	0.105	0.723	0.132
24	2800	3.051	0.495	0.523	2.267	0.437	0.120	0.618	0.094	0.729	0.192	0.662	0.101	0.676	0.128

24	2794	3.092	0.570	0.560	2.480	0.445	0.127	0.669	0.095	0.751	0.190	0.682	0.101	0.689	0.126
24	2751	3.073	0.509	0.513	2.189	0.431	0.123	0.635	0.095	0.745	0.211	0.696	0.102	0.676	0.128
24	2000	2.889	0.468	0.478	2.060	0.418	0.113	0.611	0.096	0.748	0.190	0.659	0.101	0.667	0.127
24	1500	2.826	0.533	0.507	2.175	0.412	0.120	0.611	0.100	0.753	0.187	0.679	0.097	0.666	0.121
24	700	2.783	0.448	0.511	2.189	0.468	0.126	0.661	0.102	0.784	0.192	0.675	0.097	0.625	0.115
24	300	2.357	0.777	0.453	1.985	0.476	0.124	0.654	0.109	0.813	0.204	0.708	0.099	0.635	0.113
24	150	1.997	0.913	0.410	1.844	0.400	0.116	0.629	0.101	0.782	0.192	0.666	0.094	0.614	0.104
26	3790	3.673	0.632	0.634	2.675	0.503	0.139	0.741	0.108	0.836	0.213	0.734	0.108	0.750	0.134
26	3490	3.572	0.542	0.614	2.543	0.489	0.137	0.727	0.106	0.809	0.202	0.734	0.111	0.729	0.137
27	3200	3.616	0.580	0.609	2.594	0.503	0.135	0.704	0.106	0.807	0.211	0.721	0.103	0.725	0.135
27	1600	2.856	0.475	0.485	2.103	0.438	0.115	0.642	0.101	0.741	0.194	0.686	0.102	0.665	0.123
27	815	2.813	0.439	0.491	2.232	0.460	0.119	0.661	0.102	0.745	0.187	0.656	0.096	0.647	0.117
27	750	2.692	0.414	0.507	2.087	0.429	0.125	0.653	0.098	0.754	0.199	0.652	0.097	0.609	0.110
28	4223	4.541	1.040	0.806	3.457	0.693	0.182	0.899	0.134	1.009	0.251	0.820	0.122	0.833	0.152
28	3800	4.010	0.750	0.717	3.096	0.593	0.153	0.798	0.121	0.887	0.229	0.769	0.112	0.766	0.142
28	3300	3.597	0.632	0.683	2.856	0.533	0.143	0.827	0.112	0.864	0.221	0.740	0.112	0.751	0.140
28	2000	2.782	0.514	0.481	2.088	0.410	0.117	0.650	0.102	0.747	0.201	0.663	0.098	0.650	0.122
28	1000	2.728	0.436	0.483	2.074	0.434	0.120	0.647	0.102	0.766	0.199	0.668	0.097	0.647	0.120
28	800	2.649	0.436	0.484	2.173	0.456	0.126	0.646	0.108	0.779	0.197	0.660	0.096	0.629	0.115
30	1500	2.708	0.498	0.470	2.083	0.422	0.123	0.627	0.104	0.770	0.205	0.704	0.099	0.677	0.126
31	1100	2.718	0.458	0.481	2.150	0.438	0.129	0.648	0.104	0.766	0.200	0.667	0.099	0.652	0.121
31	800	2.588	0.696	0.517	2.146	0.449	0.123	0.634	0.103	0.729	0.196	0.624	0.091	0.609	0.109
35	3650	3.931	0.557	0.655	2.873	0.569	0.141	0.806	0.120	0.915	0.244	0.810	0.121	0.830	0.138
35	3575	3.866	0.502	0.652	2.858	0.559	0.141	0.806	0.118	0.876	0.233	0.784	0.116	0.806	0.135
35	3500	3.749	0.579	0.658	2.718	0.530	0.141	0.711	0.115	0.835	0.215	0.739	0.111	0.763	0.139
35	3450	3.869	0.516	0.638	2.858	0.550	0.144	0.781	0.111	0.861	0.253	0.788	0.117	0.814	0.132
35	3437	3.466	0.529	0.585	2.597	0.496	0.151	0.750	0.114	0.850	0.222	0.745	0.113	0.757	0.134
35	3374	3.596	0.503	0.575	2.501	0.479	0.135	0.701	0.106	0.808	0.220	0.757	0.115	0.785	0.132
35	3325	3.661	0.515	0.566	2.546	0.478	0.135	0.697	0.106	0.842	0.250	0.765	0.115	0.790	0.132
35	3300	3.263	0.438	0.508	2.197	0.408	0.123	0.627	0.091	0.734	0.204	0.719	0.106	0.751	0.126
35	3250	3.058	0.428	0.465	2.123	0.384	0.118	0.558	0.088	0.703	0.195	0.685	0.103	0.707	0.121
35	3200	3.556	0.482	0.612	2.522	0.508	0.138	0.707	0.104	0.818	0.220	0.760	0.112	0.745	0.125
35	3150	3.559	0.494	0.604	2.670	0.517	0.130	0.734	0.107	0.829	0.223	0.746	0.111	0.784	0.129
35	3100	3.675	0.499	0.618	2.731	0.533	0.136	0.753	0.114	0.873	0.229	0.789	0.118	0.788	0.131
35	3000	3.568	0.509	0.610	2.662	0.503	0.136	0.741	0.116	0.851	0.224	0.765	0.113	0.793	0.132
35	2750	3.124	0.501	0.522	2.313	0.468	0.131	0.660	0.105	0.783	0.203	0.693	0.105	0.695	0.128

	2500	3.379	0.578	0.627	2.601	0.527	0.148	0.718	0.109	0.829	0.224	0.753	0.113	0.753	0.127
35	2500	3.284	0.532	0.548	2.348	0.481	0.125	0.648	0.102	0.772	0.205	0.694	0.105	0.700	0.125
35	2250	3.143	0.466	0.538	2.314	0.471	0.127	0.684	0.102	0.810	0.216	0.735	0.108	0.740	0.121
35	1500	2.999	0.431	0.523	2.300	0.471	0.119	0.707	0.103	0.814	0.217	0.721	0.107	0.717	0.120
35	1000	3.059	0.410	0.558	2.517	0.484	0.132	0.747	0.113	0.847	0.224	0.749	0.110	0.739	0.120
35	750	2.854	0.376	0.527	2.351	0.495	0.124	0.729	0.106	0.812	0.209	0.705	0.101	0.667	0.112
35	125	1.841	1.548	0.399	1.830	0.386	0.111	0.613	0.096	0.754	0.203	0.652	0.092	0.582	0.090
35	100	1.897	1.711	0.418	1.874	0.402	0.114	0.653	0.103	0.779	0.201	0.671	0.094	0.593	0.092
35	80	1.903	1.708	0.417	1.905	0.412	0.112	0.646	0.099	0.767	0.202	0.660	0.093	0.594	0.095
36	3900	3.577	0.782	0.613	2.648	0.550	0.156	0.760	0.116	0.842	0.241	0.726	0.108	0.741	0.137
36	3600	3.431	0.599	0.573	2.521	0.502	0.144	0.716	0.112	0.836	0.219	0.725	0.109	0.730	0.136
36	3200	3.210	0.522	0.540	2.382	0.443	0.118	0.676	0.099	0.756	0.224	0.705	0.104	0.723	0.134
36	2750	3.047	0.495	0.502	2.221	0.454	0.124	0.663	0.102	0.779	0.207	0.684	0.106	0.708	0.127
36	2000	2.793	0.556	0.457	2.105	0.431	0.123	0.656	0.106	0.786	0.207	0.691	0.103	0.700	0.125
36	1600	2.737	0.624	0.471	2.057	0.423	0.125	0.638	0.101	0.753	0.201	0.663	0.097	0.669	0.120
36	1000	2.783	0.483	0.484	2.149	0.444	0.120	0.660	0.100	0.732	0.200	0.669	0.101	0.686	0.125
36	800	2.665	0.473	0.466	2.119	0.455	0.128	0.680	0.105	0.756	0.200	0.653	0.097	0.637	0.115
36	600	2.554	0.507	0.492	2.041	0.436	0.126	0.660	0.106	0.787	0.216	0.668	0.097	0.627	0.114
37	2482	3.123	0.605	0.540	2.311	0.464	0.127	0.660	0.104	0.807	0.210	0.709	0.104	0.710	0.134
37	2443	2.921	0.543	0.507	2.027	0.424	0.116	0.621	0.095	0.728	0.197	0.675	0.097	0.676	0.126
37	2400	3.081	0.552	0.504	2.194	0.439	0.125	0.633	0.096	0.748	0.201	0.681	0.103	0.706	0.132
37	2350	3.016	0.504	0.491	2.146	0.442	0.124	0.633	0.100	0.745	0.196	0.691	0.101	0.706	0.128
37	2300	3.108	0.546	0.509	2.186	0.478	0.132	0.641	0.109	0.789	0.212	0.708	0.109	0.719	0.134
37	2200	2.987	0.488	0.498	2.170	0.456	0.118	0.628	0.101	0.759	0.202	0.674	0.105	0.711	0.132
37	2000	2.911	0.470	0.498	2.137	0.403	0.115	0.625	0.093	0.736	0.193	0.672	0.101	0.683	0.124
37	1750	2.747	0.510	0.490	2.067	0.434	0.117	0.627	0.098	0.769	0.197	0.691	0.100	0.673	0.123
37	1500	2.752	0.455	0.482	2.131	0.416	0.120	0.635	0.101	0.755	0.202	0.695	0.100	0.681	0.125
37	1200	2.809	0.418	0.506	2.093	0.453	0.124	0.667	0.101	0.766	0.206	0.684	0.104	0.680	0.125
37	1000	2.811	0.412	0.510	2.214	0.450	0.128	0.643	0.102	0.767	0.204	0.669	0.100	0.670	0.125
37	800	2.799	0.382	0.526	2.208	0.444	0.123	0.634	0.107	0.772	0.199	0.675	0.099	0.649	0.121
37	600	2.582	0.503	0.506	2.119	0.463	0.125	0.673	0.106	0.788	0.200	0.663	0.098	0.641	0.111

Table A.3: Ancillary data variables accompanying REE dissolved concentration data in table A.2

Station	Site Name	Lat. °N	Lon. °E	Depth m	Temp. °C	Salinity pss	Oxygen µmol/kg	Mn nmol\kg	He mol/kg	Del3HeC %
6	Menez Gwen	37.842	-31.521	810	8.7896	35.373	190.29		1.82E-09	25.4
6	Menez Gwen	37.842	-31.521	780	9.0438	35.383	189.46		1.79E-09	10.65
6	Menez Gwen	37.842	-31.521	725	9.6808	35.411	189	0.262		
8	Lucky Strike II	37.292	-32.281	1710	4.5788	35.051	246	7.481	1.88E-09	37.22
8	Lucky Strike II	37.292	-32.281	1700	4.591	35.052	246.12	7.483	1.88E-09	32.9
8	Lucky Strike II	37.292	-32.281	1690	4.6198	35.055	245.77	7.423	1.85E-09	26.58
8	Lucky Strike II	37.292	-32.281	1625	4.6614	35.058	245.47	2.949		
8	Lucky Strike II	37.292	-32.281	1200	6.0389	35.187	226.69	0.345		
8	Lucky Strike II	37.292	-32.281	720	9.7727	35.448	189.06	0.277		
8	Lucky Strike II	37.292	-32.281	550	11.301	35.513	196.92	0.301		
8	Lucky Strike II	37.292	-32.281	150	15.85	36.131	216.01			
8	Lucky Strike II	37.292	-32.281	80	17.205	36.203	217.76	0.701		
9	Saldanha	36.565	-33.43	2210	3.9413	35.009	252.28	2.184		
9	Saldanha	36.565	-33.43	2200	3.9421	35.009	252.38		1.82E-09	9.75
9	Saldanha	36.565	-33.43	1800	4.4749	35.061	248.54	0.964		
9	Saldanha	36.565	-33.43	1500	5.4249	35.183	237.27	0.406		
9	Saldanha	36.565	-33.43	1200	7.1107	35.414	214.55			
10	E off MAR	36.23	-32.652	2475	3.2302	34.952	254.72	0.354		
10	E off MAR	36.23	-32.652	2450	3.2273	34.952	254.78			
10	E off MAR	36.23	-32.652	2380	3.2802	34.955	255.4	0.341		
10	E off MAR	36.23	-32.652	2000	3.8715	34.999	255.64	0.351		
10	E off MAR	36.23	-32.652	1500	5.4305	35.182	237.32	0.334		
10	E off MAR	36.23	-32.652	780	9.7123	35.536	186.99	0.324		
10	E off MAR	36.23	-32.652	540	11.342	35.558	198.9			
11	E off MAR	36.23	-31.652	2874	2.9402	34.941	249.31			
11	E off MAR	36.23	-31.652	2774	2.9789	34.942	250.8			
11	E off MAR	36.23	-31.652	2050	3.7196	34.982	257.14			
11	E off MAR	36.23	-31.652	1800	4.2951	35.044	251.48			
11	E off MAR	36.23	-31.652	1400	5.7723	35.234	232.87			
11	E off MAR	36.23	-31.652	830	9.6985	35.573	187.07			
11	E off MAR	36.23	-31.652	600	10.913	35.526	196.99			
12	Rainbow Close E	36.23	-33.527	2350	3.939	35.008	251.26	5.696		

12	Rainbow Close E	36.23	-33.527	2320	3.9373	35.009	251.17	5.592	1.82E-09	11.3
12	Rainbow Close E	36.23	-33.527	2200	3.9354	35.01	251.55	6.236	1.83E-09	11.42
12	Rainbow Close E	36.23	-33.527	2150	3.9407	35.011	251.59	6.411	1.82E-09	10.72
12	Rainbow Close E	36.23	-33.527	2100	3.9427	35.011	251.53	6.353	1.82E-09	11.32
12	Rainbow Close E	36.23	-33.527	2000	4.3624	35.058	248.49	5.387	1.81E-09	9.87
12	Rainbow Close E	36.23	-33.527	1500	5.2269	35.163	238.89	0.725	1.8E-09	8.89
12	Rainbow Close E	36.23	-33.527	1000	7.3812	35.372	210.24			
12	Rainbow Close E	36.23	-33.527	720	9.6988	35.43	188.66			
12	Rainbow Close E	36.23	-33.527	550	11.562	35.556	196.71			
12	Rainbow Close E	36.23	-33.527	70	18.354	36.272	219.73			
13	Rainbow Close W	36.23	-34.236	2325	3.8321	34.999	252.88	3.106	1.82E-09	10.06
13	Rainbow Close W	36.23	-34.236	2200	3.8448	35.001	252.72	3.693	1.82E-09	10
13	Rainbow Close W	36.23	-34.236	2100	3.9071	35.008	252.46	3.950	1.82E-09	10.25
13	Rainbow Close W	36.23	-34.236	2000	3.9908	35.017	251.8	3.972	1.82E-09	10.49
13	Rainbow Close W	36.23	-34.236	1750	4.4624	35.069	247.15	2.193	1.82E-09	9.64
13	Rainbow Close W	36.23	-34.236	1500	5.2912	35.171	237.66	1.011	1.8E-09	8.7
13	Rainbow Close W	36.23	-34.236	1000	8.2013	35.443	197.26			
13	Rainbow Close W	36.23	-34.236	850	9.149	35.47	185.77			
13	Rainbow Close W	36.23	-34.236	700	10.138	35.454	181.2			
13	Rainbow Close W	36.23	-34.236	300	14.273	35.883	211.82			
14	Rainbow Close N	35.946	-34.154	2611	3.6313	34.977	258.14	2.336		
14	Rainbow Close N	35.946	-34.154	2550	3.6288	34.977	258.4	2.332		
14	Rainbow Close N	35.946	-34.154	2450	3.6652	34.98	258.74	2.414	1.82E-09	9.21
14	Rainbow Close N	35.946	-34.154	2260	4.0178	35.018	255.27		1.82E-09	9.37
14	Rainbow Close N	35.946	-34.154	2250	4.1196	35.029	254.32	2.420	1.81E-09	9.38
14	Rainbow Close N	35.946	-34.154	2100	4.1417	35.031	254.14		1.82E-09	10.04
14	Rainbow Close N	35.946	-34.154	1700	4.1848	35.036	253.71	1.720		
14	Rainbow Close N	35.946	-34.154	1500	4.2469	35.043	253	1.333	1.79E-09	7.37
14	Rainbow Close N	35.946	-34.154	1300	4.6214	35.084	249.45	0.895		
14	Rainbow Close N	35.946	-34.154	960	5.4914	35.191	238.29			
14	Rainbow Close N	35.946	-34.154	725	5.946	35.243	231.74			
14	Rainbow Close N	35.946	-34.154	400	9.9136	35.456	186.99			
14	Rainbow Close N	35.946	-34.154	80	18.183	36.267	220.86			
15	Rainbow Close S	35.946	-34.154	2350	3.6396	34.98	254.61	0.620		
15	Rainbow Close S	35.946	-34.154	2100	3.7515	34.991	254.75		1.82E-09	8.45
15	Rainbow Close S	35.946	-34.154	1950	4.0067	35.019	251.65	3.120	1.82E-09	9.7

15	Rainbow Close S	35.946	-34.154	1925	4.0813	35.027	250.82	2.881	1.82E-09	9.55
15	Rainbow Close S	35.946	-34.154	1900	4.1226	35.031	250.47		1.82E-09	9.58
15	Rainbow Close S	35.946	-34.154	1860	4.1861	35.039	249.79	2.672	1.82E-09	9.97
15	Rainbow Close S	35.946	-34.154	1730	4.5198	35.076	246.23	1.291	1.81E-09	9.34
15	Rainbow Close S	35.946	-34.154	1400	5.5534	35.203	234.66	0.361		
15	Rainbow Close S	35.946	-34.154	850	8.9645	35.445	189.56	0.269		
16	Rainbow Vent	36.23	-33.902	2280	3.6861	34.985	253.82			
16	Rainbow Vent	36.23	-33.902	2240	3.7011	34.986	253.99	0.648	1.82E-09	8.46
16	Rainbow Vent	36.23	-33.902	2200	3.7332	34.99	253.84		1.82E-09	8.79
16	Rainbow Vent	36.23	-33.902	2175	3.7559	34.991	253.61		1.86E-09	24.75
16	Rainbow Vent	36.23	-33.902	2150	3.7791	34.994	253.26	296.754	1.82E-09	10.66
16	Rainbow Vent	36.23	-33.902	2100	3.8179	34.998	253.3	178.328	1.82E-09	9.98
16	Rainbow Vent	36.23	-33.902	2000	3.9025	35.008	252.82		1.82E-09	11.99
16	Rainbow Vent	36.23	-33.902	1950	3.9321	35.011	252.18	6.588	1.82E-09	11
16	Rainbow Vent	36.23	-33.902	1900	4.0173	35.02	251.37		1.82E-09	10.2
16	Rainbow Vent	36.23	-33.902	1800	4.2886	35.049	248.8		1.82E-09	9.36
16	Rainbow Vent	36.23	-33.902	1400	5.7769	35.228	231.9		1.8E-09	7.4
16	Rainbow Vent	36.23	-33.902	1100	7.4957	35.43	209.02			
16	Rainbow Vent	36.23	-33.902	700	10.241	35.462	188.87			
16	Rainbow Vent	36.23	-33.902	500	11.889	35.593	196.83		1.76E-09	1.92
16	Rainbow Vent	36.23	-33.902	300	14.082	35.855	210.57		1.72E-09	-0.41
16	Rainbow Vent	36.23	-33.902	175	15.627	36.112	206.63			
16	Rainbow Vent	36.23	-33.902	120	16.22	36.21	206.62			
16	Rainbow Vent	36.23	-33.902	60	18.89	36.276	226.02			
16	Rainbow Vent	36.23	-33.902	20	19.024	36.283	228.65			
18	Rainbow N Bonus	36.381	-33.694	2550	3.7219	34.986	253.08	1.125		
18	Rainbow N Bonus	36.381	-33.694	2400	3.7084	34.986	253.46		1.83E-09	7.99
18	Rainbow N Bonus	36.381	-33.694	2300	3.722	34.988	253.53	2.385	1.83E-09	8.35
18	Rainbow N Bonus	36.381	-33.694	2200	3.7854	34.995	253.31	3.600	1.83E-09	8.47
18	Rainbow N Bonus	36.381	-33.694	2050	3.9237	35.009	252.23	4.862	1.83E-09	10.42
18	Rainbow N Bonus	36.381	-33.694	1800	4.392	35.061	247.93	2.945	1.82E-09	9.23
18	Rainbow N Bonus	36.381	-33.694	1200	6.9809	35.38	216.04			
18	Rainbow N Bonus	36.381	-33.694	690	10.066	35.476	185.89			
18	Rainbow N Bonus	36.381	-33.694	500	11.745	35.57	199.53			
38	Rainbow II	36.23	-33.902	2275	3.7942	34.994	253.75		1.83E-09	10.43
38	Rainbow II	36.23	-33.902	2274	3.7894	34.993	253.83		1.84E-09	18.13

38	Rainbow II	36.23	-33.902	2268	3.7812	34.993	253.61		1.82E-09	9.96
38	Rainbow II	36.23	-33.902	2257	3.788	34.994	253.63		1.82E-09	9.55
38	Rainbow II	36.23	-33.902	2139	3.7986	34.996	253.46		1.82E-09	11.5
38	Rainbow II	36.23	-33.902	2058	3.846	35.001	253.3		1.83E-09	11.76
38	Rainbow II	36.23	-33.902	1966	3.9484	35.012	252.37		1.83E-09	13.36
38	Rainbow II	36.23	-33.902	1925	3.9468	35.012	252.23		1.83E-09	12.85
38	Rainbow II	36.23	-33.902	1884	3.9786	35.016	252.22			
38	Rainbow II	36.23	-33.902	1800	4.3005	35.051	248.93		1.82E-09	9.82
38	Rainbow II	36.23	-33.902	1500	5.2676	35.167	238.55			
38	Rainbow II	36.23	-33.902	1300	6.2359	35.288	225.91			
38	Rainbow II	36.23	-33.902	770	9.6014	35.428	188.8			
20	S-OH1	34.533	-36.85	2250	3.5056	34.977	251.83	0.225		
20	S-OH1	34.533	-36.85	2050	3.6035	34.987	252.54	0.346	1.83E-09	8.57
20	S-OH1	34.533	-36.85	960	7.5898	35.416	201.49	0.104		
20	S-OH1	34.533	-36.85	650	9.5596	35.295	169.45	0.170		
21	Hayes Fracture Zone	33.605	-38.23	4375	2.8496	34.931	240.02			
21	Hayes Fracture Zone	33.605	-38.23	3550	2.797	34.933	240.87		1.84E-09	4.53
21	Hayes Fracture Zone	33.605	-38.23	3020	2.9034	34.941	245.5	0.261		
21	Hayes Fracture Zone	33.605	-38.23	3020	2.9036	34.941	245.68	0.261		
21	Hayes Fracture Zone	33.605	-38.23	1900	4.0297	35.03	248.29			
21	Hayes Fracture Zone	33.605	-38.23	835	9.8189	35.494	179.64	0.112		
23	Lost City	30.124	-42.12	762	10.233	35.418	171.32	0.125		
23	Lost City	30.124	-42.12	743	10.273	35.42	171.19	0.137	1.8E-09	6.09
23	Lost City	30.124	-42.12	737	10.287	35.421	171.42	0.131		
23	Lost City	30.124	-42.12	730	10.289	35.422	171.51		1.8E-09	8.88
23	Lost City	30.124	-42.12	724	10.363	35.425	171.88	0.126		
23	Lost City	30.124	-42.12	700	10.574	35.435	173.59	0.131		
23	Lost City	30.124	-42.12	600	12.412	35.645	177.75	0.116		
24	Broken Spur	29.169	-43.171	3015	2.9268	34.946	243.44	0.327		
24	Broken Spur	29.169	-43.171	2982	2.9291	34.946	243.49	0.410		
24	Broken Spur	29.169	-43.171	2879	2.9475	34.948	244.24	4.671	1.87E-09	15.76
24	Broken Spur	29.169	-43.171	2863	2.9469	34.947	244.09	9.011		
24	Broken Spur	29.169	-43.171	2843	2.9616	34.948	244.23	11.236	1.9E-09	29.42
24	Broken Spur	29.169	-43.171	2838	2.9745	34.949	244.46	2.812		
24	Broken Spur	29.169	-43.171	2815	2.9833	34.949	244.58		1.92E-09	38.02
24	Broken Spur	29.169	-43.171	2800	2.9814	34.949	244.49			

24	Broken Spur	29.169	-43.171	2794	2.9799	34.949	244.63		1.91E-09	34.93
24	Broken Spur	29.169	-43.171	2751	3.0035	34.952	245			
24	Broken Spur	29.169	-43.171	2000	3.5902	35.004	247.42	0.000		
24	Broken Spur	29.169	-43.171	1500	4.9181	35.152	233.16	0.155		
24	Broken Spur	29.169	-43.171	700	9.6886	35.385	170.49	0.151		
24	Broken Spur	29.169	-43.171	300	15.918	36.16	189.98	0.218		
24	Broken Spur	29.169	-43.171	150	18.088	36.487	199.58	0.506		
26	TAG Close N	26.36	-44.675	3790	2.681	34.923	242.31		1.86E-09	5.08
26	TAG Close N	26.36	-44.675	3490	2.6516	34.924	242.25	2.465		
27	TAG Close S	25.93	-45.019	3200	2.7086	34.931	240.98	0.710	1.84E-09	3.98
27	TAG Close S	25.93	-45.019	1600	4.8991	35.133	228.29		1.81E-09	6.54
27	TAG Close S	25.93	-45.019	815	8.8535	35.262	156.93	0.146		
27	TAG Close S	25.93	-45.019	750	10.202	35.404	160.32			
28	W off MAR	26.86	-47.23	4223	2.3447	34.895	244	0.148	1.85E-09	3.13
28	W off MAR	26.86	-47.23	3800	2.3768	34.901	243.97		1.84E-09	3.8
28	W off MAR	26.86	-47.23	3300	2.5684	34.92	242.49		1.84E-09	4.09
28	W off MAR	26.86	-47.23	2000	3.598	35.009	242.36			
28	W off MAR	26.86	-47.23	1000	6.9534	35.152	184.58	0.133		
28	W off MAR	26.86	-47.23	800	9.5585	35.323	158.02	0.132		
30	TAG Close W	26.215	-45.118	1500	4.9659	35.142	236.14	0.135		
31	TAG Close E	26.029	-44.553	1100	6.7882	35.164	186.75	0.134		
31	TAG Close E	26.029	-44.553	800	9.3109	35.313	156.35	0.122		
35	TAG	26.138	-44.826	3650	2.6672	34.924	249.92			
35	TAG	26.138	-44.826	3575	2.6612	34.924	249.9		1.85E-09	4.57
35	TAG	26.138	-44.826	3500	2.6801	34.926	249.63	3.050	1.85E-09	4.38
35	TAG	26.138	-44.826	3450	2.6818	34.926	249.8	6.057	1.86E-09	11.02
35	TAG	26.138	-44.826	3437	2.6821	34.926	249.82		1.86E-09	10.51
35	TAG	26.138	-44.826	3374	2.6846	34.926	249.49	33.998	1.88E-09	20.04
35	TAG	26.138	-44.826	3325	2.6933	34.928	249.3		1.89E-09	22.43
35	TAG	26.138	-44.826	3300	2.6854	34.926	249.33		1.94E-09	40.13
35	TAG	26.138	-44.826	3250	2.6769	34.925	249.61	12.892	1.95E-09	42.57
35	TAG	26.138	-44.826	3200	2.7379	34.933	248.9		1.87E-09	14.02
35	TAG	26.138	-44.826	3150	2.7883	34.938	248.32		1.85E-09	4.85
35	TAG	26.138	-44.826	3100	2.7955	34.939	247.89		1.85E-09	4.52
35	TAG	26.138	-44.826	3000	2.8219	34.941	248.29		1.85E-09	4.3
35	TAG	26.138	-44.826	2750	2.9596	34.953	249.34		1.84E-09	5.17

	TAG	26.138	-44.826	2500	3.0339	34.961	249.53		1.84E-09	4.92
35	TAG	26.138	-44.826	2500	3.0339	34.961	249.53		1.84E-09	4.92
35	TAG	26.138	-44.826	2250	3.2307	34.979	249.51		1.84E-09	5.71
35	TAG	26.138	-44.826	1500	4.9297	35.141	235.4		1.81E-09	7.32
35	TAG	26.138	-44.826	1000	7.1006	35.164	180.22		1.8E-09	6.08
35	TAG	26.138	-44.826	750	9.9005	35.368	158.03		1.77E-09	6.47
35	TAG	26.138	-44.826	125	22.292	37.114	215.22		1.73E-09	-1.75
35	TAG	26.138	-44.826	100	23.162	37.267	218.12		1.72E-09	-2.06
35	TAG	26.138	-44.826	80	23.155	37.267	217.67		1.72E-09	-2.01
36	TAG N Bonus	26.278	-44.731	3900	2.69	34.923	249.02	0.502	1.84E-09	6
36	TAG N Bonus	26.278	-44.731	3600	2.6566	34.923	249.57	1.120	1.85E-09	6.03
36	TAG N Bonus	26.278	-44.731	3200	2.7186	34.931	249.39	1.664	1.84E-09	6.64
36	TAG N Bonus	26.278	-44.731	2750	2.9133	34.949	249.09	0.433		
36	TAG N Bonus	26.278	-44.731	2000	3.6952	35.026	247.12	0.169		
36	TAG N Bonus	26.278	-44.731	1600	4.8105	35.128	235.13	0.141		
36	TAG N Bonus	26.278	-44.731	1000	6.7874	35.109	176.47	0.138		
36	TAG N Bonus	26.278	-44.731	800	9.2527	35.301	156.61	0.140		
36	TAG N Bonus	26.278	-44.731	600	12.746	35.714	175.57	0.136		
37	TAG Valley Wall	26.131	-44.77	2482	3.0362	34.961	249.73			
37	TAG Valley Wall	26.131	-44.77	2443	3.0438	34.962	249.63	0.221		
37	TAG Valley Wall	26.131	-44.77	2400	3.0753	34.965	249.77			
37	TAG Valley Wall	26.131	-44.77	2350	3.1094	34.968	250.1	0.215		
37	TAG Valley Wall	26.131	-44.77	2300	3.1438	34.971	250.14		1.82E-09	6.04
37	TAG Valley Wall	26.131	-44.77	2200	3.2294	34.979	250.1	0.165		
37	TAG Valley Wall	26.131	-44.77	2000	3.6942	35.023	247.54	0.155		
37	TAG Valley Wall	26.131	-44.77	1750	4.1294	35.063	241.81	0.147		
37	TAG Valley Wall	26.131	-44.77	1500	4.9225	35.141	236.15	0.137		
37	TAG Valley Wall	26.131	-44.77	1200	6.2687	35.209	209.05	0.124		
37	TAG Valley Wall	26.131	-44.77	1000	7.1635	35.172	178.61	0.134		
37	TAG Valley Wall	26.131	-44.77	800	9.3415	35.315	157.44	0.127		
37	TAG Valley Wall	26.131	-44.77	600	12.966	35.74	176.13	0.125		

Table A.4: REE concentration measurements for GEOTRACES inter-calibration. Measurements of the concentrations of REEs in a sample from 2000m depth at the BATS station are compared to those established by Van De Flierdt et al. (2012).

Study	Sample Desc.	La	Ce	Pr	Nd	Sm	Eu	Gd	Tb	Dy	Ho	Er	Tm	Yb	Lu
		pg/g	pg/g	pg/g	pg/g	pg/g	pg/g	pg/g	pg/g	pg/g	pg/g	pg/g	pg/g	pg/g	pg/g
Van de Flierdt et al. (2012)	BATS - 2000m	3.279	0.717	0.568	2.499	0.519	0.138	0.761	0.125	0.943	0.251	0.843	0.126	0.824	0.141
	2 sigma SD	0.388	0.318	0.05	0.176	0.051	0.015	0.083	0.012	0.062	0.015	0.042	0.008	0.043	0.007
This study (319)	BATS - 2000m	3.281	0.593	0.558	2.457	0.483	0.126	0.742	0.108	0.871	0.223	0.770	0.113	0.740	0.125
This study (320)	BATS - 2000m	3.232	0.576	0.543	2.393	0.473	0.124	0.727	0.112	0.871	0.223	0.759	0.113	0.745	0.123

Table A.5: Dissolved Ba concentrations and isotopic values from the JC156 expedition onboard RRS *James Cook*, GEOTRACES GA13.

Station	Lat. °N	Lon. °E	Depth m	$\delta^{138/134}$Ba ‰	2SE ‰	Ba nM	2SE nM
Rainbow (S2)	36.230	33.527	2320	0.456	0.015	52.6	0.1
Rainbow (S2)	36.230	33.527	2200	0.444	0.013	52.3	0.1
Rainbow (S2)	36.230	33.527	2100	0.437	0.013	50.9	0.1
Rainbow (S2)	36.230	33.527	1750	0.483	0.013	50.0	0.1
Rainbow (S2)	36.230	33.527	1500	0.482	0.013	48.5	0.1
Rainbow (S6)	36.230	33.902	2280	0.427	0.021	53.2	0.1
Rainbow (S6)	36.230	33.902	2200	0.433	0.014	53.5	0.1
Rainbow (S6)	36.230	33.902	2175	0.458	0.014	53.5	0.1
Rainbow (S6)	36.230	33.902	2100	0.472	0.012	53.3	0.1
Rainbow (S6)	36.230	33.902	1800	0.489	0.013	50.2	0.1
TAG (S12)	26.138	44.826	3300	0.402	0.016	70.9	0.2
TAG (S12)	26.138	44.826	3250	0.397	0.018	70.0	0.2

A.2 Publication preprints

RaDeCC Reader: Fast, accurate and automated data processing for Radium Delayed Coincidence Counting systems

Sean Selzer[1]*, Amber L. Annett[2], William B. Homoky[1,3]

1. Department of Earth Sciences, University of Oxford, South Parks Road, Oxford, OX1 3AN, UK
2. Ocean and Earth Science, University of Southampton, Waterfront Campus, National Oceanography Centre, European Way, Southampton, SO14 3ZH, UK
3. Present address: School of Earth and Environment, University of Leeds, Leeds, LS2 9JT, UK

*sean.selzer@earth.ox.ac.uk

Code Availability:

RaDeCC Reader program and supporting files can be found on GitHub

Github Repository: (https://github.com/oxradreader/RaDeCC_Reader/releases)

Authorship Statement:

S.S. conceived and wrote the RaDeCC Reader program and A.L.A. and W.B.H. contributed to its design, testing and implementation. A.L.A. provided real sample data files and S.S. carried out the validation experiments. S.S. prepared the manuscript, with edits and contributions throughout from A.L.A. and W.B.H.

Abstract

A Python program is presented to expedite the process of correcting raw data and propagating the related uncertainties from Radium Delayed Coincidence Counting (RaDeCC) instruments. The performance of the program was validated against an established method with real data. Excellent agreement between determinations of excess radium-223, actinium-227, excess radium-224, thorium-228 and radium-226 was achieved, with minor discrepancies in the

results attributed to logical improvements in our implementation. The RaDeCC Reader program is able to process one thousand data files in only a few minutes, and thereby offer distinct advantages in the processing speed combined with reliable accuracy of data processing implementations.

Keywords: Data Processing; Software Engineering; Data Assimilation; Environmental Science; Hydrogeology;

1. Introduction

Radium is a valuable tracer for environmental geochemistry due to the conservative nature of radium in seawater and the predictable rates of decay of its isotopes. Disequilibria between these isotopes can allow the quantification of rates of exchange between natural reservoirs (Cochran, 1982). The development of Radium Delayed Coincidence Counting (RaDeCC) systems has made radium-based studies in aqueous environments more feasible (Moore and Arnold, 1996). For example, radium isotopes are increasingly used to trace, quantify and advance understanding of many fundamental ocean processes in coastal (Moore, 2000; Tamborski et al., 2020), shelf sea (Hendry et al., 2019), open ocean surface (Charette et al., 2007) and deep water settings (Kipp et al., 2018).

To measure the activities of radium-223 and radium-224 in aqueous environments, sample water is commonly pumped through manganese oxide impregnated acrylic or polyethylene fibres (Moore, 1976). These fibres extract radium, its parent isotopes thorium and actinium, and other species with high affinity for MnO_2, from the water via binding to the MnO_2 functional groups present on the fibres. The precise activities of radium isotopes on these fibres can be determined by counting their daughter isotopes radon and polonium using a scintillation

counting technique that is optimally performed by the RaDeCC apparatus (https://www.radecc.com) (Moore and Arnold, 1996).

The RaDeCC system of delayed coincidence counting was originally devised by Giffin *et al.*, (1963) and forms the basis of the RaDeCC apparatus devised by Moore and Arnold, (1996). The RaDeCC apparatus measures the activities of radon isotopes – the nuclides produced from radium decay - emanating from sample fibres over the course of a counting period, herein termed "read". The flow of helium through a closed loop carries this radon between the sample fibre container and the scintillation cell. Radon decay in the scintillation cell produces an alpha particle which is detected, generating a signal which is routed to three channels: total counts, radon-219 and radon-220. The total counts channel records a count when any signal is received. In the radon-219 and radon-220 channels the system looks for a second count, corresponding to the subsequent decay of daughters polonium-215 and polonium-216 (respectively) after a short delay for the signal to stabilise: 0.01 ms for the radon-219 channel and 5.61 ms for the radon-220 channel (Moore and Cai, 2013). After these delays a gate is opened in each channel (5.6 ms and 600 ms for radon-219 and radon-220, respectively; Moore and Arnold, 1996) in which an additional signal of alpha decay is required in order to register a count. During a read the RaDeCC software logs the counts and accumulated counts per minute for each channel at regular user-defined intervals to a text file.

Factors that need to be corrected for in the raw output include: interference between the detector channels for radon-219 and -220 and chance coincidence events; the counting efficiency and background (blank) of each detector; decay that occurred between sampling and measurement; rescaling sample activities to their original sample volumes (Giffin et al., 1963; Moore and Arnold, 1996). The expressions used to propagate uncertainties associated with these corrections were derived by Garcia-Solsona *et al.*, (2008).

The amount of radium parent isotope on the MnO_2 coated fibres determines the rate of production of the radon isotope daughter, and therefore the activity sustained in the flow of helium through a closed loop between sample and the RaDeCC system. The decay of actinium and thorium on the fibres supplements the amount of 'excess' radium-223 and radium-224 that is initially present (creating supported activity) leading to the activities of radon-219 and radon-220 initially measured by the RaDeCC system. These supported activities must be accounted for to accurately determine the excess, or unsupported, activities of radium-223 and radium-224. Finally, there is the ingrowth of radon-222 from its long-lived parent isotope, radium-226, recorded by the total channel. Determining the rate of radon-222 ingrowth can be used to estimate the activity of radium-226 (Geibert et al., 2013).

To perform the necessary raw data correction and uncertainty propagation calculations, many workers construct large Excel spread sheets and individually import their saved read file outputs from RaDeCC apparatus. Although this process allows a very granular view of the raw data and can serve its purpose well, it remains time intensive and large sets of data are susceptible to user-error. A faster, user-defined automation that preserves details of the calculation processes could therefore offer significant improvements to data processing speed and the reliability of outputs. Herein, we present our approach to expedite the process of correcting raw data and propagating the related uncertainties from Radium Delayed Coincidence Counting (RaDeCC) instruments using a newly designed program, RaDeCC Reader. We prove the validity of our new method by comparing results obtained with RaDeCC Reader to those we obtained by a previously established method using real data collected from karstic spring-, coastal- and open-ocean water samples.

2. Theory

2.1 Calculation of excess radium-223 and radium-224 activities

To convert raw decay counting statistics into the activity of radium-223 or radium-224 of a sample, a number of factors must be considered and corrected for. A table of variables and their units is included for reference (Table 1). Uncertainties in the raw counts must also be propagated through each of these corrections to determine uncertainties in final calculated activities.

An erroneously registered count due to chance coincidence events (*Y CC*, in cpm) is the first correction to be made. An erroneous count can be made when a decay event that is unrelated to the isotope of interest occurs while the detector-gate for that isotope's channel is open. These can originate from the background activity in the detectors or the decay of radon-222 while the 219 or 220 channels are open. The counts per minute (cpm) attributed to chance coincidence events are subtracted from the count rate in the relevant channel. Expressions to calculate the fraction of chance coincidence events in each channel (Equations 1,2) were derived by Giffin *et al.* (1963) and were included by Garcia-Solsona *et al.* (2008), where *cpm total, cpm219* and *cpm220* are the counts per minute in the total, 220 and 219 counting channels respectively.

$$Y\ 220\ CC\ \frac{(cpm\ total - cpm220 - cpm219)^2 \times 0.01}{1-[(cpm\ total - cpm220 - cpm219) \times 0.01]} \quad (1)$$

$$Y\ 219\ CC = \frac{(cpm\ total - corr220 - cpm219)^2 \times 0.000093}{1-[(cpm\ total - corr220 - cpm219) \times 0.000093]} \quad (2)$$

These chance coincidence events are then subtracted from the counts per minute in the relevant channel to determine the coincidence corrected counts (*corr220*, *corr219*).

$$corr220 = cpm220 - Y\ 220\ CC \quad (3)$$

$$corr219 = cpm219 - Y\ 219\ CC \quad (4)$$

In certain circumstances the decays associated with radon-219 can be erroneously registered in the 220-channel. This can happen if two atoms of radon-219 decay within the time that the 220 channel is open. Radon-220 can also cause interference in the radon-219 channel since the gate for this channel is open for enough time that 2.55% of radon-220 decay events occur while the

gate is open. Expressions to account for these cross-channel interferences were devised by Giffin et al. (1963) and adapted by Moore and Arnold (1996).

$$final\ 220 = corr220 - \frac{(1.6 \times corr219)^2 \times 0.01}{1+[(1.6 \times corr219)\times 0.01]} \quad (5)$$

$$final\ 219 = corr219 - (corr220\ \times\ 0.0255) \quad (6)$$

In addition, background measurements may be run with MnO_2-coated fibres that were not used for sampling, assessing any counts due to contamination on fibre or within the RaDeCC apparatus itself, although the need for a background correction varies with sample type and application. Where required, the background count rate (in cpm) in each channel is averaged over multiple reads for each detector. The averaged background count rate from the applicable detector and channel is then subtracted from *final220* and *final219* before detector efficiencies are accounted for (*bkgcorr224*, *bkgcorr223* respectively; Equations 7,8).

$$bkgcorr224 = final220 - Average\_bkg\_220 \quad (7)$$

$$bkgcorr223 = final219 - Average\_bkg\_219 \quad (8)$$

The detection efficiencies, *E219* and *E220*, are evaluated by measuring the activities of standards with a known amount of radium-223 or radium-224 adsorbed to their fibres and comparing these measured activities (in cpm) to their known activities (in dpm) after corrections for decay since manufacture (Equations 9,10). These standards are made by adsorbing known activities of thorium-232 or actinium-227 in secular equilibrium with their daughter isotopes, radium-224 and radium-223 respectively.

$$E220 = \frac{final220\ (standard)}{thorium-232} \quad (9)$$

$$E219 = \frac{final219\ (standard)}{actinium-227} \quad (10)$$

Alternatively *E219* can be determined from *E220* using equations 11 and 12 (Moore and Cai, 2013).

$$Ratio_{E219/E220} = \frac{P_{219} \times (1 - L_{219})}{P_{220} \times (1 - L_{220})} \quad (11)$$

$$E219 = E220 \times Ratio_{E219/E220} \quad (12)$$

In which *E220* is the 220-channel system efficiency, *P* is the probability of the radon isotope decaying in the counting cell and *L* is the fractional loss due to delay and window settings. Fraction loss (*L*) will depend on the default RaDeCC apparatus time constants or those set by the operator as described by Moore and Cai (2013). The ratio *E219/E220* for the RaDeCC with default settings and normal configuration is 0.91 (Moore and Cai, 2013).

The counts per minute due to radon-219 and radon-220 are converted to disintegrations per minute (dpm) by dividing *final220* or *final219* by the detection efficiency of the channel, (*E219* or *E220*, respectively; Equations 13,14) (Giffin et al., 1963; Moore and Arnold, 1996).

$$dpm224 = \frac{bkgcorr224}{E220} \quad (13)$$

$$dpm223 = \frac{bkgcorr223}{E219} \quad (14)$$

Finally, the *dpm* values are divided by the sample *volume* (or mass) to produce the volume-corrected radium-223 (*vdpm223*) and radium-224 (*vdpm224*) sample activities (both in dpm m^{-3}) for each read (Equations 15,16).

$$\mathrm{vdpm224} = \frac{dpm224}{Volume} \times 1000 \quad (15)$$

$$vdpm223 = \frac{dpm223}{Volume} \times 1000 \quad (16)$$

To obtain the excess radium-224 and radium-223 activities of the samples at the time of sampling, two further factors must be accounted for: decay of the isotope between sampling

and measurement and any activity supported by the parent isotope. The respective parent or supporting isotopes of radium-223 and radium-224 are actinium-227 and thorium-228.

In order to distinguish the activities of parent and daughter isotopes, each sample must be analysed multiple times at different intervals relative to the time of collection. The 1st interval read, performed as soon after sampling as possible, is a measurement of radium-223 and radium-224 activity, this will be a combination of excess and supported activities. A 2nd interval, 7-10 days after sampling, can provide a more accurate radium-223 activity due to reduced interference from radium-224 and radon-220 decay (Moore, 2008), and is essential in instances where the 220/219 count rate is greater than 10, or greater than 4 and the 220 channel exceeds 5 cpm (Diego Feliu et al. 2020). Eventually, >99% of measured radium-224 and radium-223 activities will be supported by their parent isotopes. This occurs after 25 days for radium-224 and after 80 days for radium-223, and dictates the timing of 3rd and 4th intervals. In effect, 3rd and 4th interval reads provide an indirect measurement of these parent isotope activities, thorium-228 and actinium-227 respectively.

$$^{223}_{xs}Ra = \frac{^{223}_{i}Ra - ^{223}_{s}Ra}{e^{-\lambda_{223}t}} \quad (17)$$

$$^{224}_{xs}Ra = \frac{^{224}_{i}Ra - ^{224}_{s}Ra}{e^{-\lambda_{224}t}} \quad (18)$$

Excess radium-224 and excess radium-223 at the time of sampling is then calculated via equations 17 and 18, where $^{223}_{i}Ra$ and $^{224}_{i}Ra$ are the radium-223 activity of the 1st or 2nd interval read and the radium-224 activity of the 1st interval read, $^{223}_{s}Ra$ the activity supported by actinium-227 decay (4th interval) and $^{224}_{s}Ra$ the radium-224 activity supported by thorium-228 decay (3rd interval). The time between sampling (in days) and the first measurement of each isotope is denoted by *t* and the respective decay constants of radium-223 and radium-224 by λ_{223} and λ_{224}. For all calculations, including detector efficiencies, error propagation follows the equations presented in Garcia-Solsona et al. (2008).

2.2 Calculation of radium-226 activity

The activity of long-lived radium-226 is measured indirectly via the rate of ingrowth of its decay product, radon-222. The half-life of radon-222 is 3.8 days, so as radium-226 in the sample decays over the course of a read, radon-222 accumulates in the system. This accumulation is seen in the total channel, with counts in the total channel increasing throughout the read in proportion to the radium-226 activity of the sample (Geibert et al. 2013). The *slope of cpm total* versus time during a run thus provides a measure of the radium-226 activity of the sample, based on the conversion factor *'m'*, which has a theoretical value of $1.80 \pm 0.07 \cdot 10^{-4}$ min^{-1} (Diego-Feliu et al. 2020).

Each RaDeCC detector must also be calibrated by measuring a standard with known radium-226 activity, calculated as for *E220* in equation 7. Volume-corrected radium-226 activity of the sample (*vdpm*226, in dpm/m^3) is then calculated using equation 20, where '$vdpm226_{initial}$' is the initial volume corrected radium-226 activity (in cpm/m^3; equation 19) and '*E226*' is the efficiency of system in determining radium-226 activity. This method was devised by Geibert et al., (2013) and modified by Diego-Feliu et al., (2020).

$$vdpm226_{initial} = \frac{slope\ of\ cpm\ total}{m} \div Volume \times 1000 \quad (19)$$

$$vdpm226 = \frac{vdpm226_{initial}}{E226} \quad (20)$$

3. Implementation: The RaDeCC Reader Program

The RaDeCC Reader program is a collection of python scripts that quickly processes RaDeCC output files. The program works from a single folder containing all read files including those of standards and backgrounds (or blanks), sample log sheets and a small amount of user input via a graphical user interface (GUI; Figure 1). From this folder, it creates an organised directory of read files, a table of calculated detector efficiencies with propagated uncertainties and a table of corrected excess radium-223, excess radium-224, thorium-228, actinium-227 and radium-

226 activities (in dpm/m^3) (Figure 2). The tabulated outputs also detail each correction and its propagated uncertainty for each read of each sample. Additional transparency is provided by plots of counts-per-minute vs. time for the 219, 220 and total channels, produced for each read (Figure 3) as well as plots depicting any anomalous spikes that have been automatically removed. Data quality warnings and errors are also flagged alongside calculated results in output tables as outlined in Section 3.2.2.

3.1 Essential information for the program

The RaDeCC Reader program receives information in three ways: text files output by the RaDeCC apparatus, the sampling log-sheet and the graphical user interface (GUI). Information entered into the GUI entry fields are used to aid the program in file-handling and provide standard and instrument specific parameters required for the data corrections and uncertainty propagations. Once completed these GUI entries can be saved by the user and reloaded for subsequent runs of the program.

3.1.1 Directories

To start, the user sets up the following folder and contents:

C:/.../Main_folder/Read_files_and_logsheet/

C:/.../Main_folder/RaDeCC_Reader_Scripts/

The first entry fields in the GUI are the input and output directories (Figure 1a) and the logsheet. The input directory is where the program will find all the input read files and the logsheet. The output directory is where the program will place the organised read files, the logsheet file and output files.

3.1.2 Logsheets: Linear and Branched sample sets

Logsheets form the basis of the eventual output files, in which all the metadata contained within a logsheet will be included. A logsheet must contain information that is essential to data correction calculations: sample names, sample volumes and mid-point sampling times; as well

as any sub-sample names (for herein so-called ‘branched’ datasets) if applicable. There should be a column displaying each of these variables in a logsheet. Any additional information contained in a logsheet (e.g. the latitude, longitude and depth of individual samples) is preserved in the output files and will not interfere with the calculations but may prove useful for later analysis. An example logsheet file is included in the Supplementary Information. The date format convention for read files and the logsheet must be consistent and can be indicated via a tickbox in the GUI.

Data outputs can be organised differently to assist the user. How data outputs will be organised depends on whether or not the user indicates a sample set includes sub-samples. Herein sample sets that do not contain sub-samples (e.g. multiple locations sampled once, or time series at a single location) are termed ‘linear’. Sample sets with sub-samples (e.g. multiple locations each sampled at multiple times, or a series of depth profiles) are termed ‘branched’. In the case of a sample set where some samples have sub-samples, this could be processed using the branched setting. In this case, samples without subsamples would be seen as samples with one subsample each. The distinction between linear and branched can be indicated via a tickbox in the GUI.

3.1.3 File naming and identifiers

In order to acquire raw data, the program requires the text files generated by the RaDeCC systems for sample, standard and (if required) background reads. The formatting of these filenames needs to be consistent and must include information on the sample (and sub-sample) name and the detector used. For example, ‘1-StnX001-A001-010220-det1.txt’, contains the sample name ‘StnX001’, subsample name ‘A001’ and the detector name ‘det1’. The number ‘1’ at the start of the file name designates the read interval (e.g. 1 for radium-224 quantification), although this is recorded by the program it is not used in excess calculations. Instead, the program assigns a read interval automatically by calculating the elapsed time between sampling and RaDeCC analysis. It is important to note that sample and sub-sample

names must be distinct from each other, no sample name should contain another sample name within it (StnX1 and StnX10, for example). Once the first panel of entries is completed in the GUI (Figure 1a), these entries are checked by the program, and if verified, the user can proceed to the second panel in the GUI to assign details of the standards and backgrounds.

3.1.4 Information on detectors, standards and backgrounds

Upon verified completion of the first panel of entries in the GUI (Figure 1a), a second panel will appear requesting inputs for individual detectors (names, *E219/E220* ratios, radium-226 slope calibration values and radium-226 system efficiency values) and details specific to individual standards (names, dates of manufacture and initial activity) (Figure 1b). Only an identifying name is requested for background runs. If background measurements are not required then the 'No. of Background Standards' field can be set to '0' in panel 1 of the GUI (Figure 1a). These inputs are all required for the calculation of detector efficiencies and the resulting corrections to the raw data.

3.1.5 Assigning variables

The final GUI entries are the titles of log-sheet columns containing sample name, sub-sample name, sample volume, sample volume error, sampling date and sampling time. These column titles should not contain spaces and must be selected via the drop-down lists that appear in the second panel of the GUI after a log-sheet file is selected in the first (Figure 1b).

Once these details are completed and verified, the user can then proceed to run the RaDeCC Reader. A step-by-step explanation of information input and program setup is also provided in the *Instructions.md* or *Instructions.txt* files in the GitHub repository along with example data to check that the program is functioning properly.

3.2 How it works

3.2.1 Data, directories and detector efficiencies

297 Upon clicking the 'Run RaDeCC Reader' button, the directory building function will create an
298 organised directory of read and logsheet files using input from the GUI as well as sample and
299 sub-sample names in the logsheet.
300 The directory_filler function will then use each folder/sub-folder name as a search criteria and
301 search through the main folder of reads for files that match each folder name and then
302 subsample. When a match occurs, the file is copied to the folder it was matched with. Any files
303 not matching sample/sub-sample folder names or standard or background folder names will be
304 copied to the miscellaneous (*misc.*) folder.
305 Once the directory is built and populated with reads, a dataframe of detector efficiencies is
306 produced. The efficiencies calculation function searches through the appropriate standard and
307 background subfolders for each detector specified by the user in the GUI. The program creates
308 a dataframe of corrected reads for each standard with the appropriate channel efficiency for
309 each read calculated as well as a dataframe of background reads. These offer the user a more
310 granular view of read results when validating the average efficiencies displayed in the summary
311 efficiencies dataframe. These four dataframes are automatically exported as .csv files. The
312 detector efficiency of the 219-channel for each detector is calculated using the actinium-227
313 standard as well as the method devised by Moore and Cai (2013), based on system volume and
314 220-channel efficiency using the thorium-232 standard. In parallel, the two separate 219-
315 channel efficiencies are used to calculate two separate final corrected radium-223 values. Use
316 of radium-223 values based on the Moore and Cai (2013) method requires verification of an
317 *E219/E220* ratio (Section 3.1.4): the Reader includes the value determined by Moore and Cai
318 for the standard RaDeCC configuration as a default.
319 The program uses the sample name (and sub-sample name) in each row of the logsheet as
320 search criteria, finding the corresponding read files to scan. Using the data scanned from the
321 read files the program performs the appropriate corrections and related propagation of

uncertainties. For each read, these new corrected values along with their uncertainties are combined with the sample's corresponding metadata from the logsheet and entered as a new row in the read results dataframe.

3.2.2 First level corrections

Every read file for each sample/sub-sample is scanned, the interval logged data is extracted from the text file, and the first level of corrections are performed (Garcia-Solsona et al., 2008). These include:

- Chance coincidence counts per minute in the 219 and 220 channels (*Y 219 CC, Y 220 CC*)
- Corrections for 220 interference in the 219 channel (to give *final*219)
- Corrections for 219 interference in the 220 channel (to give *final*220)
- Total counts corrected for counts due to 219 or 220 (to give *corr total*)

As the program scans through a read, each interval is evaluated using the guidelines outlined by Diego-Feliu et al., (2020) for the measurement and quantification of radium-223 and radium-224 (Figure 4). For each read, the program records the percentage of intervals for which quantification of radium-223 or radium-224 is not recommended and logs these percentages in an error column of the read results dataframe. This allows the user to quickly establish whether an anomalous result might be due to cross-talk or other interferences. The scanning of read files is not obstructed by files with lines enclosed by quotation marks or extra lines added by a pause function.

Spike removal: If the number of counts in either the total, 219- or 220-channel during one time interval is higher than the next interval by more than the *'Spike sensitivity'* constant the program removes this time interval as it is considered to contain a counting anomaly - likely due to a spike in the electrical supply to the RaDeCC apparatus. If an anomaly is removed, the value of the anomaly is recorded in the *Spike_Value* column of the results dataframe. The calculated counts per minute values of each interval are then averaged over the whole read.

The *'Spike sensitivity'* constant is set at 10^6 counts by default, meaning that spike removal is inactive, but may be activated via a change in the *'Spike sensitivity'* constant value by the user to allow for higher or lower sample activities.

Radium-226 estimates from radon-222 ingrowth and Raw Data Plots: The rate of radon-222 ingrowth seen in the Total channel (*cpm total*) is calculated in order to estimate the activity of radium-226 in the sample. The equilibration time variable (0 minutes as default) allows the user to set the time required for the radon-222 activity throughout the RaDeCC circuit to accumulate sufficiently to be detectable in the total channel. The time interval is set by the user in the GUI prior to initiating a read and is the number of minutes between the software logging each line of the output file (Figure 1a). The time interval is used by the RaDeCC Reader program here to decide how many lines to miss at the start of the read file before calculating radon-222 ingrowth and therefore the radium-226 activity estimate. A plot of read-time vs. total counts per minute (*cpm total*), 219 channel counts per minute (*cpm*219) and 220 channel counts per minute (*cpm*220) for each read is saved in the '*Read Plots*' folder (Figure 3.). These plots provide a graphical view for raw data quality assessment by the user, for instance to evaluate system stability as well as the build-up of radon-222 during each read. Estimated radium-226 activity will only be calculated from reads with durations >600 minutes, shorter reads may be less reliable due to the short period for ingrowth of radon-222 to occur. In the event of a short read, the '*Err226_short_read*' error is logged in the read results dataframe.

3.2.3 Second level corrections and output

After the first level of corrections is complete, generating values for *final*219, *final*220 and *cpm total* for radium-226 estimation, the read results dataframe containing these new values is passed on to the second level of calculations. Second level corrections expand the read results dataframe with the calculated values and propagated uncertainties as described by Garcia-Solsona *et al.* (2008). Second level corrections include:

- Detector background corrections in all channels
- Corrections for detector channel efficiencies
- Corrections for sample volume, producing volume corrected activity (*vdpm*)

These final calculations complete the series of corrections and uncertainty propagations providing disintegrations per minute per 1000 L (dpm/m^3) for radium-223 and radium-224 as well as an estimate of radium-226 activity (dpm/m^3) for each read. These individual read results are saved as a table in comma-separated-value (.csv) format before being combined to calculate sample activities.

3.2.4 Sample activity calculations and outputs

The final stage of calculations is the combination of read-specific values calculated in the results dataframe to calculate excess radium-223, excess radium-224, radium-226, actinium-227 and thorium-228 activities for each sample.

The 2^{nd} and 4^{th} interval reads of each sample/sub-sample are combined using equation 13 to calculate excess radium-223. For the calculation of excess radium-224, 1^{st} and 3^{rd} interval reads are combined using equation 14. In many circumstances 1st interval reads are sufficient to accurately quantify radium-223 activity, so if 2^{nd} interval reads are unavailable, excess radium-223 is calculated using 1^{st} reads. Similarly, if 3^{rd} reads are unavailable, excess radium-224 is calculated using 4^{th} interval reads. Actinium-227 activity is essentially the supported radium-223 activity calculated for the 4^{th} (or 3^{rd}) interval read of a sample/sub-sample while thorium-228 is the supported radium-224 activity calculated for the 3^{rd} (or 4^{th}) interval read of a sample/sub-sample. If the results dataframe contains more than one read of a particular sample/sub-sample for a given interval (1^{st}-4^{th}), the average activity of the relevant reads will be used in the calculation. The radium-226 activity of a sample is determined by averaging the radium-226 activity of reads >600 minutes in duration. Any radium-226 activities that are more than one standard deviation from the mean are then removed and a new average is calculated.

The results of these final calculations are tabulated in a summary dataframe and exported as a comma-separated value (.csv) file. Any read-interval substitutions in the calculation of excess activities are logged in the error column of this summary dataframe alongside any errors raised using the logic outlined by Diego-Feliu et al. (2020) for all read results used.

4. Validation

4.1 Experimental Design

To evaluate the performance and accuracy of the RaDeCC Reader program, the processing time and corrected data outputs from real sample, standard and background determinations by RaDeCC instruments were compared to those derived from a Microsoft Excel implementation of the calculations outlined by Garcia-Solsona et al. (2008) and Geibert et al. (2013).

A total of 208 raw data files from 44 samples were used for the purpose of this evaluation. Open ocean samples (106 raw data files, 19 seawater samples) were collected from 60-100 litres of seawater using MnO_2 impregnated fibres, during the along southwest Greenland during the ICY-LAB expedition aboard RRS *Discovery* in 2017 (Hendry et al., 2019). Coastal surface seawater samples (~0.5 m depth) (40 raw data files, 9 surface samples) and karstic spring-water samples (62 raw data files, 16 samples) were collected offshore of the Calanques of Marseille-Cassis on 27–28 March 2018 aboard the R/V Antédon II, by trace-metal clean submersible pump and scuba-divers respectively (Tamborski et al., 2020).

The range of 219, 220 and total count rates (219: 0 - 6.3 cpm, 220: 0 – 16.8 cpm, total: 0 – 35 cpm) and counting times (60-4002 minutes) tested here, are realistic ranges encountered in submarine aquifer and open ocean fieldwork and 35% of the maximum quantification limit of the RaDeCC apparatus (Diego-Feliu et al., 2020). These samples, previously published in Hendry *et al*. (2019) and Tamborski et al. (2020), were calibrated using standards prepared at LEGOS, OMP (Toulouse, France) with solutions of ^{228}Th (in equilibrium with ^{232}Th) and ^{227}Ac obtained from the International Atomic Energy Agency (Monte Carlo, Monaco). Here we

repeat their raw data processing using our standardised Excel-based methodology and compare the outputs to those obtained using the RaDeCC Reader. This approach allows any disparity in results to be attributed to differences in implementation. Nine variables were compared: the corrected activities of excess radium-223, actinium-227, excess radium-224, thorium-228 and radium-226, and the propagated uncertainties for excess radium-223, actinium-227, excess radium-224 and thorium-228.

4.2 Results and Discussion:

Implementation time of either method is certain to vary between users. For new users of the RaDeCC Reader time will be needed to name and organise files and prepare logsheets. In this exercise, however, the implementation of the Excel-based methodology took an experienced user over 2 hours to process the outputs from standards, backgrounds and 30 samples; amounting to a total of 233 raw data files. This compared to a processing time of 2 minutes to perform the equivalent functions using the RaDeCC Reader, a time saving that would be magnified with larger datasets or familiarity with the required file naming conventions.

Excellent agreement ($R^2 > 0.99$, Standard Error < 0.02) was seen for the corrected activities and propagated uncertainties of excess radium-223 and excess radium-224 (Figure 5) as well as actinium-227, thorium-228 (Figure 6). The small amount of variance seen, possibly due to a difference in the treatment of background measurements, is an order of magnitude smaller than any propagated uncertainties associated with the activities determined in this study.

Radium-226 activity determined by our Excel method and the RaDeCC Reader also displayed very strong agreement, with greater variance than was seen for the short-lived radium isotopes or their supporting isotopes ($R^2 = 0.99$, Standard Error = 0.02, Figure 6). We attribute this greater variance between methods to the fact that radium-226 activities determined by RaDeCC apparatus are inherently less precise than those determined for excess radium-223, actinium-

227, excess radium-224 and thorium-228. The activity of radium-226 is measured via the ingrowth of its daughter-isotope radon-222 and therefore the slope of the activity in the total channel with time. Many workers may choose not to include a portion of measurements at the start of a read to allow for the partial pressure of radon-222 in the system to accumulate above background. This equilibrium time may not be applied uniformly, whereas the RaDeCC Reader's user defined equilibration time is applied to all reads consistently. The slope in total activity with time is also sensitive to system leaks as well as the length of time a sample is measured for, particularly for samples with low activity, and therefore should be evaluated separately for samples with markedly different total activities.

5. Conclusions

We have developed a program that simplifies and expedites the process of correcting raw RaDeCC data, propagating related uncertainties and calculating the activities of excess radium-223, actinium-227, excess radium-224, thorium-228 and radium-226. With a logsheet and read file names in the required format, the RaDeCC Reader program is capable of processing a substantial real data set in a matter of minutes, and is therefore able to save users considerable time and effort in data processing when compared to previous and widely used Excel-based methodologies. By letting users evaluate their sampling methods and analytical performance more efficiently, the RaDeCC Reader has potential to enhance experimental design, for example, during maritime research expeditions. RaDeCC Reader maintained the accuracy of results attributed to previous methods, and preserved transparency of data processing by displaying the values of each stage of calculation, providing a view of the original raw data via saved plots and flagging results with data quality warnings. We attribute minor discrepancies in calculated excess radium-223, actinium-227, excess radium-224 and thorium-228 activities between methods to a difference in background treatment by the RaDeCC Reader's implementation. This provided no significant changes to the results from samples used in our

test, however the implementation used by RaDeCC Reader mitigated the risk of greater inaccuracies that might have arisen from raw data files containing larger or more frequent counting anomalies.

Acknowledgments:

The authors gratefully acknowledge support from the UK's Natural Environment Research Council who funded S.S. through the Environmental Research Doctoral Training Partnership with University of Oxford, and A.L.A. and W.B.H. through Independent Research Fellowships (NE/P017630/1 and NE/K009532/1). We would like to thank J. Tamborski and P. van Beek who shared their RaDeCC output and sample data to validate the RaDeCC Reader across a wider range of environmental activities.

Computer Code Availability:

RaDeCC Reader, developed by Sean Selzer, Department of Earth Sciences, South Parks Rd, OX1 3AN, Oxford (01865 272000, sean.selzer@earth.ox.ac.uk). First available in 2019.

Hardware Requirements: 2 x 64-bit 2.8 GHz 8.00 GT/s CPUs, 32 GB RAM (or 16 GB of 1600 MHz DDR3 RAM), 300 GB Storage.

Written in Python 3.6, RaDeCC Reader (179 KB) is available on GitHub (https://github.com/oxradreader/RaDeCC_Reader)

References:

Charette, M.A., Gonneea, M.E., Morris, P.J., Fones, G., Planquette, H., Salter, I., Garabato, A.N., 2007. Radium isotopes as tracers of iron sources fueling a Southern Ocean phytoplankton bloom. Deep Sea Res. Part II Top. Stud. Oceanogr. 54, 1989–1998. https://doi.org/10.1016/J.DSR2.2007.06.003

Cochran, J., 1982. The oceanic chemistry of the U- and Th-series nuclides, in: Ivanovich, M., Harmon, R. (Eds.), Uranium Series Disequilibrium: Applications to Environmental

Problems. Clarendon Press, Oxford, pp. 384–431.

Diego-Feliu, M., Rodellas, V., Alorda-Kleinglass, A., Tamborski, J., van Beek, P., Heins, L., Bruach, J.M., Arnold, R., Garcia-Orellana, J., 2020. Guidelines and Limits for the Quantification of Ra Isotopes and Related Radionuclides With the Radium Delayed Coincidence Counter (RaDeCC). J. Geophys. Res. Ocean. 125. https://doi.org/10.1029/2019JC015544

Garcia-Solsona, E., Garcia-Orellana, J., Masqué, P., Dulaiova, H., 2008. Uncertainties associated with 223Ra and 224Ra measurements in water via a Delayed Coincidence Counter (RaDeCC). Mar. Chem. 109, 198–219. https://doi.org/10.1016/j.marchem.2007.11.006

Geibert, W., Rodellas, V., Annett, A., Beek, P. van, Jordi Garcia-Orellana, Hsieh, Y. Te, Masque, P., 2013. 226Ra determination via the rate of 222rn ingrowth with the radium delayed coincidence counter (RaDeCC). Limnol. Oceanogr. Methods 11, 594–603. https://doi.org/10.4319/lom.2013.11.594

Giffin, C., Kaufman, A., Broeker, W., 1963. Delayed Coincidence Counter for the Assay of Actinon and Thoron. J. Geophys. Res. 68, 1749–1757.

Hendry, K.R., Huvenne, V.A.I., Robinson, L.F., Annett, A., Badger, M., Jacobel, A.W., Ng, H.C., Opher, J., Pickering, R.A., Taylor, M.L., Bates, S.L., Cooper, A., Cushman, G.G., Goodwin, C., Hoy, S., Rowland, G., Samperiz, A., Williams, J.A., Achterberg, E.P., Arrowsmith, C., Alexander Brearley, J., Henley, S.F., Krause, J.W., Leng, M.J., Li, T., McManus, J.F., Meredith, M.P., Perkins, R., Woodward, E.M.S., 2019. The biogeochemical impact of glacial meltwater from Southwest Greenland. Prog. Oceanogr. 176, 102126. https://doi.org/10.1016/j.pocean.2019.102126

Kipp, L.E., Sanial, V., Henderson, P.B., van Beek, P., Reyss, J.-L., Hammond, D.E., Moore,

W.S., Charette, M.A., 2018. Radium isotopes as tracers of hydrothermal inputs and neutrally buoyant plume dynamics in the deep ocean. Mar. Chem. 201, 51–65. https://doi.org/10.1016/J.MARCHEM.2017.06.011

Moore, W.S., 2008. Fifteen years experience in measuring 224Ra and 223Ra by delayed-coincidence counting. Mar. Chem. 109, 188–197. https://doi.org/10.1016/j.marchem.2007.06.015

Moore, W.S., 2000. Determining coastal mixing rates using radium isotopes. Cont. Shelf Res. 20, 1993–2007. https://doi.org/10.1016/S0278-4343(00)00054-6

Moore, W.S., 1976. Sampling 228Ra in the deep ocean. Deep. Res. Oceanogr. Abstr. 23, 647–651. https://doi.org/10.1016/0011-7471(76)90007-3

Moore, W.S., Arnold, R., 1996. Measurement of 223Ra and 224 Ra in coastal waters using a delayed coincidence counter. Measurement 101, 1321–1329.

Moore, W.S., Cai, P., 2013. Calibration of RaDeCC systems for 223Ra measurements. Mar. Chem. 156, 130–137. https://doi.org/10.1016/j.marchem.2013.03.002

Tamborski, J., van Beek, P., Conan, P., Pujo-Pay, M., Odobel, C., Ghiglione, J.F., Seidel, J.L., Arfib, B., Diego-Feliu, M., Garcia-Orellana, J., Szafran, A., Souhaut, M., 2020. Submarine karstic springs as a source of nutrients and bioactive trace metals for the oligotrophic Northwest Mediterranean Sea. Sci. Total Environ. 732, 1–14. https://doi.org/10.1016/j.scitotenv.2020.139106

Figures and Tables:

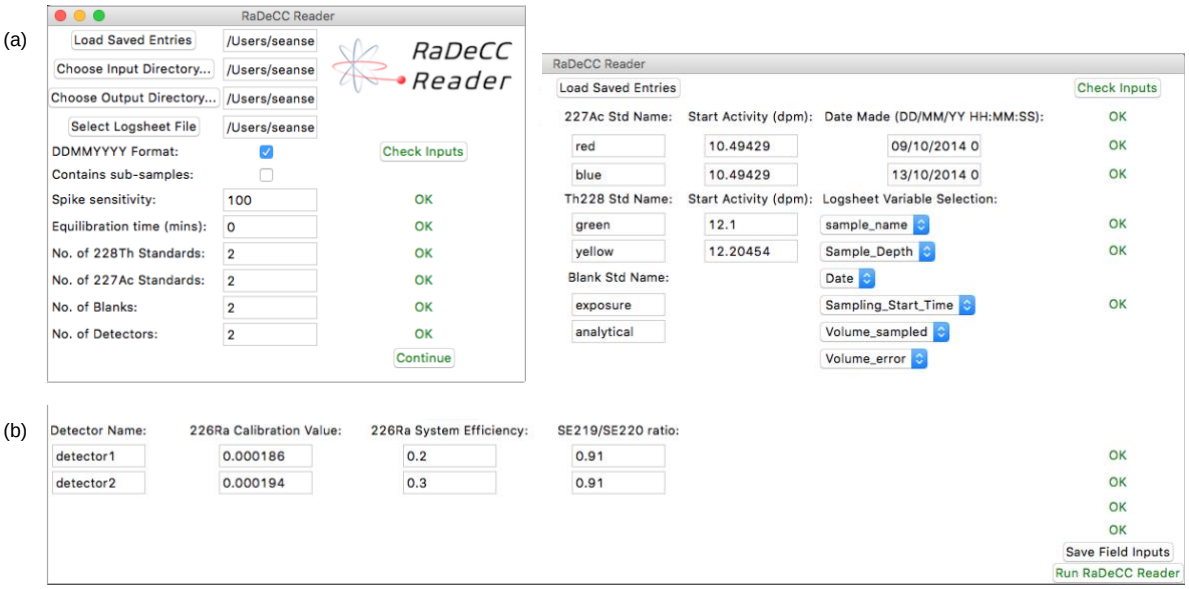

Figure 1. Details of the Graphical User Interface (GUI) used to operate RaDeCC Reader. This provides a verifiable summary of editable and necessarily user defined input parameters. Including (a) input and output file directories, date and data formats, calculation preferences, and the inventory of standards, backgrounds and detectors, and (b) details of individual detector names and efficiencies, standard names and activities, background names, and logsheet variables. In all fields of the GUI users may save and load previous inputs and check inputs before running the RaDeCC Reader programme.

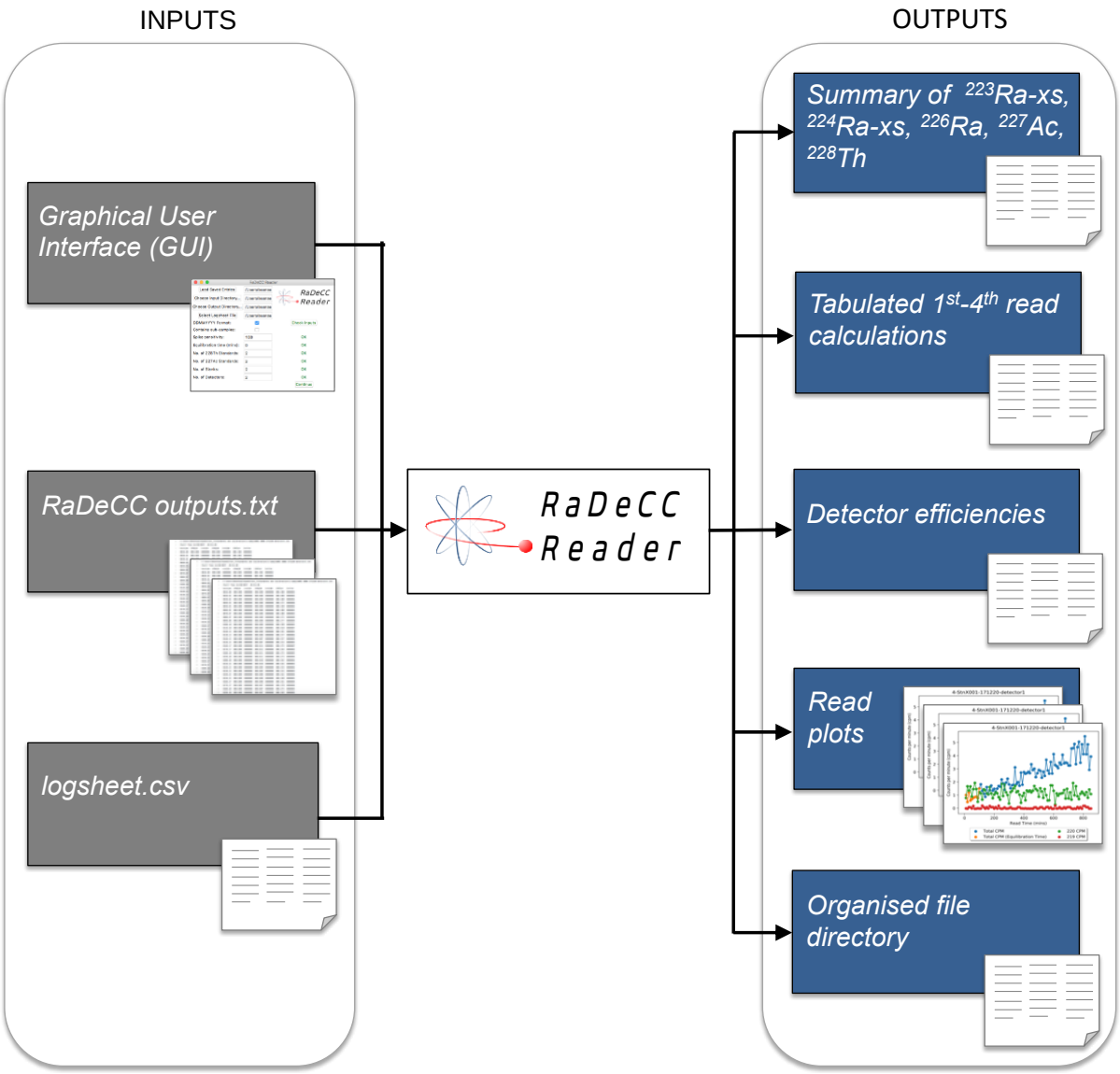

550

551 **Figure 2.** Summarised inputs and outputs of the RaDeCC Reader program.

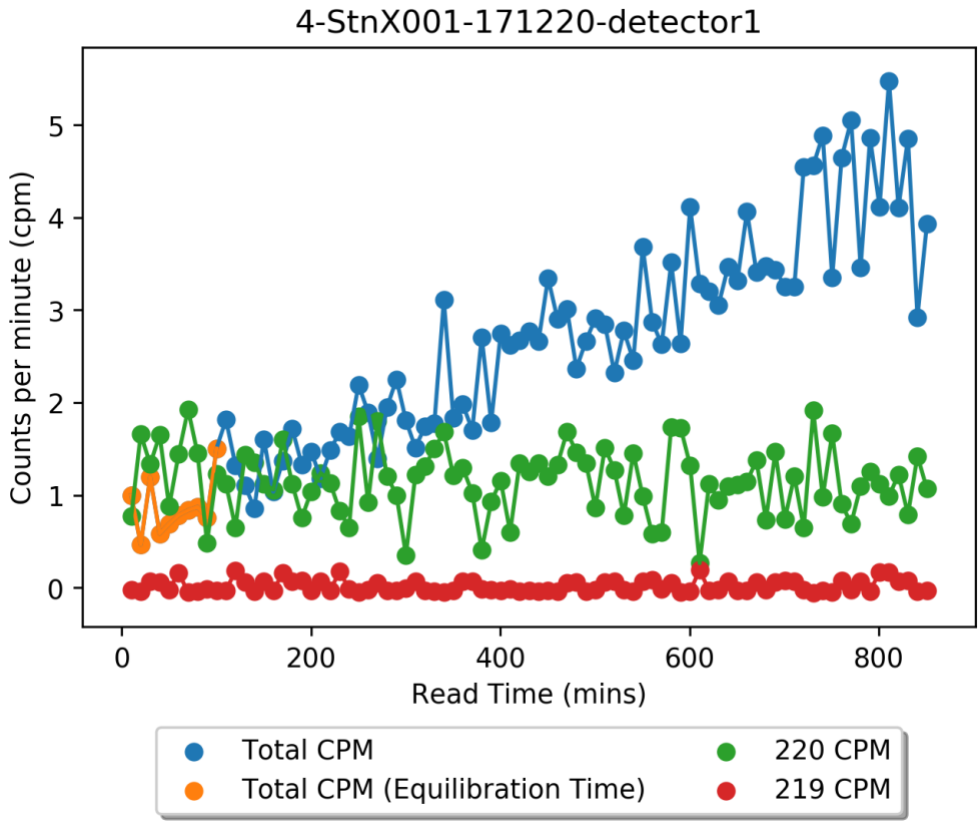

552

553 **Figure 3.** Example of a read plot produced by RaDeCC Reader of counts per minute for the
554 total, radon-219 and radon-220 channels over the course of a sample read. Spikes in counts
555 per minute (any counts that exceeded the default *'Spike sensitivity'* constant) have been
556 removed. Counts in the total channel that are used in the estimation of radium-226 activity
557 are shown in blue. Counts in the total channel that are ignored in the estimation of radium-
558 226 activity during a user-defined period of detector equilibration are shown in orange.

559

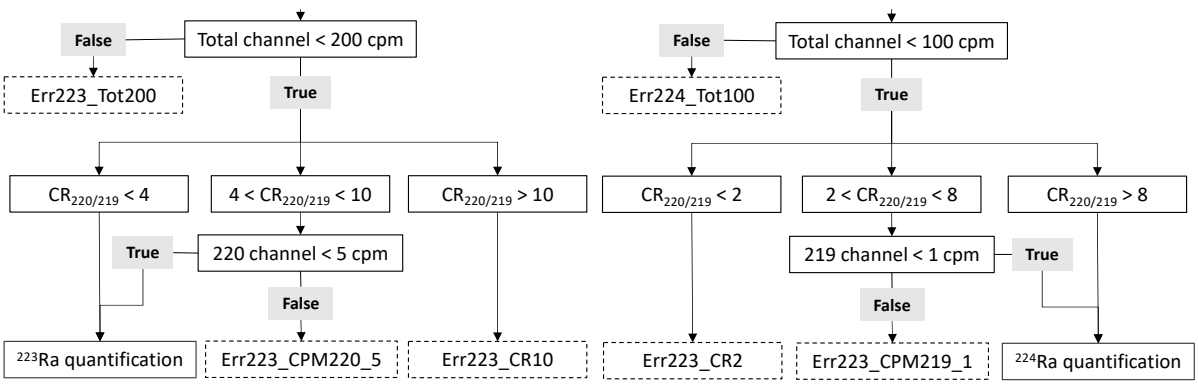

560

561 **Figure 4.** Flow charts of the guidelines for quantifying radium-223 (a) and radium-224 (b)

using RaDeCC apparatus (modified after Diego-Feliu et al. (2020). $CR_{220/219}$ is the count rate ratio of the 220-channel to the 219-channel.

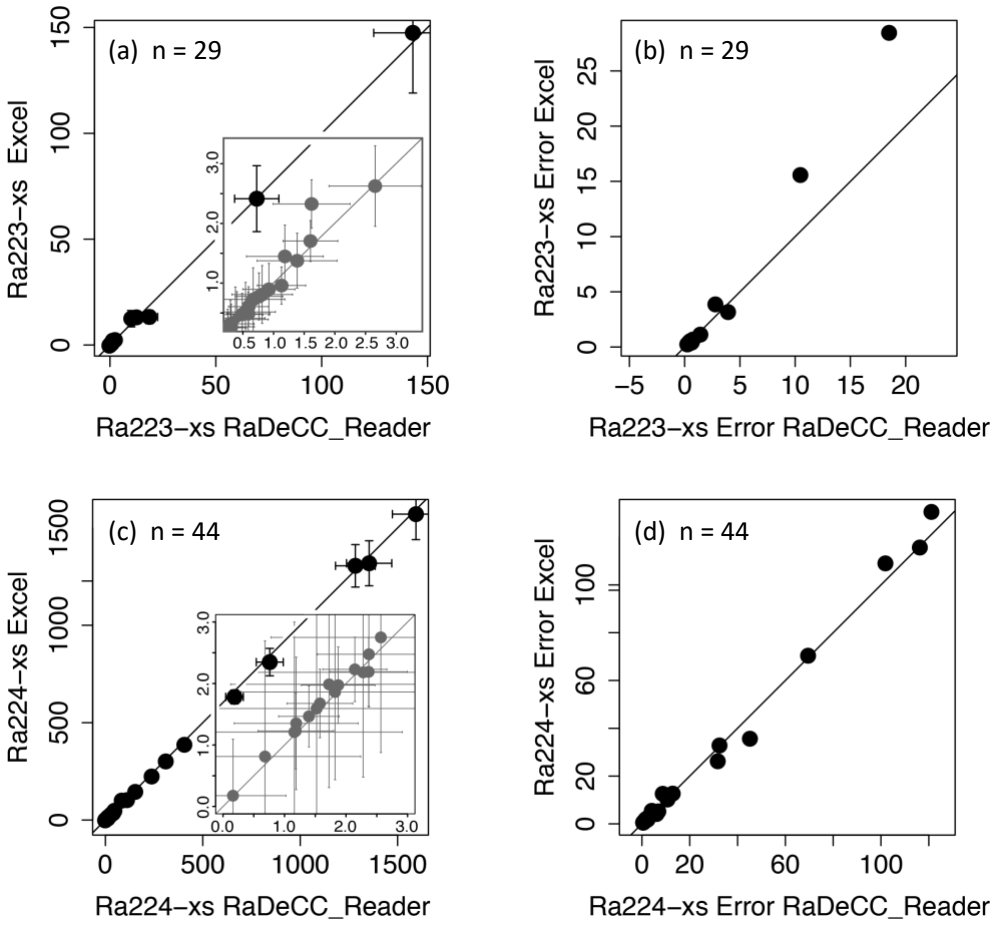

Figure 5. Validation of RaDeCC Reader outputs. Volume corrected activities and propagated uncertainties of excess radium-223 (a, b) and excess radium-223 (c, d) determined by the RaDeCC Reader program vs. an Excel implementation. Individual reads are plotted as black circles in units of dpm/m^3, relative to a 1:1 line. Inset plots (a, c) show the agreement between RaDeCC Reader program and the Excel implementation for samples in the low activity range.

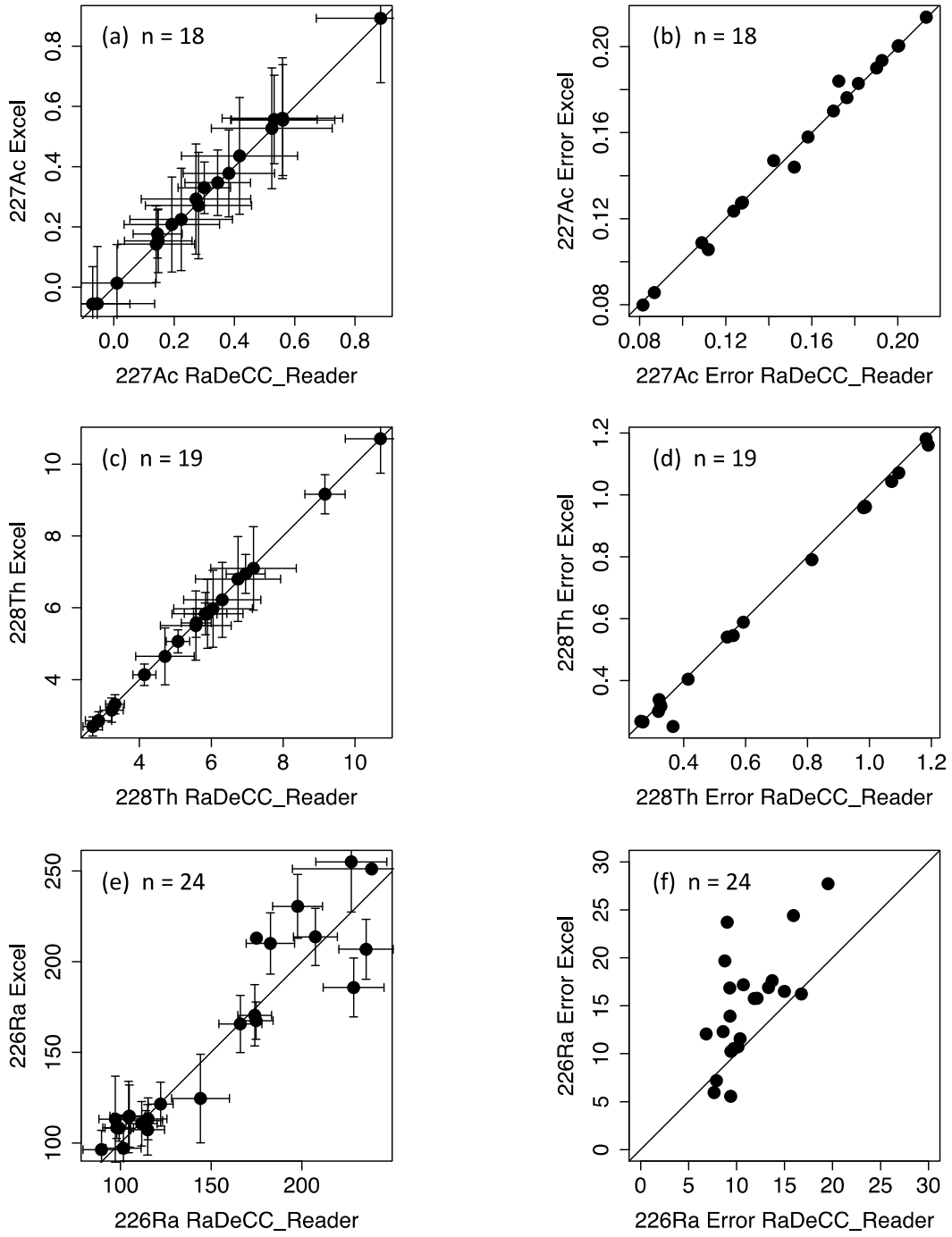

572

573 **Figure 6.** Volume corrected activities (dpm/m^3) of actinium-227 (a), thorium-228 (c) and
574 radium-226 (e). Propagated uncertainties associated with the calculation of actinium-227 (b),
575 thorium-228 (d) and radium-226 are also included. Individual samples are plotted as black
576 circles in units of dpm/m^3, relative to a 1:1 line.

577

578 **Table 1.** Glossary of variable terms used, their descriptions and units.

Variable	Description	Units
Y 219 CC	Erroneously registered 219 channel chance coincidence counts	cpm
Y 220 CC	Erroneously registered 220 channel chance coincidence counts	cpm
cpm219	counts per minute (219 channel)	cpm
cpm220	counts per minute (220 channel)	cpm
cpm total	counts per minute (total channel)	cpm
corr219	cpm219 corrected for Y 219 CC	cpm
corr220	cpm219 corrected for Y 220 CC	cpm
final219	corr219 corrected for cross-channel interference	cpm
final220	corr219 corrected for cross-channel interference	cpm
E219	Detection efficiency of the 219 channel	-
E220	Detection efficiency of the 220 channel	-
$Ratio_{219/220}$	Detection efficiency ratio of the 219 and 220 channels	-
P_{219}	Probability of radon-219 decaying in the cell	-
P_{220}	Probability of radon-220 decaying in the cell	-
L_{219}	Loss resulting from the 219 channel delay and window settings	-
L_{220}	Loss resulting from the 220 channel delay and window settings	-
bkgcorr223	final219 corrected for background	cpm
bkgcorr224	final220 corrected for background	cpm
dpm223	final219 corrected for detection efficiency	dpm
dpm224	final220 corrected for detection efficiency	dpm
vdpm223	dpm223 corrected for sample volume	dpm m^{-3}
vdpm224	dpm224 corrected for sample volume	dpm m^{-3}
$^{223}Ra_i$	vdpm223 for the initial read (including supported fraction)	dpm m^{-3}
$^{223}Ra_s$	vdpm223 for the latter read (supported fraction only)	dpm m^{-3}
$^{224}Ra_i$	vdpm224 for the initial read (including supported fraction)	dpm m^{-3}
$^{224}Ra_s$	vdpm224 for the latter read (supported fraction only)	dpm m^{-3}
λ_{223}	Decay constant for radium-223	d^{-1}
λ_{224}	Decay constant for radium-224	d^{-1}
$^{223}Ra_{xs}$	Excess radium-223 activity	dpm m^{-3}
$^{224}Ra_{xs}$	Excess radium-224 activity	dpm m^{-3}
vdpm226	radium-226 activity	dpm m^{-3}
$vdpm226_{initial}$	radium-226 activity initially measured in sample	cpm m^{-3}
slope of cpm total	Gradient of counts over time in the total channel	cpm min^{-1}
m	Radium-226 conversion factor	min^{-1}
E226	Detection efficiency for radium-226	-
Volume	Volume or mass of sample water	L, kg

579

Bibliography

Alibo, D. S. and Nozaki, Y. (1999). Rare earth elements in seawater: particle association, shale-normalization, and Ce oxidation. *Geochimica et Cosmochimica Acta*, 63(3-4):363–372.

Alt, J. C. (1995). Subseafloor processes in mid-ocean ridge hydrothermal systems. *Seafloor hydrothermal systems: Physical, chemical, biological, and geological interactions*, 91:85–114.

Annett, A. L., Henley, S. F., Van Beek, P., Souhaut, M., Ganeshram, R., Venables, H. J., Meredith, M. P., and Geibert, W. (2013). Use of radium isotopes to estimate mixing rates and trace sediment inputs to surface waters in northern Marguerite Bay, Antarctic Peninsula. *Antarctic Science*, 25(3):445–456.

Bacon, M. P. and Rosholt, J. N. (1982). Accumulation rates of Th-230, Pa-231, and some transition metals on the Bermuda Rise. *Geochimica et Cosmochimica Acta*, 46(4):651–666.

Baker, E. T. and German, C. R. (2004). On the global distribution of hydrothermal vent fields. *Mid-Ocean Ridges: Hydrothermal Interactions Between the Lithosphere and Oceans, Geophys. Monogr. Ser*, 148:245–266.

Bates, S. L., Hendry, K. R., Pryer, H. V., Kinsley, C. W., Pyle, K. M., Woodward, E. M. S., and Horner, T. J. (2017). Barium isotopes reveal role of ocean circulation on barium cycling in the Atlantic. *Geochimica et Cosmochimica Acta*, 204:286–299.

Bau, M. and Dulski, P. (1999). Comparing yttrium and rare earths in hydrothermal fluids from the Mid-Atlantic Ridge: implications for Y and REE behaviour during near-vent mixing and for the Y/Ho ratio of Proterozoic seawater. *Chemical Geology*, 155(1-2):77–90.

Beaulieu, S. E., Baker, E. T., and German, C. R. (2015). Where are the undiscovered hydrothermal vents on oceanic spreading ridges? *Deep Sea Research Part II: Topical Studies in Oceanography*, 121:202–212.

Bishop, J. K. (1988). The barite-opal-organic carbon association in oceanic particulate matter. *Nature*, 332(6162):341–343.

Boehm, A. B., Shellenbarger, G. G., and Paytan, A. (2004). Groundwater discharge: potential association with fecal indicator bacteria in the surf zone. *Environmental science & technology*, 38(13):3558–3566.

Böttcher, M. E., Neubert, N., Von Allmen, K., Samankassou, E., and Nägler, T. F. (2018). Barium isotope fractionation during the experimental transformation of aragonite to witherite and of gypsum to barite, and the effect of ion (de) solvation. *Isotopes in environmental and health studies*, 54(3):324–335.

Bourquin, M., Van Beek, P., Reyss, J.-L., Souhaut, M., Charette, M., and Jeandel, C. (2008). Comparison of techniques for pre-concentrating radium from seawater. *Marine Chemistry*, 109(3-4):226–237.

Bridgestock, L., Hsieh, Y. T., Porcelli, D., Homoky, W. B., Bryan, A., and Henderson, G. M. (2018). Controls on the barium isotope compositions of marine sediments. *Earth and Planetary Science Letters*, 481:101–110.

Bridgestock, L., Nathan, J., Hsieh, Y.-T., Holdship, P., Porcelli, D., Andersson, P. S., and Henderson, G. M. (2021). Assessing the utility of barium isotopes to trace Eurasian riverine freshwater inputs to the Arctic Ocean. *Marine Chemistry*, 236:104029.

Butterfield, D. A., McDuff, R. E., Mottl, M. J., Lilley, M. D., Lupton, J. E., and Massoth, G. J. (1994). Gradients in the composition of hydrothermal fluids from the Endeavour segment vent field: Phase separation and brine loss. *Journal of Geophysical Research: Solid Earth*, 99(B5):9561–9583.

Cao, Z., Li, Y., Rao, X., Yu, Y., Hathorne, E. C., Siebert, C., Dai, M., and Frank, M. (2020). Constraining barium isotope fractionation in the upper water column of the South China Sea. *Geochimica et Cosmochimica Acta*, 288:120–137.

Carlson, R. W., Boyet, M., and Horan, M. (2007). Chondrite barium, neodymium, and samarium isotopic heterogeneity and early earth differentiation. *Science*, 316(5828):1175–1178.

Charette, M. A., Gonneea, M. E., Morris, P. J., Statham, P., Fones, G., Planquette, H., Salter, I., and Garabato, A. N. (2007). Radium isotopes as tracers of iron sources fueling a Southern Ocean phytoplankton bloom. *Deep Sea Research Part II: Topical Studies in Oceanography*, 54(18-20):1989–1998.

Charette, M. A., Morris, P. J., Henderson, P. B., and Moore, W. S. (2014). Radium isotope distributions during the US GEOTRACES North Atlantic cruises. *Marine Chemistry*, 177:184–195.

Charette, M. A., Morris, P. J., Henderson, P. B., and Moore, W. S. (2015). Radium isotope distributions during the US GEOTRACES North Atlantic cruises. *Marine Chemistry*, 177:184–195.

Charette, M. A. and Smith, W. H. (2010). The volume of Earth's ocean. *Oceanography*, 23(2):112–114.

Charlou, J. L., Fouquet, Y., Donval, J. P., Auzende, J. M., Jean-Baptiste, P., Stievenard, M., and Michel, S. (1996). Mineral and gas chemistry of hydrothermal fluids on an ultrafast spreading ridge: East Pacific Rise, 17 to 19 S (Naudur cruise, 1993) phase separation processes controlled by volcanic and tectonic activity. *Journal of Geophysical Research: Solid Earth*, 101(B7):15899–15919.

Chung, Y. and Kim, K. (1980). Excess222Rn and the benthic boundary layer in the western and southern Indian Ocean. *Earth and Planetary Science Letters*, 49(2):351–359.

Clarke, F. W. (1889). *The relative abundance of the chemical elements*. Philosophical society of Washington.

Clarke, W. B., Beg, M., and Craig, H. (1969). Excess 3He in the sea: Evidence for terrestrial primodal helium. *Earth and Planetary Science Letters*, 6(3):213–220.

Coale, K. H., Chin, C. S., Massoth, G. J., Johnson, K. S., and Baker, E. T. (1991). In situ chemical mapping of dissolved iron and manganese in hydrothermal plumes. *Nature*, 352(6333):325–328.

Cochran, J. (1982). The oceanic chemistry of the U-and Th-series nuclides. In *Uranium series disequilibrium: applications to environmental problems*.

Colbert, S. L. and Hammond, D. E. (2007). Temporal and spatial variability of radium in the coastal ocean and its impact on computation of nearshore cross-shelf mixing rates. *Continental Shelf Research*, 27(10-11):1477–1500.

Collier, R. and Edmond, J. (1984). The trace element geochemistry of marine biogenic particulate matter. *Progress in oceanography*, 13(2):113–199.

Corliss, J. B., Dymond, J., Gordon, L. I., Edmond, J. M., von Herzen, R. P., Ballard, R. D., Green, K., Williams, D., Bainbridge, A., Crane, K., et al. (1979). Submarine thermal springs on the Galapagos Rift. *Science*, 203(4385):1073–1083.

Crockford, P. W., Wing, B. A., Paytan, A., Hodgskiss, M. S., Mayfield, K. K., Hayles, J. A., Middleton, J. E., Ahm, A.-S. C., Johnston, D. T., Caxito, F., et al. (2019). Barium-isotopic constraints on the origin of post-Marinoan barites. *Earth and Planetary Science Letters*, 519:234–244.

Dehairs, F., Chesselet, R., and Jedwab, J. (1980). Discrete suspended particles of barite and the barium cycle in the open ocean. *Earth and Planetary Science Letters*, 49(2):528–550.

Diego-Feliu, M., Rodellas, V., Alorda-Kleinglass, A., Tamborski, J., van Beek, P., Heins, L., Bruach, J. M., Arnold, R., and Garcia-Orellana, J. (2020). Guidelines and Limits for the Quantification of Ra Isotopes and Related Radionuclides With the Radium Delayed Coincidence Counter (RaDeCC). *Journal of Geophysical Research: Oceans*, 125(4).

Ditchburn, R. G., de Ronde, C. E., and Barry, B. J. (2012). Radiometric dating of volcanogenic massive sulfides and associated iron oxide crusts with an emphasis on 226Ra/Ba and 228Ra/226Ra in volcanic and hydrothermal processes at intraoceanic arcs. *Economic Geology*, 107(8):1635–1648.

Douville, E., Bienvenu, P., Charlou, J. L., Donval, J. P., Fouquet, Y., Appriou, P., and Gamo, T. (1999). Yttrium and rare earth elements in fluids from various deep-sea hydrothermal systems. *Geochimica et Cosmochimica Acta*, 63(5):627–643.

Douville, E., Charlou, J. L., Oelkers, E. H., Bienvenu, P., Jove Colon, C. F., Donval, J. P., Fouquet, Y., Prieur, D., and Appriou, P. (2002). The rainbow vent fluids (36°14'N, MAR): The influence of ultramafic rocks and phase separation on trace metal content in Mid-Atlantic Ridge hydrothermal fluids. *Chemical Geology*, 184(1-2):37–48.

Dymond, J., Suess, E., and Lyle, M. (1992). Barium in deep-sea sediment: A geochemical proxy for paleoproductivity. *Paleoceanography*, 7(2):163–181.

Elderfield, H. and Schultz, A. (1996). Mid-ocean ridge hydrothermal fluxes and the chemical composition of the ocean. *Annual Review of Earth and Planetary Sciences*, 24(1):191–224.

Elderfield, H., Upstill-Goddard, R., and Sholkovitz, E. (1990). The rare earth elements in rivers, estuaries, and coastal seas and their significance to the composition of ocean waters. *Geochimica et Cosmochimica Acta*, 54(4):971–991.

Elderfield, H., Whitfield, M., Burton, J. D., Bacon, M. P., and Liss, P. S. (1988). The Oceanic Chemistry of the Rare-Earth Elements. *Philosophical Transactions of the Royal Society A: Mathematical, Physical and Engineering Sciences*, 325(1583):105–126.

Feely, R., Baker, E., Marumo, K., Urabe, T., Ishibashi, J., Gendron, J., Lebon, G., and Okamura, K. (1996). Hydrothermal plume particles and dissolved phosphate over the superfast-spreading southern East Pacific Rise. *Geochimica et Cosmochimica Acta*, 60(13):2297–2323.

Feely, R. A., Massoth, G. J., Trefry, J. H., Baker, E. T., Paulson, A. J., and Lebon, G. T. (1994). Composition and sedimentation of hydrothermal plume particles from North Cleft segment, Juan de Fuca Ridge. *Journal of Geophysical Research: Solid Earth*, 99(B3):4985–5006.

Foster, D. A., Staubwasser, M., and Henderson, G. M. (2004). 226Ra and Ba concentrations in the Ross Sea measured with multicollector ICP mass spectrometry. *Marine Chemistry*, 87(1-2):59–71.

Fouquet, Y., Barriga, F., Charlou, J.-L., Elderfield, H., German, C., Ondreas, H., Parson, L., Radford-Knoery, J., Relvas, J., Ribeiro, A., et al. (1998). FLORES diving cruise with Nautile near the Azores-First dives on the Rainbow field: hydrothermal seawater/mantle interaction. *InterRidge News*, 7(1):24–28.

Gaillardet, J., Viers, J., and Dupré, B. (2004). Treatise on Geochemistry, volume 5, chapter Trace Elements in River Waters.

Galley, A. G. and Koski, R. (1999). Setting and characteristics of ophiolite-hosted volcanogenic massive sulfide deposits. *Reviews in economic geology*, 8:221–246.

Ganeshram, R. S., François, R., Commeau, J., and Brown-Leger, S. L. (2003). An experimental investigation of barite formation in seawater. *Geochimica et Cosmochimica Acta*, 67(14):2599–2605.

Garcia-Solsona, E., Garcia-Orellana, J., Masqué, P., and Dulaiova, H. (2008). Uncertainties associated with 223Ra and 224Ra measurements in water via a Delayed Coincidence Counter (RaDeCC). *Marine Chemistry*, 109(3-4):198–219.

Geibert, W., Rodellas, V., Annett, A., van Beek, P., Garcia-Orellana, J., Hsieh, Y.-T., and Masque, P. (2013). 226Ra determination via the rate of 222Rn ingrowth with the Radium Delayed Coincidence Counter (RaDeCC). *Limnology and Oceanography: Methods*, 11(11):594–603.

German, C., Klinkhammer, G. P., and Rudnicki, M. (1996a). The Rainbow hydrothermal plume, 36° 15' N, MAR. *Geophysical Research Letters*, 23(21):2979–2982.

German, C., Parson, L., Bougault, H., Coller, D., Critchley, M., Dapoigny, A., Day, C., Eardley, D., Fearn, A., Flewellen, C., et al. (1996b). Hydrothermal exploration near the Azores Triple Junction: tectonic control of venting at slow-spreading ridges? *Earth and Planetary Science Letters*, 138(1-4):93–104.

German, C. and Seyfried, W. (2014). 8.7-hydrothermal processes.

German, C., Thurnherr, A., Knoery, J., Charlou, J.-L., Jean-Baptiste, P., and Edmonds, H. (2010a). Heat, volume and chemical fluxes from submarine venting: A synthesis of results from the Rainbow hydrothermal field, 36 N MAR. *Deep Sea Research Part I: Oceanographic Research Papers*, 57(4):518–527.

German, C. R. (1993). A geochemical study of metalliferous sediment from the TAG hydrothermal mound, 26° 08'N, Mid-Atlantic Ridge. *Journal of Geophysical Research*, 98(B6):9683–9692.

German, C. R., Fleer, A. P., Bacon, M. P., and Edmond, J. M. (1991). Hydrothermal scavenging at the Mid-Atlantic Ridge: radionuclide distributions. *Earth and Planetary Science Letters*, 105(1-3):170–181.

German, C. R., Klinkhammer, G. P., Edmond, J. M., Mura, A., and Elderfield, H. (1990). Hydrothermal scavenging of rare-earth elements in the ocean. *Nature*, 345(6275):516–518.

German, C. R., Thurnherr, A. M., Knoery, J., Charlou, J. L., Jean-Baptiste, P., and Edmonds, H. N. (2010b). Heat, volume and chemical fluxes from submarine venting: A synthesis of results from the Rainbow hydrothermal field, 36°N MAR. *Deep-Sea Research Part I: Oceanographic Research Papers*, 57(4):518–527.

Giffin, C., Kaufman, A., and Broecker, W. (1963). Delayed coincidence counter for the assay of actinon and thoron. *Journal of Geophysical Research*, 68(6):1749–1757.

Goldschmidt, V. (1933). Grundlagen der quantitativen Geochemie. *Fortschr. Mienral. Kirst. Petrogr*, 17:112.

Gonzalez-Muñoz, M., Martinez-Ruiz, F., Morcillo, F., Martin-Ramos, J., and Paytan, A. (2012). Precipitation of barite by marine bacteria: A possible mechanism for marine barite formation. *Geology*, 40(8):675–678.

González-Munoz, M. T., Fernández-Luque, B., Martínez-Ruiz, F., Ben Chekroun, K., Arias, J. M., Rodríguez-Gallego, M., Martínez-Canamero, M., De Linares, C., and Paytan, A. (2003). Precipitation of barite by Myxococcus xanthus: possible implications for the biogeochemical cycle of barium. *Applied and Environmental Microbiology*, 69(9):5722–5725.

González-Santana, D., González-Dávila, M., Lohan, M. C., Artigue, L., Planquette, H., Sarthou, G., Tagliabue, A., and Santana-Casiano, J. M. (2021). Variability in iron (II) oxidation kinetics across diverse hydrothermal sites on the northern Mid Atlantic Ridge. *Geochimica et Cosmochimica Acta*, 297:143–157.

Gou, L.-F., Jin, Z., Galy, A., Gong, Y.-Z., Nan, X.-Y., Jin, C., Wang, X.-D., Bouchez, J., Cai, H.-M., Chen, J.-B., et al. (2020). Seasonal riverine barium isotopic variation in the middle Yellow River: Sources and fractionation. *Earth and Planetary Science Letters*, 531:115990.

Griffith, E. M. and Paytan, A. (2012). Barite in the ocean–occurrence, geochemistry and palaeoceanographic applications. *Sedimentology*, 59(6):1817–1835.

Gromet, L. P., Haskin, L. A., Korotev, R. L., and Dymek, R. F. (1984). The "North American shale composite": Its compilation, major and trace element characteristics. *Geochimica et cosmochimica acta*, 48(12):2469–2482.

Grousset, F. E., Biscaye, P. E., Revel, M., Petit, J.-R., Pye, K., Joussaume, S., and Jouzel, J. (1992). Antarctic (Dome C) ice-core dust at 18 ky BP: Isotopic constraints on origins. *Earth and Planetary Science Letters*, 111(1):175–182.

Hamilton, E. L. (1976). Variations of density and porosity with depth in deep-sea sediments. *Journal of Sedimentary Research*, 46(2):280–300.

Hannington, M. D., Jonasson, I. R., Herzig, P. M., and Petersen, S. (1995). Physical and chemical processes of seafloor mineralization at mid-ocean ridges. *Seafloor hydrothermal systems: Physical, chemical, biological, and geological interactions*, 91:115–157.

Hathorne, E. C., Haley, B., Stichel, T., Grasse, P., Zieringer, M., and Frank, M. (2012). Online preconcentration ICP-MS analysis of rare earth elements in seawater. *Geochemistry, Geophysics, Geosystems*, 13(1).

Hemsing, F., Hsieh, Y. T., Bridgestock, L., Spooner, P. T., Robinson, L. F., Frank, N., and Henderson, G. M. (2018). Barium isotopes in cold-water corals. *Earth and Planetary Science Letters*, 491:183–192.

Henderson, P. B., Morris, P. J., Moore, W. S., and Charette, M. A. (2013). Methodological advances for measuring low-level radium isotopes in seawater. *Journal of Radioanalytical and Nuclear Chemistry*, 296(1):357–362.

Hendry, K. R., Huvenne, V. A., Robinson, L. F., Annett, A., Badger, M., Jacobel, A. W., Ng, H. C., Opher, J., Pickering, R. A., Taylor, M. L., Bates, S. L., Cooper, A., Cushman, G. G., Goodwin, C., Hoy, S., Rowland, G., Samperiz, A., Williams, J. A., Achterberg, E. P., Arrowsmith, C., Alexander Brearley, J., Henley, S. F., Krause, J. W., Leng, M. J., Li, T., McManus, J. F., Meredith, M. P., Perkins, R., and Woodward, E. M. S. (2019). The biogeochemical impact of glacial meltwater from Southwest Greenland. *Progress in Oceanography*, 176(April):102126.

Holland, M. (2003). Limits to life in hydrothermal systems. *Energy and mass transfer in marine hydrothermal systems*.

Horner, T. J., Kinsley, C. W., and Nielsen, S. G. (2015). Barium-isotopic fractionation in seawater mediated by barite cycling and oceanic circulation. *Earth and Planetary Science Letters*, 430:511–522.

Horner, T. J., Pryer, H. V., Nielsen, S. G., Crockford, P. W., Gauglitz, J. M., Wing, B. A., and Ricketts, R. D. (2017). Pelagic barite precipitation at micromolar ambient sulfate. *Nature communications*, 8(1):1–11.

Hsieh, Y.-T., Bridgestock, L., Scheuermann, P. P., Seyfried Jr, W. E., and Henderson, G. M. (2021). Barium isotopes in mid-ocean ridge hydrothermal vent fluids: A source of isotopically heavy Ba to the ocean. *Geochimica et Cosmochimica Acta*, 292:348–363.

Hsieh, Y.-T., Geibert, W., Van-Beek, P., Stahl, H., Aleynik, D., and Henderson, G. M. (2013). Using the radium quartet (228Ra, 226Ra, 224Ra, and 223Ra) to estimate water mixing and radium inputs in Loch Etive, Scotland. *Limnology and oceanography*, 58(3):1089–1102.

Hsieh, Y. T. and Henderson, G. M. (2017). Barium stable isotopes in the global ocean: Tracer of Ba inputs and utilization. *Earth and Planetary Science Letters*, 473:269–278.

Hwang, D.-W., Lee, Y.-W., and Kim, G. (2005). Large submarine groundwater discharge and benthic eutrophication in Bangdu Bay on volcanic Jeju Island, Korea. *Limnology and Oceanography*, 50(5):1393–1403.

Jackson, P., Ledwell, J., and Thurnherr, A. (2010). Dispersion of a tracer on the East Pacific Rise (9 N to 10 N), including the influence of hydrothermal plumes. *Deep Sea Research Part I: Oceanographic Research Papers*, 57(1):37–52.

Jean-Baptiste, P., Bougault, H., Vangriesheim, A., Charlou, J., Radford-Knoery, J., Fouquet, Y., Needham, D., and German, C. (1998). Mantle 3He in hydrothermal vents and plume of the Lucky Strike site (MAR 37 17' N) and associated geothermal heat flux. *Earth and Planetary Science Letters*, 157(1-2):69–77.

Jean-Baptiste, P., Fourré, E., Charlou, J.-L., German, C. R., and Radford-Knoery, J. (2004). Helium isotopes at the rainbow hydrothermal site (mid-atlantic ridge, 36° 14' n). *Earth and Planetary Science Letters*, 221(1-4):325–335.

Jeandel, C., Dupre, B., Lebaron, G., Monnin, C., and Minster, J.-F. (1996). Longitudinal distributions of dissolved barium, silica and alkalinity in the western and southern Indian Ocean. *Deep Sea Research Part I: Oceanographic Research Papers*, 43(1):1–31.

Kadko, D. (1996). Radioisotopic studies of submarine hydrothermal vents. *Reviews of Geophysics*, 34(3):349–366.

Kadko, D. and Butterfield, D. A. (1998). The relationship of hydrothermal fluid composition and crustal residence time to maturity of vent fields on the juan de fuca ridge. *Geochimica et Cosmochimica Acta*, 62(9):1521–1533.

Kadko, D., Gronvold, K., and Butterfield, D. (2007). Application of radium isotopes to determine crustal residence times of hydrothermal fluids from two sites on the Reykjanes Peninsula, Iceland. *Geochimica et Cosmochimica Acta*, 71(24):6019–6029.

Kadko, D., Rosenberg, N., Lupton, J., Collier, R., and Lilley, M. (1990). Chemical reaction rates and entrainment within the Endeavour Ridge hydrothermal plume. *Earth and Planetary Science Letters*, 99(4):315–335.

Kashefi, K. and Lovley, D. R. (2003). Extending the upper temperature limit for life. *Science*, 301(5635):934–934.

Kipp, L. E., Charette, M. A., Hammond, D. E., and Moore, W. S. (2015a). Hydrothermal vents: A previously unrecognized source of actinium-227 to the deep ocean. *Marine Chemistry*, 177:583–590.

Kipp, L. E., Charette, M. A., Hammond, D. E., and Moore, W. S. (2015b). Hydrothermal vents: A previously unrecognized source of actinium-227 to the deep ocean. *Marine Chemistry*, 177:583–590.

Kipp, L. E., Sanial, V., Henderson, P. B., van Beek, P., Reyss, J.-L., Hammond, D. E., Moore, W. S., and Charette, M. A. (2018). Radium isotopes as tracers of hydrothermal inputs and neutrally buoyant plume dynamics in the deep ocean. *Marine Chemistry*, 201:51–65.

Klinkhammer, G., Chin, C., Wilson, C., and German, C. (1995). Venting from the Mid-Atlantic Ridge at 37 17' N: the Lucky Strike hydrothermal site. *Geological Society, London, Special Publications*, 87(1):87–96.

Klinkhammer, G., German, C. R., Elderfield, H., Greaves, M. J., and Mitra, A. (1994). Rare earth elements in hydrothermal fluids and plume particulates by inductively coupled plasma mass spectrometry. *Marine Chemistry*, 45(3):179–186.

Krishnaswami, S. and Turekian, K. (1982). 238U, 226Ra and 210Pb in some vent waters of the Galapagos spreading center. *Geophysical Research Letters*, 9(8):827–830.

Ku, T. L., Bischoff, J. L., and Boersma, A. (1972). Age studies of Mid-Atlantic Ridge sediments near 42°N and 20°N. *Deep-Sea Research and Oceanographic Abstracts*, 19(3):233–247.

Lacan, F., Tachikawa, K., and Jeandel, C. (2012). Neodymium isotopic composition of the oceans: A compilation of seawater data. *Chemical Geology*, 300:177–184.

Lalou, C., Thompson, G., Arnold, M., Brichet, E., Druffel, E., and Rona, P. A. (1990). Geochronology of TAG and Snake Pit hydrothermal fields; MAR - Witness to a long ans complex hydrothermal history. *Earth and Planetary Science Letters*, 97(1-2):113–128.

Lam, P. J., Ohnemus, D. C., and Auro, M. E. (2015). Size-fractionated major particle composition and concentrations from the US GEOTRACES North Atlantic Zonal Transect. *Deep Sea Research Part II: Topical Studies in Oceanography*, 116:303–320.

Le Roy, E., Sanial, V., Lacan, F., Van Beek, P., Souhaut, M., Charette, M. A., and Henderson, P. B. (2019). Insight into the measurement of dissolved 227Ac in seawater using radium delayed coincidence counter. *Marine Chemistry*, 212:64–73.

Lea, D. and Boyle, E. (1989). Barium content of benthic foraminifera controlled by bottom-water composition. *Nature*, 338(6218):751–753.

Lippold, J., Gutjahr, M., Blaser, P., Christner, E., de Carvalho Ferreira, M. L., Mulitza, S., Christl, M., Wombacher, F., Böhm, E., Antz, B., Cartapanis, O., Vogel, H., and Jaccard, S. L. (2016). Deep water provenance and dynamics of the (de)glacial Atlantic meridional overturning circulation. *Earth and Planetary Science Letters*, 445:68–78.

Lippold, J., Mulitza, S., Mollenhauer, G., Weyer, S., Heslop, D., and Christl, M. (2012). Boundary scavenging at the East Atlantic margin does not negate use of 231Pa/230Th to trace Atlantic overturning. *Earth and Planetary Science Letters*, 333:317–331.

Luek, J. L. and Beck, A. J. (2014). Radium budget of the York River estuary (VA, USA) dominated by submarine groundwater discharge with a seasonally variable groundwater end-member. *Marine Chemistry*, 165:55–65.

Lupton, J. (1998). Hydrothermal helium plumes in the Pacific Ocean. *Journal of Geophysical Research: Oceans*, 103(C8):15853–15868.

Mackey, D., O'Sullivan, J. O., and Watson, R. (2002). Iron in the western Pacific: a riverine or hydrothermal source for iron in the Equatorial Undercurrent? *Deep Sea Research Part I: Oceanographic Research Papers*, 49(5):877–893.

McDonough, W. F. (2014). *Treatise on Geochemistry: Analytical Geochemistry/inorganic Instrument Analysis/Vol. Ed. William F. McDonough*. Elsevier.

McManus, J., Berelson, W. M., Hammond, D. E., and Klinkhammer, G. P. (1999). Barium cycling in the North Pacific: Implications for the utility of Ba as a paleoproductivity and paleoalkalinity proxy. *Paleoceanography*, 14(1):53–61.

Mearns, E. W. (1988). A samarium-neodymium isotopic survey of modern river sediments from northern Britain. *Chemical Geology: Isotope Geoscience section*, 73(1):1–13.

Mills, R., Elderfield, H., and Thomson, J. (1993). A Dual Origin for the Hydrothermal Component in a Metalliferous. *Journal of Geophysical Research*, 98:9671–9681.

Mitra, A., Elderfield, H., and Greaves, M. (1994). Rare earth elements in submarine hydrothermal fluids and plumes from the Mid-Atlantic Ridge. *Marine Chemistry*, 46(3):217–235.

Monnin, C. (1999). A thermodynamic model for the solubility of barite and celestite in electrolyte solutions and seawater to 200 C and to 1 kbar. *Chemical Geology*, 153(1-4):187–209.

Monnin, C., Jeandel, C., Cattaldo, T., and Dehairs, F. (1999). The marine barite saturation state of the world's oceans. *Marine Chemistry*, 65(3-4):253–261.

Moore, W. S. (1976). Sampling 228Ra in the deep ocean. *Deep-Sea Research and Oceanographic Abstracts*, 23(7):647–651.

Moore, W. S. (2000a). Ages of continental shelf waters determined from 223Ra and 224Ra. *Journal of Geophysical Research: Oceans*, 105(C9):22117–22122.

Moore, W. S. (2000b). Determining coastal mixing rates using radium isotopes. *Continental Shelf Research*, 20(15):1993–2007.

Moore, W. S. (2008). Fifteen years experience in measuring 224Ra and 223Ra by delayed-coincidence counting. *Marine Chemistry*, 109(3-4):188–197.

Moore, W. S. and Arnold, R. (1996). Measurement of 223ra and 224ra in coastal waters using a delayed coincidence counter. *Journal of Geophysical Research: Oceans*, 101(C1):1321–1329.

Moore, W. S. and Cai, P. (2013). Calibration of radecc systems for 223ra measurements. *Marine Chemistry*, 156:130–137.

Moore, W. S. and Reid, D. F. (1973). Extraction of radium from natural waters using manganese-impregnated acrylic fibers. *Journal of Geophysical Research*, 78(36):8880–8886.

Moore, W. S., Ussler III, W., and Paull, C. K. (2008). Short-lived radium isotopes in the Hawaiian margin: Evidence for large fluid fluxes through the Puna Ridge. *Marine chemistry*, 109(3-4):421–430.

Negre, C., Zahn, R., Thomas, A. L., Masqué, P., Henderson, G. M., Martínez-Méndez, G., Hall, I. R., and Mas, J. L. (2010). Reversed flow of Atlantic deep water during the Last Glacial Maximum. *Nature*, 468(7320):84–88.

Neuholz, R., Schnetger, B., Kleint, C., Koschinsky, A., Lettmann, K., Sander, S., Türke, A., Walter, M., Zitoun, R., and Brumsack, H.-J. (2020). Near-field hydrothermal plume dynamics at Brothers Volcano (Kermadec Arc): A short-lived radium isotope study. *Chemical Geology*, 533:119379.

Nozaki, Y. (2001). Rare earth elements and their isotopes in the ocean. *Encyclopedia of Ocean Sciences*, 4:2354–2366.

Paytan, A. and Griffith, E. M. (2007). Marine barite: Recorder of variations in ocean export productivity. *Deep Sea Research Part II: Topical Studies in Oceanography*, 54(5-7):687–705.

Paytan, A., Kastner, M., and Chavez, F. (1996). Glacial to interglacial fluctuations in productivity in the equatorial Pacific as indicated by marine barite. *Science*, 274(5291):1355–1357.

Polzin, K. L., Toole, J. M., Ledwell, J. R., and Schmitt, R. W. (1997). Spatial variability of turbulent mixing in the abyssal ocean. *Science*, 276(5309):93–96.

Porcelli, D. and Swarzenski, P. W. (2003). The behavior of U-and Th-series nuclides in groundwater. *Reviews in Mineralogy and Geochemistry*, 52(1):317–361.

Roberts, N. L., McManus, J. F., Piotrowski, A. M., and McCave, I. N. (2014). Advection and scavenging controls of Pa/Th in the northern NE Atlantic. *Paleoceanography*, 29(6):668–679.

Rona, P., Klinkhammer, G., Nelsen, T., Trefry, J., and Elderfield, H. (1986). Black smokers, massive sulphides and vent biota at the Mid-Atlantic Ridge. *Nature*, 321(6065):33–37.

Rona, P. A. and Speer, K. G. (1989). An Atlantic hydrothermal plume: Trans-Atlantic geotraverse (TAG) area, Mid-Atlantic Ridge crest near 26° N. *Journal of Geophysical Research: Solid Earth*, 94(B10):13879–13893.

Rubin, S. I., King, S. L., Jahnke, R. A., and Froelich, P. N. (2003). Benthic barium and alkalinity fluxes: Is Ba an oceanic paleo-alkalinity proxy for glacial atmospheric CO2? *Geophysical Research Letters*, 30(17).

Rudnick, R. and Gao, S. (2014). 4.1 - Composition of the Continental Crust. In Holland, H. D. and Turekian, K. K., editors, *Treatise on Geochemistry (Second Edition)*, pages 1–51. Elsevier, Oxford, second edition edition.

Rudnick, R. L. and Fountain, D. M. (1995). Nature and composition of the continental crust: a lower crustal perspective. *Reviews of geophysics*, 33(3):267–309.

Rudnicki, M. and Elderfield, H. (1992). Helium, radon and manganese at the TAG and Snakepit hydrothermal vent fields, 26 and 23 N, Mid-Atlantic Ridge. *Earth and planetary science letters*, 113(3):307–321.

Rudnicki, M. and Elderfield, H. (1993). A chemical model of the buoyant and neutrally buoyant plume above the TAG vent field, 26 degrees N, Mid-Atlantic Ridge. *Geochimica et Cosmochimica Acta*, 57(13):2939–2957.

Schlitzer, R., Anderson, R. F., Dodas, E. M., Lohan, M., Geibert, W., Tagliabue, A., Bowie, A., Jeandel, C., Maldonado, M. T., Landing, W. M., Cockwell, D., Abadie, C., Abouchami, W., Achterberg, E. P., Agather, A., Aguliar-Islas, A., van Aken, H. M., Andersen, M., Archer, C., Auro, M., de Baar, H. J., Baars, O., Baker, A. R., Bakker, K., Basak, C., Baskaran, M., Bates, N. R., Bauch, D., van Beek, P., Behrens, M. K., Black, E., Bluhm, K., Bopp, L., Bouman, H., Bowman, K., Bown, J., Boyd, P., Boye, M., Boyle, E. A., Branellec, P., Bridgestock, L., Brissebrat, G., Browning, T., Bruland, K. W., Brumsack, H. J., Brzezinski, M., Buck, C. S., Buck, K. N., Buesseler, K., Bull, A., Butler, E., Cai, P., Mor, P. C., Cardinal, D., Carlson, C., Carrasco, G., Casacuberta, N., Casciotti, K. L., Castrillejo, M., Chamizo, E., Chance, R., Charette, M. A., Chaves, J. E., Cheng, H., Chever, F., Christl, M., Church, T. M., Closset, I., Colman, A., Conway, T. M., Cossa, D., Croot, P., Cullen, J. T., Cutter, G. A., Daniels, C., Dehairs, F., Deng, F., Dieu, H. T., Duggan, B., Dulaquais, G., Dumousseaud, C., Echegoyen-Sanz, Y., Edwards, R. L., Ellwood, M., Fahrbach, E., Fitzsimmons, J. N., Russell Flegal, A., Fleisher, M. Q., van de Flierdt, T., Frank, M., Friedrich, J., Fripiat, F., Fröllje, H., Galer, S. J., Gamo, T., Ganeshram, R. S., Garcia-Orellana, J., Garcia-Solsona, E., Gault-Ringold, M., George, E., Gerringa, L. J., Gilbert, M., Godoy, J. M., Goldstein, S. L., Gonzalez, S. R., Grissom, K., Hammerschmidt, C., Hartman, A., Hassler, C. S., Hathorne, E. C., Hatta, M., Hawco, N., Hayes, C. T., Heimbürger, L. E., Helgoe, J., Heller, M., Henderson, G. M., Henderson, P. B., van Heuven, S., Ho, P., Horner, T. J., Hsieh, Y. T., Huang, K. F., Humphreys, M. P., Isshiki, K., Jacquot, J. E., Janssen, D. J., Jenkins, W. J., John, S., Jones, E. M., Jones, J. L., Kadko, D. C., Kayser, R., Kenna, T. C., Khondoker, R., Kim, T., Kipp, L., Klar, J. K., Klunder, M., Kretschmer, S., Kumamoto, Y., Laan, P., Labatut, M., Lacan, F., Lam, P. J., Lambelet, M., Lamborg, C. H., Le Moigne, F. A., Le Roy, E., Lechtenfeld, O. J., Lee, J. M., Lherminier, P., Little, S., López-Lora, M., Lu, Y., Masque, P., Mawji, E., Mcclain, C. R., Measures, C., Mehic, S., Barraqueta, J. L. M., van der Merwe, P., Middag, R., Mieruch, S., Milne, A., Minami, T., Moffett, J. W., Moncoiffe, G., Moore, W. S., Morris, P. J., Morton, P. L., Nakaguchi, Y., Nakayama, N., Niedermiller, J., Nishioka, J., Nishiuchi, A., Noble, A., Obata, H., Ober, S., Ohnemus, D. C., van Ooijen, J., O'Sullivan, J., Owens, S., Pahnke, K., Paul, M., Pavia, F., Pena, L. D., Peters, B., Planchon, F., Planquette, H., Pradoux, C., Puigcorbé, V., Quay, P., Queroue, F., Radic, A., Rauschenberg, S., Rehkämper, M., Rember, R., Remenyi, T., Resing, J. A., Rickli, J., Rigaud, S., Rijkenberg, M. J., Rintoul, S., Robinson, L. F., Roca-Martí, M., Rodellas, V., Roeske, T., Rolison, J. M., Rosenberg, M., Roshan, S., Rutgers van der Loeff, M. M., Ryabenko, E., Saito, M. A., Salt, L. A., Sanial, V., Sarthou, G., Schallenberg, C., Schauer, U., Scher, H., Schlosser, C., Schnetger, B., Scott, P., Sedwick, P. N., Semiletov, I., Shelley, R., Sherrell, R. M., Shiller, A. M., Sigman, D. M., Singh, S. K., Slagter, H. A., Slater, E., Smethie, W. M., Snaith, H., Sohrin, Y., Sohst, B., Sonke, J. E., Speich, S., Steinfeldt, R., Stewart, G., Stichel, T., Stirling, C. H., Stutsman, J., Swarr, G. J., Swift, J. H., Thomas, A., Thorne, K., Till, C. P., Till, R., Townsend, A. T., Townsend, E., Tuerena, R., Twining, B. S., Vance, D., Velazquez, S., Venchiarutti, C., Villa-Alfageme, M., Vivancos, S. M., Voelker, A. H., Wake, B., Warner, M. J., Watson, R., van Weerlee, E., Alexandra Weigand, M., Weinstein, Y., Weiss, D., Wisotzki, A., Woodward, E. M. S., Wu, J., Wu, Y., Wuttig, K., Wyatt, N., Xiang, Y., Xie, R. C., Xue, Z., Yoshikawa, H., Zhang, J., Zhang, P., Zhao, Y., Zheng, L., Zheng, X. Y., Zieringer, M., Zimmer, L. A., Ziveri, P., Zunino, P., and Zurbrick, C. (2018). The GEOTRACES Intermediate Data Product 2017. *Chemical Geology*, 493(June):210–223.

Scholten, J. C., Pham, M. K., Blinova, O., Charette, M. A., Dulaiova, H., and Eriksson, M. (2010). Preparation of Mn-fiber standards for the efficiency calibration of the delayed coincidence counting system (RaDeCC). *Marine Chemistry*, 121(1-4):206–214.

Selzer, S., Annett, A. L., and Homoky, W. B. (2021). RaDeCC reader: Fast, accurate and automated data processing for Radium Delayed Coincidence Counting systems. *Computers & Geosciences*, page 104699.

Seyfried Jr, W., Pester, N. J., Ding, K., and Rough, M. (2011). Vent fluid chemistry of the Rainbow hydrothermal system (36 N, MAR): Phase equilibria and in situ pH controls on subseafloor alteration processes. *Geochimica et Cosmochimica Acta*, 75(6):1574–1593.

Sheridan, R., Houtz, R., Drake, C., and Ewing, M. (1969). Structure of continental margin off Sierra Leone, West Africa. *Journal of geophysical Research*, 74(10):2512–2530.

Speer, K. G. and Rona, P. A. (1989). A model of an Atlantic and Pacific hydrothermal plume. *Journal of Geophysical Research: Oceans*, 94(C5):6213–6220.

Stachelhaus, S. L. and Moran, S. B. (2012). A simple differential diffusion model to account for the discrepancy between [superscript¿ 223Ra-and [superscript¿ 224Ra-based eddy diffusivities. *Journal of Geophysical Research. Oceans*, 117(3).

Stichel, T., Pahnke, K., Duggan, B., Goldstein, S. L., Hartman, A. E., Paffrath, R., and Scher, H. D. (2018). TAG plume: Revisiting the hydrothermal neodymium contribution to seawater. *Frontiers in Marine Science*, 5:96.

Szitkar, F. and Dyment, J. (2015). Near-seafloor magnetics reveal tectonic rotation and deep structure at the TAG (Trans-Atlantic Geotraverse) hydrothermal site (Mid-Atlantic Ridge, 26 N). *Geology*, 43(1):87–90.

Tagliabue, A., Bopp, L., Dutay, J.-C., Bowie, A. R., Chever, F., Jean-Baptiste, P., Bucciarelli, E., Lannuzel, D., Remenyi, T., Sarthou, G., et al. (2010). Hydrothermal contribution to the oceanic dissolved iron inventory. *Nature Geoscience*, 3(4):252–256.

Tamborski, J., Bejannin, S., Garcia-Orellana, J., Souhaut, M., Charbonnier, C., Anschutz, P., Pujo-Pay, M., Conan, P., Crispi, O., Monnin, C., et al. (2018). A comparison between water circulation and terrestrially-driven dissolved silica fluxes to the Mediterranean Sea traced using radium isotopes. *Geochimica et Cosmochimica Acta*, 238:496–515.

Tamborski, J., van Beek, P., Conan, P., Pujo-Pay, M., Odobel, C., Ghiglione, J. F., Seidel, J. L., Arfib, B., Diego-Feliu, M., Garcia-Orellana, J., Szafran, A., and Souhaut, M. (2020). Submarine karstic springs as a source of nutrients and bioactive trace metals for the oligotrophic Northwest Mediterranean Sea. *Science of the Total Environment*, 732:1–14.

Taylor, S. R. and McLennan, S. M. (1985). The continental crust: its composition and evolution.

Tian, L.-L., Zeng, Z., Nan, X.-Y., Yu, H.-M., and Huang, F. (2019). Determining Ba isotopes of barite using the Na 2 CO 3 exchange reaction and double-spike method by MC-ICP-MS. *Journal of Analytical Atomic Spectrometry*, 34(7):1459–1467.

Tieman, Z. G., Stewart, B. W., Capo, R. C., Phan, T. T., Lopano, C. L., and Hakala, J. A. (2020). Barium isotopes track the source of dissolved solids in produced water from the unconventional Marcellus Shale gas play. *Environmental Science & Technology*, 54(7):4275–4285.

Toner, B. M., Fakra, S. C., Manganini, S. J., Santelli, C. M., Marcus, M. A., Moffett, J. W., Rouxel, O., German, C. R., and Edwards, K. J. (2009). Preservation of iron (II) by carbon-rich matrices in a hydrothermal plume. *Nature Geoscience*, 2(3):197–201.

Van De Flierdt, T., Pahnke, K., Amakawa, H., Andersson, P., Basak, C., Coles, B., Colin, C., Crocket, K., Frank, M., Frank, N., et al. (2012). GEOTRACES intercalibration of neodymium isotopes and rare earth element concentrations in seawater and suspended particles. Part 1: reproducibility of results for the international intercomparison. *Limnology and Oceanography: Methods*, 10(4):234–251.

Von Allmen, K., Böttcher, M. E., Samankassou, E., and Nägler, T. F. (2010). Barium isotope fractionation in the global barium cycle: First evidence from barium minerals and precipitation experiments. *Chemical Geology*, 277(1-2):70–77.

Von Damm, K. L., Edmond, J. M., Measures, C. I., and Grant, B. (1985). Chemistry of submarine hydrothermal solutions at Guaymas Basin, Gulf of California. *Geochimica et Cosmochimica Acta*, 49(11):2221–2237.

Walter, H., Van der Loeff, M. R., and Hoeltzen, H. (1997). Enhanced scavenging of 231Pa relative to 230Th in the South Atlantic south of the Polar Front: Implications for the use of the 231Pa/230Th ratio as a paleoproductivity proxy. *Earth and Planetary Science Letters*, 149(1-4):85–100.

Watson, A. J. and Ledwell, J. R. (2000). Oceanographic tracer release experiments using sulphur hexafluoride. *Journal of Geophysical Research: Oceans*, 105(C6):14325–14337.

Zheng, X.-Y., Plancherel, Y., Saito, M. A., Scott, P. M., and Henderson, G. M. (2016). Rare earth elements (REEs) in the tropical South Atlantic and quantitative deconvolution of their non-conservative behavior. *Geochimica et Cosmochimica Acta*, 177:217–237.